HARNESSING NON-COVALENT INTERACTIONS FOR FUNCTIONAL ORGANIC MATERIALS

A Dissertation

by

TIANYU YUAN

Submitted to the Office of Graduate and Professional Studies of
Texas A&M University
in partial fulfillment of the requirements for the degree of

DOCTOR OF PHILOSOPHY

Chair of Committee,	Lei Fang
Committee Members,	Sarbajit Banerjee
	Zhengdong Cheng
	Jodie Lutkenhaus
Head of Department,	Ibrahim Karaman

August 2018

Major Subject: Materials Science and Engineering

ABSTRACT

Non-covalent interactions play a crucial role in developing functional organic materials. As non-covalent interactions are reversible, dynamic and responsive to environment, multifunctional materials with excellent processability and recyclability can be designed and developed utilizing these adaptable forces. In this dissertation, different types of non-covalent interactions were harnessed in developing new functional organic materials which (i) exhibit tunable thermochromism based on the competing charge transfer interactions, (ii) composed of enantiomerically pure macroscopic helices desirable for chiral applications, and (iii) possess conjugated, rigid molecular backbones and regulated intermolecular bonds suitable for extreme operating or processing conditions.

The dissertation begins with a brief introduction of different non-covalent interactions and how they were employed in functional materials. My argument then moves on to examples demonstrating how a variety of non-covalent interactions can be used in developing new functional organic materials. In the first example, a series of donor-acceptor based thermochromic materials were designed and synthesized. These materials can be assembled in water, and solution-processed to form patterns, thin films and aerogels with a reversible thermochromic property. The color transition of donor-acceptor assemblies is resulted from the competing $\pi \rightarrow \pi^*$ and $n \rightarrow \pi^*$ charge transfer (CT) interactions. To further control the thermochromic properties of these materials, a wide range of π-electron rich donors, halogen counterions and π-electron poor acceptors have been selected and synthesized. Mechanistic studies to further understand the donor-acceptor self-assembly and color changing processes have also been conducted. Moreover, a facile method to prepare

macroscopic helical architectures with controlled handedness was introduced. The feasibility in forming large-scale enantiomerically pure helices and the chiral memory effects of these supramolecular self-assemblies are of great interest for future applications in chiral separation and catalysis. In the last example, conjugated small molecules and a conjugated ladder polymer possessing rigid coplanar backbones and self-complementary intermolecular hydrogen bonds have been developed. The intermolecular π─π interactions and hydrogen bonds of the ladder polymer rendered its excellent resistance to organic solvents, aqueous acids, and thermal treatments. This unique property allows for developments of robust polymer materials for applications associated with extreme operating or processing conditions.

DEDICATION

Dedicated to my love, Ran and to my parents.

ACKNOWLEDGEMENTS

It would be impossible to complete a journey like this without the help and support from countless people. First and foremost, I would like to express my deepest gratitude and appreciation to my advisor and mentor, Professor Lei Fang, for his guidance, encouragement and support. His vision and wisdom have constantly helped me grow academically, professionally, and personally. I would also like to thank my collaborator Professor Mark Olson at Tianjin University. He offered me precious opportunity to conduct research in his lab and he has taught me so many lessons. I really appreciate him for being not just a tremendous collaborator but also an incredible mentor.

I would also like to thank my thesis committee members. Professor Jodie Lutkenhaus, Professor Zhengdong Cheng and Professor Sarbajit Banerjee for their efforts and time in advising on my research and their generosity for allowing me to use the instruments in their labs.

My colleagues in the Fang research group have made this journey more fun and rewarding than I ever expected. Great thanks to friends and colleagues like Dr. Yang Zou, Dr. Zi-hao Guo, Dr. Yen-hao Lin, Congzhi Zhu, Jongbok Lee, Alexander Kalin, Xiaozhou Ji, Chengxu Wang, Mariela Vazquez, Sai Che, Anthony Mu, Bailey Phillips, Rafael Contrucci, Alexandra Barron and many more than can be reasonably listed.

I would also like to express my gratitude to my collaborators, including Professor Hung-Jue Sue's group, Professor Mohammad Naraghi's group and Professor Shiren Wang's group at Texas A&M University, Professor Hanying Li's group at Zhejiang University,

Professor Zunfeng Liu's group at Nankai University and all the members in the Olson Laboratory.

Lastly, I want to express my love and gratitude to my mother and father, for their unconditional support and love. Also, to my fiancée, Ran, for her love, support and patience. I love you more than I can ever express and I look forward to a lifetime with you.

CONTRIBUTORS AND FUNDING SOURCES

This work was supervised by a dissertation committee consisting of Professor Lei Fang, Professor Jodie Lutkenhaus, Professor Sarbajit Banerjee, and Professor Zhengdong Cheng of the Materials Science and Engineering Department.

Chapters 2-5 of the dissertation were completed by the student in collaboration with Professor Mark A. Olson and his group at Tianjin University, and with Professor Hung-Jue Sue's group at Texas A&M University. Chapters 6-7 of the dissertation were completed by the student, Dr. Yang Zou, Xiaozhou Ji, in collaboration with Professor Mohammad Naraghi of the Department of Aerospace Engineering.

This work was made possible in part by the American Chemical Society Petroleum Research Fund under Grant Number 54249-DN17 and the start-up funds from Texas A&M University. The Grazing Incidence X-ray Diffraction (GIXD) experiments were conducted at Argonne National Laboratory under the Advanced Photon Source user proposal GUP-44660 and GUP-55413.

TABLE OF CONTENTS

Page

LIST OF FIGURES

Page

CHAPTER 1

INTRODUCTION

1.1 General Introduction

Non-covalent interactions are pervasive between atoms and molecules. While comparing with covalent interactions, non-covalent interactions are perceived as weak in strength, yet they play an irreplaceable role in chemistry, physics, biology, and materials science.[1-3] In contrast with covalent interactions that are robust and hard to change, non-covalent interactions are reversible, dynamic, and responsive to the environment, thus are often utilized to develop multifunctional materials with excellent processability and recyclability. Although a single non-covalent bond is weak, in functional organic materials, thousands or even millions of non-covalent bonds work in concert, realizing some functionalities that would not be possible with merely covalent bonds. For example, geckos are known to have a remarkable ability to scale walls and suspend from ceilings. What tool does a gecko use to overcome gravity? It is found that on geckos' feet there are many micro-hairs which are composed of millions of spatulae. These tiny spatulae can generate attractive forces when in contact with the surface owing to different non-covalent interactions.[4-5] While the attractive force that each spatula develops with the surface might seem weak and negligible, the combined force of millions of spatulae on a single gecko foot produces a significant adhesion that supports the gecko's body weight. The reversible nature of non-covalent interactions enables geckos to move freely and rapidly. Should the geckos' foot form covalent bonds with the surface, it would be stuck in one place for its whole life. Another example of the cumulative power of "weak" non-covalent interactions is Kevlar

(poly(1,4-phenylene terephthalamide)). Kevlar possesses an extraordinarily high tensile strength-to-weight ratio and has been used to make bulletproof vests. The multiple non-covalent intermolecular interactions, mainly hydrogen bonds and π-stacking interactions between Kevlar chains, contribute greatly to its exceptional mechanical properties.[6] Multiple (multivalent) non-covalent interactions can be employed to develop a variety of organic engineering materials,[7-9] which in a few cases exhibit robustness similar to covalent arrays.

Non-covalent interactions also play an important role for the construction of functional organic materials that operate in aqueous media.[10-12] Hydrophobic effects, which describe the tendency of water molecules to move away from non-polar interface in order to minimize loss of the hydrogen bond penalty,[13] are the driving force for many processes in biological systems, including protein folding, lipid assembly, and formation of membranes.[14-15] Another non-covalent interaction that is often accompanied with hydrophobic interactions in aqueous solution is π-π interaction. π-π interaction is a special type of electrostatic attraction force that occurs between aromatic system.[16] Depending on the substituents of aromatic molecules, π-π interaction can adopt different directionality. Plane-to-plane or edge-to-plane orientations commonly exist in proteins that contain aromatic amino acids such as phenylalanine, tyrosine, and tryptophan.[17] π-π interactions are typically stronger than the van der Waals and offer a stabilizing force for protein organization and supramolecular structure formation in water.[18]

In this dissertation, two different types of functional organic materials have been developed by utilizing a variety of non-covalent interactions. In the first example, a series of donor-acceptor supramolecular materials with tunable thermochromism has been designed and fabricated based on competing charge-transfer interactions. A short

introduction to supramolecular assemblies and thermochromic materials is given in Section 1.2. In the second example, novel ladder-type small molecules and polymers with intramolecular hydrogen bonds were synthesized and studied. Section 1.3 of this chapter provides brief background information for hydrogen bonds as well as functional materials utilizing hydrogen bonds. The scope of this dissertation is then set forth in Section 1.4.

1.2 Supramolecular Assemblies and Thermochromic Materials

1.2.1 Supramolecular assemblies

Supramolecular assemblies are special types of functional organic materials that are built by non-covalent interactions. Given by the dynamic and reversible nature of non-covalent interactions, supramolecular assemblies possess many intriguing properties such as stimuli-responsiveness, self-healing and excellent processability and recyclability.[19-21] Depending on the different components and types of non-covalent interactions that construct the supramolecular assemblies, they could respond to various external stimuli at the macroscopic scale. For example, most supramolecular assemblies are thermo-responsive, as the weak non-covalent interactions are intrinsically susceptible to temperature change. A lot of supramolecular gels exhibit reversible gel-to-sol-transitions in response to temperature changes, making them promising candidates in a wide range of biomedical and pharmaceutical applications, such as drug delivery, tissue engineering, and regenerative medicine.[22-24] In addition to thermal stimuli, different chemical agents can also alter the chemical environment of supramolecular assemblies and thus influence their properties.[25-27] This chemo-responsiveness of supramolecular assemblies renders them potential candidates in applications like chemical sensing and actuation.

1.2.2 Thermochromic Materials

Thermochromic materials are materials that can change their color in response to different temperatures. To date, a wide range of substances have found to exhibit thermochromism.[28-29] There are numerous inorganic salts which can undergo phase change and concurrent color change after heating.[30-31] For instance, the red tetragonal α phase of HgI_2 reversibly turns yellow at 127 °C, forming a rhombic β phase (Figure 1.1). Similar changes are also observed in some double salts of HgI_2, even at much lower temperatures.[32]

Another well-known case in inorganic thermochromism is that many colored transition metal complexes would undergo color changes with heating. Perhaps the most drastic example of this phenomenon is shown by copper sulfate pentahydrate, which switches from blue crystals to white powder upon heating gently. The white copper sulfate powder can absorb traces amount of water and turn back to a blue color. It is well-recognized that such color change is cause by the d-d adsorption band shifting of copper ions after dehydration/hydration.[32]

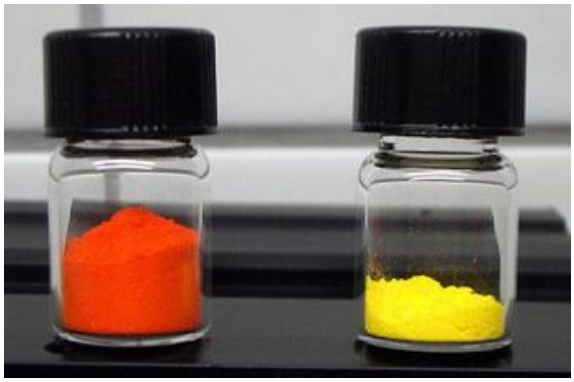

Figure 1.1 Photograph of mercury (II) iodide in different phases: α (left) and β phase (right).

Compared with inorganic thermochromes, organic thermochromes are easy to process and show great tunability; therefore, tremendous progress has been made in developing and commercializing organic thermochromes in the last decades. The most commonly used thermochromic pigments in the market currently are based on leuco dyes and cholesteric liquid crystals.[33]

Leuco dyes are a series of materials that undergo controlled chemical or physical changes resulting in a shift from a colorless state to an intense color.[34] These leuco dyes often have a non-conjugated backbone which can be reversibly converted into an extended conjugated π-system in response to various stimuli (e.g. light, heat, acid and redox species), resulting in the transition between colored and colorless states. For example, fluoran is a widely used commercial thermochromic leuco dye. Fluoran can react with acid to open its lactone rings and extend its π-conjugation, giving rise to color generation. To achieve this thermochromic property, fluoran is often mixed with an acid/developer and a high melting point solvent.[33] For instance, A mixture of colorless fluoran 9 (Figure 1.2), 4,4´-isopropylidenediphenol (BPA) and 1-hexadecanol can reversibly change its color at 48 °C. In this system, BPA is used as acidic compound and 1-hexadecanol is used as solvent. When

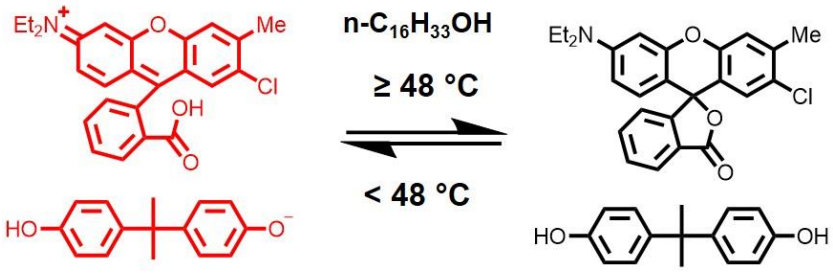

Figure 1.2 Thermochromic mechanism of fluoran 9 with BPA and1-hexadecanol.

the temperature of the system is below the melting point of 1-hexadecanol, fluoran 9 has a stronger affinity with the BPA, resulting the color-formation reaction. When the temperature is increased to above 48 °C, 1-hexadecanol becomes an inhibitor of the color-formation reaction, and fluoran 9 changed to the less conjugated colorless form.[34]

Cholesteric liquid crystals are also important thermochromic materials that have found massive usage in color textiles and other commercial products. In a cholesteric liquid crystal, the molecules are oriented in a preferred direction that varies periodically inside the crystal.[33, 35] (Figure 1.3a) They exhibit different colors at different temperatures due to the selective reflection of specific wavelengths of light from their structures. When the temperature increases, the layer spacing through the crystal changes due to thermal expansion, leading to the generation of various colors. (Figure 1.3b)

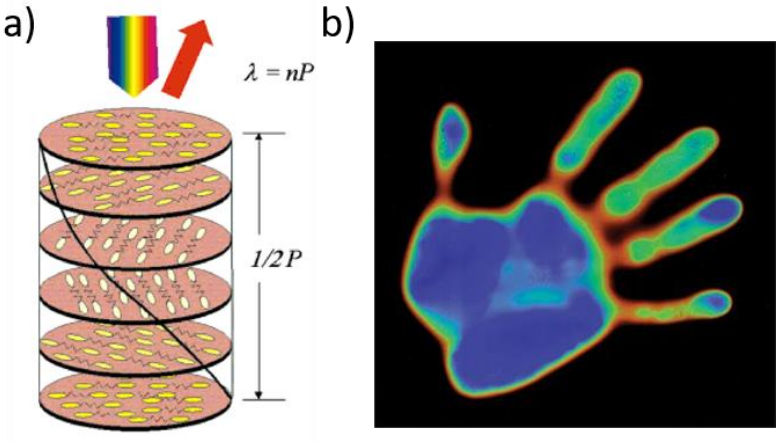

Figure 1.3 Thermochromism of cholesteric liquid crystal. a) Diagram of the structure of the cholesteric phase. Liquid crystals in the cholesteric phase reflect incident white light selectively, provided that the incident light has a wavelength satisfying the Bragg condition, $\lambda = nP$. Reprinted from ref. 35. b) Photograph of a cholesteric liquid crystal film after in contact with human's hand.

As most supramolecular assemblies are intrinsically responsive to temperature change, it seems intuitive that many supramolecular assemblies exhibit thermochromism to some extent. One of most widely studied thermochromic supramolecular assemblies is based on polydiacetylene (PDA). PDA systems consist an extended π-conjugation along their backbone, which absorbs light in the visible spectral region, thereby exhibiting color, in most cases blue at room temperature.[36] Heating the PDAs could lead to twisting of the PDA backbone, changing the amount of conjugation in the system and causing color change. Early reports on PDAs often showed irreversible thermochromism due to the irreversible molecular conformation change. To provide resilience of the PDA backbone and achieve reversible color transitions, different groups with non-covalent binding sites have been introduced to the side chain of PDA to form a supramolecular PDA network.[37-39] Ultrafast color transition was achieved in peptide-modified PDA supramolecular assemblies, where the reversible thermochromism occurs at a temperature change rate of 5000 K s^{-1}, much higher than the typical 1 K s^{-1} of other sensing polymers. Such remarkable chromatism was resulted from the formation of hierarchically assembled structure.[39]

1.3 Hydrogen Bonds and Functional Materials Utilizing Hydrogen Bonds

A hydrogen bond is an electrostatic attraction that forms between covalently-bonded hydrogen atoms and a highly electronegative atom, such as nitrogen (N), oxygen (O), or fluorine (F).[40] The importance of hydrogen bonds cannot be overstated. They are everywhere in our body, from simple molecules such as water to complicated supramolecular structures like proteins. The generation of the double helical structure of DNA also relies on the complementary hydrogen bonds between the base pairs (A-T, C-G).[41-42] Moreover,

hydrogen bonds account for the high boiling point of liquid water, relative to its low molecular mass. Without hydrogen bonds, water would be gas at room temperature and no life would be able to exist.

Not only hydrogen bonds are critical for organisms, but they have also been used to enhance mechanical properties and heat transport of functional materials. Recent studies found that the hydrogen bonds in the beta sheet of a protein in spider silk makes it a superior material with excellent mechanical properties as well as thermal conductivity.[43-44] Small molecules or polymers with strong complementary hydrogen bonds have also been synthesized to further construct supramolecular materials.[45-46] One of the pioneering work was conducted by Meijer and coworkers[47] in which they developed a unit which could form four hydrogen bonds, known as 2-ureido-4[1H]-pyrimidinone (UPy) (Figure 1.4). The self-complementary hydrogen bonds formed by UPy units have very high dimerization association constants (K_{dim} = $6*10^8$ M^{-1} in toluene) and a long lifetime on the order of seconds. [48] Application of these H-bonding units as associating end-groups in multifunctional molecules has resulted in the formation of supramolecular polymers with a molecular weight of more than 500,000 daltons at room temperature. Moreover, such Upy groups can be employed in the chain extension of telechelic polysiloxanes, polyethers, polyesters, poly(ethylene/butylenes), and polycarbonates and build supramolecular polymers.[46] The viscosities of these supramolecular polymers had a strong dependence to the temperature: a small increase in temperature led to a large reduction in viscosity, allowing for facile processing and application of these materials.

Hydrogen bonds have also been engaged to develop materials with self-healing properties. Leibler and coworkers reported a self-healing supramolecular material crosslinked by fatty dimer acids and urea based on hydrogen bonds.[49] This material showed similar mechanical behavior compared to conventional rubbers while exhibiting little creep under load and excellent recoverability. The Bao group at Stanford University used hydrogen bonds as the glue to connect different components into a self-healable supramolecular network for electronic skin applications.[50] The hydrogen-bond-crosslinked network achieved a remarkable stretchability (1200%), a high toughness of 12,000 $J \cdot m^{-1}$, and autonomous self-healability even under water. These finding showed that as a dynamic, directional and reversible interaction, hydrogen bonds plays important role in designing and developing functional organic materials.

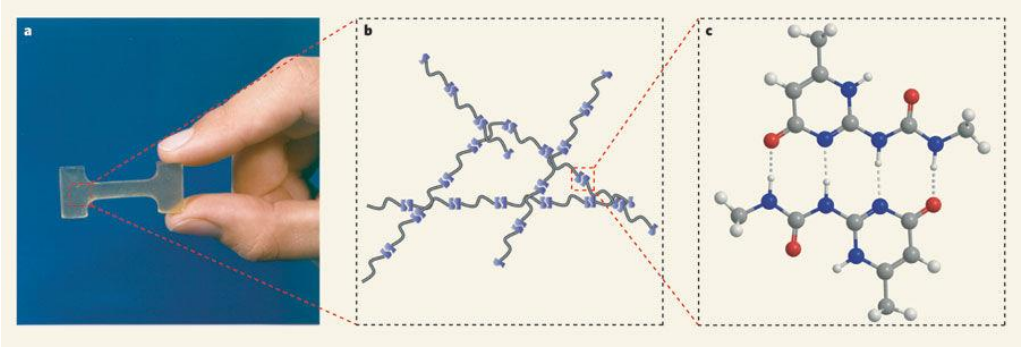

Figure 1.4 a, Photograph of a dog-bone sample made from a supramolecular polymer. b, The molecular structure is a network of monomers connected by hydrogen bonds. Each monomer consists of a hydrocarbon chain with UPy at each end. c, The UPy units form hydrogen bonds to each other (dotted lines). The monomers therefore spontaneously self-assemble to form the polymeric network. Carbon atoms are shown in grey; nitrogen in blue; oxygen in red; and hydrogen in white. Reprinted from ref. 46.

CHAPTER 2

VERSATILE THERMOCHROMIC SUPRAMOLECULAR MATERIALS BASED ON COMPETING CHARGE TRANSFER INTERACTIONS*

2.1 Introduction

On account of the commercial success of products such as the liquid crystal-based colour changing mood rings of the 1970's, the crystal violet lactone-based hyper colour t-shirts of the early 1990's, and the more recent research accounts of polydiacetylene derivatives exhibiting colorimetric change in response to temperature, the phenomenon of thermochromism is met with much intrigue both in and out of academic and industrial circles.[28-29, 51-52] Notwithstanding the obvious industrial applications for thermochromes in the development of imaging and sensing materials, examples of organic thermochromes that can be easily operated and/or processed from environmentally friendly solvents are few and far between. Supramolecular assemblies as a new class of promising organic materials could potentially be operated in a scalable and sustainable manner.[53-55] On account of the nature of non-covalent interactions, robust reversible stimuli-responses can be imparted into the functionalities of supramolecular assemblies.[56-58] As a result, these prescribed performance characteristics can be integrated together in supramolecular materials.

Supramolecular materials are built through pre-organized non-covalent interactions of building blocks. Their self-assembling nature can be tuned by temperature changes,[59-61]

* Part of this section is reprinted with permission from Versatile Thermochromic Supramolecular Materials Based on Competing Charge Transfer Interactions by Yuan, T. et al., *Advanced Functional Materials*, **2016**, 26, 8604-8612. Copyright 2016 by John Wiley and Sons.

pH changes,[62-64] photo-stimuli,[65-67] or redox species.[68-69] Controllable supramolecular materials have previously demonstrated a wide range of promising applications including drug delivery, template-directed synthesis, stimuli-responsive coatings, and cell imaging.[55, 70-73] A variety of non-covalent interactions, such as hydrogen bonding,[74-78] electrostatic forces,[72, 79] n $\rightarrow$ π^* interactions, and π-π stacking[80-81] have been utilized to construct supramolecular assemblies. Among them, n $\rightarrow$ π^* or π $\rightarrow$ π^* charge transfer (CT) interactions, which are capable of occurring in a multitude of solvents, were employed to construct superstructures in a directional nature while often resulting in a vivid concurrent colour change.[56, 82-85]

In many of the donor-acceptor CT complexes, bipyridinium moieties have largely been used as the acceptor component.[86] Bipyridinium derivatives are easily synthesized with a variety of functional groups and are strongly electron deficient, capable of engaging in π $\rightarrow$ π^* CT interactions with π-electron rich aromatics and n $\rightarrow$ π^* CT interactions with their counterions.[87-90] More interestingly, bipyridinium–based polyelectrolytes have been reported to exhibit thermochromic phenomena in the solid-state upon hydration and dehydration. Stupp[91] *et al*. demonstrated that a series of polycations with quaternary nitrogens in the repeating unit, obtained from the condensation of 4,4'-bipyridine with aromatic dihalides, exhibit a reversible bathochromic colour change when heated above 100 °C. This phenomenon was proven to result from the destruction/restoration of n $\rightarrow$ π^* CT interactions between the bipyridinium polycations and their corresponding halide counterions during hydration and dehydration of the ion-pair. It is indeed surprising to find that bound water is capable of influencing the donor-acceptor CT electronic transitions of organic compounds in

the solid-state to such an extent that results in the dramatic changing of their colours. This is a well know mechanism for the thermochromism of inorganic salt hydrates,[30] but is rarely reported for organic materials.

Here, we report a class of CT-based supramolecular materials that exerts reversible thermochromism in response to changes in temperature in the solid-state. In this system, a tetracationic bis-bipyridinium derivative serves as the charge acceptor, while the π-electron rich naphthalene derivatives and bromide counterions act as competing CT donor units. The strength of the competing CT interactions could be controlled by the hydration state of the supramolecular assemblies, leading to thermochromic supramolecular materials featuring; aqueous solution processability, versatile colour selections, scalability, and recyclability.

2.2 Result and Discussion

2.2.1 Supramolecular Assemblies Formation

We have recently shown that tetracationic bis-bipyridiniun-based gemini self-assemblies can undergo templated micellization when combined with aromatic π-electron rich molecules, leading to pronounced morphological changes of the assembled micellar superstructure in water.[92-93] Under the influence of donor-acceptor CT interactions and hydrophobic forces, di(ethylene glycol)-disubstituted 1,5-dihydroxynaphthalene (DNP-DEG) was driven to intercalate the bipyridinium units of the gemini amphiphiles which had the effect of augmenting the micellar aggregation behavior. A significant enhancement in the bis-bipyridinium-based self-assembly was realized by introducing an additional phenyl ring into the ρ-xylyl bridge through the quaternization of mono-undecylated bipyridine, with 4,4′-bis(bromomethyl)-biphenyl. **1**•4Br was isolated in 95% yield in multi-gram qualities as the

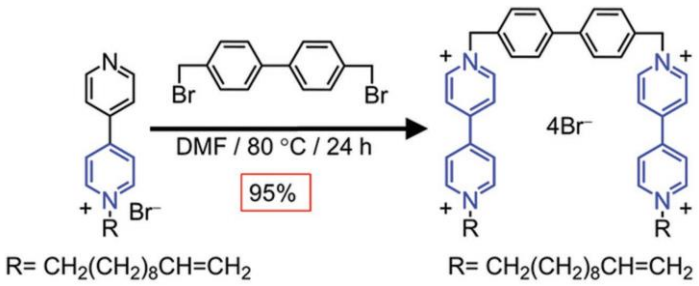

Scheme 2.1 Synthesis of **1**•4Br.

tetrabromide salt (Scheme 2.1). Upon dissolving **1**•4Br with 1 or more equivalents of DNP-DEG in water at 60 ˚C, a dramatic colour change (λ_{max} = 481 nm in water) occurred arising from the formation of a donor-acceptor CT complex between the bipyridinium head groups of **1**•4Br and DNP-DEG (Figure 2.1). The formation of the supramolecular assembly in solution was further confirmed by ^{1}H NMR spectroscopy in D_2O, by which shifts of the α and β aromatic protons of the bipyridinium recognition units were accompanied by substantial upfield shifts of the DNP-DEG aromatic protons (Figure 2.10 and 2.11). This effect is frequently observed in donor-acceptor π-π stacking systems due to CT interactions which give rise to aromatic electron shielding.[82] In our case, it indicated that the DNP-DEG molecule has adopted a face-to-face π-π stacking geometry with the bipyridinium units, with additional equivalents of DNP-DEG stacked in between two **1**•4Br molecules.

Upon cooling to room temperature, the **1**•4Br⊃DNP-DEG solution began to undergo gelation forming fiber-like superstructures comprised of the supramolecular complexes. The

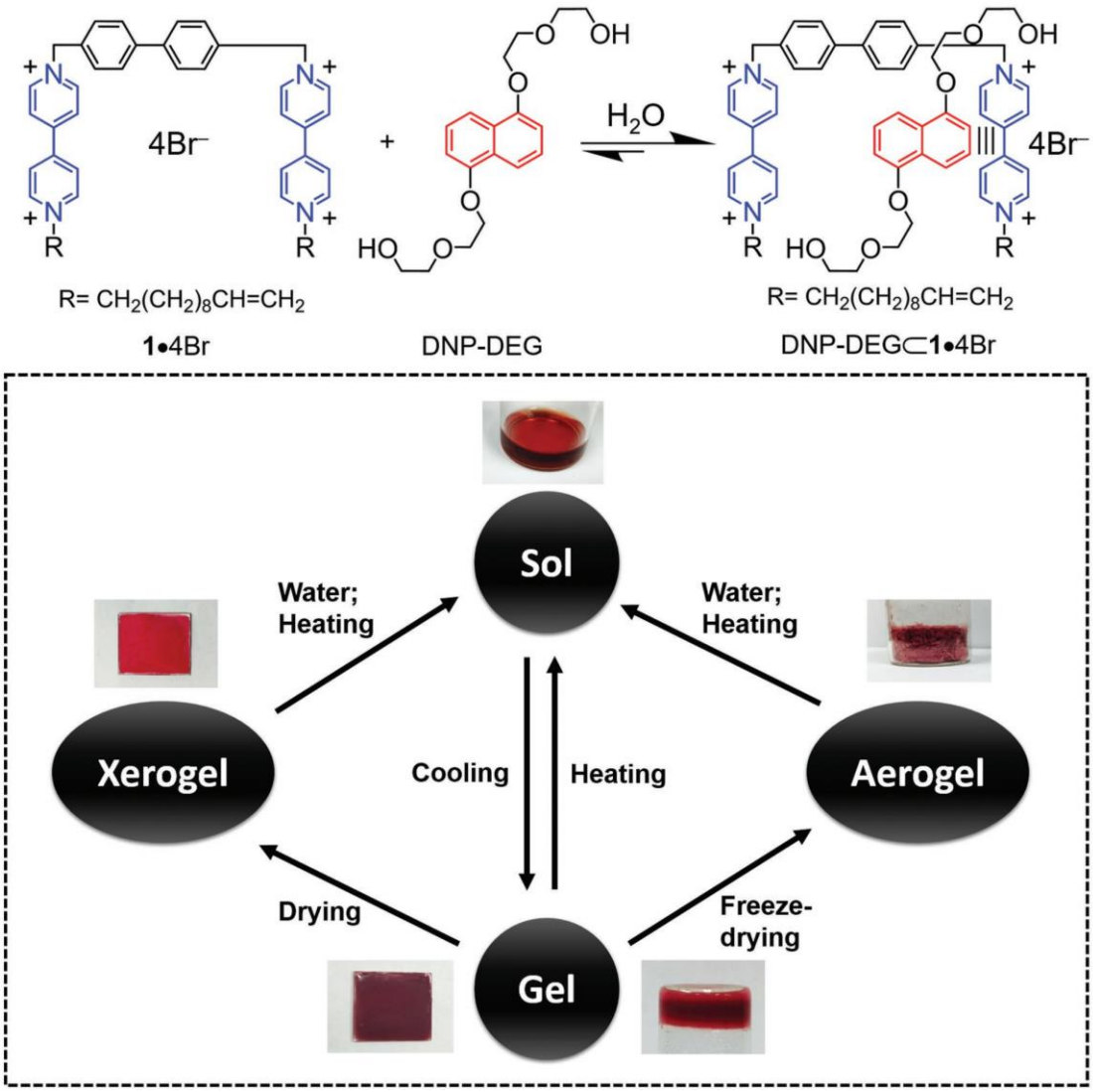

Figure 2.1 Top) Complex formation between the tetracationic host amphiphile **1**•4Br and DNP-DEG. Bottom) Schematic diagram illustrating the recyclability of the **1**•4Br⊃DNP-DEG thermochromic material. The material is easily recycled by adding hot water to the xerogel film/aerogel to dissolve the **1**•4Br⊃DNP-DEG complex. The regenerated aqueous solution had the same property as the original solution and can be used to prepare new thermochromic xerogel films/aerogels.

non-covalent nature of the CT and hydrophobic interactions drive the formation of the host-guest complex between **1**•4Br and DNP-DEG and their subsequent assembly into fibrous

superstructures. As a result, the sol-gel transition inside of the gel matrix is reversible under thermal treatment (Figure 2.1), making it possible for these donor-acceptor fibrous superstructures to be cast into uniform xerogel thin films at elevated temperatures. Supramolecular aerogels can also be prepared by freeze-drying the 1•4Br⊃DNP-DEG hydrogel, demonstrating the excellent processability of 1•4Br⊃DNP-DEG supramolecular assemblies. Moreover, by virtue of the reversible sol-gel transition,[94] such supramolecular materials can be easily recycled at all stages of their manufacture (Figure 2.1).

The fibrous morphology of 1•4Br⊃DNP-DEG in the solid state was confirmed by polarized optical microscopy, atomic force microscopy (AFM) and scanning electron microscopy (SEM). Polarized optical microscopy revealed that the fibers exhibit birefringence, indicating that the fibers were highly crystalline and well ordered (Figure 2.2a). AFM images of the thin films affirmed that the material is comprised of fibers with high aspect ratios and long lengths (Figure 2.2b). Interestingly, it was also discovered via

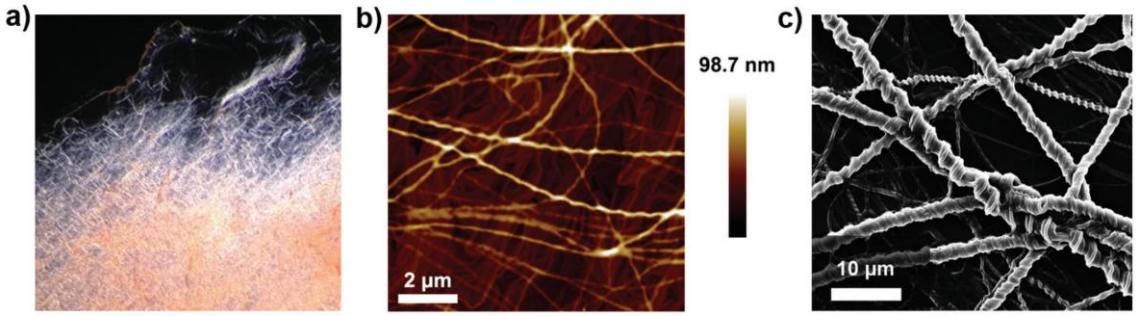

Figure 2.2 a-c) Microscopy images of the 1•4Br⊃DNP-DEG nanofibers and fiber bundles. a) Polarized optical microscope image at 100x magnification. b) Tapping-mode AFM height image of a 1•4Br⊃DNP-DEG film formed by spin-coating. c) SEM image on a drop-casted 1•4Br⊃DNP-DEG film showing the helical structure of the nanofiber complexes.

SEM imaging that the fibers composing the hydrogel matrix were helical, including a racemic amount of both left-handed and right-handed helical fibers（Figure 2.2c and Figure 2.12). Synchrotron small-angle X-ray scattering (SAXS) carried out on a sample of 1•4Br⊃DNP-DEG hydrogel at 15 °C revealed well-defined Bragg scattering peaks in the SAXS pattern indicating hexagonal packing in the highly crystalline gel phase. Specifically, the scattering peaks at q = 0.15, 0.25. 0.29, 0.37, 0.47 and 0.55 A^{-1} match the hexagonal indexing ratio of 1:√3:2:√7:3:√12, suggesting that the helical fibers are comprised of hexagonally ordered elongated micelle aggregates with a diameter of 4.4 nm (Figure 2.3a).[95-97] The symmetry breaking phenomenon in which achiral building blocks self-assemble into chiral supramolecular structures has been reported for several self-assembled molecular systems including aggregates and supramolecular gels.[55, 98-101] Previous studies on a similar donor-acceptor catenane found that incorporating a DNP unit into the molecular structure and/or superstructure introduces an element of nontopological symmetry breaking based on the possible conformations adopted by the π-stacked units.[102-107] With regards to the aggregates formed by **1**•4Br⊃DNP-DEG, the formation of the chiral helical aggregates is likely originated from the two possible offset[16] π-π stacking geometries that the DNP-DEG unit can adopt when intercalated and stacked with the π-acceptor **1**•4Br (Figure 3.3b).[102-107] Thus, upon complexation, the superstructure, **1**•4Br⊃DNP-DEG, possesses no elements of symmetry and is *a priori*, chiral. Left-handed (M) and right-handed (P) helical nanofibers were first generated racemically depending on the direction of the helical rotation adopted by the donor and acceptor layers. The chirality present in the superstructure was then most

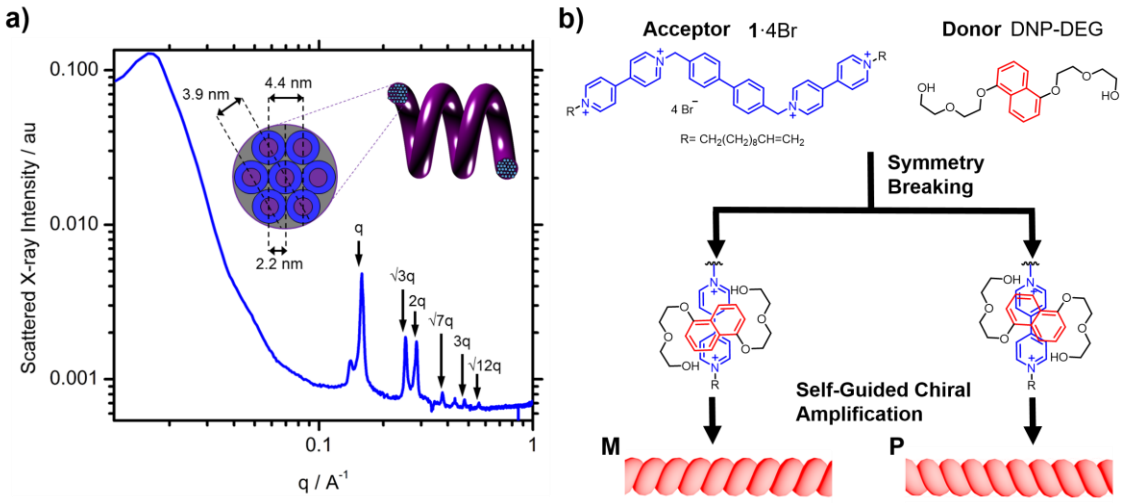

Figure 2.3 a) Synchrotron small angle X-ray scattering (SAXS) diffraction pattern obtained from a sample of **1**•4Br⊃DNP-DEG hydrogel (8 mM, 15 °C) composed of helical fibers. The Bragg scattering peaks indicated by arrows at q = 0.15, 0.25. 0.29, 0.37, 0.47 and 0.55 A^{-1} indicate hexagonal packing in the **1**•4Br⊃DNP-DEG hydrogel. b) Schematic representation of the symmetry breaking conformations of the donor-acceptor complex leading to the formation of fibers of different helical chirality.

likely amplified during fiber growth and fiber-fiber bundling, resulting in larger helical fibers (Figure 2.3b).

2.2.2 Thermochromism of 1•4Br⊃DNP-DEG Complex in Solid State

The meritorious feature of the **1**•4Br⊃DNP-DEG donor-acceptor complex is its thermochromic property in the solid state. Hot solutions of the supramolecular assemblies were used as ink to draw images on paper, for example the Texas A&M University logo (Figure 2.4a). The red colour of the image turned yellow after heating the paper to 80 °C. After the paper was removed from the heat, the reverse yellow-to-red colour change took place. Likewise, **1**•4Br⊃DNP-DEG aerogels also exhibited thermochromism, undergoing a

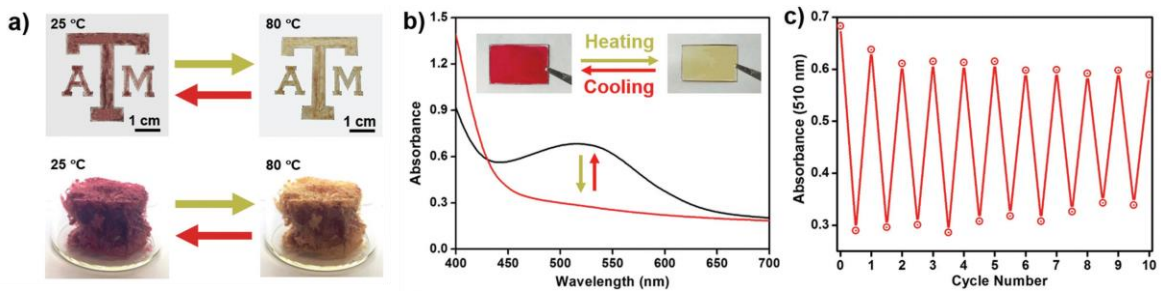

Figure 2.4 Thermochromic behaviour of **1**•4Br⊃DNP-DEG-based supramolecular materials in the solid state. a) Photographs of a **1**•4Br⊃DNP-DEG-based supramolecular materials inked pattern (top) and aerogel (bottom) at 25 °C and at the thermochromic transition temperature of 80 °C. b) Visible absorption spectra of a prepared thin film at 20 °C and 80 °C. Inset: photographs of the thin xerogel film on a glass substrate taken below and above the thermochromic transition temperature. For the cooling process the thin film was placed in a humid environment. c) Absorbance of a thin film of supramolecular assemblies at 510 nm during 10 thermal switching cycles from 20 °C to 80 °C.

colour transition from red to light yellow at 80 °C (Figure 2.4a). The colour changing process of the thin film was captured by polarized optical microscope and infrared thermography (Figure 2.15). We further quantified its thermochromic behaviour by UV-Vis spectroscopy (Figure 2.4b) whereby the $\pi \rightarrow \pi^*$ CT absorption (λ_{max} = 510 nm) disappeared upon reaching the thermochromic transition temperature, while giving rise to a new absorption shoulder peak around 350 nm, corresponding to the $n \rightarrow \pi^*$ CT interaction between the viologen moieties of **1**•4Br and its bromide counterions (Figure 2.17a). This temperature-induced colour change was reversible with little colour bleaching after 10 heating-cooling cycles (Figure 2.4c).

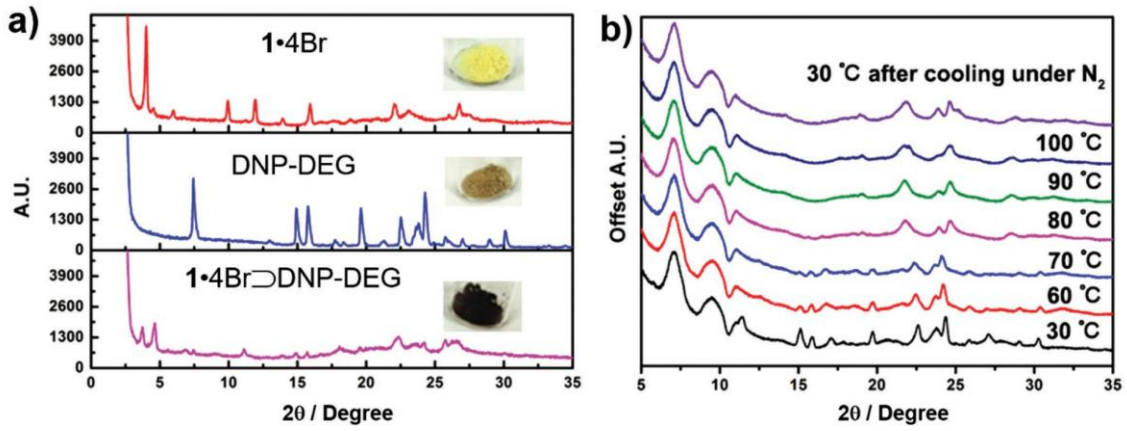

Figure 2.5 Powder x-ray diffraction (PXRD) plot. a) PXRD spectra of compounds **1**•4Br, DNP-DEG and their mixture. The inset photos show the colour of each solid. b) VT-PXRD spectra of the 1•4Br⊃DNP-DEG complex from 30 °C to 100 °C.

2.2.3 Mechanistic Studies

We hypothesized that the thermochromic property of **1**•4Br⊃DNP-DEG manifested on account of the hydration/dehydration of the ion pair, similar to that of $CuSO_4 \cdot 5H_2O$. It is well known that the blue crystals of $CuSO_4 \cdot 5H_2O$ turn white upon the formation of anhydrous $CuSO_4$ after heating. The colour change of $CuSO_4$ results from the absorption d-d band of Cu^{2+} which shifts to the near- infrared region following the removal of coordinated water molecules.[108] A series of experiments were conducted to corroborate the hypothesized thermochromic mechanism of **1**•4Br⊃DNP-DEG. First, a thin film of **1**•4Br⊃DNP-DEG on a glass substrate was placed in a N_2 glove box and heated to 80 °C. The film turned yellow upon heating, but never recovered to the original red colour after cooling to room temperature as a result of the low moisture level in the glove box. The red colour, however, was only restored after the sample was moved into ambient air for several minutes. The recovery

process was much faster (only took 10 seconds) when the sample was exposed to high humidity (Figure 2.13). In addition, powder X-ray diffraction (PXRD) was utilized to study the structural change in the solid state during heating. We first prepared the CT complex in the solid-state whereby **1**•4Br and DNP-DEG in a 1:1 stochiometric ratio were mixed and ground by mortar and pestle. The mixture turned a deep-red colour resembling that of the solution complex and the gel. As shown in Figure 2.5, a drastically different PXRD peak profile of the ground product was observed, compared to those of the individual reactants, confirming that complexation had taken place between the donor and acceptor. A series of variable temperature powder x-ray diffraction (VT-PXRD) tests were subsequently carried out from 30 °C to 100 °C. Diffraction peaks of the complex remained the same from 30-70 °C, suggesting that the donor-acceptor complex did not undergo structural change below 70 °C and was stable. At the thermochromic transition temperature (80 °C), the positions of the diffraction peaks changed substantially in concurrence with the colour change, indicating that the colour change originated from a structural change in the packing of the donor-acceptor charge transfer complex upon the removal of coordinated water molecules. After heating the sample to 100 °C and then cooling to 30 °C under dry N_2, the diffraction peaks of the sample showed little change from the ones seen at 100 °C, agreeing with the fact that the restoration of the crystal packing mode could not take place without the presence of water (Figure 2.5). These phenomena confirmed the important role that water molecules were playing in the observed thermochromism.

Based on the aforementioned experimental results and precedent literature reports,[67, 91, 109-110] the mechanism of the thermochromic behaviour in these materials can be attributed

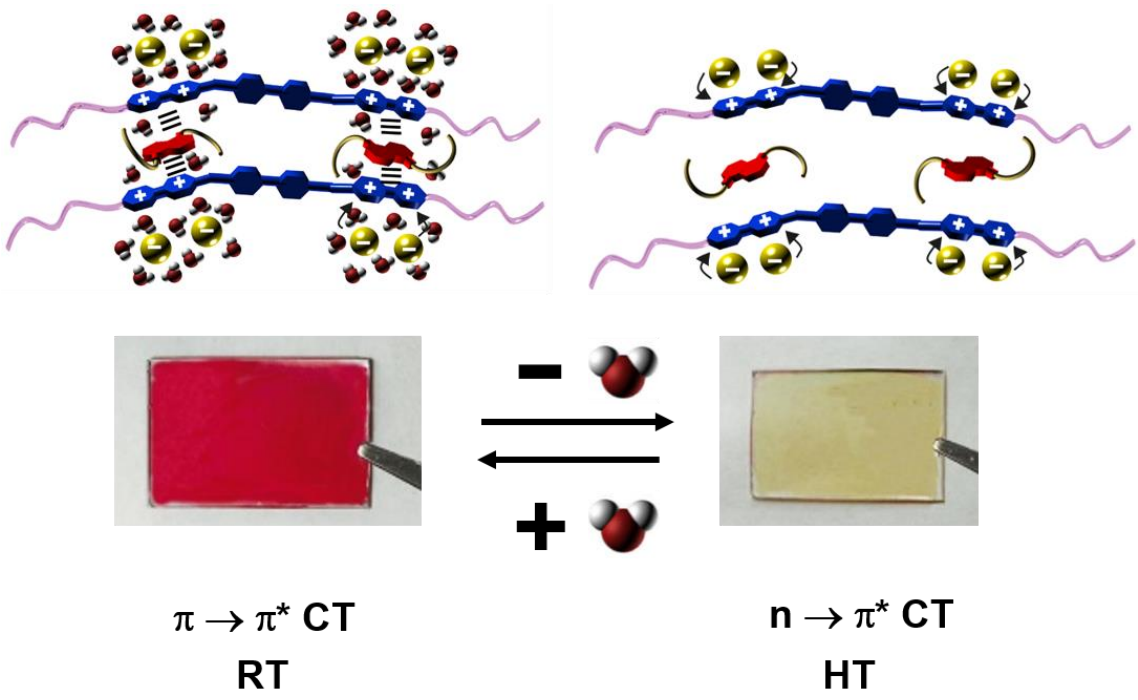

Figure 2.6 Schematic illustration of the proposed solid-state thermochromic mechanism in **1**•4Br⊃DNP-DEG-based supramolecular assemblies alongside the corresponding photographs of the thin film on a glass substrate. At room temperature (top) and under ambient air, waters of hydration are incorporated into the ion-pairs hygroscopically effectively weakening the bromide-to-bipyridinium n → π* CT interaction. Under these conditions the DNP-DEG-to-bipyridinium π → π* CT interaction is dominant giving the thin film its characteristic red colour. Upon heating to the thermochromic transition temperature (bottom) the waters of hydration for the ion-pair are liberated allowing for the bromide-to-bipyridinium n → π* CT interaction to dominate giving the thin film its characteristic yellow colour. Under these conditions strong intermolecular polarization within the ion-pair prevent the bipyridinium from forming addition CT complexes with the neutral π-electron rich DNP-DEG.

to competing CT interactions (Figure 2.6). In this case the donor-acceptor π → π* CT interactions between the π-electron rich DNP-DEG donor and the dicationic viologen acceptors are jockeying for position against the n → π* CT interactions between the viologen units and their bromide counterions. With coordinating water molecules in place hydrating

the ion pairs, the $\pi \rightarrow \pi^*$ CT interaction takes precedence giving rise to a red coloured solid-state complex. After the dissociation of bound water molecules at elevated temperatures, the $n \rightarrow \pi^*$ CT interaction between the bromide anions and the viologen units dominates, resulting in the diminishing of the $\pi \rightarrow \pi^*$ CT band and the corresponding red to yellow colour change. Comparison of the absorption spectrums of a **1**•4Br⊃DNP-DEG thin film measured above the thermochromic transition temperature and a thin film of **1**•4Br in the absence of donor, revealed that both spectrums contain the $n \rightarrow \pi^*$ CT absorption peak around 350 nm which is responsible for the yellow colour change (Figure 2.17b).

2.2.4 Towards Tunable Thermochromism

Owing to the multitudinous selection of π-electron rich donor and π-electron poor acceptor molecules capable of forming supramolecular complexes, the strategy employed herein could lead to the development of a series of thermochromic materials with varying colour transformations. To illustrate the versatility of this approach, we prepared a new supramolecular material using di(ethylene glycol)-disubstituted 1,5-diaminonaphthalene (DAN-DEG) as the donor. DAN-DEG is a more electron-rich donor than DNP-DEG,[111] resulting in a stronger donor-acceptor $\pi \rightarrow \pi^*$ CT interaction. The supramolecular complex between **1**•4Br and DAN-DEG also exhibited reversible sol-gel transition (Figure 2.14) and could be altered, processed into thermochromic thin films. Thin films that formed from **1**•4Br⊃DAN-DEG were visibly green in colour at room temperature due to increased CT interaction and corresponding red-shifted CT absorption band (Figure 2.17a). When heated to 90 °C, the thermochromic transition temperature for this new donor-acceptor pair, the film turned light yellow, mirroring that of **1**•4Br⊃DNP-DEG in the absence of waters of

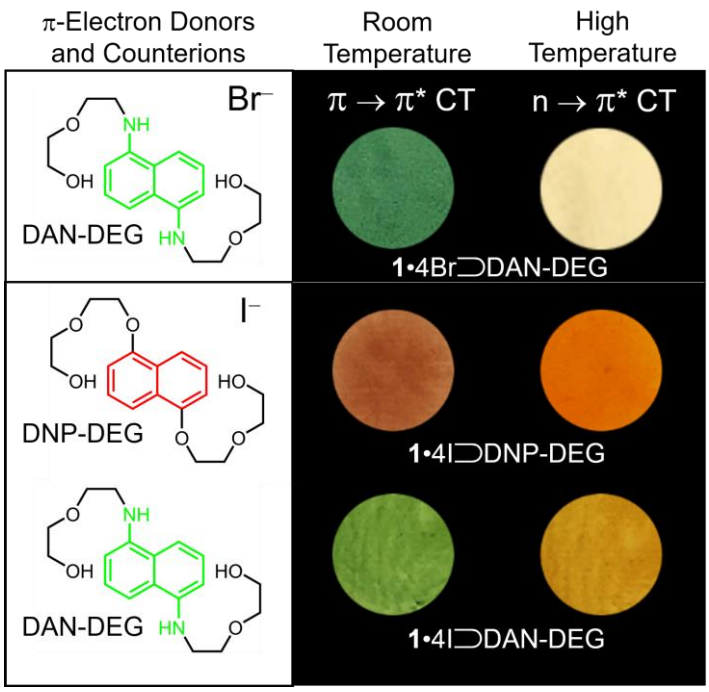

Figure 2.7 Structural formulas and photographs of thermochromic thin films depicting the versatility of the thermochromic supramolecular materials towards tuning both the room temperature and high temperature colour palette. Replacing the neutral donor, DNP-DEG, with the more π-electron rich DAN-DEG, gave rise to green coloured thin films at room temperature (top, bottom), reflecting the DAN-DEG-to-bipyridinium π → π* CT interaction. Counterion exchange of **1**•4Br from the tetrabromide to the tetraiodide gave rise to orange coloured thin films at high temperatures (middle, bottom), corresponding to the iodide-to-bipyridinium n → π* CT interaction.

hydration (Figure 2.7 and Figure 2.17b). Like the 1•4Br⊃DNP-DEG film, the colour of the 1•4Br⊃DAN-DEG film was able to be restored back to green after cooling it to room temperature in ambient air. Similarly, by changing the counterions of the tetracationic amphiphile, 1•4Br, the donor-acceptor n → π* CT interactions could be effectively changing the materials colour at elevated temperatures. To demonstrate this process we prepared 1•4I by counterion exchange. The tetraiodide amphiphile 1•4I itself is visibly orange in the solid

state. Upon complexation with DNP-DEG and DAN-DEG, the resulting supramolecular complexes, 1•4I⊃DNP-DEG and 1•4I⊃DAN-DEG, also gave rise to red and green coloured solutions respectively. These solutions were then casted into thermochromic thin films. When heated above the thermochromic transition temperature of 140 °C, the films turned orange in colour resembling the distinctive colour of the iodide-to-bipyridinium n $\rightarrow$ π^* CT (Figure 2.7). These experimental insights support the conclusion that the colour of the supramolecular assembly film at room temperature is determined by the composition of the acceptor and the π-electron rich donor and their corresponding $\pi \rightarrow \pi^*$ CT interaction. Furthermore, the film's colour after reaching the thermochromic transition temperature, is determined by the composition of the acceptor and counterion pair and their corresponding n $\rightarrow$ π^* CT interaction.

2.3 Conclusion

In conclusion, we have developed a novel class of functional bis-bipyridinium-based supramolecular materials, which can easily be synthesized in a multi-gram scale and processed from water via a reversible sol-gel transition. Self-assembled complexes of amphiphile **1**•4Br with π-electron rich naphthalene-based derivatives resulted in the formation of long helical nanofibers in water. Inks, thin films and aerogels processed from these solutions exhibited dramatic reversible colour changes upon reaching the thermochromic transition temperature. In this system, the tetracationic amphiphile, **1**•4Br, serves as a charge acceptor while π-electron rich molecular templates and halogen counterions participate in the thermochromic mechanism as competing CT donor units. The strength of the competing CT interactions can be actuated based on the hydration state of the

supramolecular assemblies. The removal of coordinating water molecules at elevated temperatures favours ion-pair formation between the bis-bipyridinium groups and their halide counterions, leading to a dehydration induced structural change. Under these conditions, the colour of the thermochromic material is principally derived from n $\rightarrow$ π^* CT interactions between the ion-pair on account of the strong intermolecular polarization which decreases the ability of the bipyridinium groups to form additional CT complexes with neutral π-electron rich donors.[67, 109-110, 112] When the material is then cooled, coordinating water molecules are reincorporated hygroscopically from ambient air, effectively hydrating the ion-pair and shifting the intermolecular polarization towards the $\pi \rightarrow \pi^*$ CT interactions. We effectively demonstrated that based on this mechanism of competing $\pi \rightarrow \pi^*$ with n $\rightarrow$ π^* CT interactions, it is possible to tune the colour observed at room temperature by changing the π-electron donor from DNP-DEG to DAN-DEG and similarly change the high temperature colour by changing the halide counterion from bromide to iodide. As a result of the reversible nature of the non-covalent interactions that bind together the supramolecular assemblies, these thermochromic materials are readily recyclable at all stages of their manufacture. This work lays the foundation for synthesizing a series of supramolecular materials exhibiting tunable thermochromic properties, with hue variation based on a myriad of potential π-electron donor, acceptor and counterion combinations.

2.4 Experimental Section

General Information: Chemicals were purchased from Sigma-Aldrich and used as received without further purification. 4,4'-bis(bromomethyl)-1,1'-biphenyl, DNP-DEG and DAN-DEG were synthesized according to procedure reported in the literature.[103, 111]

Deuterated solvents (Cambridge Isotope Laboratories) for NMR spectroscopic analyses were used as received. ^{1}H and ^{13}C NMR spectra were recorded on a Bruker Avance 300 MHz spectrometer. The ^{13}C NMR spectra were run at 75 MHz. Uv-Vis spectra were measured on a Shimadzu UV-2600 spectrophotometer. Polarized optical microscope images were obtained using an Olympus CX31-P polarizing microscope. Atomic force microscopy (AFM) images were recorded with a Bruker Dimension Icon AFM in a tapping mode and processed using NanoScope Analysis. Powder X-ray Diffraction spectra were acquired on a Bruker D8 Advance. Scanning electron microscopy (SEM) images were taken by a FEI Quanta 600 FE-SEM. Small-angle X-ray scattering (SAXS) measurements were made using the pin-hole set-up at the undulator beamline 12ID-C (12 keV) at the Advanced Photon Source at Argonne National Laboratory. The sample-to-detector distance was such as to provide a detecting range for momentum transfer of 0.01 $Å^{-1} < q < 0.6$ $Å^{-1}$. The scattering vector, q, was calibrated using a silver behenate standard at $q = 1.076$ $Å^{-1}$. The 2D scattering

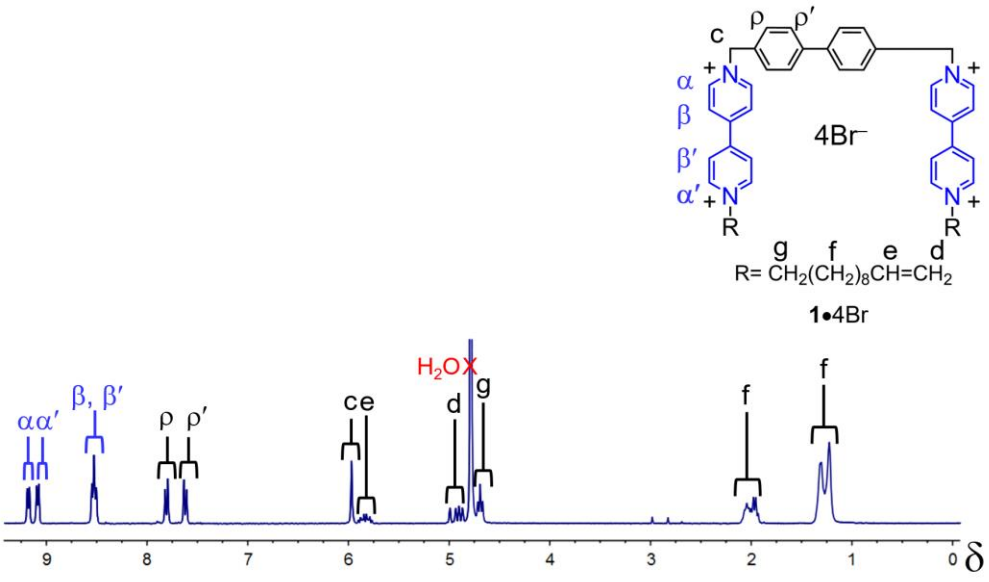

Figure 2.8 The ^{1}H NMR spectra of **1**•4Br (300 MHz, D_2O).

images were azimuthally averaged to produce plots of scattered intensity, $I(q)$, versus scattering vector q, where $q = 4\pi/\lambda(\sin\theta)$.

*Synthesis of **1**•4Br*: Mono-undecylated bipyridine (2.86 g, 7.35 mmol) and 4,4'-bis(bromomethyl)-1,1'-biphenyl (1 g, 2.94 mmol) were combined in dry degassed DMF (100 mL) and the mixture was heated at 80 °C while stirring for 24 h. The reaction mixture was cooled and a yellow precipitate was collected by filtration. The yellow precipitate was then washed with DMF and ethyl ether three times each and dried in vacuo to afford the tetracationic product **1**•4Br (3.14 g, 95%) as a yellow solid. **1**•4Br :Mp: Decomposes at 286–301 °C. ^{1}H NMR (D_2O, 300 MHz, 25 °C): δ = 1.16–1.40 (br d, 24H), 1.92–2.12 (br m, 8H), 4.70 (t, J = 7.30 Hz, 4H), 4.87–5.00 (m, 4H), 5.84 (m, 2H), 5.98 (s, 4H), 7.63 (d, J = 8.22 Hz, 4H), 7.82 (d, J = 8.22 Hz, 4H), 8.54 (t, J = 7.00 Hz, 8H), 9.10 (d, J = 6.97 Hz, 4H), 9.19 (d, J = 6.97 Hz, 4H) ^{13}C NMR (DMF-D7, 100 MHz, 25 °C): δ = 24.99, 27.81, 28.03, 28.10,

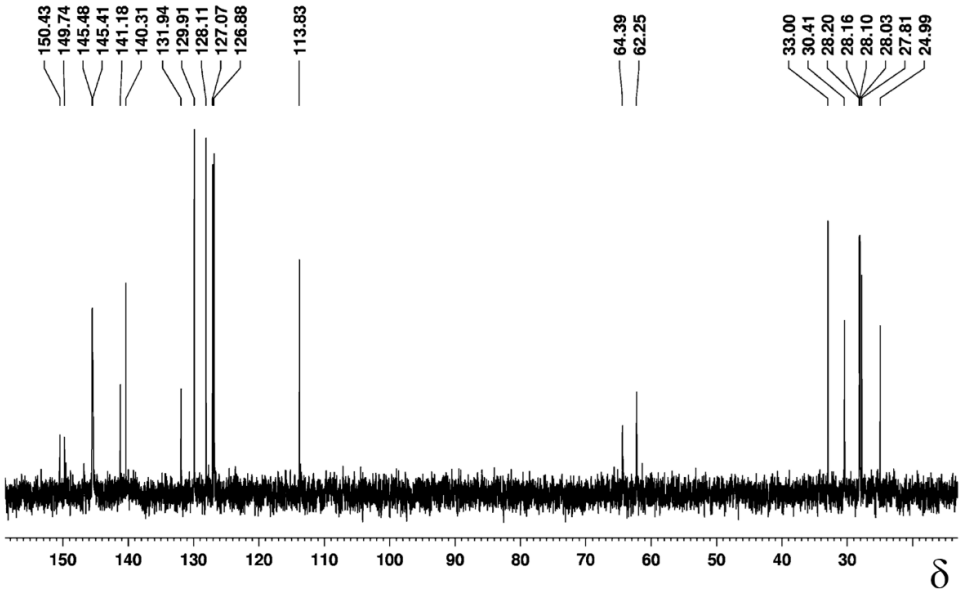

Figure 2.9 The ^{13}C NMR spectra of **1**•4Br (75 MHz, D_2O).

28.16, 28.20, 30.41, 33.00, 62.25, 64.39, 113.83, 126.88, 127.07, 128.11, 129.91, 131.94, 140.31, 141.18, 145.41, 145.48, 149.74, 150.43; HRMS (ESI): m/z calculated for $[M - Br]^+$, $C_{56}H_{70}Br_3N_4$: 1039.31; found: 1039.3072.

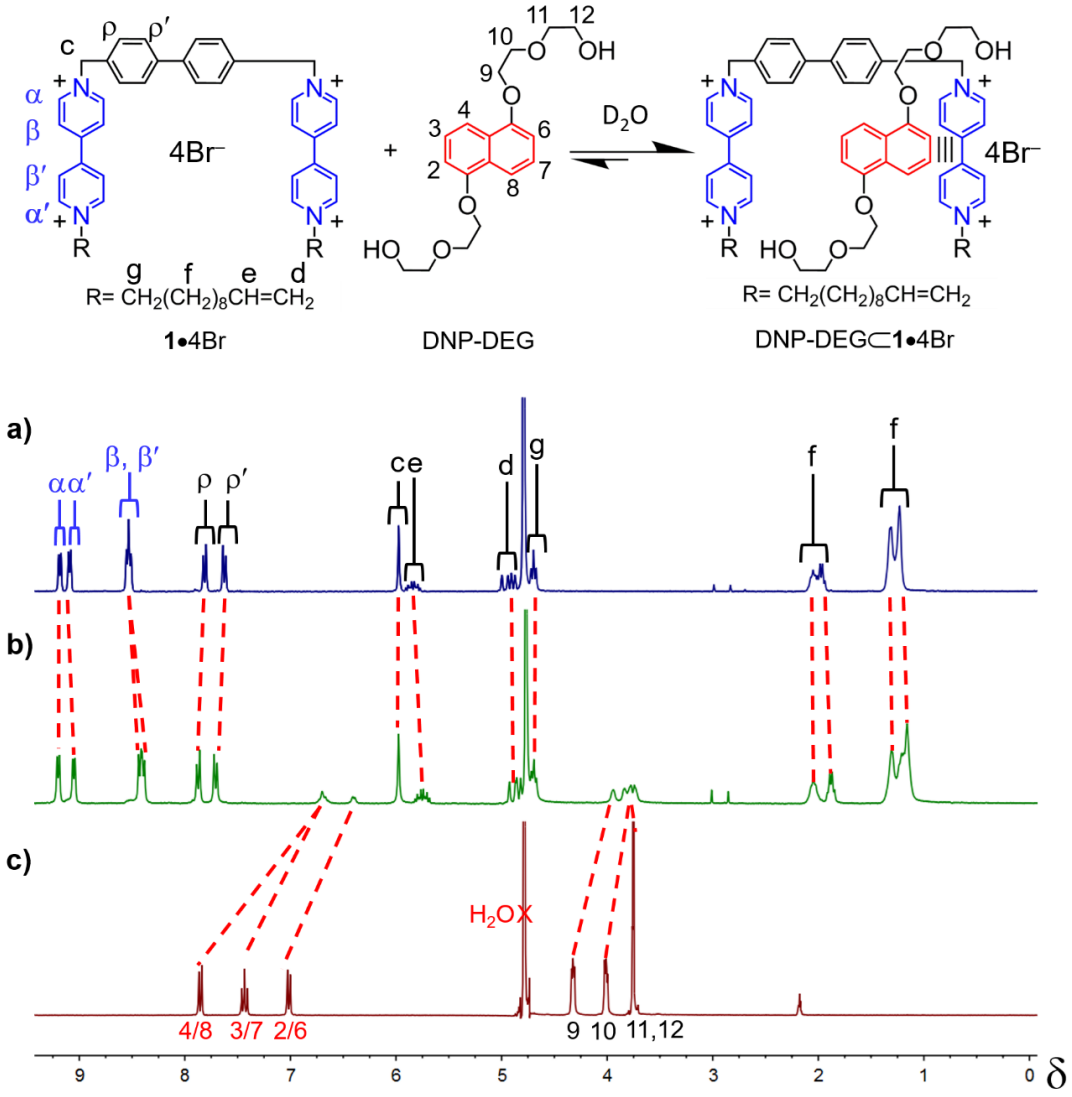

Figure 2.10 Top) Complex formation between the tetracationic host amphiphile **1**•4Br and DNP-DEG. Bottom) ^{1}H NMR spectra of an 8×10^{-3} M solution of **1**•4Br (300 MHz, D_2O) a) Spectrum of **1**•4Br with peak assignments. b) Spectrum of **1**•4Br with 1 equivalent of DNP-DEG taken at 25 °C. c) Spectrum of DNP-DEG.

*Preparation of **1**•4Br⊃DNP-DEG Hydrogels, Thin Films and Aerogels:* 26.85 mg of **1**•4Br (8 mM) and 8.07 mg of DNP-DEG (8 mM) were added into 3 mL of distilled water. The solution was kept stirring at 60 ℃ until all the compounds were fully dissolved. The supramolecular amphiphile-based hydrogel formed upon cooling. Gentle heating of the hydrogel regenerated the solution. This process of sol-gel transition was demonstrated to be fully reversible. The **1**•4Br⊃DNP-DEG xerogel film was formed by drop casting a solution of hot **1**•4Br⊃DNP-DEG (100 µL at 60 ℃) onto a glass slide. Upon cooling, the drop-casted solutions formed a uniform hydrogel. Hydrogel samples prepared in this manner were left overnight for drying under ambient air to afford **1**•4Br⊃DNP-DEG xerogel thin films. For the AFM measurements, 60 µL of a hot **1**•4Br⊃DNP-DEG solution was added onto a 1 cm^2 silicon substrate and spin-coated at a speed of 3000 rpm for 30 s. The thin film was then formed by drying the substrate under ambient air. For SEM measurements, 60 µL of a hot **1**•4Br⊃DNP-DEG solution was drop-casted onto a 1 cm^2 silicon substrate and left to dry. The **1**•4Br⊃DNP-DEG aerogel was obtained by freeze-drying of the **1**•4Br⊃DNP-DEG hydrogel using Labconco FreeZone Benchtop Freeze Dry System.

Thermochromic Transition Experiments in a N_2 Glove Box: A **1**•4Br⊃DNP-DEG xerogel film coated onto a glass substrate was put into a N_2 glove box and heated to 80 °C. After the colour of the film changed, the film was then cooled down to room temperature. The film originally had a red colour prior to heating, and its colour changed to yellow upon reaching the thermochromic transition temperature of 80 °C. After cooling the glass to room temperature and waiting for 20 minutes, the thin film still remained yellow in colour. The

glass was then taken out of the glove box and exposed to high humidity which had the effect of restoring the red colour after 20 s.

*Solid State Reaction of **1**•4Br with DNP-DEG and Powder X-ray Diffraction:* 111.9 mg of **1**•4Br (100 mmol) and 33. 7 mg of DNP-DEG (100 mmol) were added to a mortar

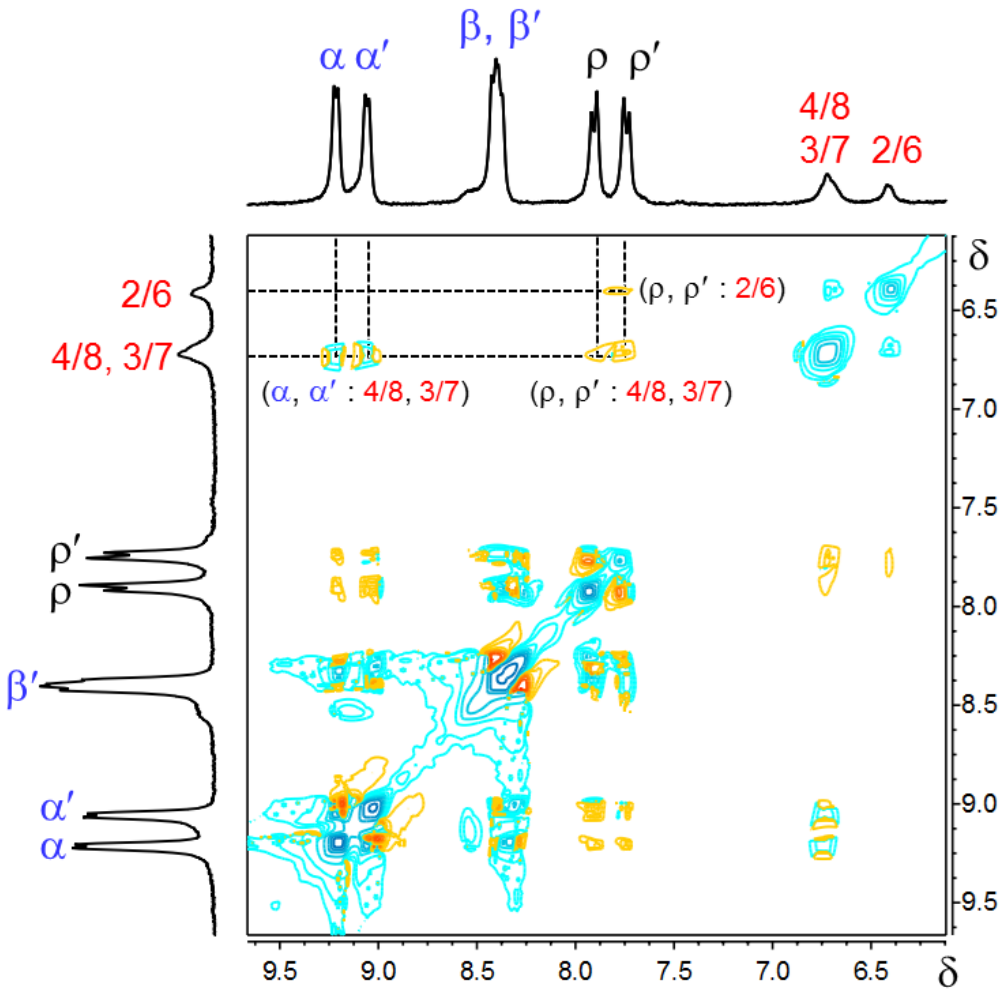

Figure 2.11 2D-NOESY spectrum of an 8×10^{-3} M solution of **1**•4Br (300 MHz, D_2O) with 1 equivalent of DNP-DEG taken at 25 °C. The spectrum clearly shows through space interactions between the aromatic protons of DNP-DEG and both the ρ protons of the biphenyl bridging group and α protons of the bipyridinium groups of **1**•4Br. These through space interactions suggest that the DNP-DEG guest is bound and π stacked with **1**•4Br.

and ground by pestle. **1**•4Br solid is yellow in colour and DNP-DEG is a solid which is brown in colour. Upon mixing, the complex **1**•4Br⊃DNP-DEG formed with a dark red colour (Figure 2.5a). The complex **1**•4Br⊃DNP-DEG was studied by powder X-ray diffraction. For the variable temperature powder X-ray diffraction (VT-PXRD) test, the temperature was first increased from 30 °C to 60 °C and then increased with a step of 10 °C every 10 minutes to 100 °C. The sample was then cooled down under N_2 flow and an additional test on the cooled sample was conducted. The diffraction angle from 0-5 ^{o} was not acquired due to the geometry restrictions of VT-PXRD.

Preparation of **1**•*4Br⊃DAN-DEG Hydrogels and Thin Films:* 26.85 mg of **1**•4Br (8 mM) and 8.02 mg of DAN-DEG (8 mM) were added into 3 mL of distilled water. The solution was kept stirring at 70 ℃ until all the compounds were fully dissolved. The supramolecular amphiphile-based hydrogel formed upon cooling. Gentle heating of the hydrogel regenerated the solution. This process of sol-gel transition was demonstrated to be fully reversible. The **1**•4Br⊃DAN-DEG xerogel film was formed by drop casting a solution of hot **1**•4Br⊃DNP-DEG (100 µL at 70 ℃) onto a glass slide. Upon cooling, the drop-casted solution formed a uniform hydrogel. Hydrogel samples prepared in this manner were left overnight for drying under ambient air to afford **1**•4Br⊃DAN-DEG xerogel thin films.

Counterion Exchange and Preparation of 1•4I⊃DNP-DEG and 1•4I⊃DAN-DEG Thin Films: 1.1g of **1**•4Br (1 mmol) was dissolved in 100 mL of hot water and a saturated aqueous solution of potassium iodide was added dropwise until no further precipitate formed. The orange precipitate was then filtered and washed three times with 100 mL of distilled water and dried under vacuum to afford **1**•4I. For thin film preparation, 19.6 mg of

1•4I (5 mM) was added into 3 mL of distilled water and heated to boiling. 20.17 mg of DNP-DEG (20 mM) was then added to the **1**•4I solution to form the **1**•4I⊃DNP-DEG complex. The **1**•4I⊃DNP-DEG thin film was formed by drop casting a solution of hot **1**•4I⊃DNP-DEG (100 μL at 90 ℃) onto a glass slide. The film was then dried under ambient air to afford the **1**•4I⊃DNP-DEG thin film. Likewise, a processable solution of **1**•4I⊃DAN-DEG was formed by adding 20.05 mg of DAN-DEG (20 mM) into a boiling solution (3 mL of distilled water) of **1**•4I (5 mM). The **1**•4I⊃DAN-DEG thin film was formed by drop casting a solution of hot **1**•4I⊃DAN-DEG (100 μL at 90 ℃) onto a glass slide. The film was then dried under ambient air to afford the **1**•4I⊃DAN-DEG thin film. Due to the poor solubility of **1**•4I in water, **1**•4I⊃DNP-DEG and **1**•4I⊃DAN-DEG did not form stable hydrogels.

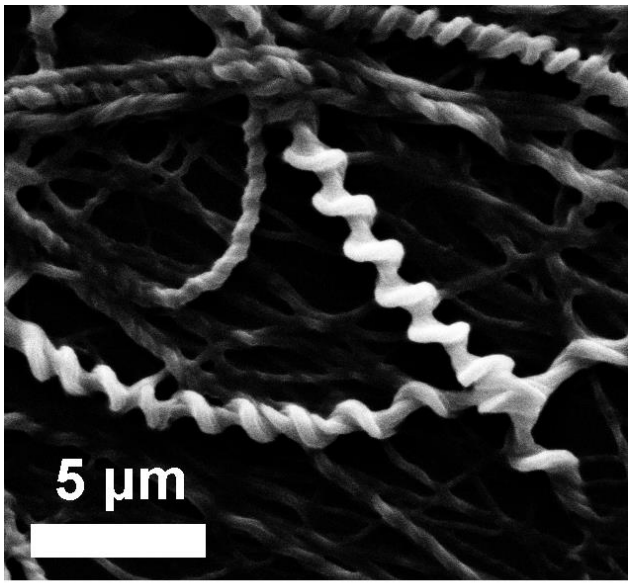

Figure 2.12 Scanning electron microscopy image of **1**•4Br⊃DNP-DEG supramolecular fibers with different helicities.

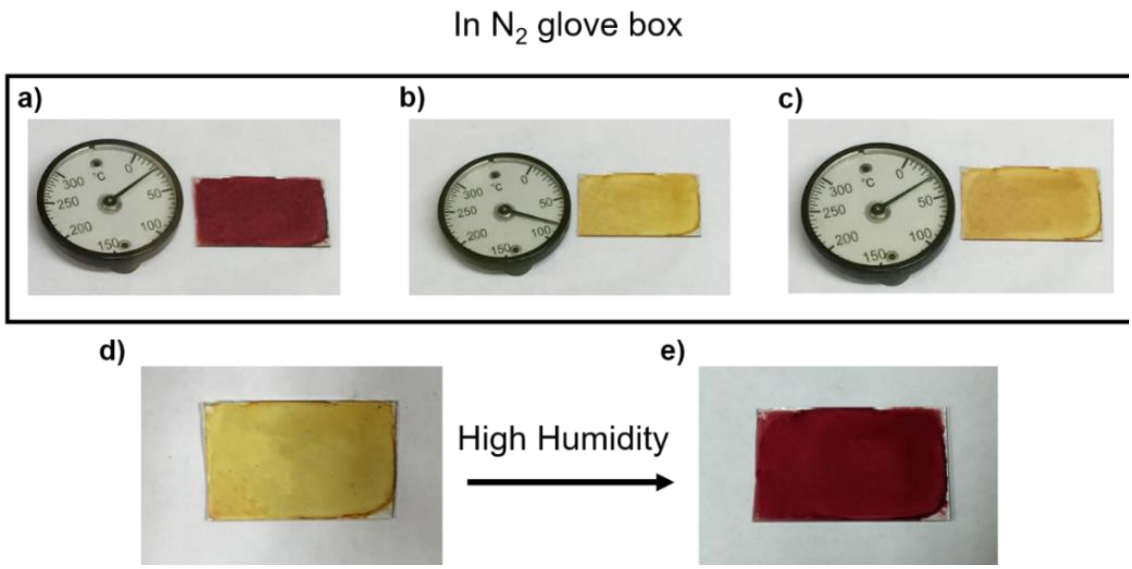

Figure 2.13 a-c) The colour of a **1**•4Br⊃DNP-DEG thin film at different temperatures in a N_2 glove box. a) At room temperature; b) at 80 °C; c) after cooling down to room temperature. d-e) The supramolecular assembly film taken from glove box before d) and after e) exposure to high humidity.

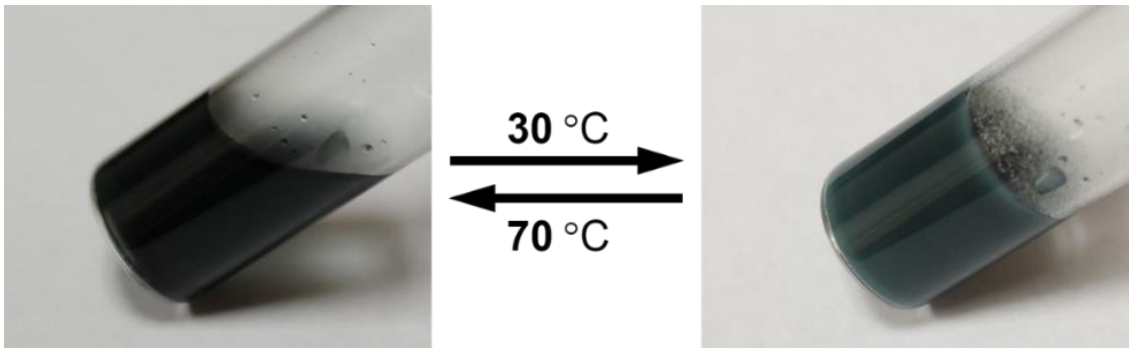

Figure 2.14 The sol-gel transition of **1**•4Br⊃DAN-DEG supramolecular assemblies.

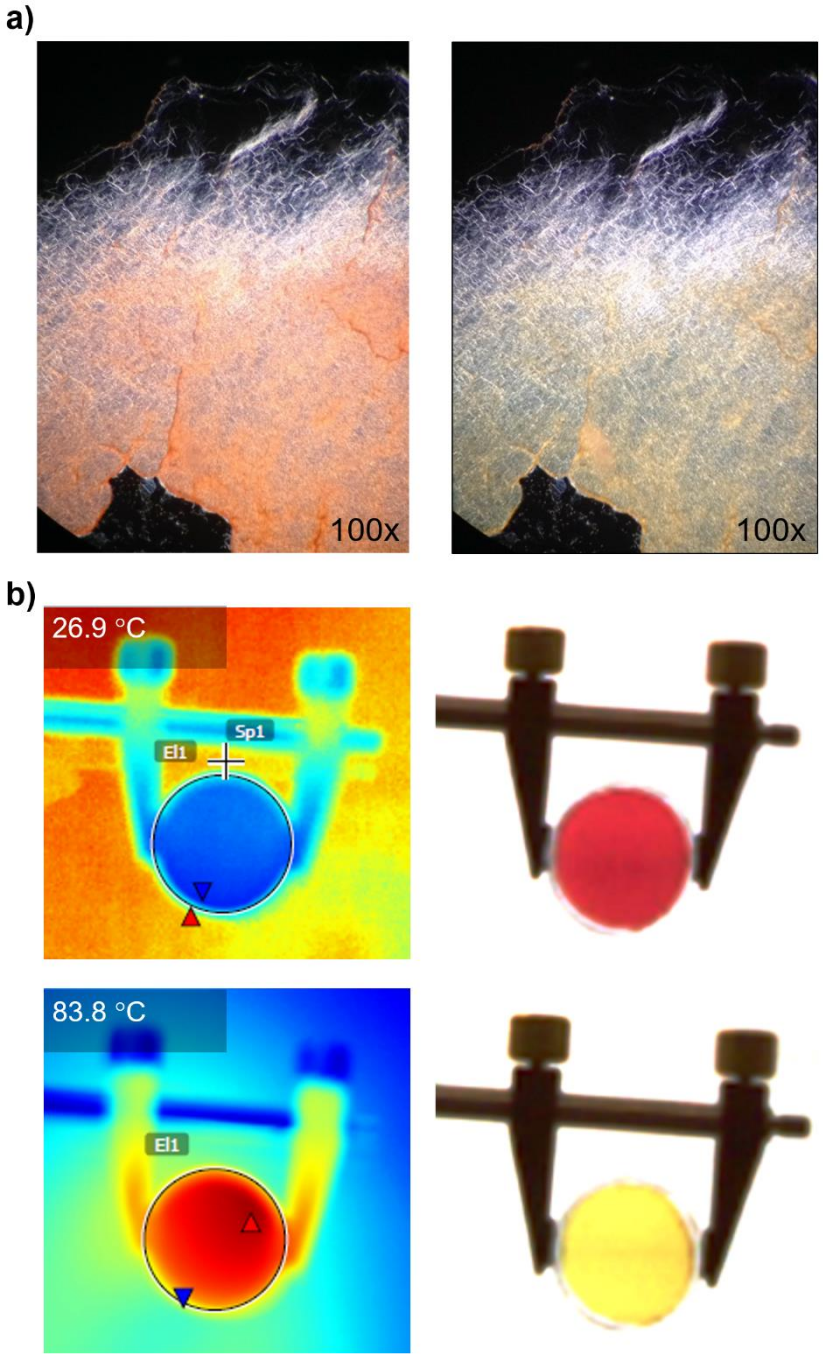

Figure 2.15 a) Polarized optical microscopy images of a **1**•4Br⊃DNP-DEG film at room temperature (left) and at 85 °C (right). b) Infrared thermographs and corresponding photographs of a **1**•4Br⊃DNP-DEG film at room temperature (top) and at high temperature (bottom) taken at the point of thermochromic transition. The temperature in the upper left hand corner indicates the average temperature on the surface of the sample.

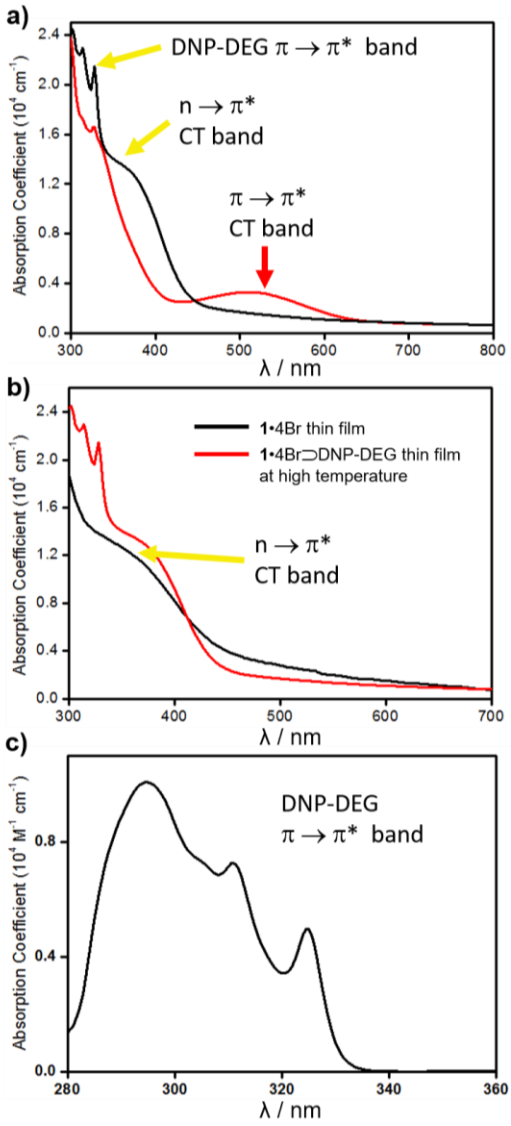

Figure 2.16 Uv-Vis absorption spectra of thin films of both **1**•4Br⊃DNP-DEG and **1**•4Br showing the competing CT interactions in the **1**•4Br⊃DNP-DEG supramolecular assemblies. a) Absorption spectrum of a **1**•4Br⊃DNP-DEG thin film before (red trace) and after (black trace) reaching the thermochromic transition temperature. The disappearance of the absorption band at 510 nm and the emerged shoulder peak at 350 nm after heating are due to the destruction of the $\pi \rightarrow \pi^*$ CT interaction and restoration of the $n \rightarrow \pi^*$ CT interaction. b) Comparison of the absorption spectrums of a **1**•4Br⊃DNP-DEG thin film at high temperature and a thin film of 1•4Br. Both spectrums show the $n \rightarrow \pi^*$ CT absorption peak around 350 nm. c) Uv absorption spectra of a 1×10^{-5} M aqueous solution of DNP-DEG.

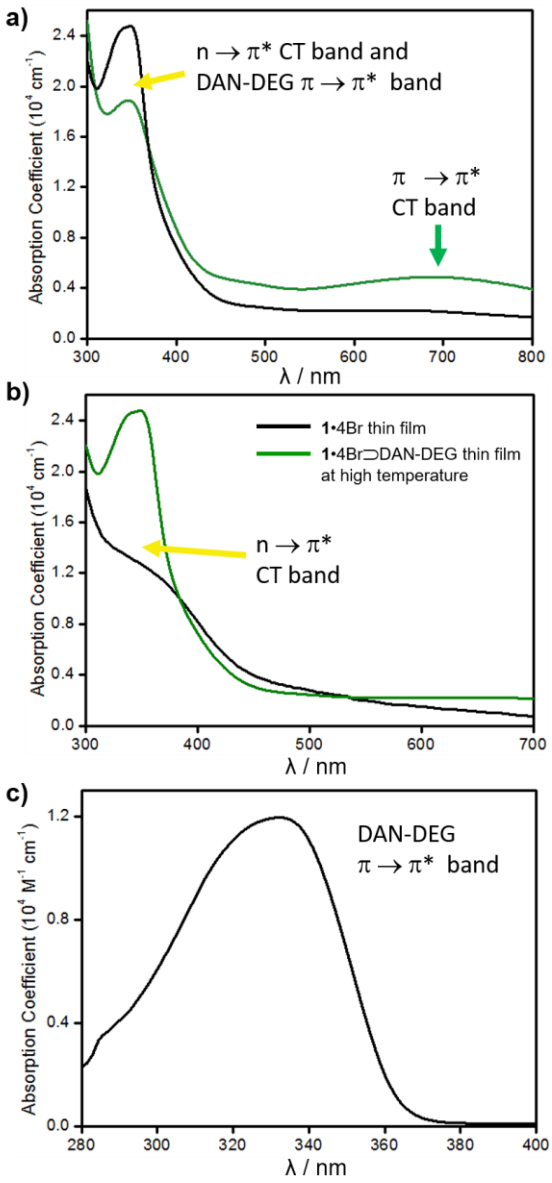

Figure 2.17 UV-Vis absorption spectra of thin films of both **1**•4Br⊃DAN-DEG and **1**•4Br showing the competing CT interactions in the **1**•4Br⊃DAN-DEG supramolecular assemblies. a) Absorption spectrum of a **1**•4Br⊃DAN-DEG thin film before (green line) and after (black line) reaching the thermochromic transition temperature. The disappeared of the absorption band at 700 nm after heating is due to the destruction of the $\pi \rightarrow \pi^*$ CT interaction. b) Comparison of the absorption spectrums of a **1**•4Br⊃DAN-DEG thin film at high temperature and a thin film of 1•4Br. Both spectrums show the $n \rightarrow \pi^*$ CT absorption peak around 350 nm. c) Uv absorption spectra of a 1×10^{-5} M aqueous solution of DNP-DAN.

CHAPTER 3

TUNABLE THERMOCHROMISM OF MULTIFUNCTIONAL CHARGE TRANSFER-BASED SUPRAMOLECULAR MATERIALS ASSEMBLED IN WATER*

3.1 Introduction

Supramolecular materials has become an emerging interdisciplinary research area that has attracted considerable attention from scientific communities on account of the modularity of their structural components, inherent reversibility, and overall versatility.[21, 85, 113] In recent decades, supramolecular self-assemblies that can respond to various external stimuli, such as changes in temperature,[114-115] pH,[116-117] and magnetic fields,[118-119] have been developed and used in a variety of applications in the areas of biomedical technology,[120-122] sensors,[123-124] energy storage,[125-127] and optical/electronic devices.[128-130] The use of supramolecular materials undoubtedly stems from the reversible non-covalent interactions from which they are assembled, endowing them with dynamic properties that can be designed and controlled in a prescribed manner. The incorporation of π-donor-acceptor charge-transfer (CT) interactions into supramolecular materials brings to the table a multitude of advantages on account of (i) their tunable optical properties through the adjustment of the frontier orbitals of the π-donors and/or acceptors; (ii) the directional nature (iii) their compatibility with aqueous environments. In this context, imparting CT-based

* Part of this section is reprinted with permission from Tunable Thermochromism of Multifunctional Charge Transfer-Based Supramolecular Materials Assembled in Water by Yuan, T. et al., *Chemistry of Materials*, **2017**, 29, 9937-9945.

functional supramolecular materials with actively controlled optical responses, such as thermochromism, emerges as an ideal strategy to construct optically responsive assemblies.

Thermochromics are a category of stimuli-responsive materials that have found mass usage and profitability. The ability of thermochromic materials to change color at different temperatures has been applied to various applications in manufacturing and process control, including advertising, product labels, quality control, security printing, and industrial designs. Smart windows glazed with thermochromic coatings have also been developed to control the heat flux into buildings in response to temperature changes for a more cost-efficient living.[131-133] To date, a broad range of compounds have been found to exhibit color change with changes in temperature,[28-29] including leuco dyes,[134-135] cholesteric liquid crystals,[136-137] photonic crystals,[138-139] polydiacetylene derivatives,[140-142] and numerous metal oxide and metal complexes.[30-31] Until now, however, only limited examples of thermochromic donor-acceptor CT-based supramolecular materials have been reported,[143-145] and facile processing of these materials remains a challenge.

Bipyridinium moieties have been used as building blocks to form CT donor-acceptor complexes[146] and CT hydrogels.[147-150] Recently, we developed a novel class of thermochromic supramolecular materials that were comprised of an amphiphilic π-electron deficient bis-bipyridinium acceptor and a π-electron rich naphthalene-derived donor.[151] From the alternating CT donor-acceptor π-stacks of these two components, fibrous supramolecular structures can be self-assembled in water, leading to easily processed, recyclable thermochromic hydrogels, aerogels, and xerogel films.[151] Herein, we report a new series of thermochromic CT supramolecular materials composed of a series of commercially available donors – namely, the neurotransmitter melatonin and its analogue bioisosteres. By

variation of the molecular structures of the donors, the strength of the CT interactions can be tuned, giving rise to a variety of selectable colors and thermochromic transition temperatures. Thermochromic aerogels and thin films of these materials were prepared from environment-friendly solvents. Furthermore, to demonstrate the simple processing of these materials, ink-jet printing was employed to generate thermochromic patterns with excellent quality. These thermochromic materials also show a favorable compatibility with commercial inks, allowing an extending color options for different applications.

3.2 Results and Discussion

3.2.1 Preparation and Characterization of Supramolecular Assemblies

A series of melatonin and melatonin analogue bioisosteres, namely, agomelatine (**2a**), N-acetyltryptamine (**2b**), melatonin (**2c**), N-acetylserotonin (**2d**) and 5-methoxytryptophol (**2e**) (**Scheme 3.1**) were selected as the π-donor components for the

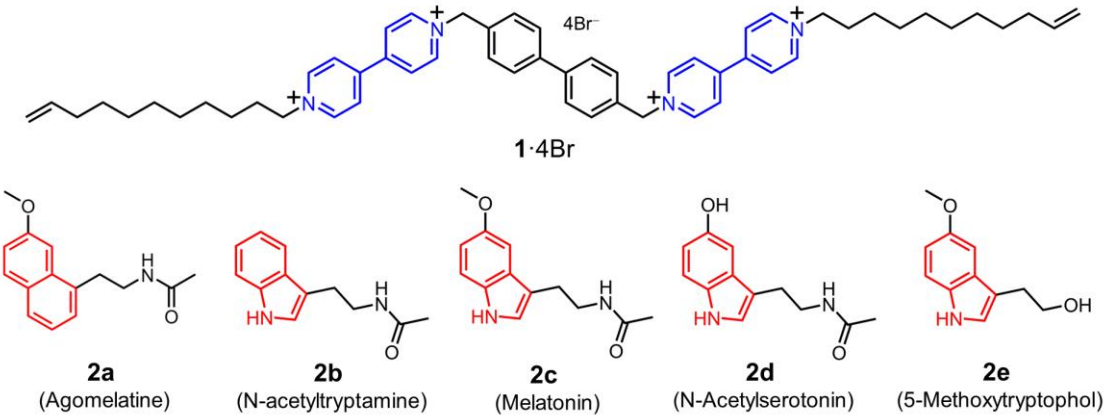

Scheme 3.1 Structural formulas of the amphiphilic bis-bipyridinium π-acceptor **1**·4Br and π-donors: melatonin (**2c**) and its analogue bioisosteres **2a**, **2b**, **2d**, and **2e**.

construction of CT supramolecular assemblies. These compounds were all commercially available, water soluble, and π-electron rich, capable of engaging in CT interactions with the bis-bipyridnium π-electron acceptor, **1**·4Br. Although the donor molecules are structurally similar, they possess different oxidation potentials and thus have varying π-electron donating abilities. With variations in the strength of the CT interactions between this cohort of donors and **1**·4Br, a diverse combination of colors and thermochromic transition temperatures can be expected.

Supramolecular assemblies composed of compounds **1**·4Br and **2a—2e** were prepared in aqueous solution. Upon dissolving **1**·4Br with two molar equivalents of one of the donors (**2a—2e**) in water at 80 °C, a dramatic color change occurred, corresponding to the $\pi \rightarrow \pi^*$ CT interaction of the donor-acceptor complex (**1**·4Br⊃**2a—2e**). For each CT complex formed between **1**·4Br and **2a**, **2b**, **2c**, or **2d**, a sol-gel transition was observed upon cooling to room temperature. The complex, **1**·4Br⊃**2e**, did not form a stable hydrogel, which likely resulted from the relatively higher solubility of **2e** in water.[152] The sol-gel transitions for complexes **1**·4Br⊃**2a—2d** were reversible through heating-cooling cycles (Figure 3.8). The room temperature colors of these supramolecular CT assemblies were donor dependent: complex **1**·4Br⊃**2a** giving rise to an orange color; while the colors of the other CT assemblies grew increasingly darker from **2b** to **2e**. As a result, a broad range of room temperature colors were accessed.

The binding of the donor analogues **2a—2e** to **1**·4Br were characterized in D_2O using ^{1}H NMR spectroscopy. Downfield shifts of the signals corresponding to the α and β

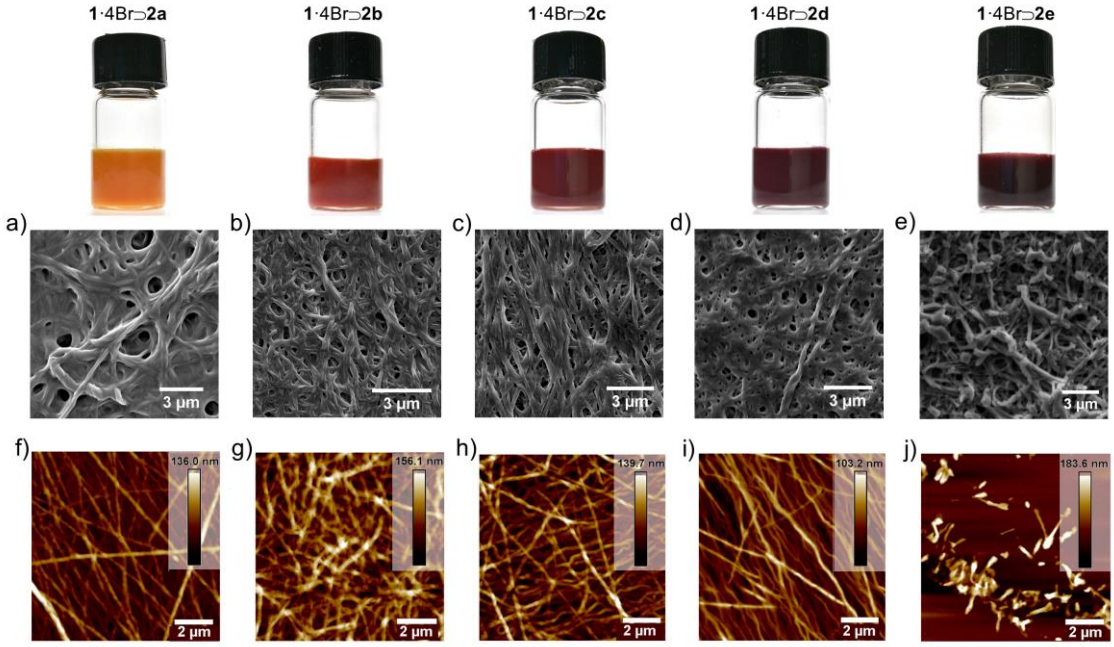

Figure 3.1 Photographic and microscopic images of **1**·4Br⊃**2a—2d** supramolecular assemblies. Solution of supramolecular assemblies were formed by dissolving the donor (16 mM) and the acceptor (8 mM) in water at 80 °C. a-e) SEM images of **1**·4Br⊃**2a—2e** films which were formed by drop-casting. f-j) Tapping-mode AFM height images of **1**·4Br⊃**2a—2e** films which were formed by spin-coating (10 × 10 µm).

protons, in relation to the nitrogen atoms on the bipyridinium units, were observed when compared to the ^{1}H NMR spectra of **1**·4Br in the absence of donor. (Figure 3.10-3.14) Concomitant shifts of the signals corresponding to the aromatic protons of the donors were also observed. The π-electron shielding induced shifts and signal broadening upon increasing the concentration of the donor-acceptor pair occur due to CT interactions between **1**·4Br and analogues **2a—2e**, and greatly suggests that face-to-face π-π stacking of the donor-acceptor pair has resulted and that superstructure assemblies have begun to form.[82] The solid-state morphology of the CT assemblies of **1**·4Br⊃**2a—2e** were imaged by scanning

electron microscopy (SEM). The SEM images of **1**·4Br⊃**2a─2d** (Figure 3.1a-d) revealed that the hydrogels were in fact entangled self-assembled fibers in a 3D porous network. Contradistinctively, flakes and rod-like aggregates were observed (Figure 3.1e) for complex **1**·4Br⊃**2e**, which explained its inability to form a stable hydrogel. The morphology of superstructures **1**·4Br⊃**2a─2e** was also investigated (Figure 3.1f-j) by atomic force microscopy (AFM) on spin-coated smooth film samples. Again, samples of **1**·4Br⊃**2a─2d** displayed continuous fibrous networks, while sample **1**·4Br⊃**2e** only formed separated rod-like aggregates. These results indicate that the gelation process was directly determined by the micro-scale morphology of the CT assembled superstructures. The donor-acceptor binding stoichiometries which make up the CT-assembled superstructures were determined by directly analyzing the formed supramolecular fibers using ^{1}H NMR spectroscopy. The integrated peak areas of the ^{1}H NMR signals for the digested solution of the fibrous assemblies revealed a consistent molar ratio of 2:1 between the donor and the acceptor regardless of the donor type (**2a─2e**) and the initial donor-acceptor ratio in the stock solution (Figure 3.15─3.19).

To characterize the mechanical properties of these hydrogels, oscillatory rheology measurements were conducted. All samples displayed viscoelastic behavior during the testing, with a higher storage modulus G' than the loss modulus G", confirming the solid-like nature of the hydrogels. (Figure 3.21) Moreover, the storage moduli of the **1**·4Br⊃**2a** supramolecular hydrogel (G' = 1.8×10^3 Pa) was much lower than that of **1**·4Br⊃**2b** (9.2×10^3 Pa), 1·4Br⊃**2c** (9.0×10^3 Pa) and **1**·4Br⊃**2d** (3×10^4 Pa). This difference is attributed to

the slightly lower crosslinking density of the **1**·4Br⊃**2a**-based fiber network as observed by AFM and SEM (Figure 3.1).

3.2.2 Thermochromic Properties

Xerogel films of the **1**·4Br⊃**2a–2e** superstructure assemblies were drop-cast followed by drying under ambient conditions (Figure 3.2a). The resulting xerogel films were formed reversibly thermochromic with different transition temperatures. Reminiscent of the π→π* CT color trend observed for the complexes in water, the colors of the xerogel films trend towards darker hues from **1**·4Br⊃**2a** to **1**·4Br⊃**2e**. In a similar fashion, the thermochromic transition temperatures of these films increased broadly from 45 to 105 °C changing from complexes **1**·4Br⊃**2a** to **1**·4Br⊃**2e** (Figure 3.2b-f). All color changing processes were characterized by solid state UV-vis absorption spectroscopy. The thermochromic mechanism was attributed to the competition of two different CT interactions. The π→π* optical transition originating from the CT interactions between the π-electron rich donors and the tetracationic acceptor, **1**·4Br, are contested by the n→π* optical transition originating from the CT interactions between **1**·4Br and its bromide counterions. Below the thermochromic transition temperature, the π→π* CT absorption band dominated, giving rise to the darker color that was visible at room temperature. Above the thermochromic transition temperature, the counter anions are free of bound water molecules, allowing them to outcompete the π-electron rich donors in interacting with the acceptor. As a result, a dominating n→ π* absorption band emerged, effectively changing the visible color of the material to a lighter one upon heating.[151]

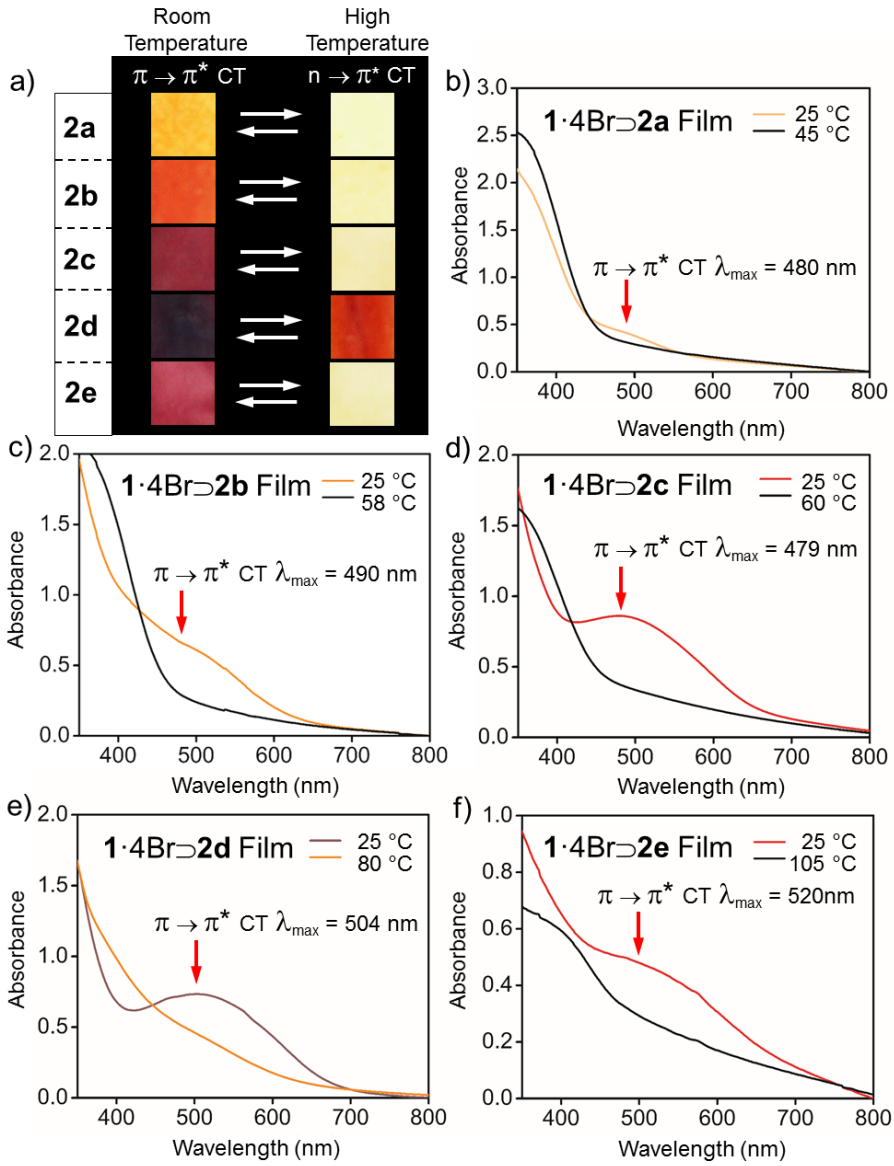

Figure 3.2 Photographs (a) of thermochromic films prepared using donors **2a–2e** at room temperature and above the thermochromic transition temperature and their corresponding UV-Visible absorption spectra (b-f). b) **1**·4Br⊃**2a**. c) **1**·4Br⊃**2b**. d) **1**·4Br⊃**2c**. e) **1**·4Br⊃**2d**. f) **1**·4Br⊃**2e**.

The ability of these materials to form gels offered the possibility to prepare "smart" aerogels that display color changes in response to thermal stimuli. Aerogels are ultra-light,

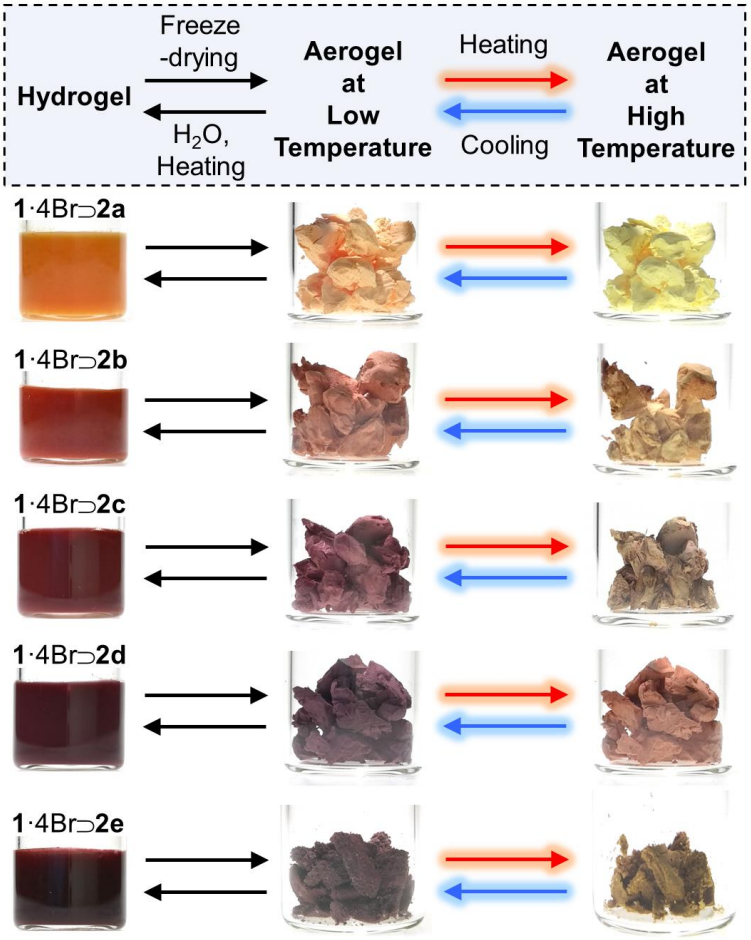

Figure 3.3 Preparation and thermochromism of supramolecular aerogels. Photographic images showing the hydrogels and the color change of the aerogels at room temperature and at high temperature.

high-surface-area materials, in which the solvent inside the precursor hydrogel or organogel is replaced with air through the process of cryodessication or supercritical drying.[94, 153] Through freeze-drying of the **1**·4Br⊃**2a–2e** hydrogels, aerogels of different colors were obtained. These aerogels exhibited (Figure 3.3) similar thermochromic behavior as their corresponding xerogel films, changing to the characteristic light colors after reaching the

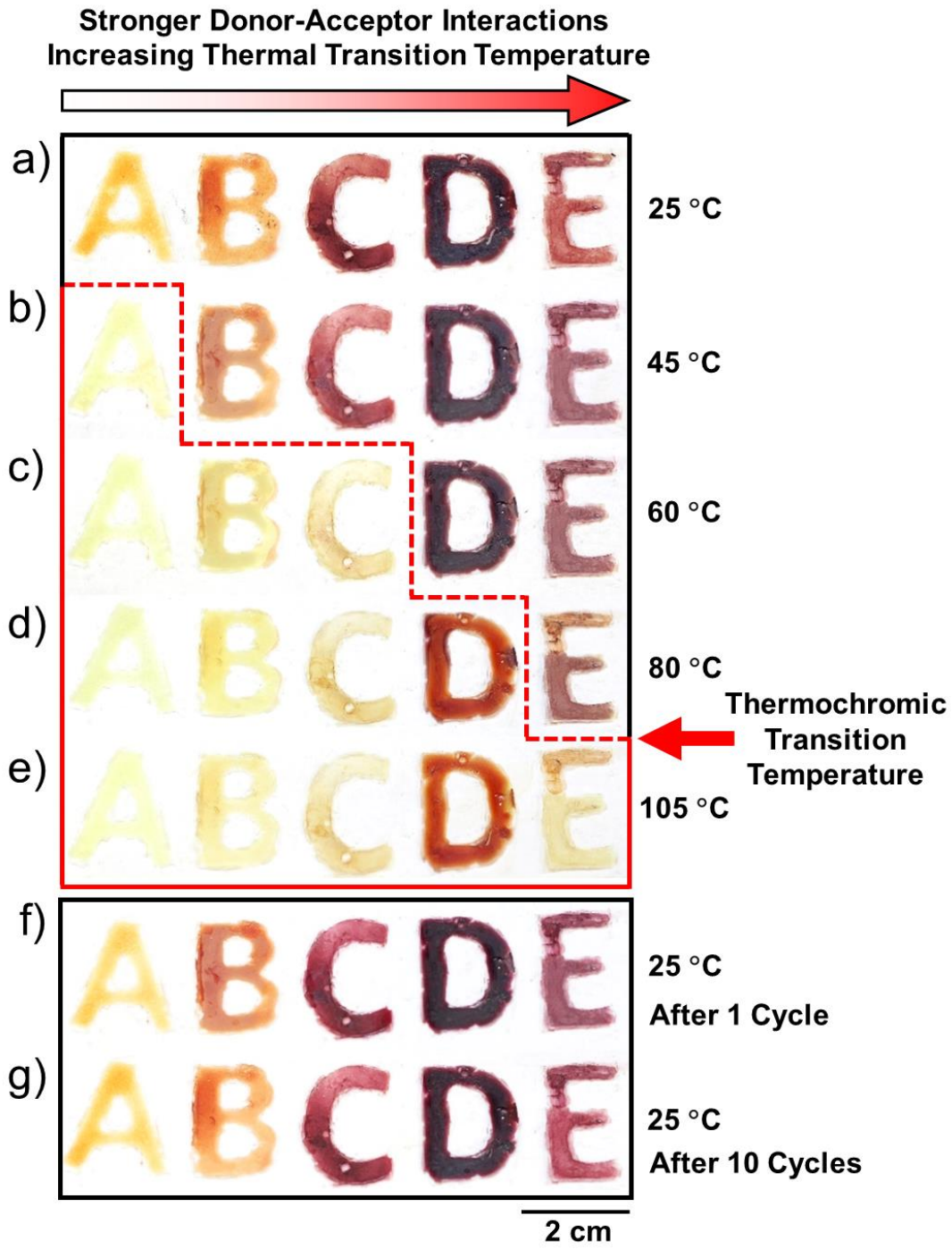

Figure 3.4 Photographic images of thermochromic patterns at different temperatures. The letters "A, B, C, D, and E" were written on a glass substrate in the sequence of **1**·4Br⊃**2a** to **1**·4Br⊃**2e**, respectively. a) at 25 °C. b) at 45 °C. c) at 60 °C. d) at 80 °C. e) at 105 °C. f) at 25 °C after first cooling. g) at 25 °C after 10 heating-cooling cycles.

Additionally, given the fact that only non-covalent interactions took place during the gelation process, these aerogels can be easily recycled by dissolving in hot water to regenerate the stock solution precursor.

The versatile feature of these supramolecular complexes allowed for the development of a series of inks that changes color on demand at different temperatures. Meanwhile, excellent solubility of the donor-acceptor components made these materials easily processable with environment-friendly solvents. Thermochromic inks with different colors were prepared by dissolving the acceptor and donor at a 1:2 molar ratio in a water/ethanol mixed solvent (8×10^{-3} M **1**·4Br with 2 molar equivalents of donor, V_{water} : $V_{ethanol}$ = 9:1). Then such inks were used to write letter patterns "A, B, C, D, and E" on a glass substrate in the sequence of **1**·4Br⊃**2a** to **1**·4Br⊃**2e**, respectively (Figure 3.4a-e). Upon heating of the glass substrate to 45 °C, the color of letter "A", corresponding to complex **1**·4Br⊃**2a**, switched from orange to yellow, while the color of the other letters remained unchanged. When the temperature of the glass was increased to 60 °C, the letters "B" and "C", corresponding to complexes **1**·4Br⊃**2b** and **1**·4Br⊃**2c** respectively, underwent a thermochromic transition to yellow. Heating the samples to 80 °C caused the letter "D", corresponding to complex **1**·4Br⊃**2d**, to undergo a color transition from plum to orange. Lastly, the letter "E", complex **1**·4Br⊃**2e**, changed from red to yellow when the glass reached a temperature of 105 °C. In order to thoroughly test the reversibility of these supramolecular materials, the glass substrate was first heated to 105 °C to ensure that all color transitions had taken place. Once cooled down to room temperature in a humid environment, the color of all patterns shifted back (Figure 3.4f) within several seconds. After

10 heating-cooling cycles, the thermochromic patterns still exhibited (Figure 3.4g) excellent reversibility. Much the same as their corresponding aerogels, the inked thermochromic patterns can be easily recycled (Figure 3.20) using hot water and applied again multiple times.

Moving forward to more practical applications, the thermochromic inks were integrated with commercial inks and applied with rubber stamps to generate desired heat responsive patterns with a wide range of colors and transition temperatures. **1**·4Br⊃**2c**, **1**·4Br⊃**2d,** and **1**·4Br⊃**2e** were loaded to a rubber stamp and the stamp was pressed onto a white paper to create (Figure 3.5a-c, upper) a "TAMU & TJU" pattern, which exhibited similar thermochromic transitions as the aforementioned patterns on glass. For the sake of achieving a more diversified color palette, **1**·4Br⊃**2c**, **1**·4Br⊃**2d**, and **1**·4Br⊃**2e** thermochromic inks were mixed with a commercial blue-colored ink in a volume ratio of

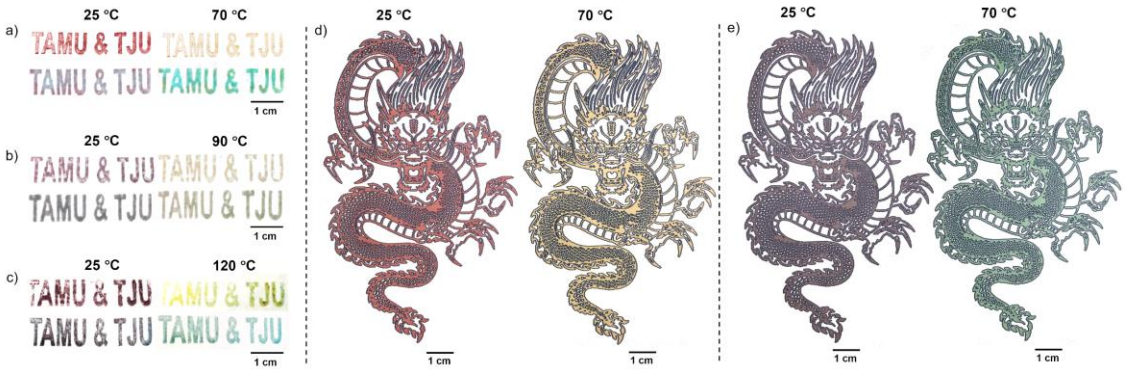

Figure 3.5 Photographic images of thermochromic patterns formed through stamping (a-c) and inkjet printing (d-e) using pristine solutions of supramolecular assemblies (a-c, upper and d) and solutions mixed with a commercial cyan-colored ink (a-c, lower and e) at temperatures below and above the thermochromic transition. a) **1**·4Br⊃**2c**. b) **1**·4Br⊃**2d**. c) **1**·4Br⊃**2e**. d-e) **1**·4Br⊃**2c**.

5:1 ($V_{thermochromic\ ink}$: $V_{blue\ ink}$ = 5:1). The patterns generated from the mixed ink exhibited (Figure 3.5a-c, lower) the same thermochromic transition temperatures while offering more color options. It is also noteworthy that the mixed ink afforded more uniform and defect free patterns compared to the original inks.

As a facile, low cost and high throughout solution processing method, inkjet-printing provides an attractive way to deposit functional materials on paper substrates.[94, 154-155] We also produced high resolution heat responsive patterns through inkjet printing. To demonstrate this function, pristine ink was prepared in a water/ethanol mixed solvent (2.5×10^{-2} M **1**·4Br with 2 molar equivalents of donor **2c**, V_{water}:$V_{ethanol}$ = 1.0:0.6) and used to fill a conventional inkjet office printer ink cartridge which was then employed to print (Figure 3.5d) an image of a Chinese dragon on standard A4-sized printing paper. The inkjet-printed image exhibited fully reversible thermochromic behavior in accordance with the previously described written and stamped patterns. To obtain a more diversified color palette, **1**·4Br⊃**2e** thermochromic inks were mixed with a commercially available blue-colored ink in a volume ratio of 20:1 and subjected to inkjet printing. Similar to the patterns generated through the stamping of mixed inks, the mixed ink-based inkjet-printed patterns exhibited (Figure 3.5e) the same thermochromic transition temperatures while offering extended color options. Inkjet printing using these mixed inks was also employed to produce high quality thermochromic text copy (Figure 3.6) whose small characters can easily be discerned. These results suggested favorable compatibility between the supramolecular thermochromic materials and commercial inks and inkjet printing technology. Further augmentation of the performance of these thermochromic inks can be realized with a multitude of additives.

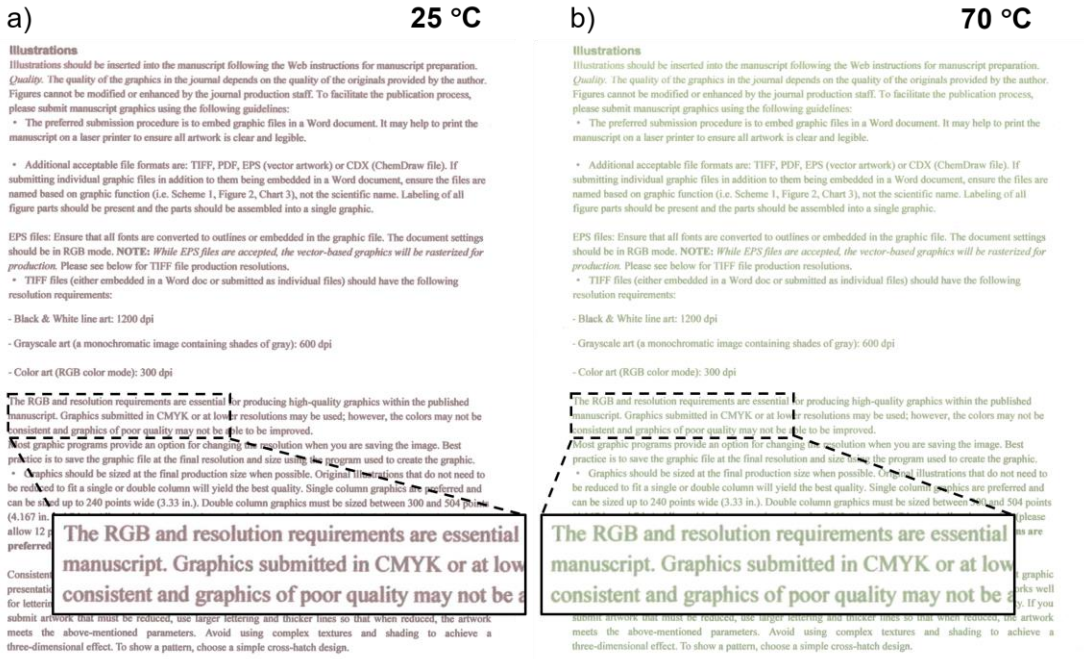

Figure 3.6 Photographs of inkjet-printed text using a solution of 1·4Br⊃**2c** mixed with commercial cyan-colored ink ($V_{thermochromic\ ink}$:$V_{blue\ ink}$ = 20:1) at temperatures (a) below and (b) above the thermochromic transition.

3.2.3 Mechanistic Investigations

Commercially available melatonin and its bioisostere analogues have a strong π-electron donating ability and are widely used as antioxidant supplements and pharmaceuticals.[156] The employment of their ability to form CT complexes for practical applications has not been widely explored.[157] To correlate the π-electron donating abilities of these compounds with their CT properties and the ability to participate in supramolecular thermochromics, the electrochemical properties of **2a**–**2e** were investigated by cyclic voltammetry. π-electron donors **2a**–**2e** have similar cyclic voltammograms (Figure 3.22),

characterized by a single irreversible anodic wave corresponding to an irreversible oxidation process and confirming the electron donating abilities of melatonin and its bioisosteres. According to the measured oxidation potentials, **2a** (E_{ox} = +1.50 V) and **2b** (E_{ox} = +1.20 V) possesses the first and second weakest electron donating ability, respectively, while **2c**-**2e** are stronger electron donors with similar oxidation potentials (E_{ox} = +1.08, +1.09, and +1.12 V respectively). The data clearly indicated that the donor with stronger electron donating ability leads to a stronger absorption band and a higher thermochromic transition temperature.[158]

Bipyridinium-based polyelectrolytes and small molecules have been reported[91, 159] to exhibit thermochromic properties based on the hydration states of the molecules during heating-cooling cycles. The thermochromic transition resulted from the on/off switching of the ion-dipole interactions of the counterions and the coordinating water molecules, effectively altering the dynamic competition between the $\pi \rightarrow \pi^*$ CT band and the $n \rightarrow \pi^*$ CT band.[151] In order to further explore the hydration/dehydration process of coordinating water molecules, thermal analysis of xerogel **1**·4Br⊃**2c** was carried out using differential scanning calorimetry (DSC) in a sealed aluminum pan (Figure 3.7 inset). Two reversible endothermic peaks, I/I' and II/II' (58 and 83 °C) were observed. The first transition at 58 °C correlated well with the thermochomic transition temperature of the **1**·4Br⊃**2c** xerogel film. Variable temperature powder X-ray diffraction (VT-PXRD) measurements were carried out from 30 °C to 90 °C under dry N_2 (Figure 3.23). A dramatic change in the diffraction pattern of the sample took place above 80 °C, indicating the presence of a significant change in the packing mode of the donor-acceptor complex, corresponding to the second endothermic peak at 83 °C observed by DSC. Upon cooling the xerogel to 30 °C under dry N_2, the diffraction peaks

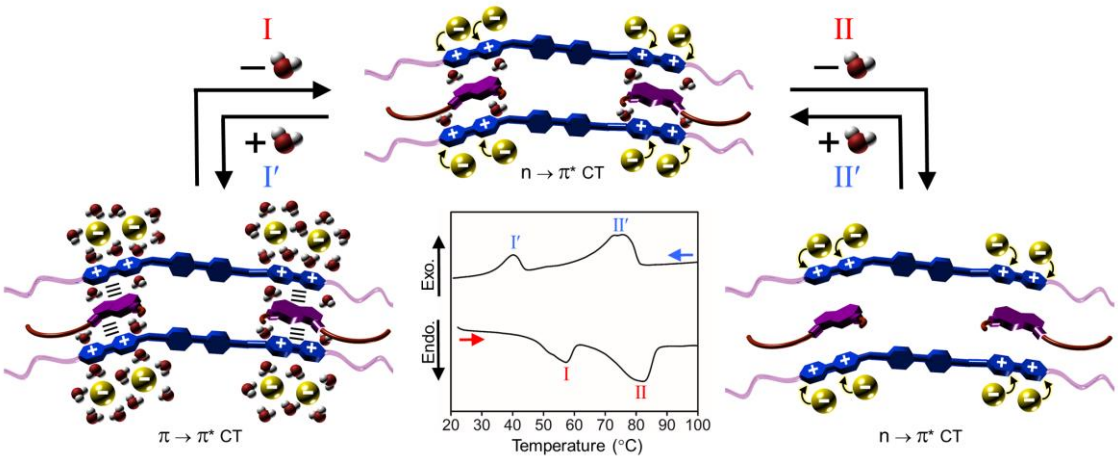

Figure 3.7 (inset) DSC curve of **1**·4Br⊃**2c** xerogel and the schematic illustration of the proposed structural change of **1**·4Br⊃2c xerogel during heating. The first transition at 58 °C (I) represents the first dissociation of coordinating water molecules and it is this step which is correlated with the thermochomic transition temperature of **1**·4Br⊃**2c**. The second transition at 83 °C (II) represents the second and final dissociation of coordinating water molecules and is correlated with a significant change in the packing mode of **1**·4Br⊃**2c**. Transitions I' and II' represent the two-step rehydration of the CT complex.

remained indistinguishable from the one seen at 90 °C, suggesting that such a change in the packing mode was not reversible without water. The packing mode change of **1**·4Br⊃**2c** and the two observed endothermic peaks were attributed to the dissociation of different types of bound water from the complex, similar to those observed for inorganic salt hydrates.[160] For example, copper sulfate pentahydrate – which is also thermochromic/hydrochromic – is known for having three different types of bound water within its crystal structure, each of which show endothermic peaks at different temperatures when heating.[161] Precedent literature has also reported the presence of two different types of bound water in bipyridnium-based polyelectrolytes.[162] Combining these data, we believe that there were two

types of bound water in the **1**·4Br⊃**2c** donor-acceptor complex (Figure 3.7, processes I/II and I'/II'). The thermochromic transition was correlated with the dissociation of coordinating water molecules at the lower temperature (58~60 °C). This dehydration process liberated the bromide counterions from engaging in ion-dipole interactions with water, such that they were then free to intimately involve themselves in a stronger polarization with the bipyridinium groups of **1**·4Br. At this juncture, the n→π* CT interactions between the ion-pair were established which effectively inhibited the ability of the bipyridinium groups of **1**·4Br to form additional CT interactions with π-electron rich molecular donors. The material then changed color and this process was fully reversible in a sealed or moist environment.

3.3 Conclusion

In conclusion, a new series of reversible thermochromic supramolecular materials have been developed using a bipyridinium-derived amphiphile, in conjunction with commercially available melatonin and its analogue bioisosteres. The CT interactions among the π-stacked donors and acceptors triggered the formation of an entangled fibrous morphology in water. These materials can be easily self-assembled and processed into multiple functional forms – including xerogels and aerogels – with excellent recyclability. Universal thermochromic behavior was observed in all these forms. The thermochromic transition temperature of this series can be tailored within the range of 45 to 105 °C by varying the donors. Stamped and ink-jet printed thermochromic patterns can be prepared from their aqueous solutions which also showed favorable compatibility with commercial inks. In addition, an in-depth mechanistic study revealed that two types of water molecules were bound to the supramolecular materials with differing strengths, and that the more

weakly bound water is responsible for the thermochromic transitions. Overall, this work presents a novel series of donor-acceptor CT-based supramolecular materials which feature versatile processability and tunable thermochromic properties. The unfolded design principles and underlining mechanism in this work provide essential insights for the future development of reversible and recyclable thermochromic supramolecular materials.

3.4 Experimental Section

3.4.1 Materials

Agomelatine (**2a**), melatonin (**2c**), and N-Acetylserotonin (**2d**) were purchased from TCI America; N-acetyltryptamine (**2b**) and 5-Methoxytryptophol (**2e**) were purchased from Cayman Chemical. All the compounds were used as received without further purification. **1**·4Br was synthesized according to procedure reported in the literature.[151] Deuterated solvents (Cambridge Isotope Laboratories) for NMR spectroscopic analyses were used as received.

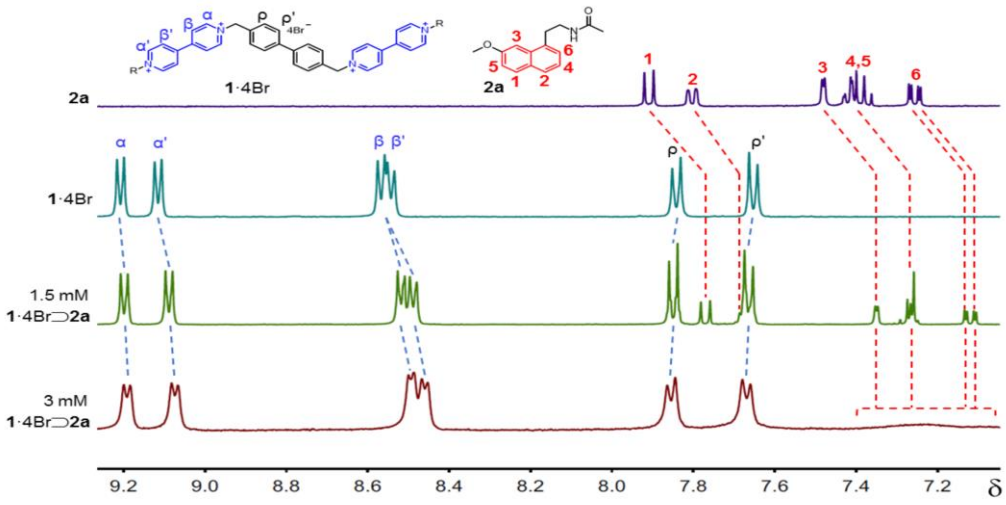

Figure 3.8 Stacked ^{1}H NMR spectra of a 1.5×10^{-3} M solution of **2a**, **1**·4Br, and **1**·4Br with 2 equivalents of **2a** at both 1.5×10^{-3} M and 3×10^{-3} M. (400 MHz, D_2O, 298 K)

3.4.2 Sol-gel Synthesis and Preparation of Thin Films and Aerogels

1·4Br (26.9 mg, .024 mmol) and **2a** (11.7 mg, .048 mmol) were added into distilled water (3 mL). The solution was kept stirring at 80 ℃ until all the material was fully dissolved. The supramolecular hydrogel **1**·4Br⊃**2a** was formed through sol-gel transition upon cooling. Hydrogel samples prepared in this manner were left overnight for drying under ambient air to afford **1**·4Br⊃**2a** xerogel films. Similarly, the hydrogels and films of **1**·4Br⊃**2b**-**2d** were prepared in a similar manner. Films of **1**·4Br⊃**2e** for UV-Vis absorption spectroscopy were prepared with an acceptor concentration of 2 mM and a donor concentration of 4 mM in water.

To prepare the samples for SEM analysis, hot solutions of **1**·4Br⊃**2a—2e** (100 μL at 80 ℃) were drop-cast onto a 1 cm^2 silicon substrate and left to dry. To prepare the samples for AFM analysis, hot solutions of **1**·4Br⊃**2a—2e** (100 μL at 80 ℃) were added onto a 1 cm^2 silicon substrate and spin-cast (2000 rpm for 60 s). Aerogels of **1**·4Br⊃**2a—2d** were obtained by freeze-drying of their corresponding hydrogels using a Christ Alpha 1-2 LD-plus freeze dryer.

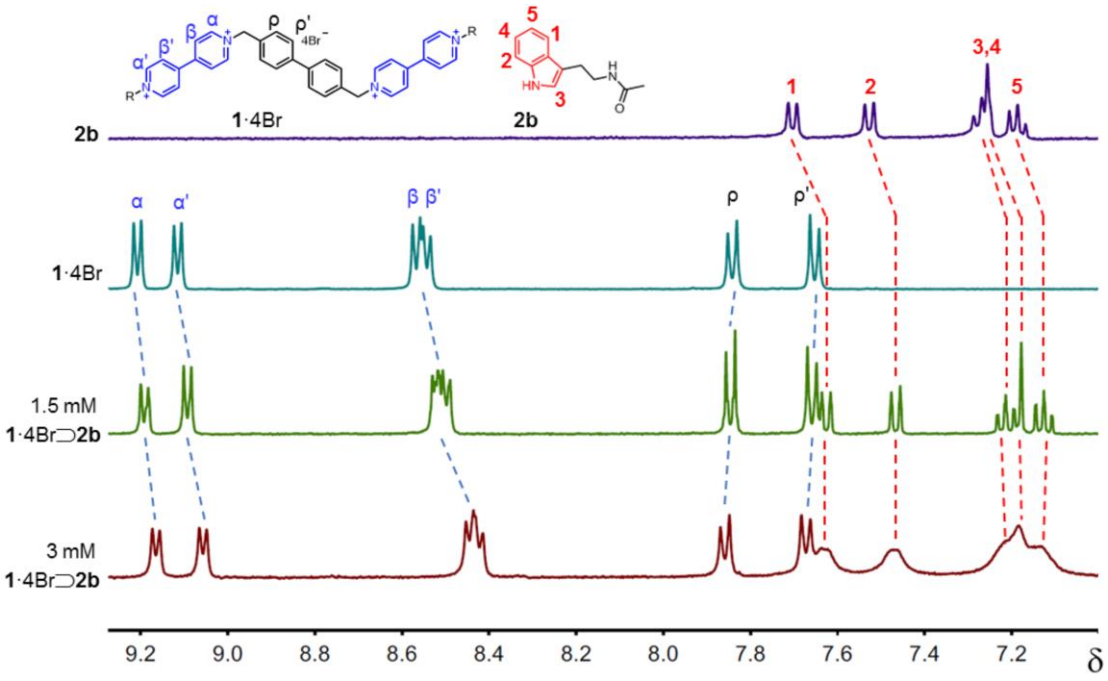

Figure 3.9 Stacked ^{1}H NMR spectra of a 1.5×10^{-3} M solution of **2b**, **1**·4Br, and **1**·4Br with 2 equivalents of **2b** at both 1.5×10^{-3} M and 3×10^{-3} M. (400 MHz, D_2O, 298 K)

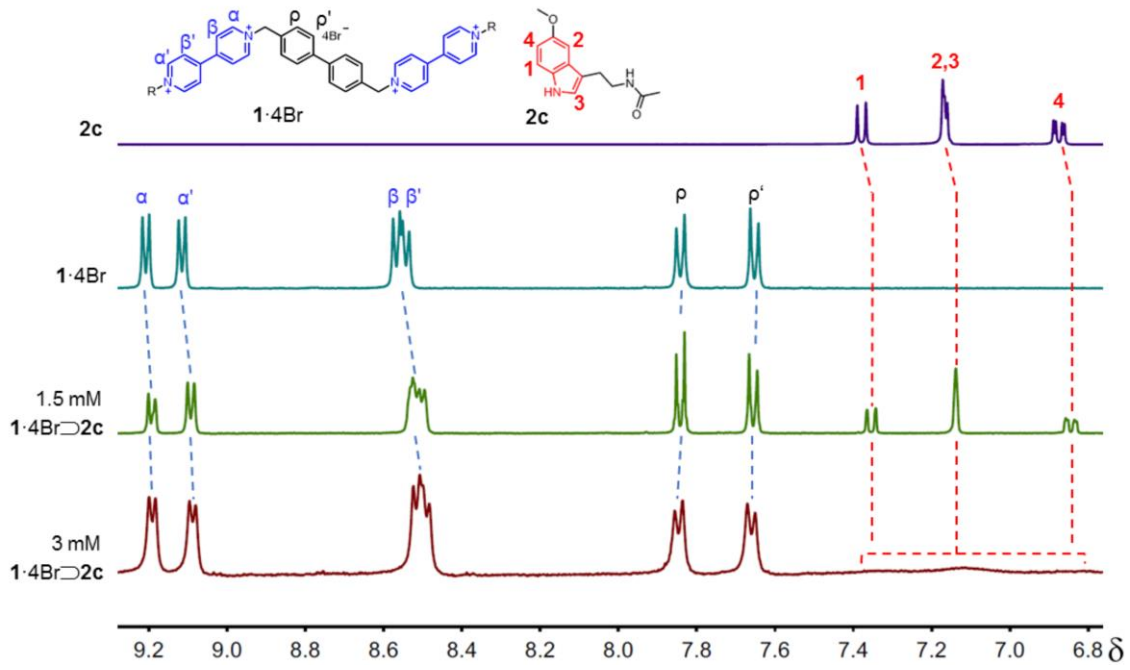

Figure 3.10 Stacked ^{1}H NMR spectra of a 1.5×10^{-3} M solution of **2c**, **1**·4Br, and **1**·4Br with 2 equivalents of **2c** at both 1.5×10^{-3} M and 3×10^{-3} M. (400 MHz, D_2O, 298 K)

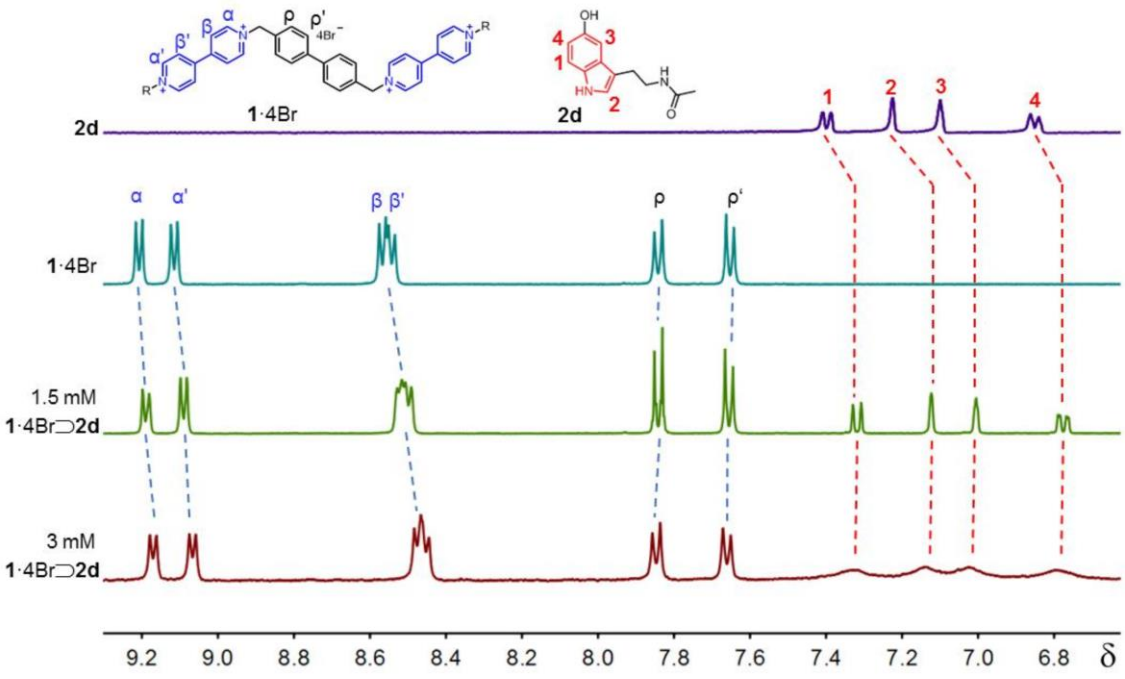

Figure 3.11 Stacked ^{1}H NMR spectra of a 1.5×10^{-3} M solution of **2d**, **1**·4Br, and **1**·4Br with 2 equivalents of **2d** at both 1.5×10^{-3} M and 3×10^{-3} M. (400 MHz, D_2O, 298 K)

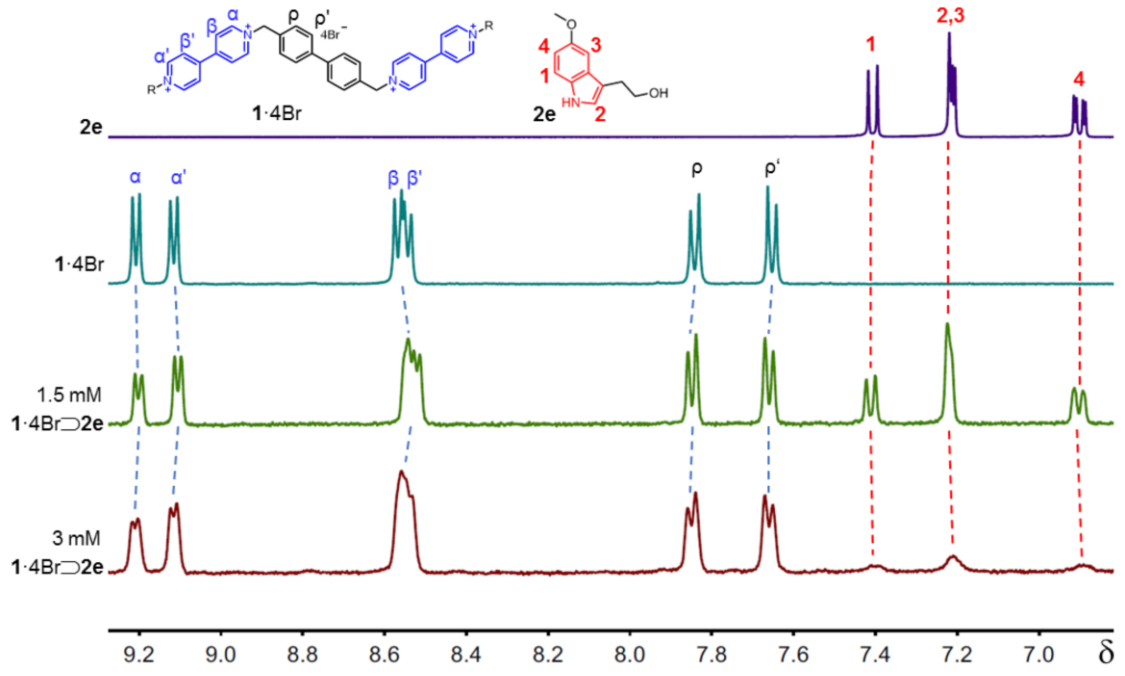

Figure 3.12 Stacked ^{1}H NMR spectra of a 1.5×10^{-3} M solution of **2e**, **1**·4Br, and **1**·4Br with 2 equivalents of **2e** at both 1.5×10^{-3} M and 3×10^{-3} M. (400 MHz, D_2O, 298 K)

3.4.3 Donor-Acceptor Stoichiometry Determination

In order to determine the donor-acceptor stoichiometry present in the supramolecular assemblies, **1**·4Br (9.0 mg, .008 mmol) and **2a** (1.9 mg, .008 mmol) were added into distilled water (1 mL) and heated at 80 ℃ until all the material was fully dissolved. After the formation of superstructure upon cooling, 3 mL of cold water (0 ℃) was added into the system and the mixture was vortexed for 1 minute. The mixture was then filtered with a polyamide membrane (Whatman NL 17) and dried under vacuum at room temperature. Similarly, supramolecular assemblies comprised of **1**·4Br⊃**2a** were prepared from solutions which contained different donor-acceptor ratios (2:1, 3:1). This process was then repeated to obtain samples of supramolecular assemblies comprised of **1**·4Br⊃**2b—2e**. These samples were then taken up in D_2O and subjected to analysis using ^{1}H-NMR spectroscopy whereby

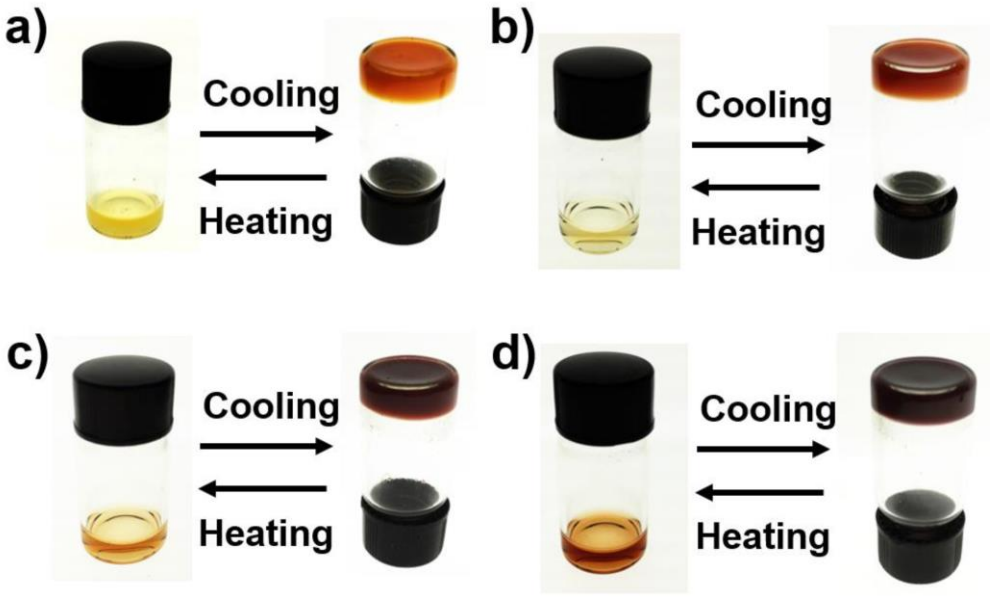

Figure 3.13 Photographs of the reversible sol-gel transition of **1**·4Br⊃**2a—2d** supramolecular complexes.

the ratio of the integrated peak areas of the appropriate proton signals corresponding to the donor and the acceptor were used to unambiguously determine their stoichiometry.

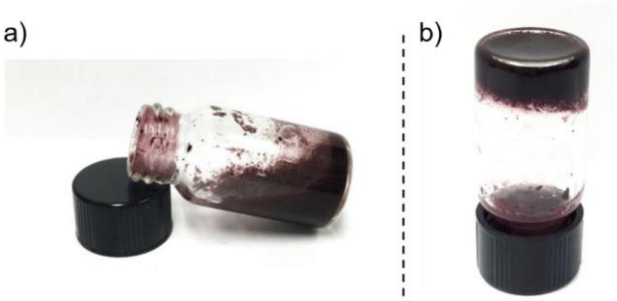

Figure 3.14 Photograph of the **1**·4Br⊃**2e** complex with different donor to acceptor molar ratios after cooling from a hot solution. a) **1**·4Br (8×10^{-3} M) with 2 equivalents of **2e** (16×10^{-3} M); No stable hydrogel was formed. b) **1**·4Br (8×10^{-3} M) with 4 equivalents of **2e** (32×10^{-3} M); Weak hydrogel was formed.

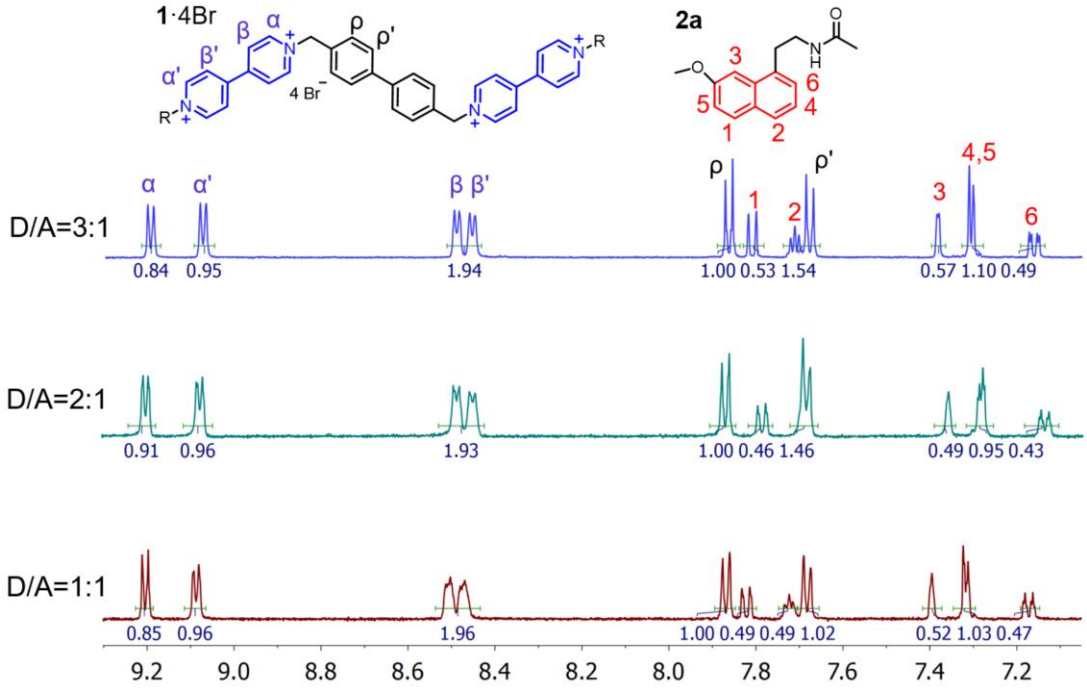

Figure 3.15 Stacked ^{1}H NMR spectra of **1**·4Br⊃**2a** complex prepared from different donor to acceptor molar ratios (D/A=1:1; D/A=2:1; D/A=3:1). (500 MHz, D_2O, 298 K)

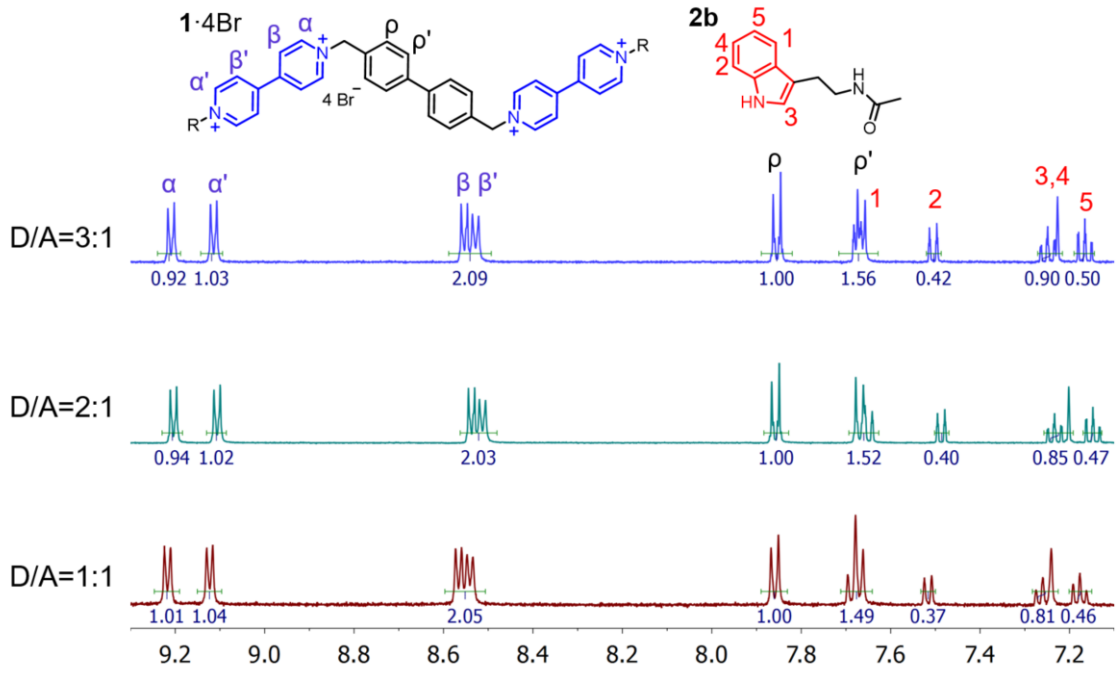

Figure 3.16 Stacked ^{1}H NMR spectra of **1**·4Br⊃**2b** complex prepared from different donor to acceptor molar ratios (D/A=1:1; D/A=2:1; D/A=3:1). (500 MHz, D_2O, 298 K)

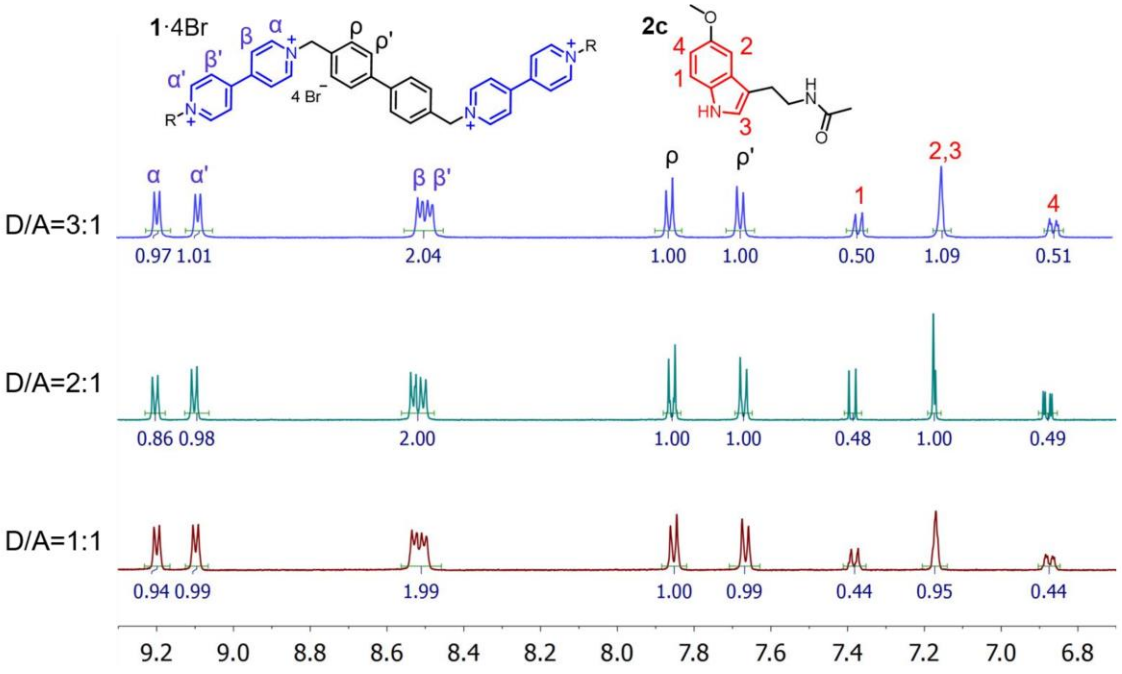

Figure 3.17 Stacked ^{1}H NMR spectra of **1**·4Br⊃**2c** complex prepared from different donor to acceptor molar ratios (D/A=1:1; D/A=2:1; D/A=3:1). (500 MHz, D_2O, 298 K)

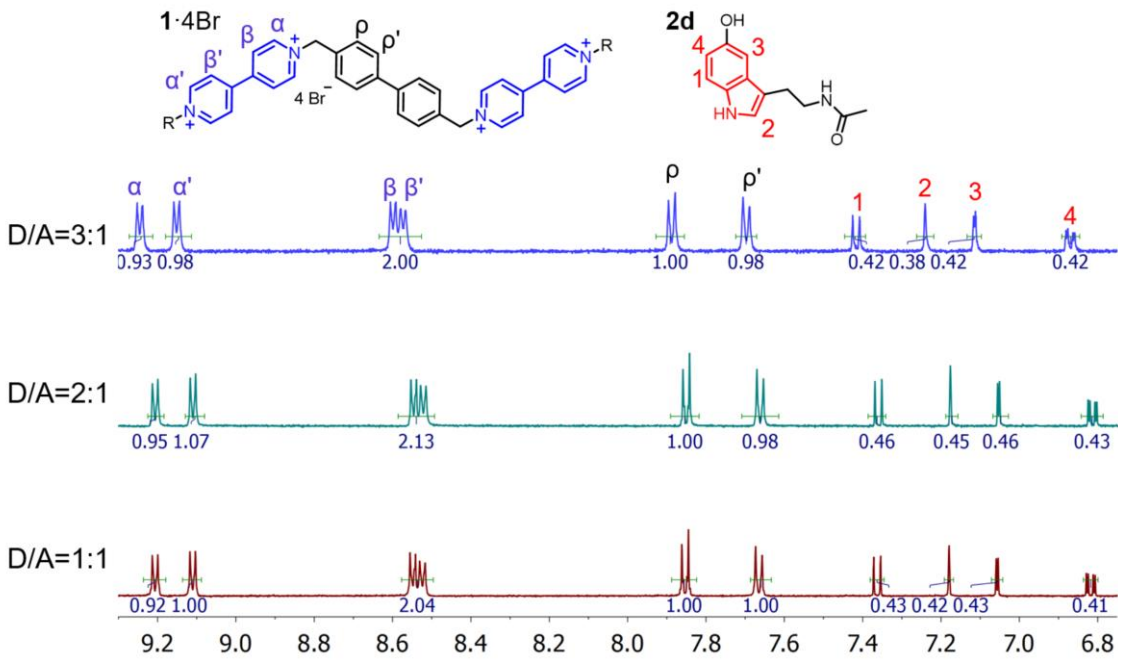

Figure 3.18 Stacked ^{1}H NMR spectra of **1**·4Br⊃**2d** complex prepared from different donor to acceptor molar ratios (D/A=1:1; D/A=2:1; D/A=3:1). (500 MHz, D_2O, 298 K)

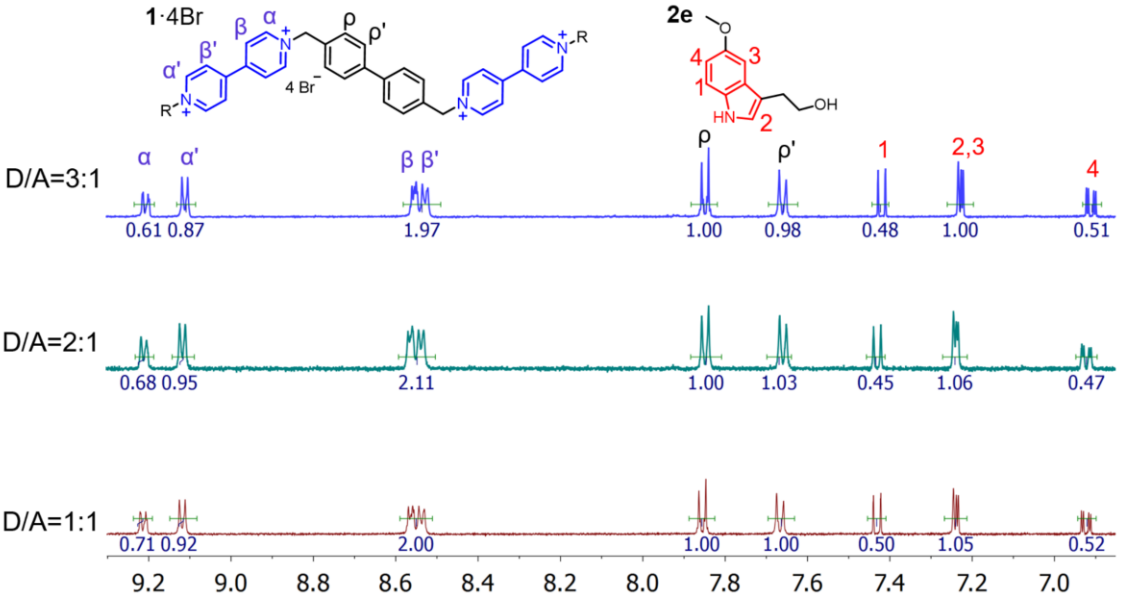

Figure 3.19 Stacked ^{1}H NMR spectra of **1**·4Br⊃**2e** complex prepared from different donor to acceptor molar ratios (D/A=1:1; D/A=2:1; D/A=3:1). (500 MHz, D_2O, 298 K)

3.4.4 Preparation of thermochromic inks and thermochromic patterns

To prepare the thermochromic inks used on the glass substrate, **1**·4Br (26.9 mg, .024 mmol) and **2a** (11.7 mg, .048 mmol) were added into a water/ethanol mixed solvent (V_{water} : $V_{ethanol}$ = 9:1, 3 mL). The solution was kept stirring at 60 ℃ until all the material was fully dissolved. The hot solution of **1**·4Br⊃**2a** was drop-cast to a glass substrate with an "A"-shaped mask to form the pattern. **1**·4Br⊃**2b**-**2e** thermochromic inks were prepared in the same manner and applied to the glass to generate patterns from "B" to "E", respectively.

To prepare the thermochromic inks used in rubber stamps, **1**·4Br (100 mg, .089 mmol) and **2c** (41.5 mg, .179 mmol) were added into an ethanol/water binary solvent mixture (3 mL, V_{water}: $V_{ethanol}$ = 1:9) and sonicated for 1 minute until all of the material was fully dissolved. **1**·4Br⊃**2d** and **1**·4Br⊃**2e** thermochromic inks were prepared in the same manner. For generating diversified color patterns, **1**·4Br⊃**2b**, **1**·4Br⊃**2d**, and **1**·4Br⊃**2e** thermochromic inks were mixed with a commercial blue-colored ink in a volume ratio of 5:1 ($V_{thermochromic\ ink}$: $V_{blue\ ink}$ = 5:1). Thermochromic inks were then loaded to a rubber stamp and the stamp was pressed onto a white paper to create a "TAMU & TJU" pattern. The rubber stamp and ExcelMark Self-Inking blue ink were purchased from rubberstamp.com.

To prepare the thermochromic inks used for inkjet printing, **1**·4Br (166.1 mg, 0.149 mmol) and **2c** (41.5 mg, 0.297 mmol) were added into an ethanol/water binary solvent mixture (6 mL, V_{water}: $V_{ethanol}$ = 1.0:0.6) and heated until all of the material was fully dissolved. This solution was then directly injected into an empty inkjet printer ink cartridge and used to replace the black ink cartridge in a conventional office inkjet printer. To prepare thermochromic mixed ink solutions for the inkjet printing of more diversified color patterns,

a commercial blue-colored ink (ExcelMark Self-Inking blue ink) was added to the original **1**·4Br⊃**2c** thermochromic solution in a volume ratio of 20:1. This modified ink was then ink-jet printed through the aforementioned method.

3.4.5 Characterization

^{1}H NMR spectra were recorded at room temperature on a Varian Inova 500 MHz spectrometer. UV-Vis spectra were measured on a Shimadzu UV-2600 spectrophotometer. Atomic force microscopy (AFM) images were recorded with a Bruker Dimension Icon AFM in a tapping mode and processed using NanoScope Analysis. Scanning electron microscopy (SEM) images were taken by a FEI Quanta 600 FE-SEM. Oscillatory rheology experiments were performed at 20 °C using a TA Instrument RSA-G2 Solids Analyzer on each **1**·4Br⊃**2a—2d** hydrogel sample at a strain amplitude of 0.1%. Differential scanning calorimetry (DSC) was conducted on a **1**·4Br⊃**2a** xerogel sample placed in a sealed aluminum pan using a TA Instruments DSC Q20 from 20 °C to 100 °C with a ramp rate of 2 °C/min. For the variable temperature powder X-ray diffraction (VT-PXRD) test, the temperature was increased from 30 °C to 90 °C with a step of 10 °C every 30 minutes, then cooled down to 30 °C. VT-PXRD spectra were collected on a **1**·4Br⊃**2a** xerogel sample at each temperature under dry N_2 flow. Cyclic voltammetry (CV) experiments were carried out at room temperature in argon-purged acetonitrile, with a CHI voltammetric analyzer. *n*-Bu4PF6 (0.1 M) was used as the supporting electrolyte. The conventional three-electrode configuration consists of a glassy carbon working electrode, a platinum wire counter electrode, and an Ag/AgCl reference electrode. Cyclic voltammograms were obtained at a scan rate of 100 mV.

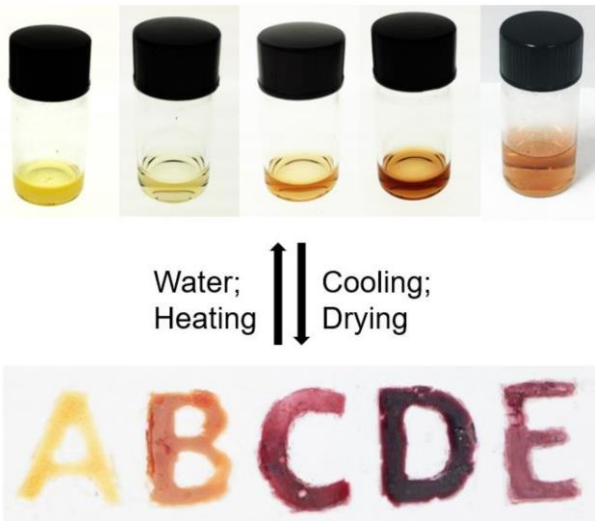

Figure 3.20 Photographs demonstrating the recyclability of the thermochromic materials based on **1**·4Br⊃**2a**-**2e**. These materials can be easily recycled by dissolving in hot water. The regenerated aqueous solutions can be used to prepare new thermochromic patterns.

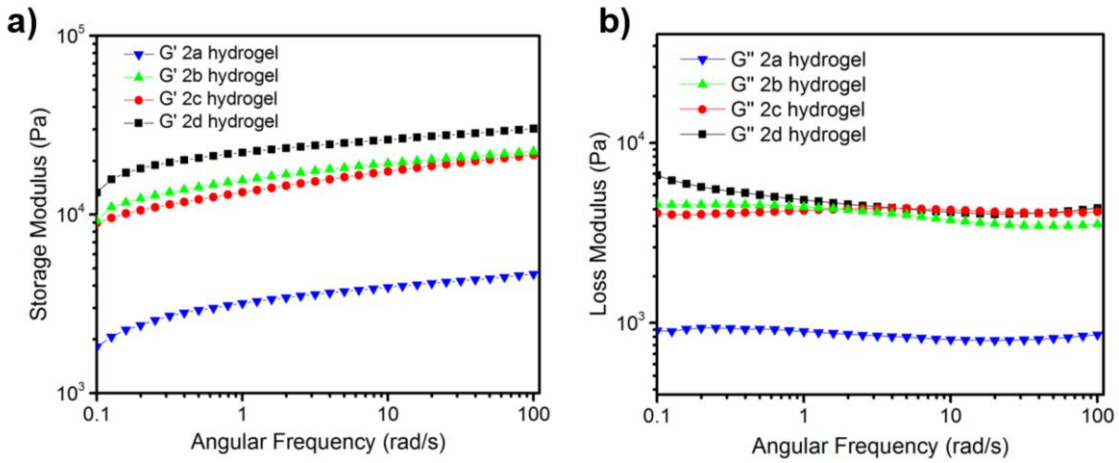

Figure 3.21 Oscillatory rheology frequency sweeps at 20 °C of a) storage modulus G' and b) loss modulus G" of **1**·4Br⊃**2a—2d** hydrogels.

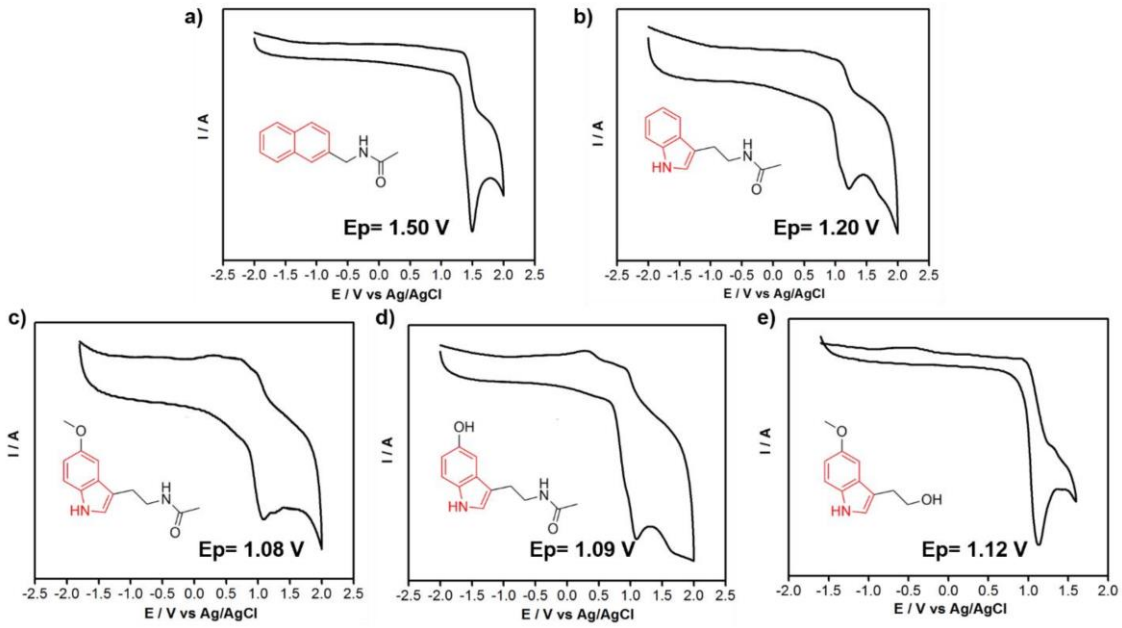

Figure 3.22 Cyclic voltammograms of a) **2a**, b) **2b**, c) **2c**, d) **2d**, and e) **2e** recorded at 100 mV s^{-1} in argon-purged MeCN at room temperature. The concentrations of the samples and the supporting electrolyte, tetrabutylammonium hexafluorophosphate, were 1 mM and 0.1 M, respectively.

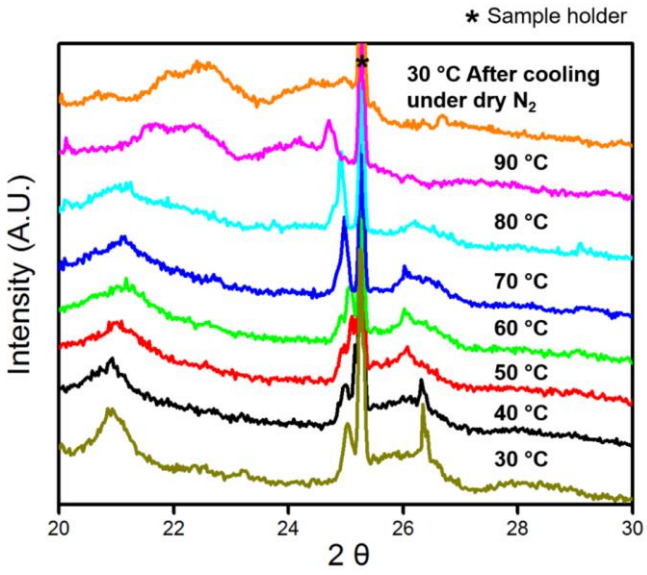

Figure 3.23 Variable temperature powder X-ray diffraction patterns of the **1**·4Br⊃**2c** complex recorded from 30 to 90 °C.

CHAPTER 4

ELUCIDATING THE STRUCTURE-PROPERTY RELATIONSHIPS OF DIFFERENT ACCEPTORS AND COUNTERIONS IN THERMOCHROMIC SUPRAMOLECULAR MATERIALS

4.1 Introduction

Structure-property relationships play a crucial role in directing and guiding the molecular design principles which pave the way to new and exciting function materials. This is especially true for supramolecular material and polymer chemists who use their knowledge the structure-property relationships which govern non-covalent interactions in an effort to exert control over the behavior of molecular entities and their ensembles. Non-covalent interactions, such as hydrogen bonding,[163-164] metal coordination,[165] electrostatic forces,[79, 166-167] ion-dipole interactions, and π─π stacking all play essential roles in structuring supramolecular assemblies, often times leading to tunable properties capable of responding to external stimuli such as changes in temperature,[59-61] pH,[62-64] wavelength of light irradiation,[65-67] and redox state.[68-69] Owing to the dynamic and tunable nature of non-covalent interactions, supramolecular assemblies have been widely applied in various fields and applications such as template-directed synthesis,[168] the production of biomedical materials,[121-122] sensor development,[123-124] energy storage,[125-126] and the fabrication of optical and/or electronic devices.[129]

Equally intriguing, is the recent progress in the development of stimuli-responsive chromatic organic materials which can change their color in response to various stimuli, all of which can be designed and engineered for a particular application. Arguably the most

well-known of the stimuli-responsive chromatic materials are the thermochromes. Reversible thermochromic materials have captured the attention of both academic and industrial scientists alike and are now commonplace in popular culture because of their ability to change color in response to different temperatures, with various applications as sensors,[169-170] in smart windows,[133] rewritable paper,[171] inks,[172] and in textiles/wearables. As a material property, thermochromism is typically achieved using one of two possible approaches, one which is based on material phase transformations, [173-176] and the other which relies on temperature-induced molecular structural changes of a chromophore. [177]

Recently, we developed a new class of thermochromic supramolecular material which is comprised of a π-electron deficient bis-bipyridinium gemini surfactant acceptor with halogen counterions and a π-electron rich guest, di(ethylene glycol)-disubstituted 1,5-dihydroxynaphthalene.[151] In aqueous solution, the bis-bipyridinium amphiphile engages in donor-acceptor charge transfer (CT) π-π stacking interactions with the naphthalene derivative. This supramolecular interaction results in their long-range self-assembly forming helical fibers leading to hydrogelation, ultimately facilitating their material processing into thermochromic aerogels and xerogel films from aqueous solutions. Unlike the aforementioned thermochromes, the thermochromic mechanism of these new materials in the solid state is a result of competing $n \rightarrow \pi^*$ and $\pi \rightarrow \pi^*$ donor-acceptor CT interactions. More specifically, the bis-bipyridinium acceptor is capable of engaging in both $\pi \rightarrow \pi^*$ CT interactions with the naphthalene-based donor and $n \rightarrow \pi^*$ CT interactions with its own counterions, with each interaction having a unique CT absorption band and thus its own characteristic color. Coordinating water molecules which the material absorbs

hygroscopically go on to form ion-dipole interactions with the halogen counterions, at which point the n $\rightarrow \pi^*$ CT interactions are suppressed and the $\pi \rightarrow \pi^*$ CT interactions dominate. Thus the heating and cooling of these materials results in the dehydration-hydration of the bipyridinium-halogen ion-pairs thus inducing their reversible color change.

Aside from its scalability, recyclability, and ease of processing from environmentally friendly solvents, another attractive feature of this thermochromic system is its inherent modularity. By varying the chemical structure of the π-electron rich donors and the acceptor's accompanying counterions, the strength of donor-acceptor CT interactions can be tuned, leading to pronounced changes in the material's color palette and its thermochromic transition temperature. [178] At this stage however, very little is known about the role that the structure of the bipyridinium-based gemini surfactant acceptor plays in endowing this thermochromic system with its material properties despite the widely-reported use of similar derivatives in analogous so-called "supramolecular amphiphile" systems. Herein we report on the design and synthesis of a series of bipyridinium-based gemini surfactants with differing bridging groups and elucidate the structure-property relationships which 1) bestow upon them the ability to form hydrogels, 2) govern hydrogel strength, and 3) influence their solid-state thermochromic transition temperature and color when interacting with the electron-rich donor, melatonin.

4.2 Results and Discussion

4.2.1 Gemini Surfactant Acceptor and Their Ability to Form Templated Helical Network-based Hydrogels

Gemini surfactants, unlike conventional single linear hydrocarbon chain surfactants, are comprised of two linear hydrocarbon chain surfactant monomers which have been covalently joined to one another through a bridging unit. The bridging spacer itself can vary widely in structure from short to long spacers, from rigid to flexible, and from polar to nonpolar in nature. In terms of material performance, gemini surfactants are typically more surface active than their run of the mill linear counterparts. This enhanced performance of gemini surfactants is due in part by the fact that there is no negative entropic contribution to the free energy of their self-assembly/micellization ($\Delta G°_M$) from the joining of two free linear monomers. For gemini surfactants, the two surfactant monomers are essentially covalently preorganized by the bridging spacer unit. Perhaps the most obvious structural consequence of the bridging spacer group in gemini surfactants that is also partly responsible for their "nonclassical" behavior is the diminished ability of the two hydrocarbon chains of a single gemini surfactant to engage with one another effectively. Thus the bridging unit of gemini surfactants is an important structural parameter which can be easily modified and from which structure-property relationships can be teased out.

In previous work, we discovered that bipyridinium-based amphiphiles which have been joined together with a biphenyl bridge formed bundled helical fibers leading to hydrogelation upon molecular templation with the neurotransmitter melatonin and other π-electron rich donors.[151, 178] This ability to form long self-assembled fibers leading to gelation ultimately proved to be a crucial property that facilitated the material processing of the

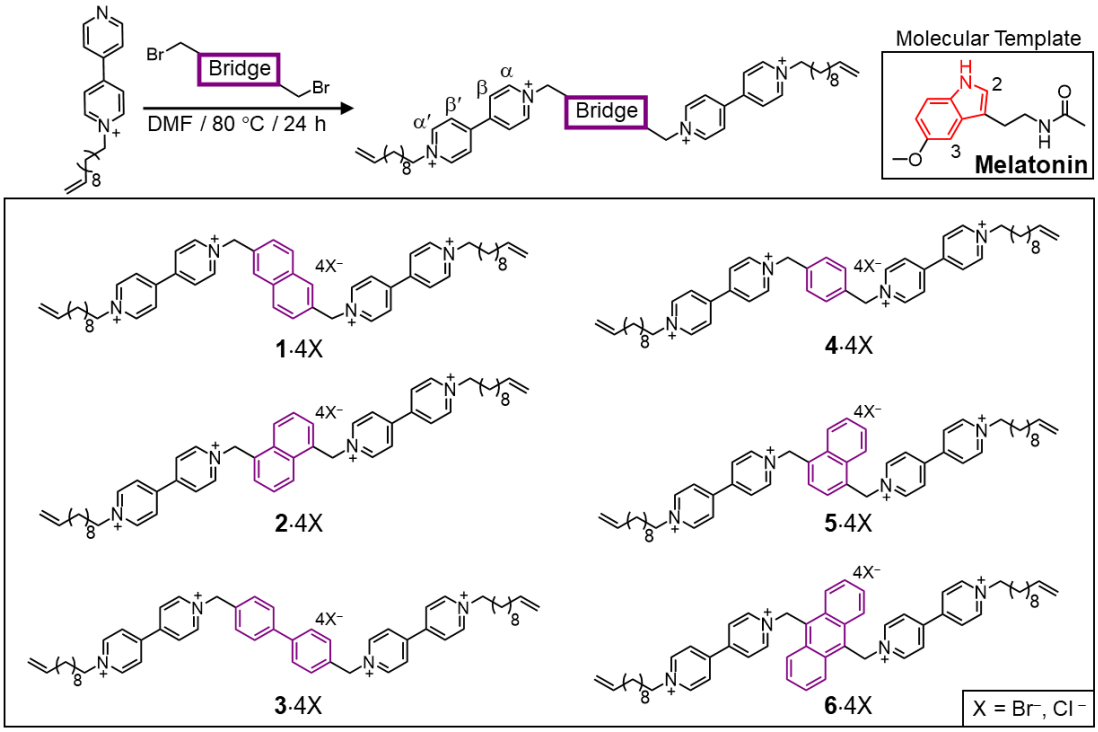

Scheme 4.1 (top) General synthetic route for the synthesis of gemini surfactants **1**-**6**·4X and their (bottom) structural formulas.

amphiphiles into functional xerogel films and aerogels. Contradistinctively, this surprising property was not observed [92-93, 178] for donor-acceptor templated bipyridinium derivatives which are bridged by a single phenyl group. This early observation made it very clear that the material processability of bipyridinium-based gemini supramolecular amphiphiles depended not only on the π-electron donating ability of the molecular templates with which they engage with, but is also dependent on the structural factors of the gemini bridging unit of the amphiphile itself. Thus in order to further elucidate the structure-property relationships of this class of gemini surfactants we synthesized a series of six bipyridinium-based amphiphiles bearing different bridging units (Scheme 4.1) and studied their material

properties when templated with the π-electron donor, melatonin, as both tetrachloride and tetrabromide salts.

Upon mixing relatively dilute solutions (≈ 3×10^{-3} M) of amphiphiles **1**-**6**·4X with 1 or more equivalents of melatonin in water, a vivid color change could be observed corresponding to the formation of a donor-acceptor CT absorption band stemming from the formation of a CT complex between the bipyridinium head groups of the amphiphiles and melatonin. When combined at concentrations of 1×10^{-2} M or greater with two equivalents of melatonin in water through gentle heating, amphiphiles **1**-**3**·4X displayed contrastingly different solution behavior than amphiphiles **4**-**6**·4X. More specifically, both the tetrabromide and tetrachloride salts of **1**-**3**·4X all formed stable hydrogels with melatonin upon cooling (Figure 4.1, top), while no hydrogels were observed for amphiphiles **4**-**6**·4X (Figure 4.12). Rather than forming gels, the cooled aqueous solutions of **4**-**6**·4Br formed strongly colored precipitates whereas solutions of **4**-**6**·4Cl remained as translucent colored solutions owing to the increased solubility of the tetrachloride salts.

Polarized light optical microscopic analysis of the hydrogels revealed that the gels are comprised (Figure 4.1a-f) of a network of entangled supramolecular fibers. The fibers were found to exhibit strong birefringence which indicates that the fibers were crystalline with long range order. The solid-state morphology of the xerogel films prepared from the hydrogels were imaged by both scanning electron microscope (SEM) (Figure 4.1g-l) and transmission electron microscopy (TEM) (Figure 4.1m-r). Both SEM and TEM further confirmed the entangled fibrous morphology of CT assemblies. Interestingly, much like the fibers assembled from a similar bis-bipyridinium acceptor and a dihydroxynaphthalene-

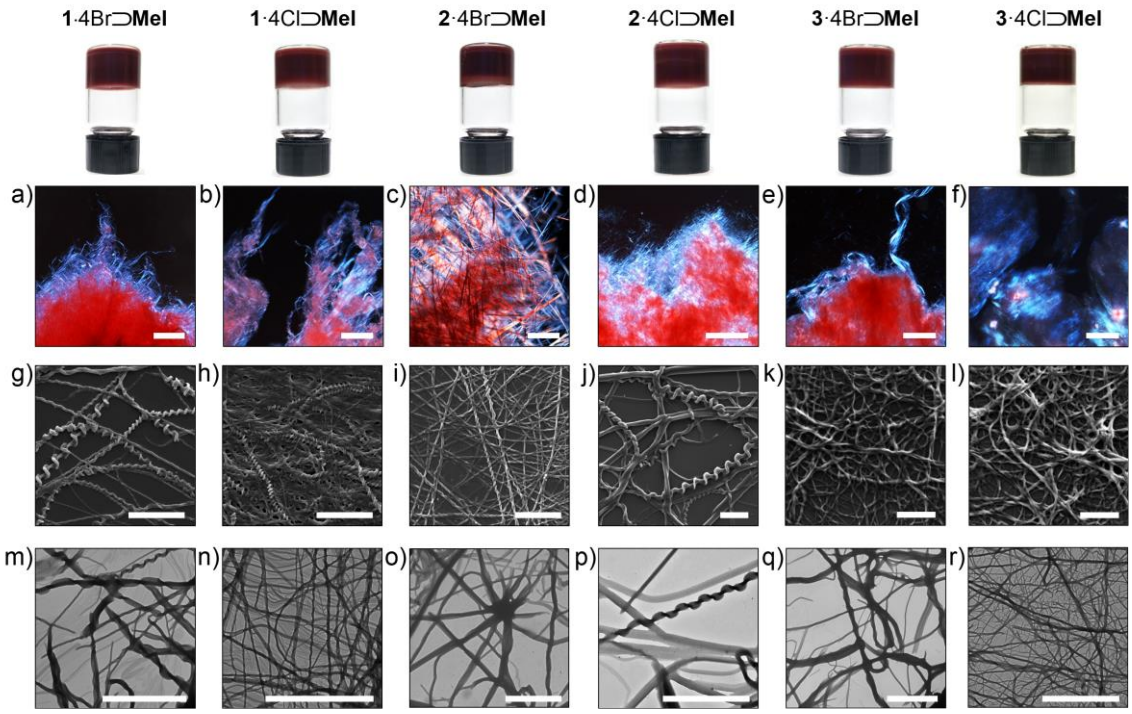

Figure 4.1 Photographs (top), polarized light optical microscopy (**a**–**f**), SEM (**g**–**l**) and TEM (**m**–**r**) images of melatonin-templated hydrogels comprised of surfactants **1**-**3**·4X. The scale bars in figures **a**–**f** are 200 μm, and in figures **g**–**r** are 5 μm.

based π-electron rich donor previously reported,[151] a racemic mixture of helical fibers with different handedness were clearly observed by SEM and TEM. The formation of chiral helical aggregates without the presence of a chiral molecular template most likely resulted from "non-topological symmetry breaking" which manifests during the DA complex formation and subsequently amplified during self-assembly, fiber growth, and fiber bundling.[151] In contrast, no supramolecular fibers were observed in the melatonin-templated solutions and precipitates of amphiphiles **4**-**6**·4X.

4.2.2 Hydrogel Rheological Analysis and Sol-gel-sol Transition Process Monitoring

To characterize the mechanical properties of these hydrogels, dynamic viscoelastic rheology measurements were conducted for the amphiphile-melatonin hydrogels as both the bromide and chloride salts. All hydrogel samples displayed viscoelastic behavior during the testing, each possessing a higher sheer storage modulus (G′) than the sheer loss modulus (G′′), confirming the solid-like nature of the hydrogels (Figure 4.13). Hydrogels which were produced from the bromide salts of **1**-**3**·4X were consistently found to have higher G′ and G′′ values than their chloride counterparts. A direct comparison of the different amphiphiles with one another revealed that hydrogels comprised of **3**·4X and melatonin had the strongest ability to store deformation energy in an elastic manner suggesting that this material had the strongest molecular interactions holding the gel together. Amphiphile-melatonin hydrogels comprised of amphiphile **1**·4X were found to have the second strongest molecular interactions holding it together while complexes comprised of **2**·4X had the weakest ability to store deformation energy. Variable temperature viscosity measurements (Figure 4.14) of these materials revealed that the hydrogelation temperature in all cases was consistently about 9 °C lower on average than the melting temperature. Both the hydrogelation and melting temperature of the bromide salt-based materials were also found to be about 19 °C higher than their corresponding chloride salts on account of the increased aqueous solubility of the chloride salts.

4.2.3 ^{1}H NMR Spectroscopy and Linear Sweep Voltammetric Analysis

In an effort to elucidate any clues which may reveal the origin of the discordant gelation behavior of **1**-**3**·4X versus **4**-**6**·4X, solutions of amphiphiles **1**-**6**·4Cl (3×10^{-3} M)

with two molar equivalents of melatonin were characterized in D_2O by ^1H NMR spectroscopy (Figures 4.5─4.10). Prominent shifts of the signals corresponding to the α ($\Delta\delta$ ranging from 0.02–0.18 ppm) and β ($\Delta\delta$ ranging from 0.07–0.33 ppm) aromatic protons of the π-electron deficient bipyridinium units for all gemini acceptors were observed and accompanied by similar shifts of the signals corresponding to the aromatic protons of the melatonin template. The observed shifts are typical of complex formation on account of donor-acceptor π-π stacking interactions in which the acceptor bipyridinium units have experienced π-electron shielding. In the case of amphiphiles **1**-**6**·4Cl, the data indicated that melatonin has engaged in a face-to-face π-π stacking geometry in an intercalating manner with the bipyridinium head groups. Upon closer inspection of the stacked ^1H-NMR spectra for amphiphiles **1**-**3**·4Cl (Figures 4.5, 4.6, 4.7) versus **4**-**6**·4Cl (Figures 4.8, 4.8, 4.10) in the presence of 2 molar equivalents of the melatonin template, differences in the peak splitting for the signals corresponding to the indolic proton and the proton which is meta with respect to the indolic nitrogen and beta to the ethyl acetamide group can be observed. When melatonin is added to amphiphiles **1**-**3**·4Cl, the melatonin aromatic protons 2 and 3, which clearly have overlapping resonance signals in the absence of amphiphile, shift by $\Delta\delta$ = 0.14, 0.17, and 0.15 ppm for **1**-**3**·4Cl respectively and remain overlapped. However, when melatonin is added to solutions of amphiphiles **4**-**6**·4Cl, the resonance signals for the melatonin aromatic protons 2 and 3 split into two non-overlapping signals. This experimental observation suggests the existence of two types of binding geometries which are distinctly different from one another for acceptors **1**-**3**·4Cl versus **4**-**6**·4Cl. The observed splitting in the signals for protons 2 and 3 of melatonin is due to “symmetry breaking” upon

formation of an intramolecular host-guest complex with amphiphiles **4**-**6**·4Cl, whereby protons 2 and 3 of the melatonin template find themselves held within different chemical environments within the cavity of a single host amphiphile which is adopting a symmetrical "horseshoe-shaped" conformation. When melatonin is bound with amphiphiles **1**-**3**·4Cl, the lack of splitting in the resonance signals for protons 2 and 3 of melatonin suggests that these bipyridinium-based hosts are adopting an "open linear" conformation whereby melatonin is bound intermolecularly between stacking amphiphiles forming a "non-symmetry breaking" complex. From a structural perspective, the data provides evidence to suggest that there is significant tail-to-tail intramolecular interactions for amphiphiles **4**-**6**·4Cl in aqueous solution which allow it to adopt a "horseshoe-shaped" conformation.

In order to gain qualitative insight into the strength of the donor-acceptor $\pi \rightarrow \pi^*$ CT interactions which contribute favorably to complex formation, the electrochemical properties of amphiphiles **1**-**6**·4Cl were investigated by linear sweep voltammetry both with and without one molar equivalent of the melatonin template. The electrochemical reduction and oxidation potentials of bipyridinium derivatives provide insight into the donor-acceptor CT interactions in which they are actively participating. For a single bipyridinium recognition unit, this electrochemical process is characterized by two consecutive reversible monoelectron reduction waves which gives rise to three oxidation states, namely $Bipy^{2+}$ + 1e ⇆ $Bipy^{\bullet+}$ + 1e ⇆ Bipy. Symmetrical bis-bipyridinium tetracationic compounds such as amphiphiles **1**-**6**·4X are characterized by two reversible two-electron processes addressing both bipyridiniums of a single compound. In aqueous solutions however, it is often the first of the two-electron reduction processes that is electrochemically addressable. The fully

reduced bipyridinium species which is generated after the second two-electron reduction process is electrochemically irreversible[37] in aqueous solutions on account of the fact that it is uncharged and insoluble in H_2O.

Linear sweep voltammograms of the amphiphiles were measured from 0 to –0.6 V in order to characterize the first two-electron reduction process whose half wave potentials versus a Ag/AgCl reference electrode are listed in Table 1. Based on the values of the half wave reduction potential ($E_{1/2}$ red.) for each of the amphiphiles, it is clear that changing the bridging unit alters the bipyridinium unit's electron accepting ability. However, the electron accepting ability of the amphiphiles does not appear to correlate with amphiphiles **1**-**3**·4Cl's

Amphiphile	$E_{1/2}$ (red.) [b] mV	$E_{1/2}$ (red. templated)[c] mV	$\Delta E_{1/2}$[d] mV
1·4Cl	–418	–392	26
2·4Cl	–412	–410[x]	2
3·4Cl	–402	–350	52
4·4Cl	–432	–412	20
5·4Cl	–414	–410	4
6·4Cl	–406	–406, –374	0, 32

Table 4.1 Half Wave Reduction Potentials ($E_{1/2}$) of **1**-**6**·4Cl and **1**-**6**·4Cl with One Molar Equivalent of Melatonin Determined by Linear Sweep Voltammetry[a]. [a] Measured against a Ag/AgCl reference electrode using 1 mM samples of amphiphiles in H_2O with 30 mM NaBr as supporting electrolyte. Scan rate = 100 mV/s with a 2 mV step size using a glassy carbon working electrode and a platinum counter electrode at 298 K. [b]Measured in the absence of melatonin. [c]Measured in the prescence of melatonin. [d]Taken as the difference between $E_{1/2}$(red.) and $E_{1/2}$(red. templated).

ability to form supramolecular fibers in solution and undergo hydrogelation. On one hand, with a reduction potential of –402 mV in the absence of template, amphiphile **3**·4Cl has the strongest electron accepting ability of the series and readily gelates under templation conditions. On the other hand, the second strongest electron acceptor is **6**·4Cl with a reduction potential of –406 mV yet **6**·4Cl does not undergo hydrogelation in the presence of a molecular template. It was also observed that upon templation, the half wave reduction potential for each amphiphile experienced an anodic shift in the presence of one molar equivalent of melatonin ($E_{1/2}$ red. templated). The magnitude of the anodic shift ($\Delta E_{1/2}$) is a quantitative measure of the extent of the CT interaction between the π-electron rich donor template and the π-electron deficient bipyridinium acceptor groups of amphiphiles **1**-**6**·4Cl. The data suggests that the extent of the CT interactions between the melatonin template and the amphiphiles also does not correlate with the amphiphile's ability to form fibers and undergo hydrogelation. Interestingly though, there is a correlation between the extent of the CT interaction between the donor and acceptors for amphiphiles **1**-**3**·4Cl and the sheer storage (G') and loss modulus (G'') of the hydrogels which they form when under the influence of molecular templation with melatonin. Thus the strength of the molecular interactions holding the hydrogel together is determined by the strength of the CT interactions between the donor and the acceptor components of the material.

4.2.4 Gemini Surfactant Structural Analysis

As previously pointed out, the "nonclassical" behavior of gemini surfactants is due in part by the decreased ability of their two hydrocarbon chains to interact with one each other in aqueous solution. This of course is dependent on the structural dimensions of the

gemini amphiphile's bridging units. A sufficiently elongated bridge will ensure that the two hydrophobic tails cannot adequately interface with one another while under the influence of hydrophobic interactions in aqueous solutions. Upon comparing the structural dimensions of the gemini amphiphile's bridging units (Scheme 4.2), a clear and obvious trend was observed.

The bridging units of amphiphiles **4**-**6**·4X grow increasingly in one dimension which does not increase the distance between the bipyridinium recognition units and thus does not increase the distance between the two hydrophobic tails. The phenylene bridge of **4**·4X

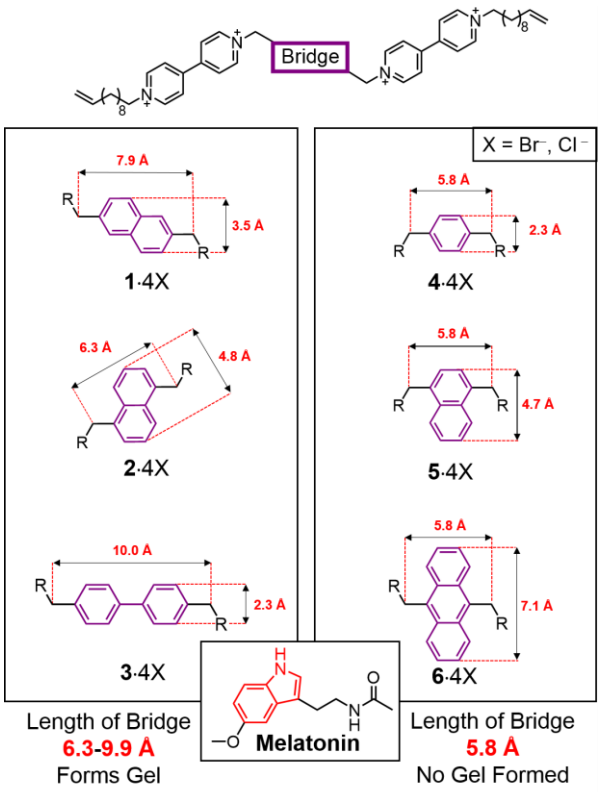

Scheme 4.2 Molecular dimension of different acceptors **1**-**6**·4X.

measures at 2.3 Å in length with a perpendicular width of 5.8 Å across the para-methylene carbons. The length is further augmented to 4.7 Å and finally to 7.1 Å for the 1,4-disubstituted naphthalene and the 9,10-disubstituted anthracene bridges of amphiphiles **5**·4X and **6**·4X respectively while the perpendicular width across the methylene carbons remained unaltered. Unlike amphiphiles **4**-**6**·4X, the bridging units of **1**-**3**·4X are substantially wider in the dimension which increases the distance between their two hydrophobic tails. The width of the 2,6-disubstituted naphthalene bridge across the methylene carbons of amphiphile **1**·4X measures at 7.9 Å while for the 1,5-disubstituted naphthalene and the biphenyl bridges of amphiphiles **2**·4X and **3**·4X, this length is 6.3 Å and 10.0 Å respectively. Hydrogelation only occurs for solutions of melatonin templated gemini amphiphiles with bridge lengths of 6.3 Å and larger (Scheme 4.2, left side). Templated solutions of amphiphiles **4**-**6**·4X which bear a fixed bridge length of 5.8 Å across the methylene carbons did not hydrogelate despite increasing in length in one dimension which does not increase the distance between the hydrophobic tails (Scheme 4.2, right side). The lack of supramolecular fiber formation in melatonin templated aqueous solutions of **4**-**6**·4X indicated that the supramolecular polymerization of these gemini amphiphiles is not favored when the acceptor has a short bridge.

The bridge length that determines the distance between the two hydrophobic tails of gemini amphiphiles is a crucial structural parameter that ultimately controls the solvated molecular conformation of the amphiphiles in aqueous solution. When forced to reside among water molecules, non-polar hydrocarbon chains are surrounded by a tightly packed

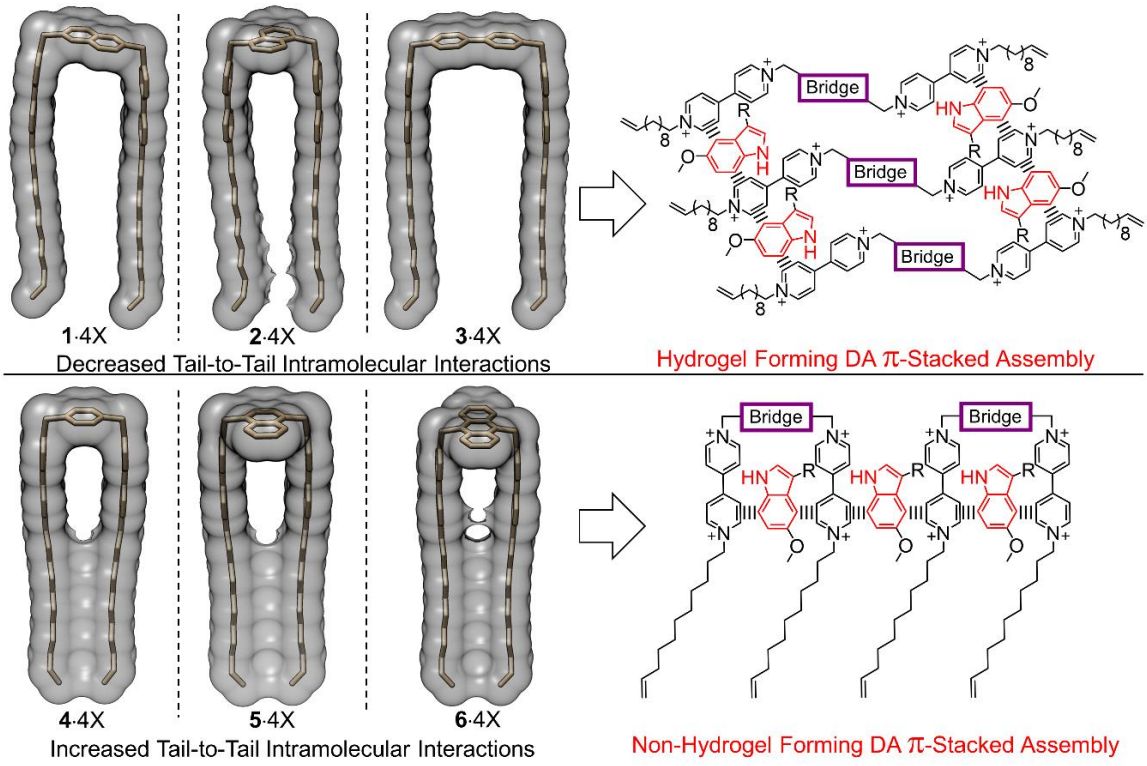

Figure 4.2 (left) Stick representations of energy minimized molecular models overlaid with a solvent-excluded Connolly molecular surface (probe size = 1.4 Å to approximate the radius of a water molecule) for surfactants **1**-**6**·4X illustrating the decreased tail-to-tail intramolecular interactions for **1**-**3**·4X (top) which lead to (top, right) linear hydrogel forming π-stacked assemblies and the increased tail-to-tail intramolecular interactions for **4**-**6**·4X (bottom) which lead to (bottom, right) non-hydrogel forming π-stacked assemblies.

and highly ordered water cage. There is a tremendous entropic gain from the release of structured water molecules from about the non-polar hydrocarbon chains of solubilized amphiphiles upon amphiphile aggregation. In many cases this entropic gain is substantial enough to overcome the entropic loss that accompanies the self-assembly of amphiphiles thus favoring micellization in aqueous solution by way of the hydrophobic effect. The

hydrophobic effect is increasingly more important for gemini amphiphiles bearing two non-polar hydrocarbon chains, which we can think of as having already undergone self-assembly by virtue of the bridging group which links them. If the bridging group is sufficiently short, then the two hydrocarbon chains within a single gemini amphiphile will interact favorably with one another. Contact between the two tails will cause the release of structured water to the bulk solution resulting in fewer water molecules being in direct contact with any individual hydrocarbon chain. In this case, the gemini amphiphile will adopt a "horseshoe-shaped" molecular conformation stabilized by hydrophobic interactions in aqueous solution. However if the gemini amphiphile bridging group is long enough to allow for water molecules to form ordered water cages around each of the two hydrocarbon chains within a single molecule then these two chains will have little to no favorable interactions with one another. At this stage the hydrophobic effect will drive the gemini amphiphile to adopt a linear molecular conformation in solution and the entropic gain from the release of structured water molecules about the two hydrocarbon chains will come about by the clustering of linear molecular stacks.

Stick representations of energy minimized molecular models which have been overlaid with a solvent-excluded Connolly molecular surface (probe size = 1.4 Å to approximate the radius of a water molecule) for amphiphiles **1**-**6**·4X, reveal that the bridging groups of amphiphiles **1**-**3**·4X are long enough to effectively space apart the hydrocarbon chains to allow for water molecules to decrease their tail-to-tail intermolecular interactions (Figure 4.2). These amphiphiles most likely then go on to adopt a linear conformation in solution leading to a hydrogel forming donor-acceptor π-stacked assembly. With a bridging group width of 5.8 Å, the hydrocarbon chains of amphiphiles **4**-**6**·4X are in close enough

proximity to one another to prevent water molecules from forming structured water cages around each chain. These amphiphiles ostensibly go on to adopt a "horseshoe-shaped" conformation. Here melatonin can bind in an intercalating fashion between the bipyridinium units of a single amphiphile and in-between contiguously assembled amphiphiles in a non-hydrogel forming donor-acceptor π-stacked assembly.

4.2.5 Thermochromism of Melatonin-Templated Gemini Surfactants 1-3·4X in the Solid State

Xerogel thin films which exhibit reversible thermochromism in the solid state were easily processed from heated aqueous solutions of **1**-**3**·4X as either the tetrachloride or tetrabromide salt with 2 molar equivalents of melatonin. The processed films appear red in color at room temperature under ambient humidity and undergo a remarkable color change, appearing yellow upon heating (Figure 4.3). The thermochromic reversibility of the films were found to be quite robust, capable of surviving an extended number of heating-cooling cycles as confirmed by solid state UV-Vis absorption spectroscopy (Figure 4.4). In a similar fashion, aerogels prepared from lyophilization of the templated hydrogels comprised of surfactants **1**-**3**·4X also exhibited robust thermochromism (Figure 4.3). The solid state thermochromism of these materials was the result of competing donor-acceptor CT interactions. The color of the donor-acceptor complex at room temperature is derived from the $\pi \rightarrow \pi^*$ CT interactions between the two organic components of the complex, namely the π-electron rich donor, melatonin, and the tetracationic π-electron deficient bis-bipyridinium acceptor. At elevated temperatures, the color of these materials is derived from the $n \rightarrow \pi^*$ CT interactions between the acceptor and its halogen counterions. The modulation of the

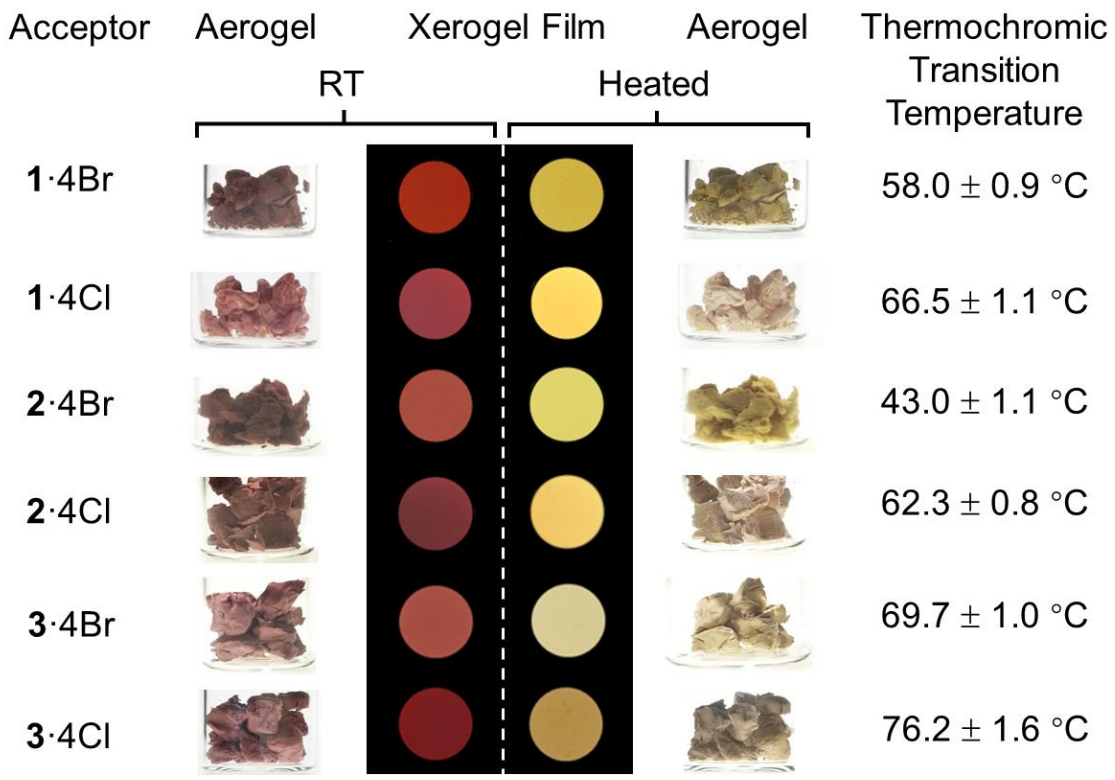

Figure 4.3 Thermochromic behaviour of processed materials derived from melatonin-templated amphiphiles **1**-**3**·4X in the solid state as depicted by photographs of aerogels and cropped xerogel film color swatches at 25 °C (left) and at their corresponding thermochromic transition temperature (right).

two competing CT interactions was brought to bear by the hydration/dehydration of the ion-pair. At temperatures below the thermochromic transition temperature, the $\pi \rightarrow \pi^*$ CT interaction dominates, visibly producing a characteristic red color. This phenomenon is due to the effects of bound water molecules –which the material adsorbs hygroscopically– coordinating to the charged bipyridiniums and its halide counterions, which in effect , disturbs the electronic transitions between the ion-pair. Thus the thermochromic transition point for these materials is the temperature at which the hydrated ion-pair loses its

coordinating waters allowing for the n→π* CT interactions within the ion-pair to outcompete the π→π* CT interactions within the complex, the net result of which is the dramatic change in the materials color.

A comparison of the thermochromic transition temperatures between tetrabromide salts and their tetrachloride counterparts revealed the transition temperatures of the tetrachloride salts to be consistently higher. Interestingly, the difference in the thermochromic transition temperature between the two different halogen species for a particular surfactant was the smallest for **3**·4X and slightly larger for **1**·4X, with the largest differential measured at 19.3 °C for **2**·4X. Additionally, surfactant **3**·4X also possessed the highest thermochromic transition temperature in both the tetrabromide and the tetrachloride series at 69.7 ± 1.1 °C and 76.2 ± 1.6 °C respectively. **1**·4X had the second highest set of transition temperatures (58.0 ± 0.9 °C and 66.5 ± 1.1 °C) and **2**·4X the lowest (43.0 ± 1.1 °C and 62.3 ± 0.8 °C). This trend correlates with the observed trends present in the sheer storage (G') and loss modulus (G'') of the surfactants' corresponding hydrogels and the magnitude of the anodic shifts ($\Delta E_{1/2}$) of their bipyridinium reduction potentials as measured by linear sweep voltammetry. Hence the thermochromic transition temperature for the surfactants in the solid state is strongly correlated to the strength of the donor-acceptor CT interactions of the surfactants with melatonin in solution. In this case for example, **3**·4X, which possesses the strongest donor-acceptor CT interaction with melatonin, has the highest thermochromic transition temperature, and this transition temperature is less effected by a change in the identity of the halide counterion.

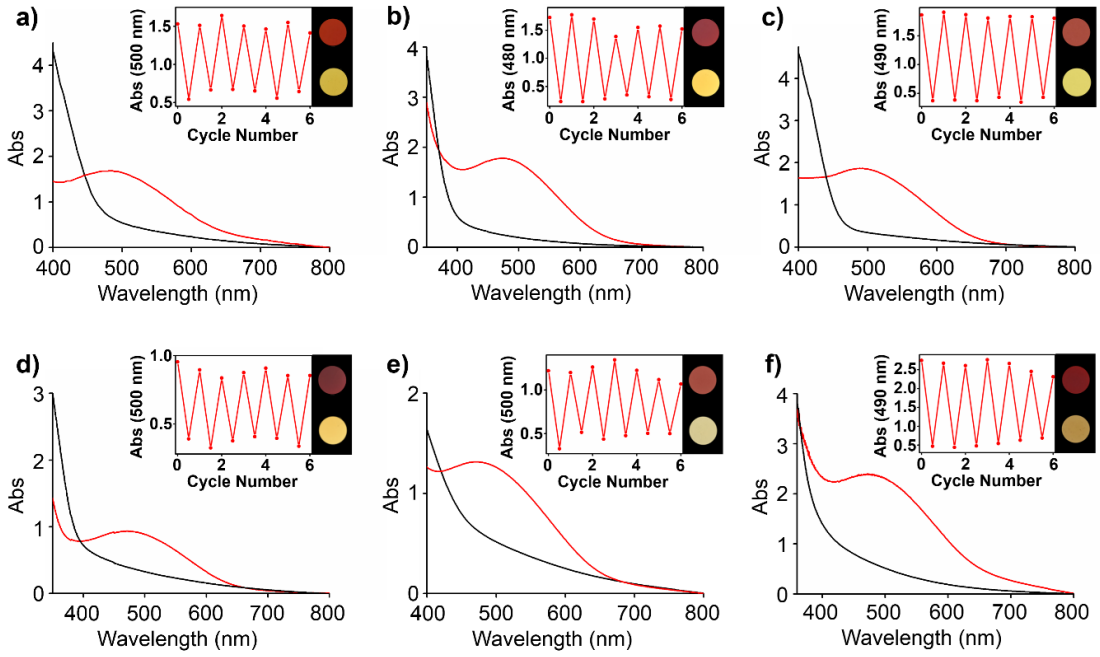

Figure 4.4 UV-visible absorption spectra of thermochromic films at room temperature and at thermochromic transition temperature. Inset color patterns show the thermochromism of each complex xerogel film formed by drop-casting. **a**), **c**), and **e**) are **1**-**3**·4Br⊃**Mel**, **b**), **d**), and **f**) are **1**-**3**·4Cl⊃**Mel.**

4.2.6 Inkjet printing of thermochromic supramolecular materials

The meritorious feature of these thermochromic supramolecular materials is their excellent processability. Using a conventional inkjet office printer, thermochromic patterns of the "Wiley" logo were obtained using aqueous-ethanolic inks comprised of templated amphiphiles **1**-**3**·4X (Figure 4.5). The thermochromic inks were prepared by dissolving **1**-**3**·4X and melatonin in a mixed solvent solution of water and ethanol, and were injected to an empty printer ink cartridge. The printed patterns all exhibited reversible thermochromic properties similar to the xerogel films, changing in color from red to yellow in the case of

the tetrabromide salts (Figure 4.4a, c, and, e) and from red to crème in the case of the tetrachloride salts (Figure 4.4b, d, and f), after reaching their respective color transition temperatures. Structural variations of the amphiphile's bridging group did not play a significant role in their inkjet printability. However it must be noted that the tetrachloride variants of the amphiphiles do possess increased solubility in the ink solutions as prepared allowing for more concentrated inks to be produced from those samples.

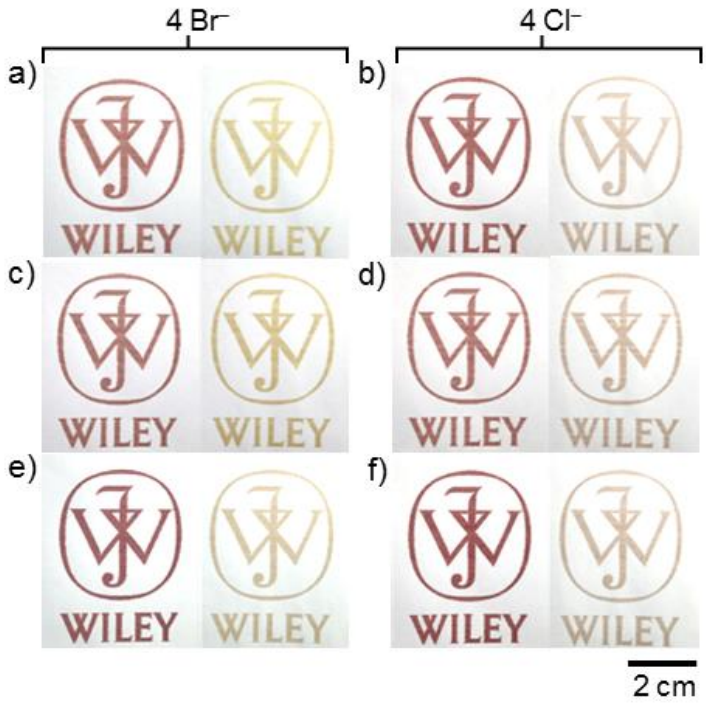

Figure 4.5 Inkjet printed patterns of **1**-**3**·4X⊃**Mel** below (left) and above thermochromic temperature**. a**) **1**·4Br⊃**Mel**, **b**) **1**·4Cl⊃**Mel**, **c**) **2**·4Br⊃**Mel**, **d**) **2**·4Cl⊃**Mel**, **e**) **3**·4Br⊃**Mel**, **f**) **3**·4Cl⊃**Mel**.

4.3 Conclusion

The use of bipyridinium-based supramolecular amphiphiles to develop chemical systems which undergo template-directed self-assembly have been widely reported in literature. In some cases these materials, when under the influence of donor-acceptor CT-based molecular templation, go on to form interesting aggregate superstructures in solution ranging from oblate spheroidal micelles to linear fibers. Examples can also be found in which templation has led to hydrogelation. In any case, the material processability of supramolecular amphiphiles leading to device fabrication, functional materials, and the performance of these products hinges on structure-property relationships which are not incredibly well understood. Investigations into the new series of bis-bipyridinium gemini surfactants possessing differing bridging groups reported here have provided new insights and helped to elucidate the structure-property relationships which exercise authority over their ability to form helical fibrilar networked-based hydrogels, the strength of these hydrogels, and the solid-state thermochromic performance characteristics of materials processed from these CT complexes.

To summarize these structure-property relationships, it was found that the length of the gemini surfactant bridge which establishes the distance between the two hydrophobic tails in the acceptors plays a dominate role in determining their ability to undergo hydrogelation under templation conditions. Bridge lengths of 6.3 Å and larger imparted the ability to easily form helical fibers in solution leading to hydrogelation. Increases in the bridge length perpendicular to this dimension which does not affect the distance between the hydrophobic tails is of little consequence. In addition, the identity of the counterions for the tetracationic acceptors have no effect on the hydrogelation ability of donor-acceptor

complexes. However, they do impact the temperature at which gelation and melting occurs, as well as the strength of the gels, with the tetrabromide salts forming stronger hydrogels with higher gelation and melting temperatures than their tetrachloride counterparts. The strength of the hydrogels was also found to be positively correlated with the magnitude of the templating donor-acceptor CT interaction in solution.

Perhaps more provocative is the fact that the solid state thermochromic transition temperature of the aerogels, xerogel films, and inkjet printed patterns were found to be positively correlated with the magnitude of the templating donor-acceptor CT interaction in solution as measured by linear sweep voltammetry. The thermochromic transition temperature can be further augmented by employing counterions for the tetracationic acceptor which can form stronger ion-dipole interactions with coordinating water molecules. For example, it is more favorable for chloride to undergo hydration, having a standard molar Gibbs free energy of hydration ($\Delta G°_{hydro}$) of -347 kJ·mol^{-1} (-82.9 kcal·mol^{-1}), than bromide, whose $\Delta G°_{hydro}$ is -321 kJ·mol^{-1} (-76.7 kcal·mol^{-1}). In all cases, the tetrachloride-based materials switched at higher temperatures as compared to their tetrabromide counterparts and were distinctly crème in color at elevated temperatures whereas the tetrabromides were yellow. These data indicates that in the case of competing CT interactions, whereby $\pi \rightarrow \pi^*$ and $n \rightarrow \pi^*$ CT interactions are pitted against one another in this system, increases in the strength of the $\pi \rightarrow \pi^*$ CT interactions between the bipyridinium units and the melatonin template, results in the concomitant decrease in the magnitude of the $n \rightarrow \pi^*$ CT interaction between the bipyridinium units and its halide counterions. This shift in the intermolecular polarization towards the $\pi \rightarrow \pi^*$ CT interaction between the organic components of the

complex strengthens the ion-dipole interaction between coordinating water molecules and the halide counterions three non-covalent bonds away, thereby increasing the thermochromic transition temperature of the material. Thus we have shown that by tuning the π-electron accepting ability of the surfactant to such an extent that it goes on to form donor-acceptor CT complexes of differing strengths with a given π-electron rich donor template, we can effectively tune the thermochromic performance characteristics of these complexes in the solid state.

4.4 Experimental Section

4.4.1 Materials and General Methods

Starting materials and reagents were purchased from Tokyo Chemical Industry and used as received. 1,4-dibromo-methylnaphthalene, [179] 1,5-dibromo-methylnaphthalene, [179] and mono-undecylated bipyridine[92] were synthesized following procedures reported in the literature. All reactions were performed under an argon atmosphere and in dry solvents unless otherwise noted. Analytical thin-layer chromatography (TLC) was performed on aluminum sheets, percolated with silica gel GF254, visualized by exposure to ultraviolet light. Deuterated solvents (Cambridge Isotope Laboratories) for NMR spectroscopic analyses were used as received. ^{1}H and ^{13}C NMR spectra were recorded on a Bruker Advance III 400 MHz spectrometer. Chemical shifts are reported in ppm relative to the residual signal of the solvent (D_2O: δ 4.79 ppm). The peak patterns are defined as follows: s, singlet; d, doublet; t, triplet; q, quartet; m, multiplet; dd, doublet of doublets, and br, broad peak. The coupling constants J, are reported in Hertz (Hz). High resolution mass spectrometry (HRMS) was obtained on a QTOF micro spectrometer. UV-Vis spectra were

recorded on a HITACHI U-3900 spectrophotometer. Viscosity experiments were performed on a SV-10 A&D Sine wave Vibro Viscometer. Aerogels were prepared using a CHRIST Alpha 1-2 LD plus Freeze dryer. Melting points and color change temperatures of assemblies were recorded on a RY-1 Melting point apparatus. SEM images on drop-casted films were taken by a FEI Quanta 600 FE-SEM. TEM samples were prepared by adding 1 μL of hot assembly solution onto carbon-coated copper grid. The TEM images were taken by a JOEL 1200 EX electron microscope at an accelerating voltage of 100 kV. Prints were taken by Canon printer iP2780.

4.4.2 Design and Synthesis of **1**-**6**

Synthesis of **3**[151] and **4**[92] were followed the published literatures. Synthesis of **1**·4Br: 2,6-Bis (bromomethyl) naphthalene (0.5g, 1.59 mmol) was added to a solution of mono-undecylated bipyridine (2.48g, 6.37 mmol) in dry DMF (15 mL), and the mixture was stirred at 80 °C for 24 h. The reaction mixture was cooled and a yellow precipitate was collected by filtration. The yellow precipitate was then washed with DMF and diethyl ether three times each and dried in vacuo to afford the tetracationic product **1**·4Br (1.71 g, 98%) as a yellow solid. MP: Carbonize at 293 °C. ^{1}H NMR (400 MHz, D_2O, 25 °C): δ = 1.26–1.35 (br d, 24H), 1.99–2.08 (br m, 8H), 4.73 (t, *J* = 7.07 Hz, 4H), 4.90 (d, *J* = 10.47 Hz, 2H), 4.99 (d, *J* = 16.97 Hz, 2H), 5.85 (m, 2H), 6.15 (s, 4H), 7.67 (d, *J* = 8.51 Hz, 2H), 8.11 (d, *J* = 8.45 Hz, 2H), 8.16 (s, 2H), 8.56 (dd, *J* = 6.13 Hz, 13.3 Hz, 8H), 9.12 (d, *J* = 6.13 Hz, 4H), 9.25 (d, *J* = 6.23 Hz, 4H).

2·4Br, **5**·4Br, and **6**·4Br were prepared following analogous procedures.

2·4Br. Yellow solid. 85% yield. MP: Carbonize at 293 °C. ^{1}H NMR (400 MHz, D_2O, 25 °C): δ = 1.30 (br d, 24H), 1.97–2.08 (br m, 8H), 4.73 (s, 4H), 4.88 (s, 2H), 4.96 (d, *J* = 17.42 Hz, 2H), 5.83 (m, 2H), 6.53 (s, 4H), 7.76–7.85 (m, 4H), 8.21 (d, *J* = 8.54 Hz, 2H), 8.54 (s, 8H), 9.14 (dd, *J* = 6.30 Hz, 17.48 Hz, 8H).

3·4Br. Yellow solid. 92% yield. MP: Carbonize at 299 °C. ^{1}H NMR (400 MHz , D_2O, 25 °C): δ = 1.42 – 1.15 (br, m, 24H), 2.04 (br, m, 8H), 4.72 (t, *J* = 7.29 Hz, 4H), 4.92 (d, *J* = 10.13 Hz, 2H), 5.00 (d, *J* = 17.30 Hz, 2H), 5.86 (m, 2H), 6.00 (s, 4H), 7.65 (d, *J* = 8.26 Hz, 4H), 7.84 (d, *J* = 8.19 Hz, 4H), 8.56 (dd, *J* = 6.81 Hz, 9.60 Hz, 8H), 9.11 (d, *J* = 6.88 Hz, 4H), 9.21 (d, *J* = 6.83 Hz, 4H).

4·4Br. Yellow solid. 96% yield. MP: Carbonize at 298 °C. ^{1}H NMR (400 MHz , D_2O, 25 °C): δ = 1.24 – 1.34 (br, m, 24H), 2.16 – 1.88 (br, m, 8H), 4.73 (t, *J* = 7.09 Hz, 4H), 4.86 (d, *J* = 10.43 Hz, 2H), 4.95 (d, *J* = 17.31 Hz, 2H), 5.82 (m, 2H), 6.00 (s, 4H), 7.66 (s, 4H), 8.56 (dd, *J* = 6.58 Hz, 9.29 Hz, 8H), 9.12 (d, *J* = 6.41 Hz, 4H), 9.20 (d, *J* = 6.51 Hz, 4H).

5·4Br. Yellow solid. 94% yield. MP: Carbonize at 289 °C. ^{1}H NMR (400 MHz , D_2O, 25 °C): δ = 1.24 – 1.34 (m, 24H), 1.97 (dd, *J* = 6.83 Hz, 15.19 Hz, 4H), 2.07 (m, 4H), 4.72 (t, *J* = 7.19 Hz, 4H), 4.86 (m, 2H), 4.96 (dd, *J* = 2.09 Hz, 17.03 Hz, 2H), 5.82 (m, 2H), 6.54 (s, 4H), 7.74 (dd, *J* = 3.24, 6.47 Hz, 2H), 7.82 (s, 2H), 8.10 (dd, *J* = 3.29 Hz, 6.24 Hz, 2H), 8.54 (m, 8H), 9.11 (d, *J* = 6.88 Hz, 4H), 9.19 (d, *J* = 6.88 Hz, 4H).

6·4Br. Yellow solid. 96% yield. MP: Carbonize at 259 °C. ^{1}H NMR (400 MHz, D_2O, 25 °C): δ = 1.26 (br d, 24H), 2.10 – 1.90 (br m, 8H), 4.69 (s, 4H), 4.85 (d, *J* = 10.40 Hz, 2H), 4.94 (d, *J* = 17.20 Hz, 1H), 5.81 (m, 2H), 7.08 (s, 4H), 7.81 (d, *J* = 5.20 Hz, 4H), 8.50 – 8.40 (br m, 12H), 9.05 (dd, *J* = 5.60 Hz, 15.20 Hz, 8H).

Counterion Exchange from **1**·4Br to **1**·4Cl: 1.19 g of **1**·4Br (1.09 mmol) was dissolved in 100 mL of hot water and a saturated aqueous solution of $NH_4 \cdot PF_6$ (Ammonium Hexafluorophosphate) was added dropwise until no further precipitate formed. The off-white precipitate was then filtered and washed three times with 100 mL of distilled water and three times with 100 mL of diethyl ether and dried under vacuum to afford **1**·4PF_6. Then **1**·4PF_6 was dissolved in 100 mL of hot MeCN and a saturated MeCN solution of Tetrabutylammonium Chloride was added dropwise until no more precipitate formed. The solution was cool down to room tempareture, then filtered and washed three times with 100 mL MeCN and three times with 100 mL of diethyl ether and dried under vacuum to afford the tetracationic product **1**·4Cl (0.91 g, 91%) as a yellow solid. MP: Carbonize at 269 °C. ^{1}H NMR (D_2O, 400 MHz, 25 °C): δ = 1.17–1.29 (br m, 24H), 1.91 (d, *J* = 5.44 Hz, 4H), 2.02 (s, 4H), 4.68 (s, 4H), 4.83 (d, *J* = 10.27 Hz, 2H), 4.91 (d, *J* = 17.15 Hz, 2H), 5.74–5.79 (m, 2H), 6.09 (s, 4H), 7.62 (d, *J* = 7.56 Hz, 2H), 8.05–8.06 (m, 2H), 8.11 (s, 2H), 8.52 (d, *J* = 18.58 Hz, 8H), 9.08 (s, 4H), 9.21 (s, 4H). ^{13}C NMR (D_2O, 400 MHz, 25 °C): δ= 25.06, 27.91, 28.08, 28.16, 28.25, 28.27, 30.47, 33.02, 62.33, 64.84, 113.91, 126.75, 126.96, 127.20, 129.21, 130.05, 131.43, 133.27, 140.24, 145.51, 145.70, 149.72, 150.48. IR (KBr): 3420.48 (w, b), 3043.23 (w), 2985.35 (m), 2923.22 (s), 2852.46 (m), 1639.82 (s), 1562.12 (w), 1447.94 (m), 1365.39 (w), 1228.10 (w), 1178.33 (w), 908.37 (w), 831.15 (w), 802.64 (w), 718.68 (w) cm^{-1}. HRMS (ESI): m/z calculated for $[M-H]^+$, $C_{54}H_{67}Cl_4N_4$: 913.4097; found: 913.4091.

2·4Cl, **3**·4Cl, **4**·4Cl, **5**·4Cl, and **6**·4Cl were prepared following analogous procedures.

2·4Cl. Yellow solid. 93% yield. MP: Carbonize at 285 °C. ^{1}H NMR (D_2O, 400 MHz, 25 °C): δ = 1.27–1.37 (br m, 24H), 1.99 (q, *J* = 7.05 Hz, 4H), 2.1 (m, 4H), 4.74 (d, *J* = 7.20 Hz, 4H), 4.88 (d, *J* = 10.20 Hz, 2H), 4.98 (d, *J* = 17.34 Hz, 2H), 5.84 (m, 2H), 6.56 (s, 4H), 7.79–7.82 (m, 2H), 7.86 (d, *J* = 7.01 Hz, 2H), 8.24 (d, *J* = 8.42 Hz, 2H), 8.55–8.57 (m, 8H), 9.16 (dd, *J* = 6.88 Hz, 17.99 Hz, 8H). ^{13}C NMR (D_2O, 400 MHz, 25 °C): δ = 24.97, 27.80, 28.07, 28.11, 28.15, 28.19, 30.41, 33.01, 62.32, 62.41, 113.85, 125.56, 126.92, 127.08, 127.64, 128.47, 131.10, 131.57, 140.31, 145.36, 145.46, 149.68, 150.58. IR (KBr): 3405.34 (m, b), 3111.99 (w), 3046.67 (w), 2919.26 (s), 2851.34 (m), 1637.03 (s), 1555.93 (m), 1503.56 (w), 1468.71 (w), 1441.61 (m), 1357.88 (m), 1216.92 (w), 1174.61 (w), 1151.86 (w), 835.15 (m), 800.65 (m), 788.57 (m), 720.19 (w), 546.32 (w), 506.24 (w) cm^{-1}. HRMS (ESI): m/z calculated for $[M-H]^+$, $C_{54}H_{67}Cl_4N_4$: 913.4097; found: 913.4093.

3·4Cl. Yellow solid. 89.7% yield. MP: Carbonize at 246 °C. ^{1}H NMR (400 MHz, D_2O, 25 °C): δ = 1.27 (br, m , 24H), 2.13 – 1.89 (br, m, 8H), 4.77 – 4.71 (t, *J* = 7.00 Hz, 4H), 4.89 (d, *J* = 10.11 Hz, 2H), 4.96 (d, *J* = 17.33 Hz, 2H), 5.82 (m, 2H), 6.02 (s, 4H), 7.68 (d, *J* = 7.49 Hz, 4H), 7.84 (d, *J* = 7.49 Hz, 4H), 8.62 – 8.54 (m, 8H), 9.14 (d, *J* = 5.69 Hz, 4H), 9.24 (d, *J* = 5.57 Hz, 4H). ^{13}C NMR (D_2O, 400 MHz, 25 °C): δ= 25.04, 27.89, 28.08, 28.16, 28.25, 28.26, 30.45, 33.04, 62.31, 64.48, 113.90, 126.92, 127.13, 128.15, 129.96, 132.08, 140.26, 141.19, 145.50, 145.55, 149.73, 150.39. IR (KBr): 3425.34 (m, b), 3113.02 (w), 3040.88 (m), 3000.33 (m), 2924.37 (s), 2853.57 (m), 1638.79 (s), 1557.51 (m), 1502.07 (m), 1442.13 (s), 1353.03 (w), 1222.90 (w), 1174.52 (w), 1156.73 (w), 909.15 (w), 858.20 (w), 831.92 (w), 788.53 (m), 616.84 (w), 483.98 (w) cm^{-1}. HRMS (ESI): m/z calculated for $[M-H]^+$, $C_{56}H_{69}Cl_4N_4$: 939.4254; found: 939.4236.

4·4Cl**.** Yellow solid. 99.4% yield. MP: Carbonize at 261 °C. ^{1}H NMR (400 MHz, D_2O, 25 °C): δ = 1.42 – 1.17 (m, 24H), 2.03 (m, 8H), 4.75 (d, *J* = 7.14 Hz, 4H), 4.89 (d, *J* = 10.21 Hz, 2H), 4.98 (d, *J* = 17.35 Hz, 2H), 5.91 – 5.78 (m, 2H), 6.03 (s, 4H), 7.70 (s, 4H), 8.59 (dd, *J* = 6.93 Hz, 9.46 Hz, 8H), 9.15 (d, *J* = 6.82 Hz, 4H), 9.23 (d, *J* = 6.84 Hz, 4H). ^{13}C NMR (D_2O, 400 MHz, 25 °C): δ = 24.14, 26.99, 27.24, 27.29, 27.33, 27.38, 29.59, 32.17, 61.46, 63.33, 113.03, 118.27, 126.08, 126.36, 129.50, 133.38, 139.37, 144.63, 144.78, 148.81, 149.61. IR (KBr): 3410.39 (m,b), 3113.62 (w), 3038.85 (m), 2980.38 (m), 2922.11 (s), 2852.00 (m), 1637.69 (s), 1555.10 (m), 1503.16 (w), 1465.88 (m), 1443.05 (m), 1350.19 (w), 1279.98 (w), 1175.79 (w), 1154.78 (w), 828.71 (m), 770.84 (m), 608.57 (w), 510.68 (w) cm^{-1}. HRMS (ESI): m/z calculated for $[M-H]^+$, $C_{50}H_{65}Cl_4N_4$: 863.3939; found: 863.3968.

5·4Cl. Yellow solid. 92% yield. MP: Carbonize at 265 °C. ^{1}H NMR (D_2O, 400 MHz, 25 °C): δ = 1.21–1.39 (m, 24H), 1.96 (q, *J* = 6.74 Hz, 15.40 Hz, 4H), 2.10 (m, 4H), 4.75 (t, *J* = 7.23 Hz, 4H), 4.86 (m, 2H), 4.95 (dd, *J* = 1.96 Hz, 17.31 Hz, 2H), 5.81 (m, 2H), 6.57 (s, 4H), 7.77 (dd, *J* = 3.23 Hz, 6.43 Hz, 2H), 7.87 (s, 2H), 8.14 (dd, *J* = 3.26 Hz, 6.34 Hz, 2H), 8.58 (t, *J* = 7.18 Hz, 8H), 9.15 (d, *J* = 6.81 Hz, 4H), 9.23 (d, *J* = 6.81 Hz, 4H). ^{13}C NMR (D_2O, 400 MHz, 25 °C): δ = 25.00, 27.83, 28.07, 28.12, 28.17, 28.21, 30.43, 33.02, 62.23, 62.33, 113.87, 123.77, 126.94, 127.15, 128.62, 129.76, 130.43, 131.35, 140.35, 145.46, 149.68, 150.69. IR (KBr): 3408.28 (w,b), 3121.05 (w), 3046.60 (m), 2985.64 (m), 2922.83 (s), 2852.13 (m), 1638.31 (s), 1560.82 (w), 1509.76 (w), 1449.15 (m), 1380.70 (w), 1351.95 (w), 1229.29 (m), 1162.53 (w), 909.24 (w), 869.46 (w), 829.98 (w), 788.75 (w), 757.63 (w), 715.22 (w) cm^{-1}. HRMS (ESI): m/z calculated for $[M-H]^+$, $C_{54}H_{67}Cl_4N_4$: 913.4097; found: 913.4070.

6·4Cl. Yellow solid. 75% yield. MP: Carbonize at 252 °C. ^{1}H NMR (D_2O, 400 MHz, 25 °C): δ = 1.21–1.32 (br m, 24H), 1.98 (br m, 8H), 4.72 (s, 4H), 4.84 (d, *J* = 11.03Hz, 2H), 4.93 (d, *J* = 17.26 Hz, 2H), 5.79 (m, 2H), 6.91 (s, 4H), 7.87 (d, *J* = 6.26 Hz, 4H), 8.39 (s, 4H), 8.49 (m, 8H), 9.00 (d, *J* = 5.04 Hz, 4H), 9.10 (d, *J* = 5.42 Hz, 4H). ^{13}C NMR (D_2O, 400 MHz, 25 °C): δ= 25.02, 27.86, 28.07, 28.13, 28.21, 28.24, 30.43, 33.01, 56.46, 62.32, 113.88, 123.84, 124.98, 126.92, 127.15, 128.92, 131.19, 140.29, 144.89, 145.46, 149.56, 150.47. IR (KBr): 3418.14 (m,b), 3034.01 (m), 2998.65 (m), 2918.50 (s), 2851.59 (m), 1633.29 (s), 1553.51 (w), 1502.06 (w), 1444.27 (m), 1359.87 (w), 1219.95 (w), 1175.06 (w), 1147.77 (w), 834.35 (m), 820.34 (m), 789.38 (w), 758.76 (w), 717.46 (w), 599.70 (w), 554.32 (w) cm^{-1}. HRMS (ESI): m/z calculated for $[M-H]^+$, $C_{58}H_{69}Cl_4N_4$: 963.4255; found: 963.4271.

4.4.3 Sol-gel Synthesis and Preparation of Hydrogels, Xerogel Thin Films, and Aerogels

Preparation of **1**·4Br⊃**Mel** hydrogels, thin films, and aerogels: 10.93 mg of **1**·4Br (0.01 mmol) and 4.64 mg of Melatonin (0.02 mmol) were added to 1 mL of distilled water. The solution was gently heated until all the compounds were fully dissolved. The supramolecular amphiphile-based **1**·4Br⊃**Mel** hydrogel was formed upon cooling. Gentle heating of the hydrogel regenerated the solution. This process of sol–gel transition was demonstrated to be fully reversible. The **1**·4Br⊃**Mel** xerogel thin film was formed by drop casting a solution of hot **1**·4Br⊃**Mel** (100 μL at 60 °C) onto a glass slide. Upon cooling, the drop-casted solutions formed a uniform hydrogel. Hydrogel samples prepared in this manner were left overnight for drying under ambient air to afford **1**·4Br⊃**Mel** xerogel thin films. The **1**·4Br⊃**Mel** aerogel was formed by freeze-drying the hydrogel in a freeze-dryer for 10

hours. Hydrogels, thin films, and aerogels of **1**·4Cl⊃**Mel**, **2**·4X⊃**Mel**, and **3**·4X⊃**Mel** were prepared in a similar approach. Melting temperature of **1**·4Cl⊃**Mel** and **2**·4Br⊃**Mel**, **2**·4Cl⊃**Mel**, **3**·4Br⊃**Mel** and **3**·4Cl⊃**Mel** hydrogels are recorded as 37 °C, 39 °C, 21.5 °C, 47 °C, 33.5 °C respectively.

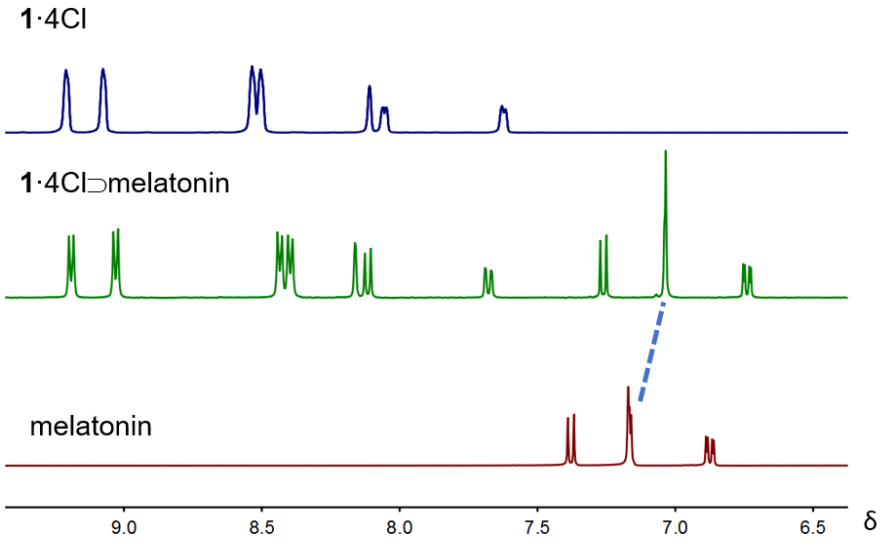

Figure 4.6 Stacked ^{1}H NMR spectra of **1**·4Cl(blue), melatonin(red) and **1**·4Cl ⊃Melatonin(green) in D_2O (400 MHz, RT).

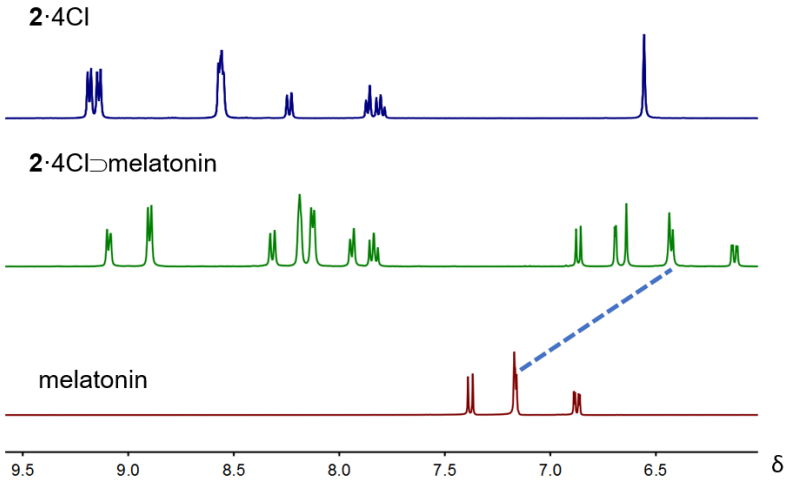

Figure 4.7 Stacked ^{1}H NMR spectra of **2**·4Cl(blue), melatonin(red) and **2**·4Cl ⊃Melatonin(green) in D_2O (400 MHz, RT).

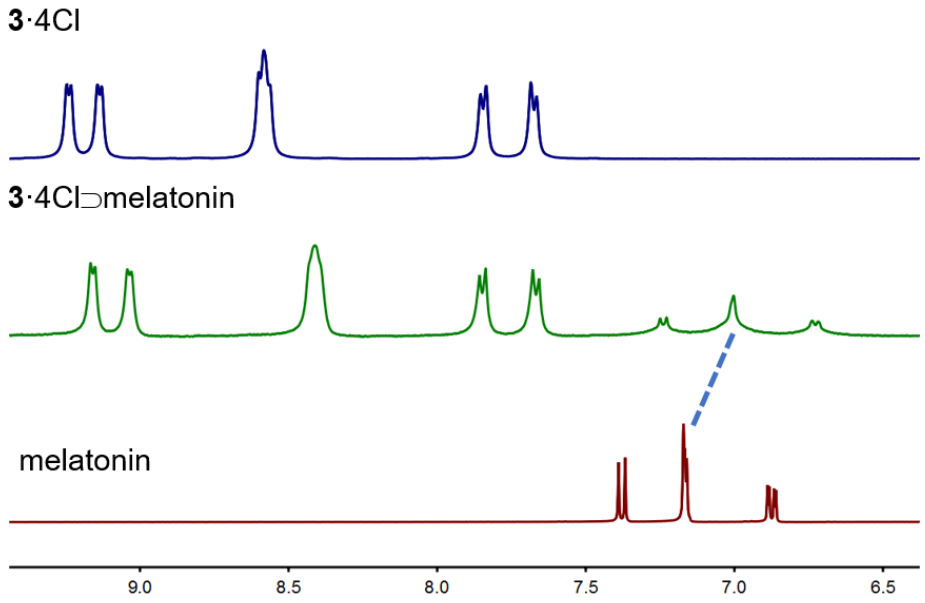

Figure 4.8 Stacked ^{1}H NMR spectra of **3**·4Cl(blue), melatonin(red) and **3**·4Cl ⊃Melatonin(green) in D_2O (400 MHz, RT).

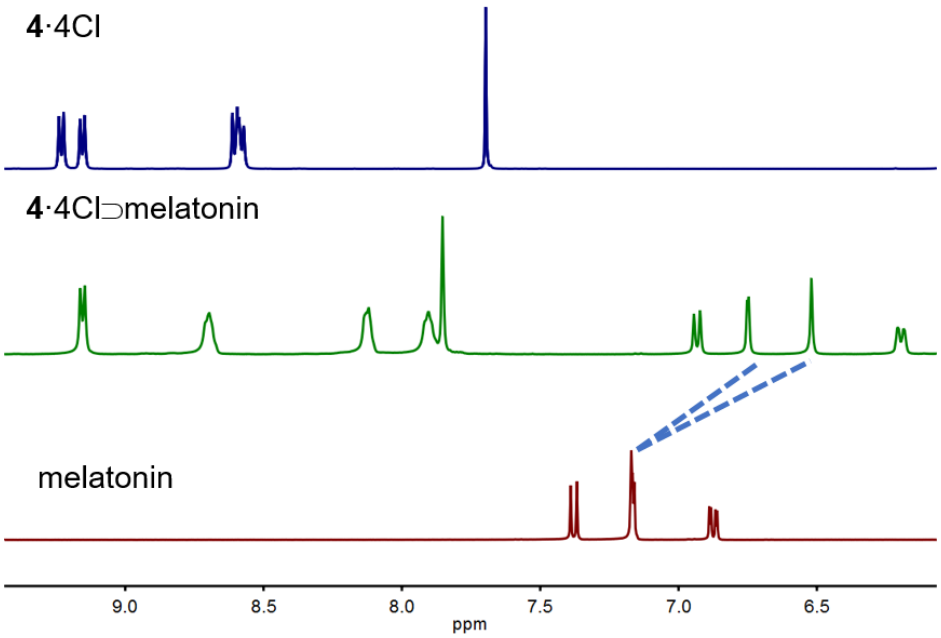

Figure 4.9 Stacked ^{1}H NMR spectra of **4**·4Cl(blue), melatonin(red) and **4**·4Cl ⊃Melatonin(green) in D_2O (400 MHz, RT).

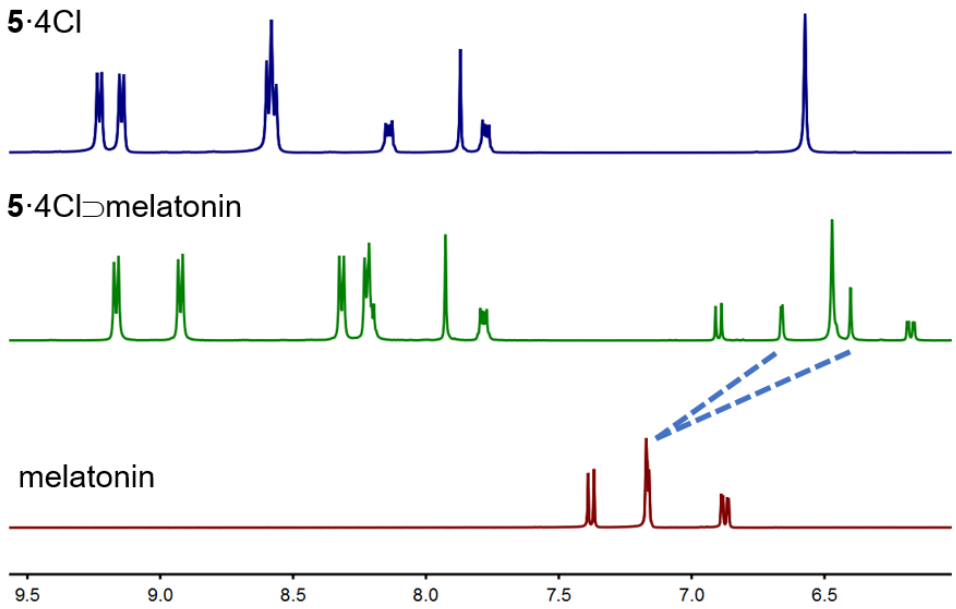

Figure 4.10 Stacked ^{1}H NMR spectra of **5**·4Cl(blue), melatonin(red) and **5**·4Cl ⊃Melatonin(green) in D_2O (400 MHz, RT).

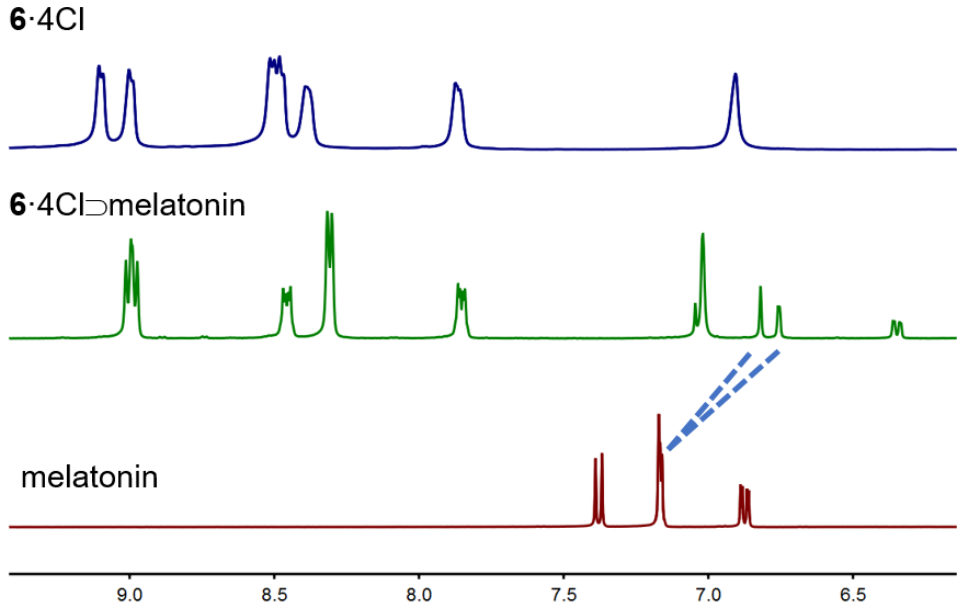

Figure 4.11 Stacked ^{1}H NMR spectra of **6**·4Cl(blue), melatonin(red) and **6**·4Cl ⊃Melatonin(green) in D_2O (400 MHz, RT).

4.4.4 Thermochromic Transition Experiment

UV-vis measurements of **1**·4Br⊃**Mel** xerogel thin film: 200 μL of a hot **1**·4Br⊃**Mel** solution (60 °C) was added onto a 1 mm cuvette, then left overnight for drying in ambient air to afford **1**·4Br⊃**Mel** xerogel thin film which was further used for measuring the UV-Vis spectra. The film had a red color at room temperature, and its color changed to yellow upon reaching the thermochromic transition temperature. The UV-Vis spectra of yellow film was then recorded. After cooling the glass to room temperature and waiting for 20 min, the thin film goes back to red color again. The UV-Vis spectra of the thin film during 5 hot-cooling cycles were recorded.

Inkjet printing: 191.2 mg of **1**·4Br (0.175 mmol) and 81.3 mg of melatonin (0.35 mmol) were added into a water/ethanol mixed solvent (V_{water}:$V_{ethanol}$ = 1:1, 5 mL) The solution was gently heated until all the compounds were fully dissolved. This ink was then injected into an empty inkjet printer ink cartridge and used to replace the black ink cartridge in a conventional office inkjet printer. Similarly, inks of **1**·4Cl⊃Mel, **2**·4X⊃**Mel**, **3**·4X⊃**Mel**, and **3**·4Cl⊃**Mel** inks were prepared and used to print thermochromic patterns. The inkjet-printed patterns showed the same thermochromism as the supramolecular aerogels.

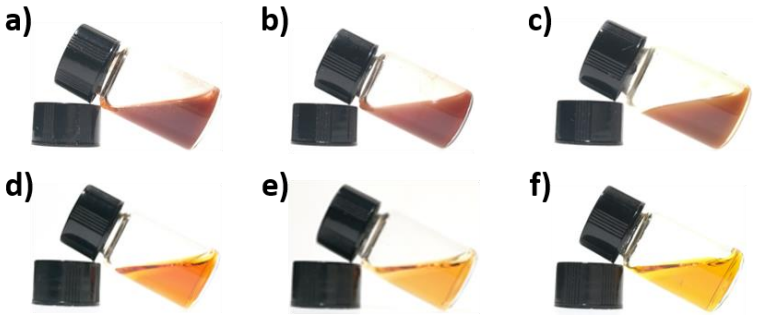

Figure 4.12 Photographs of the **a**) **4**·4Br⊃**Mel**, and **b**) **5**·4Br⊃**Mel**, **c**) **6**·4Br⊃**Mel**, **d**) **4**·4Cl⊃**Mel**, **e**) **5**·4Cl⊃**Mel**, **f**) **6**·4Cl⊃**Mel** complexes in aqueous solution. No hydrogels were formed.

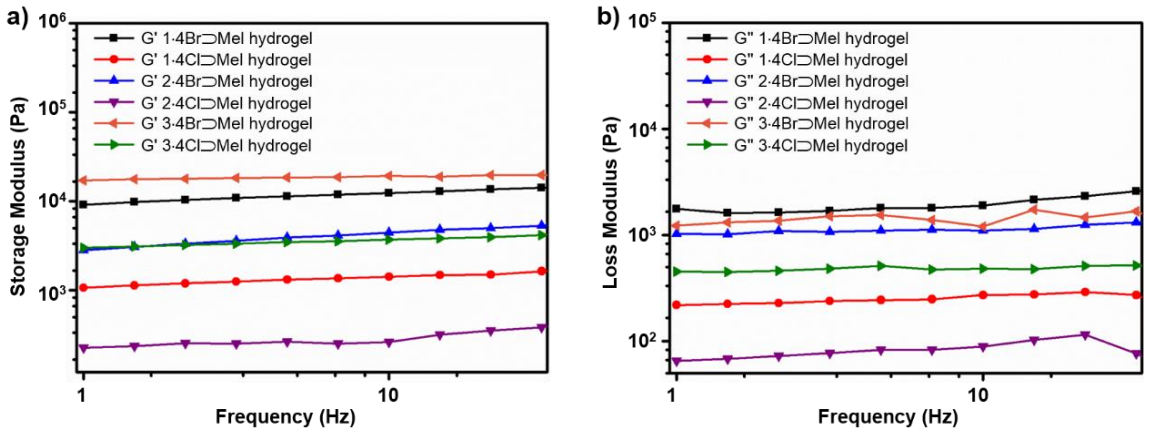

Figure 4.13 Oscillatory rheology frequency sweeps of **a**) storage modulus G' and **b**) loss modulus G" of **1**-**3**·4X⊃**Mel** hydrogels.

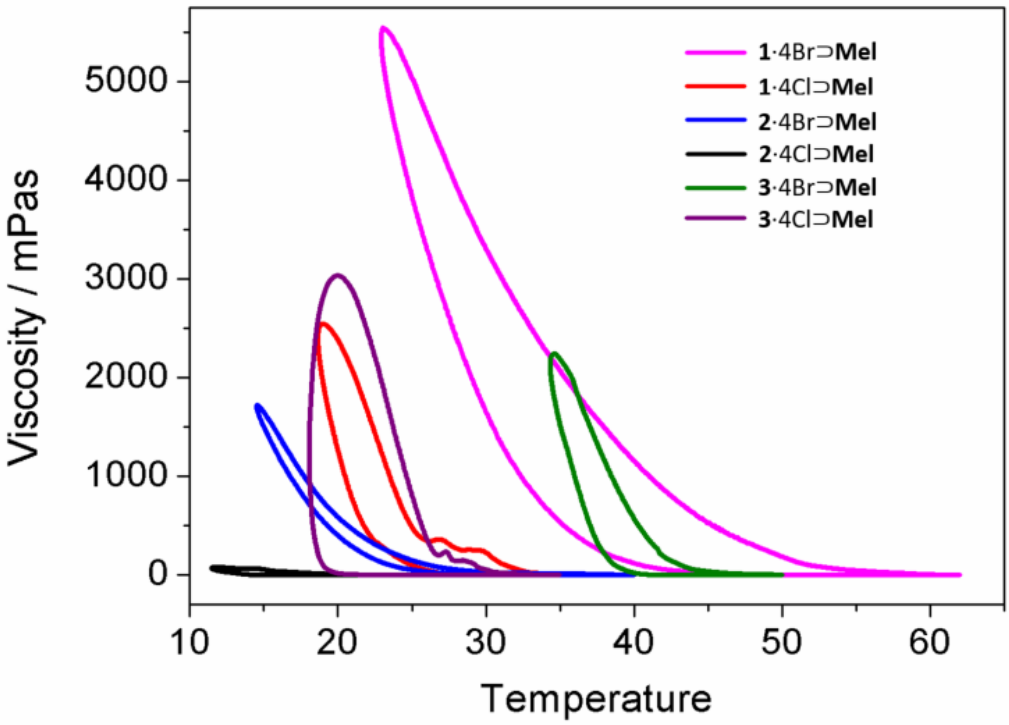

	1·4Br⊃ Melatonin	**1**·4Br⊃ Melatonin	**1**·4Br⊃ Melatonin	**1**·4Br⊃ Melatonin	**1**·4Br⊃ Melatonin	**1**·4Br⊃ Melatonin
Gelation Point / ℃	50	28	30	14	41	19
Melting Point / ℃	60	37	39	21.5	47	33.5

Figure 4.14 Viscosity plot of sol-gel-sol transition process.

CHAPTER 5

ASSEMBLY AND CHIRAL MEMORY EFFECT OF DYNAMIC MACROSCOPIC SUPRAMOLECULAR HELICES

5.1 Introduction

The rational design of modular molecular systems which undergo programmed self-assembly represents a powerful and promising method to generate supramolecular architectures with diverse shapes, functions, and applications.[180-182] Fabricating macroscopic self-assemblies via the bottom-up approach allows for facile materials processing,[183-184] characterization,[185-186] and better control over desired material's performance.[187-190] Helicity, in particular, is an important structural motif to be incorporated into supramolecular architectures. Since the discovery of the α-helix of proteins[191] and the right-handed double helix of DNA[41], researchers have extensively investigated the construction of synthetic helical systems in efforts to mimic the sophisticated structures and functions of natural helices.[192-194] It is an intriguing scientific challenge to translate molecular scale chirality into macroscopic helicity within self-assembled architectures to further our fundamental understanding of chirality and its practical applications. The investigation of such processes not only provides insight into the mechanism of biological chiral translation,[195-196] but also leads to the development of new materials for applications in chiral separation,[197] optical devices,[198] and actuators.[199-200] The development of macroscopic helical systems through self-assembly and the control of their chiral handedness, however, is still quite rare and more extensive studies are urgently needed.[201-202]

The employment of the chiral memory effect[203-205] represents an important strategy, among other methods such as chirality transfer,[206-209] amplification,[210-213] and reversion[214-215], by which to control the helicity of dynamic supramolecular self-assembled structures. Through the chiral memory effect, chirality can be first introduced and subsequently preserved after substitution or removal of the individual components which impart chiral information to the supramolecular system. Using this method, one can achieve the preparation of enantiomerically pure supramolecular structures composed entirely of achiral building blocks.[101, 216] Exploiting chiral memory in most supramolecular assemblies, however, remains a challenging task as the dynamic exchange of the structural components often disturbs the non-covalent interactions that hold the assembly together, leading to dissociation of the supramolecular architecture.[193, 217]

Herein, we report the assembly and chiral memory effect of a novel class of supramolecular helical architectures whose size reach sub-millimeter in length. The dynamic yet robust nature of these helices allowed for efficient component exchange and the establishment of chiral memory which enabled the construction of enantiomerically pure macroscopic helices from achiral components.

5.2 Results and Discussion

In a previous study, we developed a series of donor-acceptor supramolecular assemblies that can form nano- and meso-scale fibers in aqueous solution.[151] These materials were composed of two components: an amphiphilic π-electron-deficient *bis*-bipyridinium-based acceptor (**1**·4Br) and a π-electron-rich donor. Although both the donor and the acceptor were achiral molecules, the resulting self-assembled fibers were helical, exhibiting

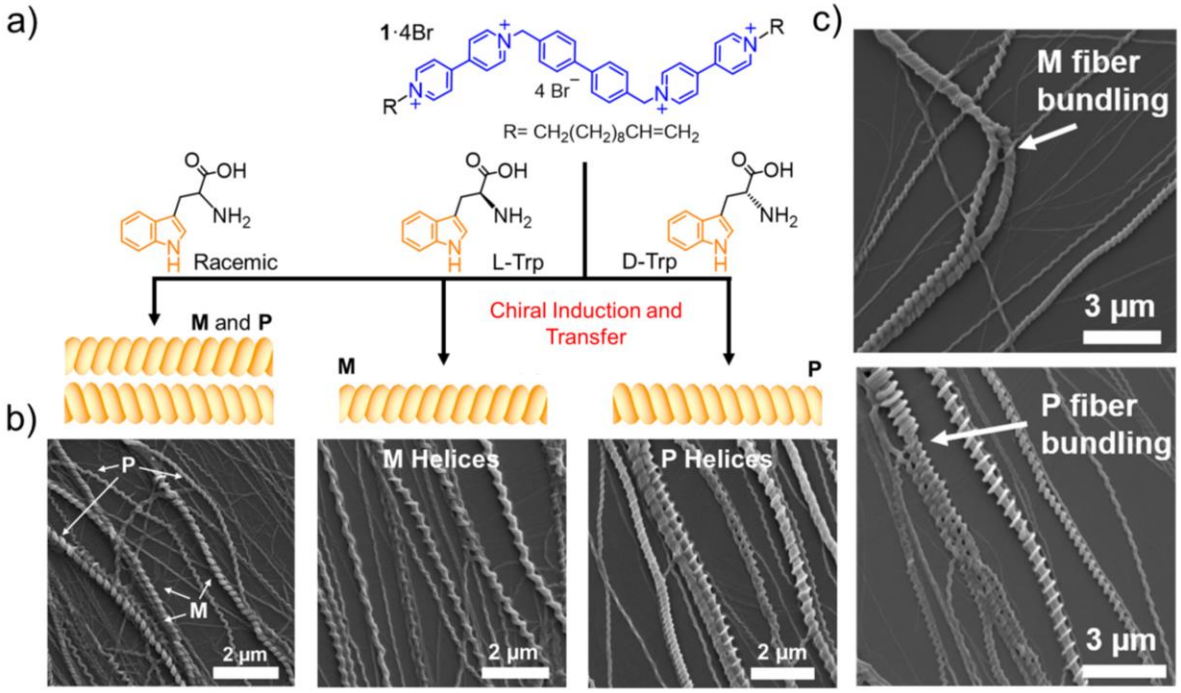

Figure 5.1 a) Structural formulas of the π-electron acceptor **1**·4Br and chiral donors D- and L-Trp, and a schematic representation of the formation of helices of different chiral handedness. b) SEM images of helical supramolecular fibers formed upon mixing **1**·4Br with racemic L/D-Trp (left), L-Trp (center) and D-Trp (right). c) SEM images depicting M fiber bundling (top) and P fiber bundling (bottom) leading to larger fibers whose helical handedness is conserved.

a racemic mixture of handedness without any external chiral influence. In this study, a chiral α-amino acid donor,[209, 218-220] tryptophan (Trp), was exploited to direct the formation of enantiomerically pure self-assembled architectures (Figure 5.1a). Trp was selected as it possesses π-electron donating ability as an indole-cored natural amino acid.[221-223] The addition of L-Trp to an aqueous solution of **1**·4Br resulted in a vivid color change originating from the donor-acceptor charge-transfer interaction between the π-electron rich indole moiety and the π-electron poor bis-bipyridinium head groups. The charge-transfer

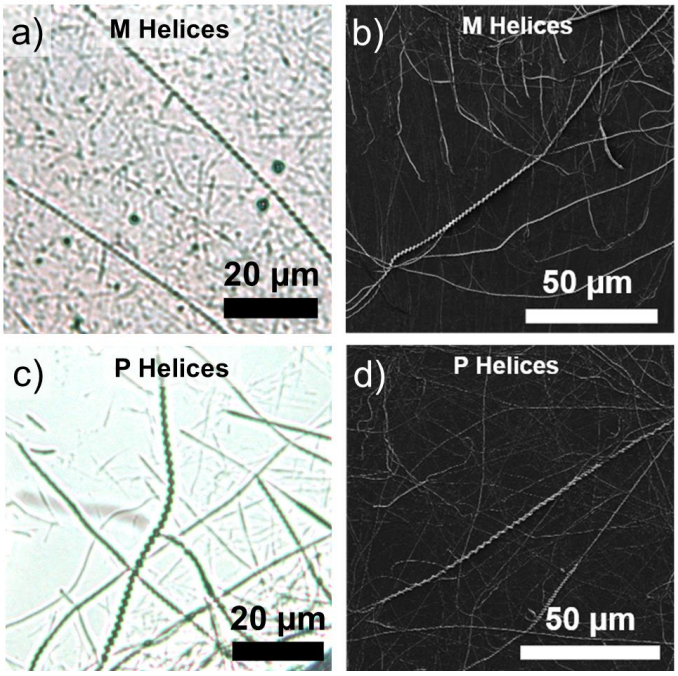

Figure 5.2 Optical microscopy a,c) and SEM images b,d) of helical supramolecular fibers on the order of hundreds of micrometers in length formed upon mixing **1**·4Br with L-Trp giving rise to M helices (a-b) and D-Trp giving rise to P helices (c-d).

interaction between **1**·4Br and L-Trp was confirmed by the emergence of an absorption band centered at 400 nm in its UV-Vis absorption spectrum (Figure 5.5). Higher concentrations of the donor and acceptor led to gelation of the aqueous solution, which was reversible under thermal treatment (Figure 5.6). The hydrogel matrix was comprised of highly-entangled supramolecular fibers, similar to those formed by **1**·4Br and other achiral donors.[151, 178] In contrast to the racemic amount of left-handed (M) and right-handed (P) helical fibers formed with achiral donors, a dominating presence of M fibers was observed (Figure 5.1b center and 1c top) by Scanning Electron Microscopy (SEM). To correlate the molecular chirality of the templating amino acid with the observed helicity, D-Trp was also used to perform the

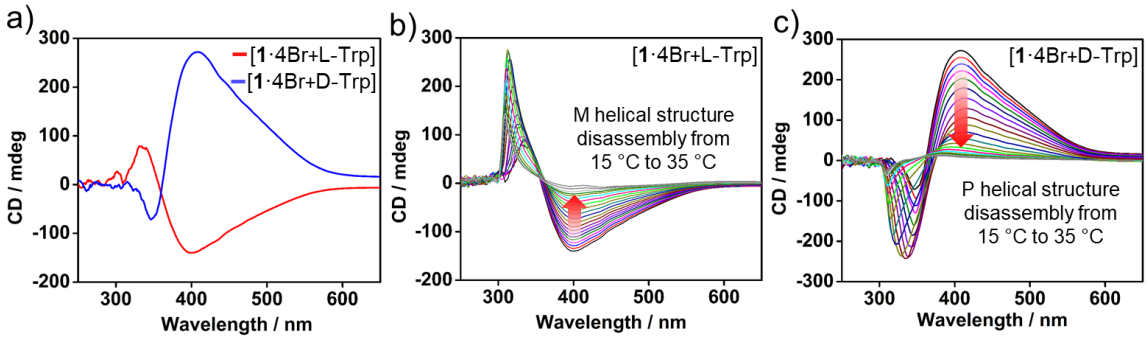

Figure 5.3 UV-Vis CD spectra spectra of the helical fibers [**1**·4Br+D/L-Trp] in water (**1**·4Br: 6 mM, Trp: 12 mM) measured in a quartz cuvette with a 2 mm path length. a) CD spectra of [**1**·4Br+D-Trp] (blue line) and [**1**·4Br+L-Trp] (red line) at 15 °C. b) and c)Variable temperature CD spectra for [**1**·4Br+D-Trp] and [**1**·4Br+L-Trp] with temperature increased from 15 °C to 35 °C.

same experiment, and consequently led to the formation of P fibers (Figure 5.1b right and 1c bottom). In addition, when using the racemic mixture of L- and D-Trp as the donors, a racemic amount of M and P fibers were obtained (Figure 5.1b left). The helical fibers were constructed upon complex formation of the donor and the acceptor, followed by their contiguous self-assembly. The chiral donor Trp first interacts with the achiral bipyridinium units of the acceptor **1**·4Br via donor-acceptor π-π stacking interactions, creating a chiral complex seed, [**1**·4Br+Trp]. The chirality of [**1**·4Br+Trp] is subsequently translated into enantiomerically pure helical fibers during the self-assembly process.

Fiber-fiber bundling was observed by SEM (Figure 5.1c), in which multiple smaller fibers merged and generated thicker ones while maintaining the original helicity, thus affording macroscopic enantiomerically pure helices of increasing size. This bottom-up process was surprisingly efficient and robust, generating single-handed helices under a wide range of processing conditions (drop-casting, spin-casting, precipitation, recrystallization,

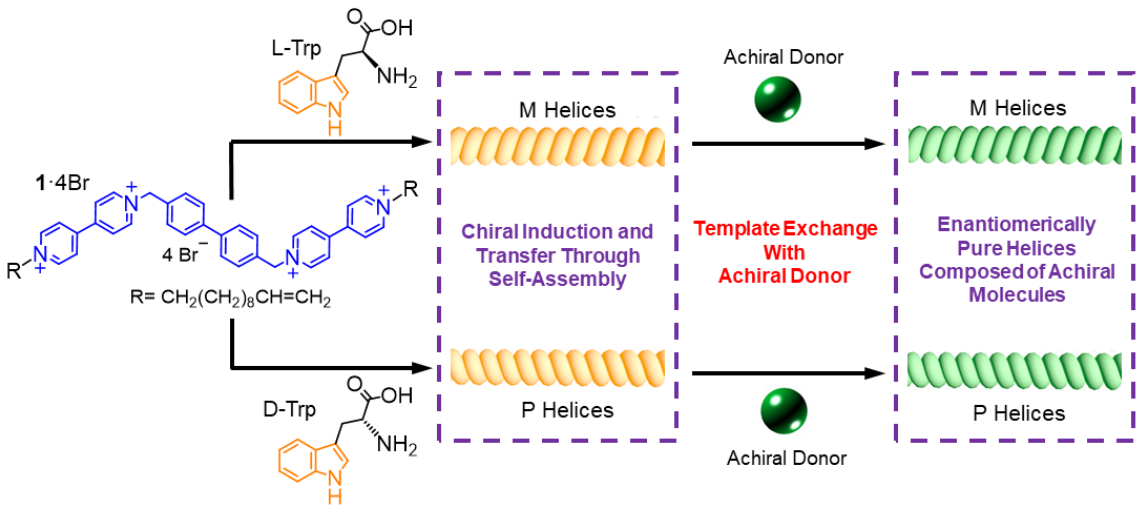

Scheme 5.1 Formation of enantiomerically pure helices that are composed of achiral molecular components by way of template exchange with an achiral donor.

etc.). With conditions allowing for slower fiber growth,[224] helices with lengths of hundreds of micrometers were observed by both SEM and even optical microscopy (Figure 5.2), which has been rarely reported in precedent research.[201, 225-226]

To further investigate the supramolecular helicity, UV-Vis circular dichroism (CD) spectroscopy was conducted on samples of [**1**·4Br+L-Trp] and [**1**·4Br+D-Trp]. The CD spectrum of the helical fibers of [**1**·4Br+L-Trp] showed a negative Cotton Effect centered at 400 nm, whereas a mirrored spectrum was observed for that of [**1**·4Br+D-Trp] (Figure 5.3a). Solutions comprised solely of the free donors, L- or D-Trp, were not CD active in this wavelength range (Figure 5.7), so they did not exert any influence on the CD spectra of the self-assembled helices. Based on these data, the Cotton Effect centered at 400 nm was attributed to the enantiomeric excess of single-handed helices that exhibited a charge-transfer absorption band at that wavelength, but not a result of the presence of the discrete

chiral Trp molecules. Indeed, variable temperature experiments showed that the Cotton Effect diminished upon heating to 35 °C as the fibrous aggregates dissociated into their discrete molecular components in water (Figure 5.3b-c).

In order to test the dynamic nature of these macroscopic helical architectures and the potential for a chiral memory effect, the chiral Trp donors were replaced with the achiral donors, melatonin and di(ethylene glycol)-disubstituted 1,5-diaminonaphthalene (DAN-DEG). On account of the fact that melatonin interacts much stronger with bis-bipyridinium derivatives than Trp,[223] as evidenced by ^{1}H-NMR spectroscopic analysis (Figure 5.9), it was possible to exchange Trp with melatonin following the formation of enantiomerically pure helical fibers.[227] In this "donor-exchange" approach (Scheme 5.1), L-Trp or D-Trp enantiomers were first added to a solution of **1**·4Br to generate pure M or P helices, respectively. The helical fibers were then immersed in an aqueous solution of melatonin to undergo the exchange process. The color of the gelled helical fibers changed from orange to dark red, resembling the characteristic color of [**1**·4Br+melatonin], indicating that Trp was displaced by melatonin in the donor-acceptor complex (Figure 5.4). Together both SEM imaging and UV-Vis CD spectroscopy demonstrated that the fibers retained their handedness following the donor-exchange process. (Figure 5.4, Figure 5.12). The experiment was also performed using the other achiral donor, DAN-DEG, which possesses an even stronger π-electron donating ability (Figure 5.9). Upon soaking in an aqueous solution of DAN-DEG, the gelled helical fibers changed from orange to green, reflecting the characteristic color of the [**1**·4Br+DAN-DEG] charge-transfer complex and indicating that Trp was exchanged by DAN-DEG in the complex. Again, SEM imaging and UV-Vis CD

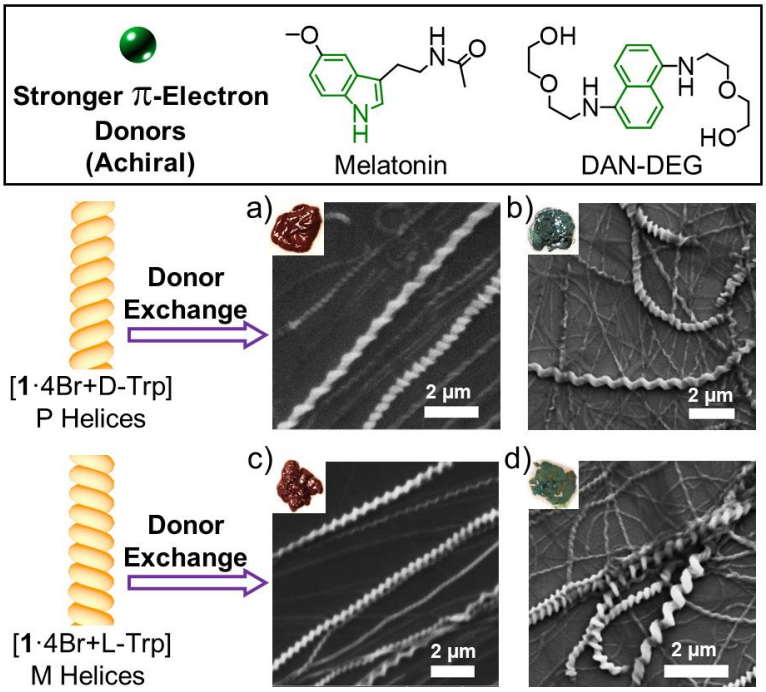

Figure 5.4 SEM images of the P helices after donor-exchange with a) melatonin and b) DAN-DEG; and M helices after donor-exchange with c) melatonin and d) DAN-DEG. The inset photograph images showed that the helical self-assemblies changed color from orange to red [**1**·4Br+melatonin] or green [**1**·4Br+DAN-DEG] after donor-exchange.

spectroscopy confirmed that these fibers retained their handedness following the donor-exchange process. (Figure 5.3, Figure 5.13).

To further quantify the efficiency of the donor-exchange processes, the chemical composition of the helical fibers following donor-exchange was analyzed by ^{1}H-NMR spectroscopy. After donor-exchange with melatonin, the resulting fibers were dissolved in warm D_2O. The ^{1}H-NMR spectrum revealed that most of the Trp had been displaced, indicating an exchange conversion of over 95% (Figure 5.10). More impressively, when DAN-DEG was used to displace Trp, no detectable proton NMR signals associated with Trp were observed for the dissolved donor exchanged helical fibers, indicating a quantitative

conversion and complete removal of Trp during the donor-exchange process (Figure 5.11). The high donor-exchange efficiency of DAN-DEG can be attributed to its stronger π-electron donating ability compared to melatonin (Figure 5.9). Through this highly efficient approach, enantiomerically pure helices were constructed from achiral components (**1**·4Br and melatonin or **1**·4Br and DAN-DEG), while the chiral templates, D- or L-Trp, can be reclaimed and recycled for further use. The feasibility in forming such enantiomerically pure helices and the chiral memory effects of these supramolecular architectures are of great interest for future applications in chiral separation and catalysis. For example, chiral nano-/microstructures of active metals for asymmetric catalysis can potentially be prepared by templation using these viologen-derived helices[209, 228] in a cost-effective manner.

5.3 Conclusion

In conclusion, we have demonstrated control over the helical handedness of a novel class of donor-acceptor supramolecular assemblies. The chirality of the donor, Trp, was efficiently translated into the macroscopic helicity of fibers with lengths up to sub-millimeters through self-assembly. These helical supramolecular architectures were found to be dynamic which allowed for the efficient exchange of their donor components, but were also sufficiently robust as to permit the retention of their helicity and enantiomeric purity during the exchange. Owing to the chiral memory effect present in this material, this approach represents an efficient method in constructing enantiomerically pure supramolecular helical architectures from achiral components while recycling the enantiomerically pure chiral template. Overall, this system marks significant advances in the investigation of macroscale chiral translation and chiral memory effects.

5.4 Experimental Section

5.4.1 Materials and Characterization

L-tryptophan (L-Trp), D-tryptophan (D-Trp) and melatonin were purchased from TCI America; All the compounds were used as received without further purification. Compounds **1**·4Br and di(ethylene glycol)-disubstituted 1,5-diaminonaphthalene (DAN-DEG) were synthesized according to procedures reported in the literature.[111, 151] Milli-Q water (18.2 MΩ·cm) was used in all cases. Deuterated solvents (Cambridge Isotope Laboratories) for NMR spectroscopic analyses were used as received. ^{1}H NMR spectra were recorded at room temperature on a Varian Inova 500 MHz spectrometer. UV-Vis spectra were measured on a Shimadzu UV-2600 spectrophotometer with a .5 cm path length cuvette. Optical microscope images were taken under a Leica DM2500P microscope. Scanning electron microscopy (SEM) images were taken under a FEI Quanta 600 FE-SEM. Circular Dichroism (CD) spectra were obtained using a Bio-Logic MOS-500 spectrometer. For the variable temperature circular dichroism (VT-CD) experiments, the temperature was increased from 15 °C to 35 °C in increments of 1 °C every 20 minutes.

5.4.2 Preparation of 1·4Br⊃Trp Helical Self-Assemblies in Water

The acceptor **1**·4Br (9.0 mg, .008 mmol) and the donor L-tryptophan (3.3 mg, .016 mmol) were combined in Milli-Q water (2 mL). The solution was kept stirring at 80 ℃ until all the material was fully dissolved. A vivid orange color emerged when the solution cooled down to room temperature, confirming the charge-transfer interactions between **1**·4Br and L-Tryptophan. Another sample with a higher concentration was prepared in the same manner by combining **1**·4Br (17.9 mg, .016 mmol) and L-Tryptophan (6.5 mg, .032 mmol) in Milli-

Q water (2 mL). Supramolecular hydrogels [**1**·4Br+L-Trp] were formed following a sol-gel transition upon cooling. Samples of [**1**·4Br+L-Trp] for CD spectroscopy were prepared in a 2 mm cuvette with an acceptor concentration of 6 mM and a donor concentration of 12 mM in water. As a control experiment, CD spectra was measured for 12 mM solutions comprised solely of L-Tryptophan or D-Tryptophan (Figure 5.8). Optical microscopy imaging was conducted on samples of [**1**·4Br+L-Trp] which were prepared with an acceptor concentration of 4 mM and a donor concentration of 8 mM in water. These samples were dropcast onto a glass microscope slide and allowed to undergo gelation and subsequently directly imaged by optical microscopy. Samples for SEM analysis, (100 μL of 2 mM **1**·4Br acceptor with two equivalents of L-Tryptophan donor in water) were drop-casted onto a 1 cm^2 silicon substrate and allowed to dry. The samples of [**1**·4Br+D-Trp] for CD analysis, optical microscopy and SEM were prepared in a similar manner. Thin films of [**1**·4Br+Trp] for SEM analysis were prepared by drop-casting aqueous solutions of **1**·4Br and a racemic mixture of both enantiomers of tryptophan (100 μL of 2 mM **1**·4Br with one equivalence L-Tryptophan and D-Tryptophan).

5.4.3 Sergeants-and-Soldiers Experiments

Melatonin (11.1 mg, .048 mmol), L-Tryptophan (1.0 mg, 0.0048 mmol) and **1**·4Br (26.9 mg, .0024 mmol) were dissolved in Milli-Q water (3 mL) at 80 °C. Subsequently, 100 μL of the hot solution was drop-casted onto a 1 cm^2 silicon substrate and allowed to dry. Samples using D-Tryptophan were also prepared in a similar manner. The dried thin films were examined using SEM. The speculated enantiomerically selective, “sergeants-and-soldiers” chiral amplification effect was not observed.

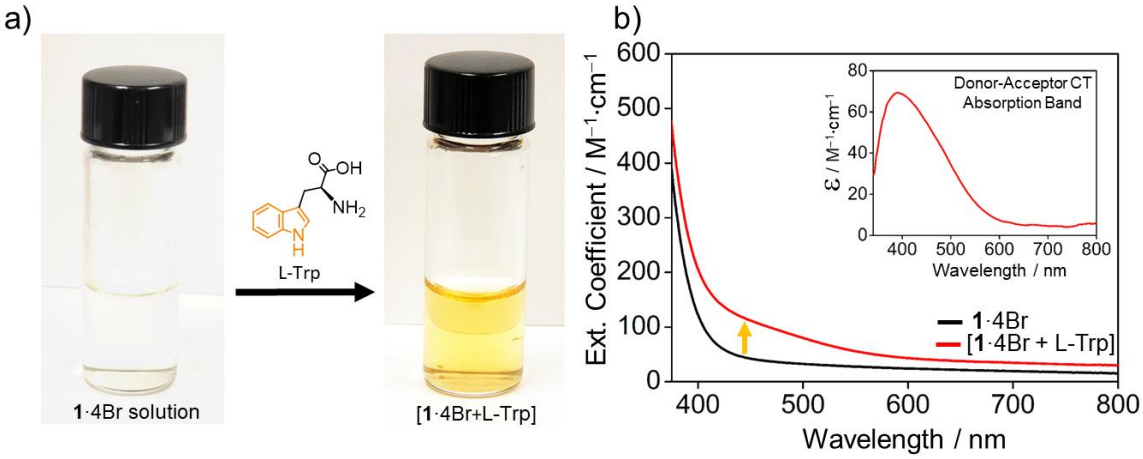

Figure 5.5 a) Photographic images and b) UV-Vis absorption spectra of a 4 mM aqueous solution of **1**·4Br before and after adding 2 equivalents of L-tryptophan (L-trp) and the absorption spectrum of [1·4Br + L-trp] blanked with the absorption spectrum of 1·4Br (inset) depicting the resolved donor-acceptor charge transfer band centered at 400 nm. The color change and the rise of charge-transfer absorption band confirmed the interactions between **1**·4Br and L-tryptophan.

Figure 5.6 Reversible sol-gel transition of [**1**·4Br+L-Trp]. (**1**·4Br**:** 8 mM, L-Tryptophan: 16 mM)

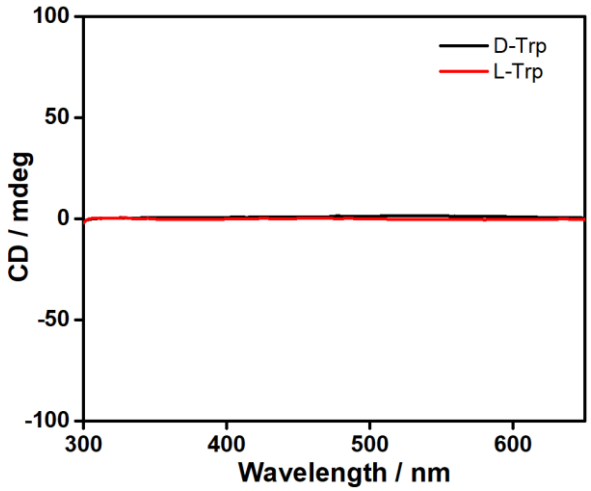

Figure 5.7 CD spectra of the donors, D-Tryptophan and L-Tryptophan in water (12 mM, 25 °C). No cotton effect was observed in the visible region for the donors.

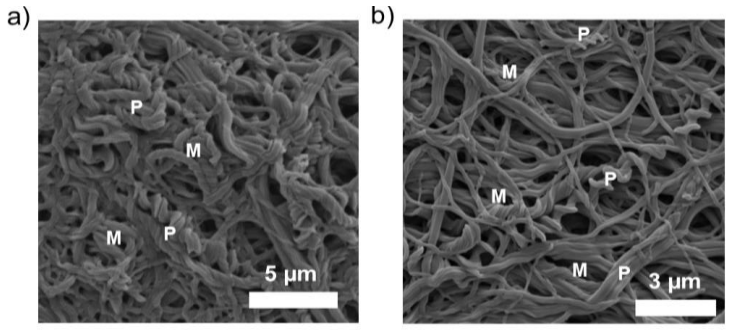

Figure 5.8 Sergeants-and-soldiers experiment: trace amount of a) L-Tryptophan or b) D-Tryptophan was combined with melatonin to form supramolecular helical fibers with **1**·4Br. Roughly equal amounts of M and P helices were observed in both cases, indicating that the sergeants-and-soldiers effect does not play a role in this templated assembly process.

5.4.4 Donor-Exchange Experiments

1·4Br (17.9 mg, .016 mmol) and L-Tryptophan (6.5 mg, .032 mmol) were combined in Milli-Q water (2 mL) and heated at 80 °C until the materials were fully dissolved. Supramolecular hydrogels [**1**·4Br+L-Trp] were formed upon cooling and carefully collected. The hydrogels were subsequently immersed into an aqueous solution of melatonin (2 mL,

16 mM) for 2 hours at room temperature. The resulting [**1**·4Br+melatonin] hydrogel was then collected and soaked in a Milli-Q water solution for 2 hours at room temperature to remove any free unassembled molecules. The hydrogel was filtered with a polyamide membrane (Whatman NL 17) and dried under vacuum at room temperature. Supramolecular helical fibers [**1**·4Br+melatonin] exchanged from [**1**·4Br+D-Trp] were prepared in the similar manner. Donor-exchange experiments were also performed in which the achiral donor, DAN-DEG, was used to obtain samples of supramolecular assemblies comprised of [**1**·4Br+DAN-DEG]. All samples were then dissolved in warm D_2O and subjected to analysis using ^{1}H-NMR spectroscopy.

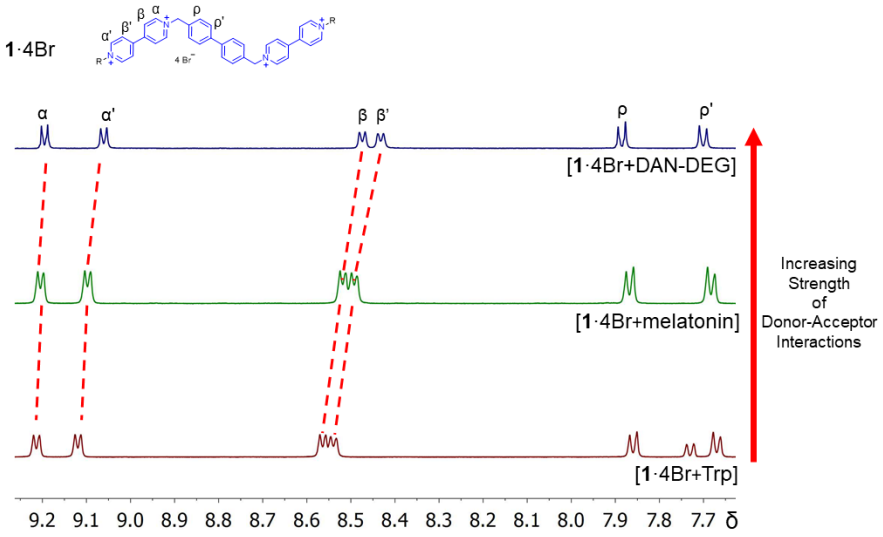

Figure 5.9 Stacked ^{1}H-NMR spectra of a 2 mM solution of **1**·4Br with 2 equivalents of DAN-DEG (top), with 2 equivalents of melatonin (center), and 2 equivalents of tryptophan (bottom). (500 MHz, D_2O, 298K)

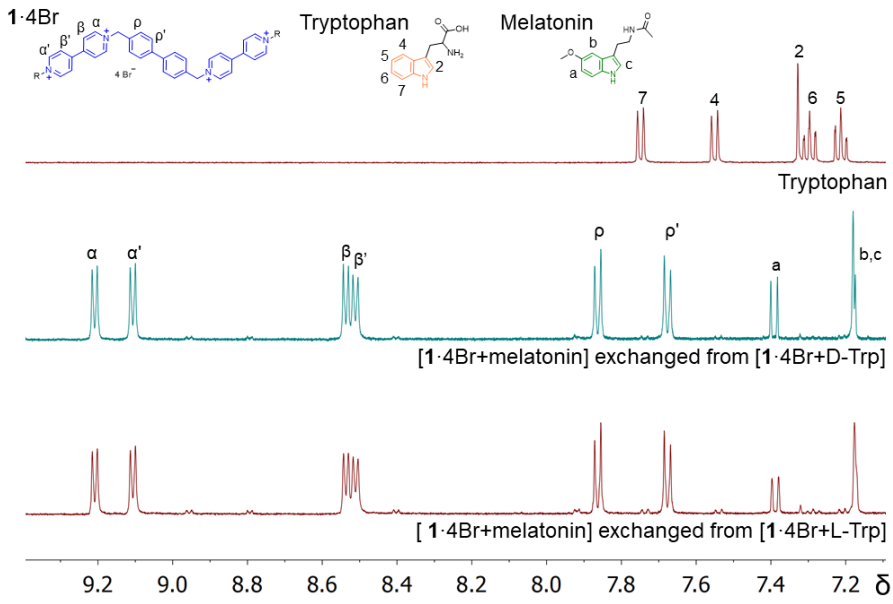

Figure 5.10 Stacked ^{1}H-NMR spectra of pure Tryptophan (top), and the complex [**1**·4Br+melatonin] which was prepared from donor exchange in which the achiral donor, Melatonin, was substituted in place of D-Tryptophan (center), and L-Tryptophan (bottom). (500 MHz, D_2O, 298K)

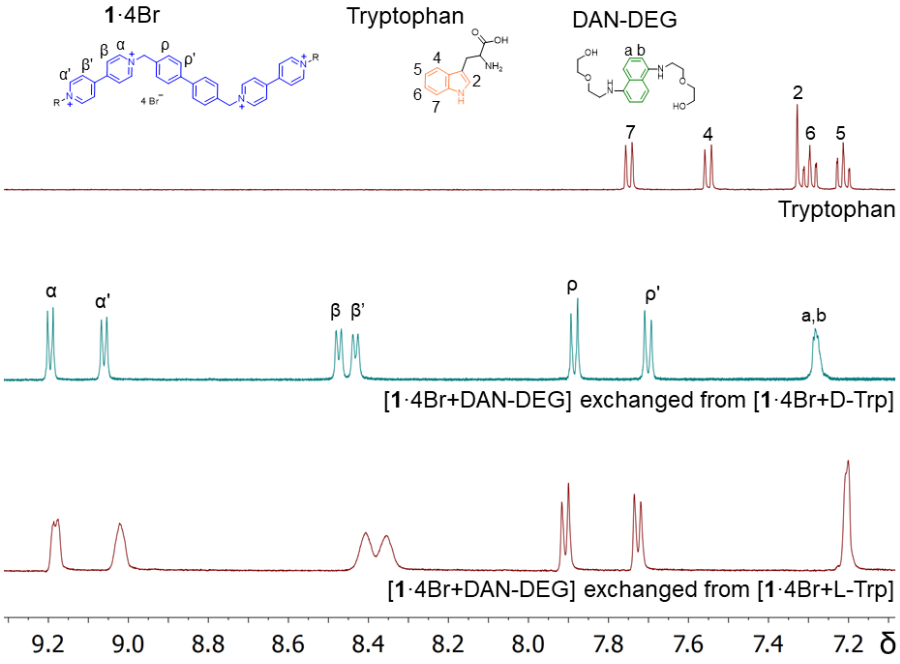

Figure 5.11 Stacked ^{1}H-NMR spectra of pure Tryptophan (top), and both a dilute (center) and concentrated (bottom) solution of the [**1**·4Br+DAN-DEG] complex prepared from donor-exchange in which the achiral donor, DAN-DEG, was substituted in place of L-Tryptophan. (500 MHz, D_2O, 298K)

Samples for SEM analysis (100 µL of 2 mM **1**·4Br acceptor with two equivalents of L-Tryptophan donor in water) were drop-casted onto a 1 cm^2 silicon substrate and allowed to dry to yield a thin film of [**1**·4Br+L-Trp] helical fibers. 100 µL of an aqueous solution of melatonin (16 mmol) was then added on top of the [**1**·4Br+L-Trp] films to initiate the donor-exchange process and the sample was left to dry before SEM sample analysis. Thin film samples initially comprised of **1**·4Br and D-Tryptophan were prepared and also subjected to the donor-exchange process in a similar manner. Donor-exchange experiments were also performed in which the achiral donor, DAN-DEG, was employed to obtain thin films comprised of [**1**·4Br+DAN-DEG].

[**1**·4Br+L-Trp] samples for CD analysis were prepared by combining **1**·4Br and L-Tryptophan in water (6 mM **1**·4Br with two equivalents of L-Tryptophan) and transferred into a 0.5 mm demountable cuvette. The solution was then allowed to dry in the cuvette and its CD spectra were recorded. The cuvette was later immersed into an aqueous solution of melatonin (16 mM) to initiate the donor-exchange process. After 10 minutes, the color of the complexes changed to dark red and the cuvette was collected and allowed to dry under ambient conditions. The CD spectra following donor-exchange were then recorded. In a similar fashion, [**1**·4Br+D-Trp] samples were prepared and their CD spectra before and after donor-exchange were recorded. CD spectra before and after donor-exchange were also measured using the donor DAN-DEG as the achiral substitute. The Cotton effects of the helical self-assembled fibers remained the same following the donor-exchange process, indicating that the helicity of these supramolecular assemblies remained intact.

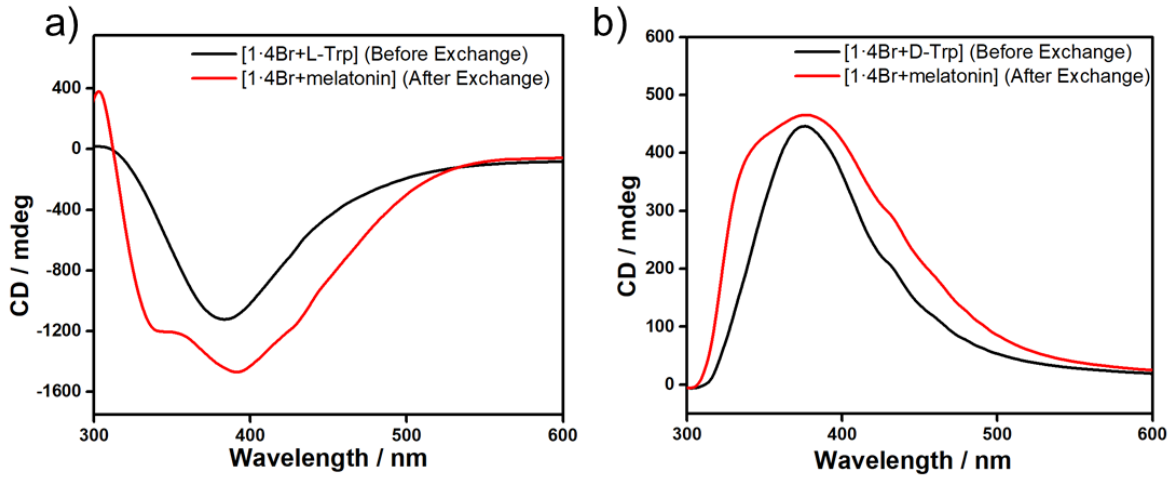

Figure 5.12 CD spectra of the helical donor-templated fibers a) [**1**·4Br+L-Trp] and b) [**1**·4Br+D-Trp] in water before (black trace) and after (red trace) the donor-exchange process in which the achiral donor, melatonin, is substituted in.

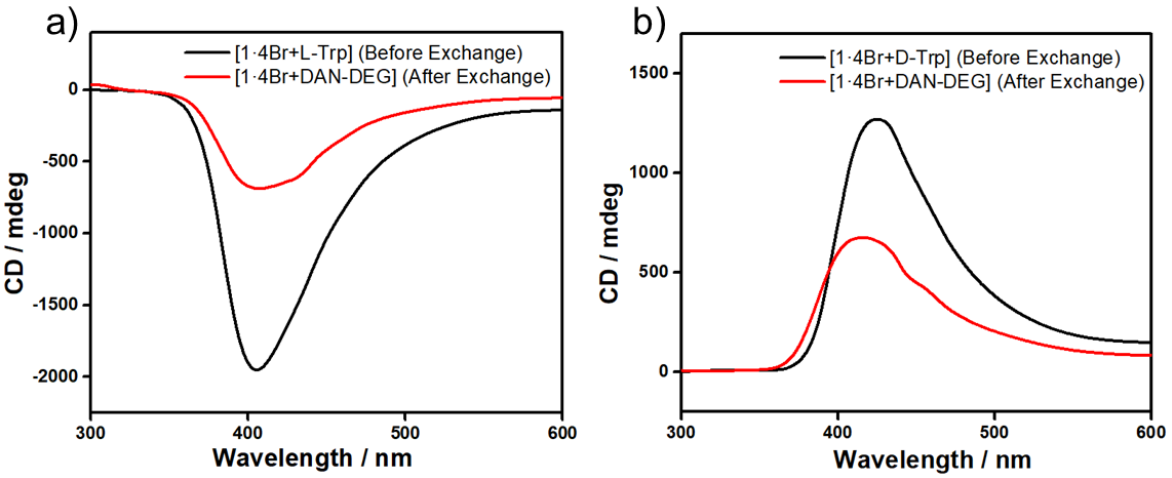

Figure 5.13 CD spectra of the helical donor-templated fibers a) [**1**·4Br+L-Trp] and b) [**1**·4Br+D-Trp] in water before (black trace) and after (red trace) the donor-exchange process in which the achiral donor, DAN-DEG, is substituted in. The Cotton effects of helical fibers remained in the same position and did not invert sign, indicating that the helicity of these materials remained intact following the donor-exchange process. The significant decrease in the intensity of the CD signal most likely resulted from the partially dissolving of the fibers during donor-exchange process.

CHAPTER 6

SYNTHESIS OF CORE-EXTENDED QUINACRIDONE DERIVATIVES WITH INTACT HYDROGEN BONDS*

6.1 Introduction

As a highly stable, red-colored pigment, quinacridone (Figure 6.1) was first synthesized 100 years ago.[229] Since the 1950s, the ink and pigment industry have been producing and using quinacridone and its derivatives extensively,[230] taking advantage of their vivid color, exceptional weather fastness, excellent environmental stability, low toxicity, and ability to be mass-produced. Similar to many other conventional pigments such as perylene diimide[231-232]and isoindigo,[233-235] quinacridone has attracted significant research attention from organic electronics and photovoltaics communities in the past few years. [236-241] It has been demonstrated that quinacridone could serve as a promising building block for optoelectronic applications due to its high charge carrier mobility in field-effect transistor devices [236] (μ_h = 0.2, μ_e = 0.01 cm^2 V^{-1} s^{-1}) and promising attributes as active materials for organic solar cells. [235, 240-243] Quinacridone derivatives also showed high photoluminescent efficiencies and excellent electrochemical stabilities and were thus useful for organic light-emitting materials. [239, 244-245] The H-bonding ability plays a pivotal role in governing the materials' properties of quinacridone.[236, 246]On the rigid backbone, two sets of carbonyl and

* Part of this section is reprinted with permission from Solution-Processable Core-Extended Quinacridone Derivatives with Intact Hydrogen Bonds by Zou, Y. et al., *Organic Letters*, **2015**, 12, 3146-3149. Copyright 2015 by American Chemical Society.

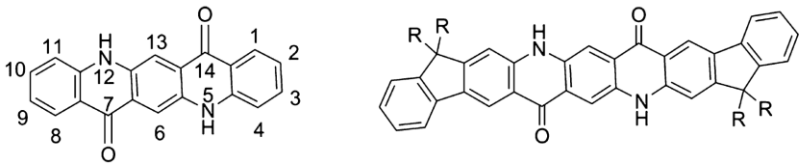

Figure 6.1 Structural formula of quinacridone and IFQA.

N-H functions are organized in a centrosymmetrical manner, so that a pair of strong and complementary hydrogen-bonds (H-bonds) can be formed intermolecularly. These H-bonding interactions not only guide the solid-state packing mode of quinacridone derivatives but also lead to their high thermal, chemical, and photochemical stability. [236, 246] Unfortunately, such a strong intermolecular interaction often also deteriorates the solubility and solution processability of most H-bond-containing quinacridone derivatives. In contrast, one of the most efficient ways to solubilize a quinacridone derivative was converting the N-H H-bond donors at the N5/12 positions into N-alkylated groups.[247-251] However, the fascinating property features brought about by H-bonds were diminished at the same time. Therefore, it is an intriguing challenge to synthesize solution-processable quinacridone derivatives while maintaining their H-bonding ability.

From a synthetic perspective, there is still an ongoing demand for a scalable and industry friendly approach to the production of quinacridone derivatives. So far, annulation of the quinacridone core requires either reflux in high boiling point solvents (Dowtherm A or α-chloronaphthalene) [239, 252-253] or treatment with hot concentrated acids. [254] These harsh conditions limited the choice of substrate and also increased the cost for mass production. In

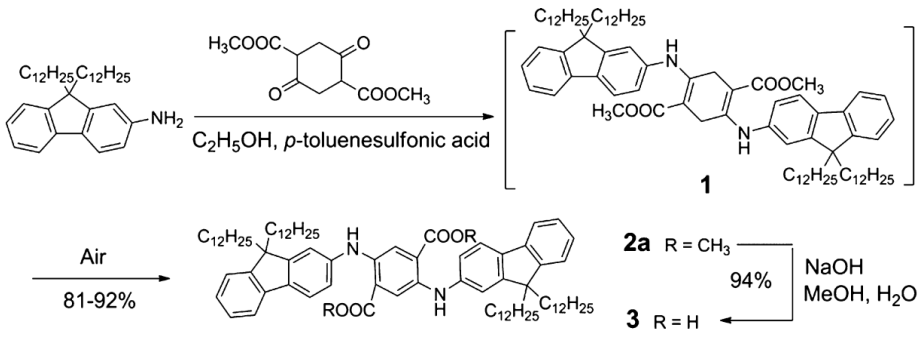

Scheme 6.1 One-pot synthesis of intermediates **2a** followed by hydrolysis to 3.

addition, toxic oxidants (e.g., nitrobenzene or chloranil) [252-253] were often required, resulting in severe negative impact on the environment during the mass production of quinacridone compounds. Addressing both aforementioned challenges together, we report a scalable and facile synthesis that affords solution-processable quinacridone derivatives with intact H-bonding ability. To achieve this goal, we designed a unique synthetic target─core-extended indene-fused quinacridone (IFQA, Figure 6.1). On this 9-ring-fused backbone, solubilizing alkyl chains can be easily installed on the bridging sp3 positions of the indene component rather than on the nitrogen atoms in the central quinacridone core. The H-bond-donating feature of the N-H group can therefore be retained. In terms of cost, the main starting material of IFQA (i.e., fluorene) is an inexpensive, mass produced commodity chemical as a byproduct of the coke industry. [255]Taking advantage of the good solubility and high regioselectivity of fluorene starting materials, we developed a cost-effective and environmentally benign synthetic route, "condensation followed by annulation", for general construction of soluble quinacridone derivatives.

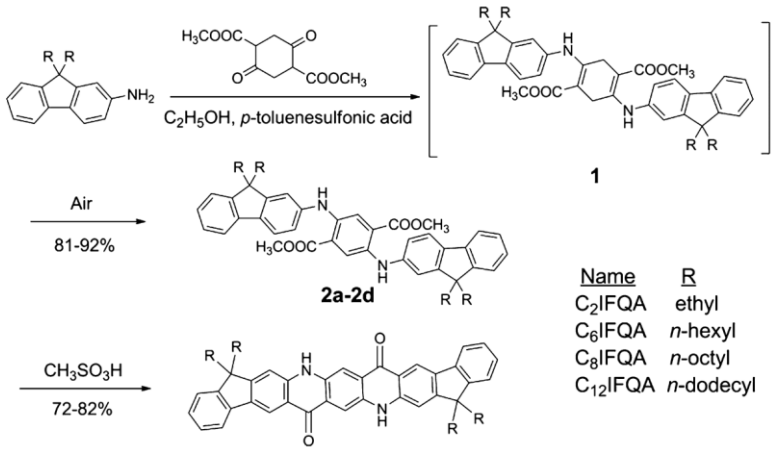

Scheme 6.2 Optimized two-step "condensation followed by annulation" synthetic route to **C_nIFQA**.

6.2 Result and Discussion

The synthetic route of IFQA began (Scheme 6.1) with imine condensation between 2-amino-9,9-dialkylfluorene and dimethylsuccinyl succinate (DMSS) in a 2:1 stoichiometric ratio, which led to intermediate 1. Surprisingly, the central cyclohexadiene ring of 1 can be quantitatively oxidized into the benzene ring in situ by air. [256] As a result, the desired aniline derivative **2a** could be prepared in one pot without the addition of any toxic oxidant, marking a significant improvement over conventional methods.

To optimize the subsequent annulation reaction, dodecylfunctionalized **2a** was selected as the model compound for the condition screening. Ester groups in **2a** were first hydrolyzed by NaOH in methanol to give dicarboxylic acid 3. The annulation reaction of 3 relied on heat or acid-promoted electrophilic aromatic substitution between the fluorene moieties and the carboxylic acid groups (Table 1). In preliminary tests, no reaction was

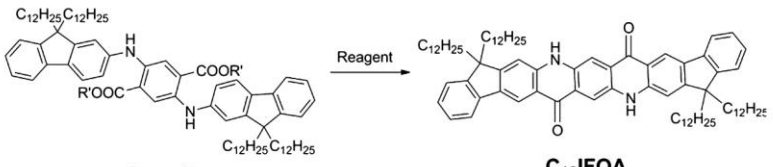

entry	R′	reagent	temp (°C)	yield (%)[b]
1	H	α-chloronaphthalene	263	0
2	H	PPA	140	18
3	H	PPA + silica gel[c]	140	35
4	H	Eaton′s reagent	140	38
5	H	H_2SO_4	140	0
6	H	CH_3SO_3H[d]	120	84
7	CH_3	CH_3SO_3H[d]	140	82

[a]Reaction conditions: 10 equiv of reagent (v/w), 24 h. [b]Isolated yield. [c]Dispersed on silica gel and mixed with PPA. [d]Reaction was conducted for 12 h.

Table 6.1 Optimization of the Ring Annulation Reaction Conditions

observed in thermal conditions such as refluxing in α- chloronaphthalene at 263 °C. Conventional acidic conditions, such as polyphosphoric acid (PPA), [254] Eaton's reagent, and concentrated sulfuric acid, all afforded yields lower than 40% and gave a large amount of polar byproducts, which were likely formed by undesired introduction of sulfonate or phosphonate groups onto the aromatic backbone. The best condition was found to be heating at 120 °C in pure methanesulfonic acid (MSA), giving an 84% isolated yield and no polar byproduct. It should also be noted that this condition resulted in only the linear IFQA without the formation of its angular-shaped regioisomer, showing the high regioselectivity of fluorene unit as a Friedel-Crafts nucleophile. Further optimization revealed that diester precursor **2a** could also be directly annulated in MSA to afford the final IFQA product. Although the yield (82%) was slightly lower than that from 3, this strategy allowed for

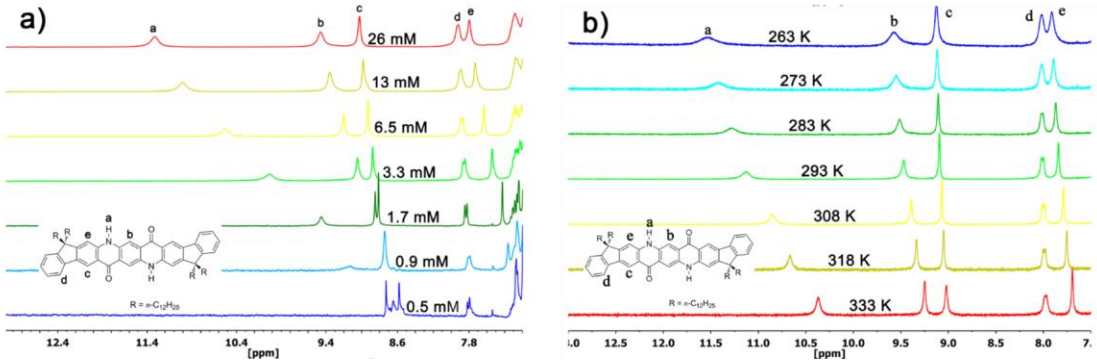

Figure 6.2 (a) Room temperature variable concentration and (b) variable-temperature ^{1}H NMR spectra of C_{12}IFQA in $CDCl_3$.

skipping the hydrolysis step, making the synthesis of IFQA a concise two-step route with an overall yield of ~75%. A series of IFQA derivatives (**C_nIFQA**) with ethyl (C_2), hexyl (C_6), octyl (C_8), and dodecyl (C_{12}) side chains were synthesized on up to a 10 g scale using this "condensation followed by annulation" method (Scheme 6.2). All intermediates and products were fully characterized by ^{1}H NMR, ^{13}C NMR, and high-resolution mass spectrometry. ^{1}H-^{1}H COSY and NOESY NMR spectra were recorded to fully elucidate the structure and to unambiguously assign the resonance peaks (see Figure 6.4-6.5). Thermogravimetric analysis of C_nIFQA showed a clear weight loss in the range of 400-480 °C, corresponding to the decomposition of the alkyl groups. Carbonization yield at 600 °C agreed well with the theoretical percentage of the quinacridone backbone in each compound (see the Supporting Information). All **C_nIFQA** derivatives were soluble in mixed solvents such as chloroform/ethanol, hexane/ethanol, toluene/DMSO. With longer dodecyl chains grafted, **C_{12}IFQA** was even soluble in hexane or heptane up to 1.5 mg/mL. The good solubility of **C_nIFQA** paved the way for their solution-phase characterization and solution

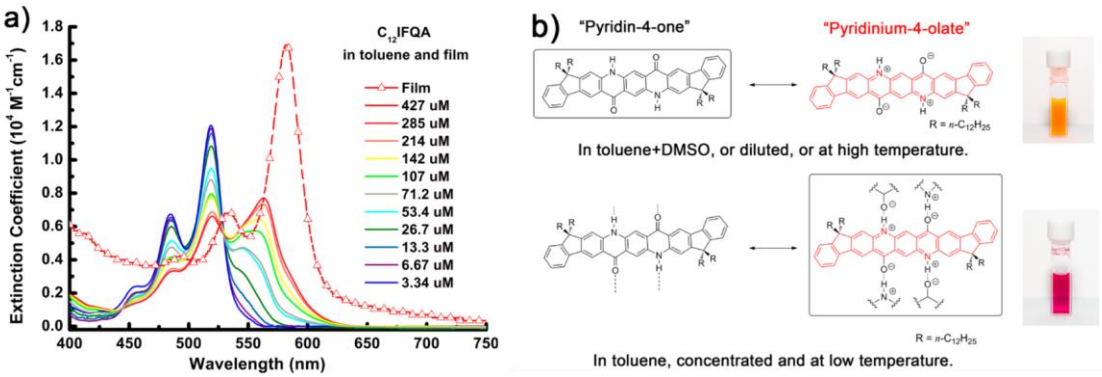

Figure 6.3 (a) Concentration-dependent UV-vis spectra of **C_{12}IFQA** in toluene and in the thin film state at room temperature. Solution spectra are in absolute molar absorption coefficient. The thin film spectrum was normalized based on the isosbestic saddle point. (b) Schematic diagram describing the impact of H-bonds on the resonance contribution of **C_{12}IFQA** with the predominant species encircled. Corresponding photographic images of the solution are shown.

processing. This novel "condensation followed by annulation" method is particularly suitable for large-scale synthesis of quinacridone derivatives. Compared to the prevailing three-step synthetic routes of quinacridone that often require toxic oxidants and high boiling point solvents,[239, 253] this method involved only two highly efficient steps from aromatic amine and DMSS. Furthermore, the products can be easily purified by recrystallization without chromatography. Such a simplified procedure would reduce the cost dramatically for potential mass production. Finally, both reaction solvents (ethanol and MSA) used in this procedure were low cost, nontoxic, and had minimal environmental impact.[257]

To investigate the H-bonding property, concentration-dependent and variable-temperature ^{1}H NMR spectra of **C_{12}IFQA** were recorded in $CDCl_3$ (Figure 6.2). Either when the concentration was decreased or when the temperature was increased, the characteristic

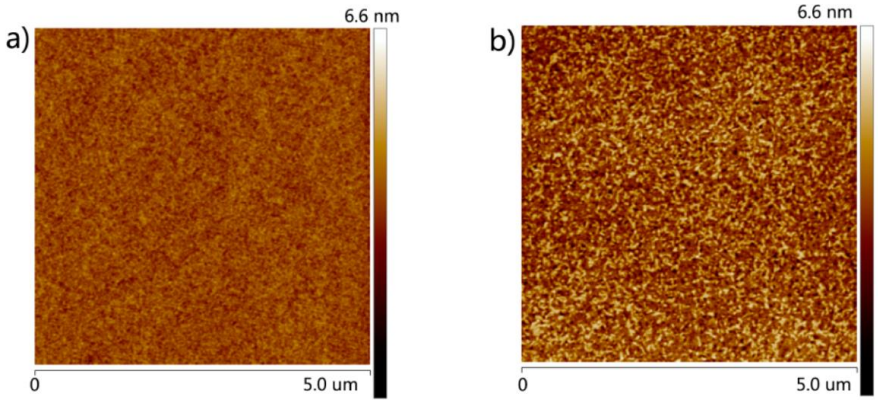

Figure 6.4 AFM images (5 × 5 μm) of **C_8IFQA** thin film prepared by spin-coating method (a) before and (b) after thermal annealing at 210 °C.

^{1}H NMR resonance peak for the N-H group shifted upfield, indicating the dissociation of the H bonds under these conditions.[258-259] Concentration-dependent UV-vis absorption spectra of C12IFQA were recorded (Figure 6.3a) in toluene. At low concentration (<5 μmol/L), the absorption λ_{max} was at 518 nm with two additional characteristic vibrational progression peaks at 484 and 455 nm. After the concentration was increased, a red-shifted absorption band with λ_{max} = 565 nm emerged. This change in absorption originated from the alternated resonance contribution of IFQA molecules induced by H-bonds (Figure 6.3b). When the H-bond was not formed, the resonance form of "pyridine-4-one" dominated in discrete IFQA molecules. With the intermolecular H-bonds, the "pyridinium-4-olate" resonance form, however, became more favorable because of the change in N-H acidity and C=O bond strength. [260-261] The clear isosbestic point at 526 nm indicated that the absorption was caused by only two distinctive species─isolated IFQA and H-bonded IFQA, which were related linearly by stoichiometry. [253, 262]Based on the variable concentration UV-vis spectra, free Gibbs energy change (ΔG°) for the H-bonded association of each **C_{12}IFQA** molecule was

estimated to be -4.5 kcal/mol using an isodesmic aggregation model (see the Experimental Section).[263]This value matched well with the strength of a typical N-H-involved H-bond (1.9-3.1 kcal/mol for each H-bond).[264] It should be noted that π-π stacking interaction of IFQA was not taken into account in this solution-phase investigation because the corresponding ΔG° magnitude was estimated[249] to be <1 kcal mol^{-1} at 298 K on an N-alkylated quinacridone derivative. Upon the addition of a H-bond competing solvent such as DMSO into the concentrated solution, as expected, the spectrum revolved back to the shape of a diluted solution, as a result of competitive dissociation of intermolecular H-bonds (see Experimental Section). A clear self-quenching of fluorescent emission was also observed while increasing the concentration of **C_{12}IFQA** in solution, as a result of the intermolecular aggregation (see the Experimental Section). Solid-state UV-vis spectrum of **C_{12}IFQA** was similar to that in concentrated nonpolar solvent (Figure 6.3a), except that the spectrum was slightly further redshifted, indicating a complete H-bonded form and possible π-π stacking interaction in the thin film. These experimental results unambiguously confirmed the H-bonding ability of **C_{12}IFQA** in solution and in the solid state. The same phenomena were also observed for **C_8IFQA** (see the Experimental Section). IFQA derivatives can be easily processed into uniform thin films, due to their good solubility in common organic solvents. For example, C_8IFQA thin film was spin-cast for a general morphological investigation. The thin film showed good uniformity under an optical microscope and an atomic force microscope (AFM). According to AFM (Figure 6.4), the root mean square (rms) roughness of the film was 0.31 nm. After being annealed, the film remained uniform with a slightly higher rms of 0.73 nm. The excellent film-forming ability of the compound enabled the preparation of homogeneous and stable thin films from solution, allowing for future

investigation of their properties and for application in thin film devices, including charge carrier mobility, exciton diffusion length, and thermal conductivity.

6.3 Conclusion

In conclusion, a series of core-extended quinacridone derivatives with intact H-bonds were synthesized by a novel "condensation followed by annulation" strategy. This highly efficient, environmentally benign, and cost-effective route enabled the preparation of these soluble quinacridone-derived materials in large scale. Their H-bonding ability was confirmed by solution-phase ^{1}H NMR and UV-vis spectroscopy experiments. Uniform films can be easily cast by spin-coating. Facile synthesis and unique combination of properties of IFQA derivatives render them promising building blocks for the construction of materials for high-performance dyes and optoelectronic devices.

6.4 Experimental Section

6.4.1 General Method

Unless otherwise indicated, all starting materials were obtained from commercial suppliers and were used without further purification, including dimethyl succinyl succinate (DMSS), p-toluenesulfonic acid (PTSA), methanesulfonic acid and potassium carbonate. Reaction solvents were purified by solvent purification system prior to use. 2-amino-9,9-dialkylfluorene was prepared according to the literature[1] . 1H and 13C NMR spectra were obtained by Varian Inova 300 MHz, ^{1}H-^{1}H COSY and NOESY NMR were obtained by Varian Inova 500 MHz at room temperature and processed by MestReNova 6.1.0. Chemical shifts are reported in ppm relative to the signals corresponding to the residual non-deuterated solvents ($CDCl_3$: δ 7.26, d_6-DMSO: δ 2.50 for ^{1}H, and 77.16 for ^{13}C at room temperature).

High-resolution matrix-assisted laser desorption/ionization time-of-flight (HR-MALDI-TOF) mass spectra were performed on Applied Biosystems 4800 TOF Analyzer. Thermogravimetric analysis (TGA) was undertaken with a TA Q500 thermogravimetric analyzer. Differential scanning calorimetry (DSC) was performed on a TA Q20 differential scanning calorimeter at a heating rate of 10 °C min^{-1} from 40 to 300 °C under argon atmosphere. UV-Vis absorption spectra were recorded using a Shimadzu UV-2600 UV-Vis Spectrophotometer. Fluorescent emission spectra were measured on Horiba Fluoromax-4. Cyclic voltammetry (CV) was carried out in nitrogen-purged dichloromethane (oxidation scan) at room temperature with a CHI voltammetric analyzer. n-Bu_4PF_6 (0.1 M) was used as the supporting electrolyte. The conventional three-electrode configuration consists of a platinum working electrode, a platinum wire auxiliary electrode, and an Ag wire pseudoreference electrode with ferrocenium-ferrocene (Fc^+ /Fc) as the 4 internal standard. Cyclic voltammograms were obtained at a scan rate of 100 mV s^{-1}. Thin film processing of **C_8IFQA**: **C_8IFQA** solutions in toluene (2 mg/mL) were added to Uv-Ozone cleaned silicon wafer. **C_8IFQA** thin films were formed by spin-coating with the condition of 500 rpm for 7 seconds then 2000 rpm for 13 seconds. After casting, the films were thermally annealed at 210 ºC for 0.5 h inside a glovebox. The morphology of films before and after thermal annealing was examined by optical microscope and atomic force microscopy.

6.4.2 Synthesis

Synthesis of **2a─2d:** DMSS (1.00 g, 4.38 mmol, 1.00 equiv.), 2-amino-9,9-ethylfluorene (2.50 g, 10.52 mmol, 2.40 equiv.), PTSA (0.17 g, 0.88 mmol. 0.20 equiv.) were mixed in 50 mL ethanol. The mixture was refluxed under air for 12h before it was

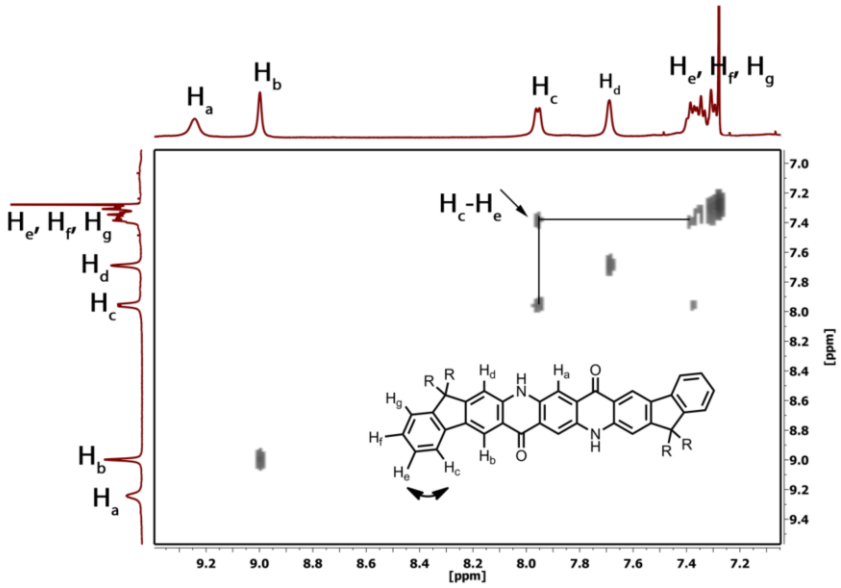

Figure 6.5 500 MHz ^{1}H-^{1}H COSY NMR spectrum of **C_{12}IFQA** in $CDCl_3$ at RT.

cooled to room temperature. The crude product was collected by filtration and washed with ethanol to give a bright-red solid as the pure product. (2.60 g, 89%). ^{1}H NMR (300 MHz, $CDCl_3$, 298 K) δ = 0.40 (t, 12H, J = 7.5 Hz), 2.00-2.03 (m, 8H), 3.85 (s. 6H), 7.13 (b, 2H), 7.28-7.33 (m, 6H), 7,66 (b, 4H), 8.09 (s, 2H). ^{13}C NMR (75 MHz, $CDCl_3$, 298K) δ = 8.66, 32.94, 52.25, 56.15, 115.01, 118.03, 118.50, 119.05, 119.47, 120.72, 122.86, 126.29, 126.98, 138.22, 140.94, 141.58, 149.60, 151.36, 168.11. HR-MALDI-TOF MS: calcd for $[M + H]^+$ m/z = 665.8391, found m/z = 665.8392. Compounds **2c**-**2a** were synthesized according to the same procedure. **2c**. Red solid. 2.1 g. Yield: 92%. ^{1}H NMR (300 MHz, $CDCl_3$, 298K) δ = 0.68-0.79 (b, 18H), 1.08 (b, 26H), 1.87 (m, 8H), 3.87 (s. 6H), 7.18 (b, 4H), 7.25-7.33 (m, 6H), 7.63-7.65 (m, 4H), 8.07 (s, 2H). ^{13}C NMR (75 MHz, $CDCl_3$, 298K) δ = 14.14, 22.77, 23.95, 29.99, 31.68, 40.65, 52.37, 55.14, 114.41, 118.40, 118.73, 119.01, 120.62, 122.88,

126.19, 126.85, 135.72, 138.66, 141.19, 150.32, 152.25, 168.18. HR-MALDI-TOF MS: calcd for $[M + H]^+$ m/z = 889.5883, found m/z = 889.5837. **2b**. Red solid. 12.2 g. Yield: 86%. ^{1}H NMR (300 MHz, $CDCl_3$, 298K) δ = 0.70-0.83 (b, 18H), 0.85-1.23 (m, 42H), 1.94 (m, 8H), 3.88 (s. 6H), 7.19 (b, 4H), 7.25-7.34 (m, 6H), 7.64 (b, 4H), 8.10 (s, 2H). ^{13}C NMR (75 MHz, $CDCl_3$, 298K) δ =14.21, 22.74, 23.98, 29.43, 30.33, 31.94, 40.63, 52.41, 55.16, 114.42, 118.39, 118.73, 119.02, 120.64, 122.92, 126.20, 126.85, 135.74, 138.06, 141.20, 150.35, 152.58, 168.22. HR-MALDI-TOF MS: calcd for [M + H] + m/z = 1001.7135, found m/z = 100.7190. **2a**. Red solid. 9.8 g. Yield: 81%. ^{1}H NMR (300 MHz, $CDCl_3$, 298K) δ = 0.72-0.90 (b, 18H), 1.09-1.29 (m, 74H), 1.95 (m, 8H), 3.89 (s. 6H), 7.20 (b, 4H), 7.28-7.34 (m, 6H), 7.64-7.67 (m, 4H), 8.11 (s, 2H). ^{13}C NMR (75 MHz, $CDCl_3$, 298K) δ = 14.26, 22.83, 24.00, 29.49, 29.73, 29.76, 29.78, 30.35, 32.05, 40.66, 52.37, 55.15, 114.40, 118.35, 118.67, 118.75, 119.02, 120.62, 122.89, 126.19, 126.85, 135.71, 138.05, 141.20, 150.33, 152.56, 168.19. HR-MALDI-TOF MS: calcd for $[M + H]^+$ m/z = 1225.9634, found m/z = 1225.9608.

Synthesize of **C_2IFQA**: Compound **2a** (1g, 1.51 mmol) was mixed with methanesulfonic acid (10 mL) and the mixture was heated to 140 °C under nitrogen for 12h. The resulting deep-green solution was poured into water and the precipitate was collected by filtration. After being washed with water and ethanol, the solid was recrystallized from chloroform/methanol to give the product as a violet powder. 0.74 g. Yield: 82%. ^{1}H NMR (300 MHz, $CDCl_3$ + 20% d_6-DMSO, 298K) δ = 0.29 (t, 12H, J = 7.5 Hz), 2.01-2.03 (m, 8H), 7.24-7.30 (m, 6H), 7.72-7.74 (m, 2H), 8.59 (s, 2H), 8.62 (s, 2H), 11.51 (b, 2H). 13C NMR was not obtained due to limited solubility. HR-MALDI-TOF MS: calcd for $[M + H]^+$ m/z =

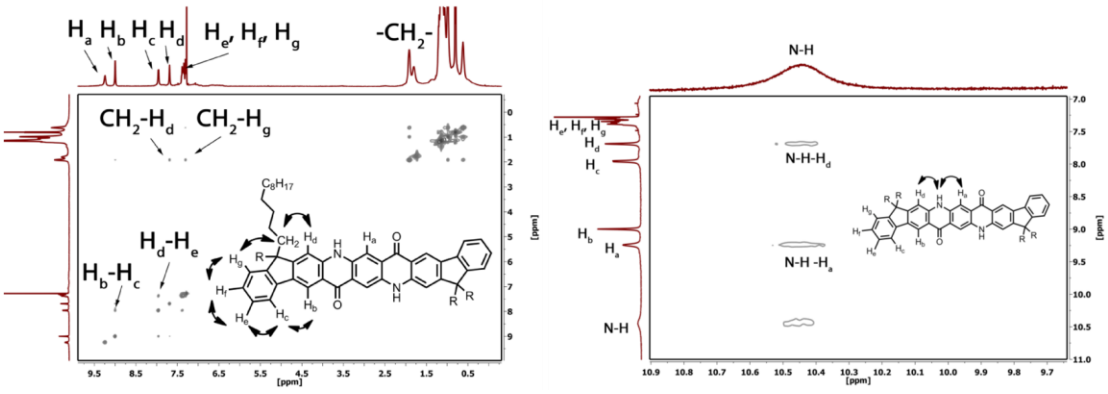

Figure 6.6 500 MHz ^{1}H-^{1}H NOESY NMR spectrum of **C_{12}IFQA** in $CDCl_3$ at RT.

601.7554, found m/z = 601.7569. Compounds **C_6IFQA-C_{12}IFQA** were synthesized according to the same procedure. **C_6IFQA**: Violet powder. 2.2 g. Yield: 80%. 1H NMR (300 MHz, $CDCl_3$ + 20% d_6-DMSO, 298K) δ = 0.58-0.68 (m, 18H), 0.96-1.03 (m, 26H), 1.92-1.98 (m, 8H), 7.23-7.29 (m, 6H), 7.71-7.74 (m, 2H), 8.59 (s, 2H), 8.61 (s, 2H), 11.42 (b, 2H). 13C NMR (75 MHz, $CDCl_3$ + 20% d_6-DMSO, 298K) δ = 13.30, 21.74, 23.09, 30.70, 40.32, 54.56, 119.74, 113.41, 115.92, 118.31, 118.98, 122.18, 124.43, 126.47, 134.25, 134.35, 139.50, 141.42, 148.88, 157.27, 159.51. HR-MALDI-TOF MS: calcd for $[M + H]^+$ m/z = 825.5359, found m/z = 825.5370. **C_8IFQA**: Violet powder. 10.8 g. Yield: 79%. 1H NMR (300 MHz, $CDCl_3$ + 20% d_6-DMSO, 298K) δ = 0.58-0.72 (m, 18H), 0.97-1.03 (m, 42H), 1.92-1.97 (m, 8H), 7.23-7.37 (m, 6H), 7.71-7.74 (m, 2H), 8.58 (s, 2H), 8.60 (s, 2H), 11.46 (b, 2H). ^{13}C NMR (75 MHz, $CDCl_3$ + 20% d_6-DMSO, 298K) δ = 13.11, 21.48, 28.10, 28.16, 28.90, 30.66, 54.29, 110.14, 113.18, 115.64, 118.06, 118.75, 121.95, 124.19, 126.25, 134.02, 134.10, 139.22, 141.20, 148.60, 157.01, 177.21. HR-MALDI-TOF MS: calcd for

$[M + H]^+$ m/z = 937.6611, found m/z =937.6564. **C_{12}IFQA**: Violet powder. 8.8 g. Yield: 72%. ^{1}H NMR (300 MHz, $CDCl_3$, 298K) δ = 0.579-0.78 (m, 18H), 0.80-1.25 (m, 42H), 1.88 (b, 8H), 7.26-7.37 (m, 6H), 7.70 (s, 2H), 7.94-7.96 (m, 2H), 9.00 (s, 2H), 9.27 (s, 2H), 10.59 (b, 2H). ^{13}C NMR (75 MHz, $CDCl_3$, 298K) δ = 14.07, 22.66, 23.85, 29.29, 29.37, 29.67, 29.73, 30.04, 31.88, 41.22, 55.62, 111.78, 114.82, 116.45, 119.47, 120.52, 122.87, 125.58, 127.13, 127.56, 135.15, 136.47, 140.04, 142.71, 149.73, 159.43, 164.99, 179.52. HR-MALDI-TOF MS: calcd for $[M + H]^+$ m/z = 1161.9115, found m/z = 1161.9056.

6.4.3 Solubility and thermal properties of **C_nIFQA**

Compound	Solubility (mg/mL)			T_m (^oC)	T_d[c] (^oC)	Theoretical QA backbone[d] (%)	Carbonization yield[e] (%)
	Toluene	THF	Toluene+DMSO				
C_2IFQA	I[a]	I	I	> 300	466	81.3	81.3
C_6IFQA	I	S[b]	S	> 300	422	59.2	59.8
C_8IFQA	2	>30	S	> 300	413	52.0	52.5
C_{12}IFQA	>30	>30	>30	212	414	42.0	42.6

[a] I = insoluble; [b] S = soluble; [c] 5% weight loss, measured at a scan rate of 10 °C/min from 40 to 900 °C under nitrogen; [d] Weight percentage of the IFQA backbone excluding the sp^3 alkyl groups, calculated from molecular formula; [e] Experimental carbonization yield at 600 ^{o}C measured by TGA.

Table 6.2 Solubility and thermal properties of **C_nIFQA**.

6.4.4 TGA analysis of **C_nIFQA**

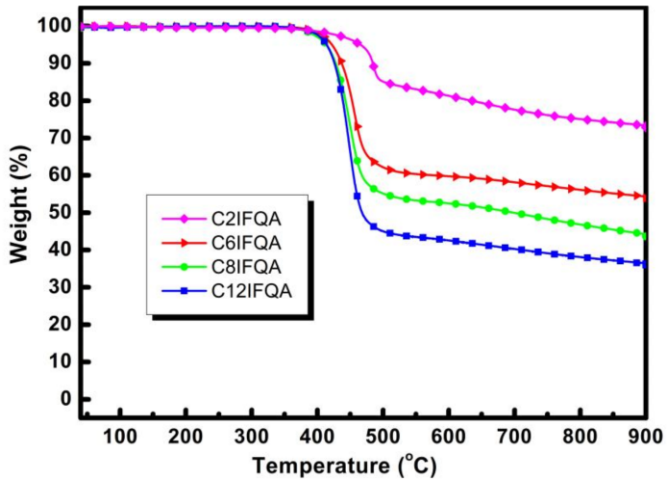

Figure 6.7 TGA curves of **C_nIFQA**. Measurement was performed at a scan rate of 10 °C/min from 40 to 900 °C under nitrogen.

6.4.5 DSC analysis of **C_nIFQA**

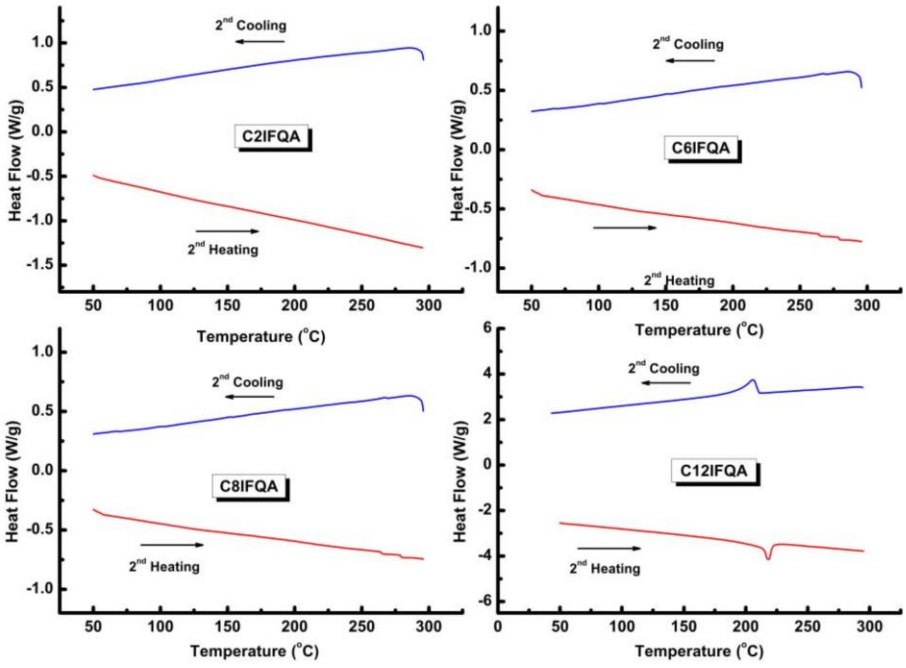

Figure 6.8 DSC curves of **C_nIFQA**. Measurement was performed at a scan rate of 10 °C/min from 40 to 300 °C under argon for two cycles.

6.4.6 Absorption spectrum of **C_{12}IFQA** in toluene with DMSO

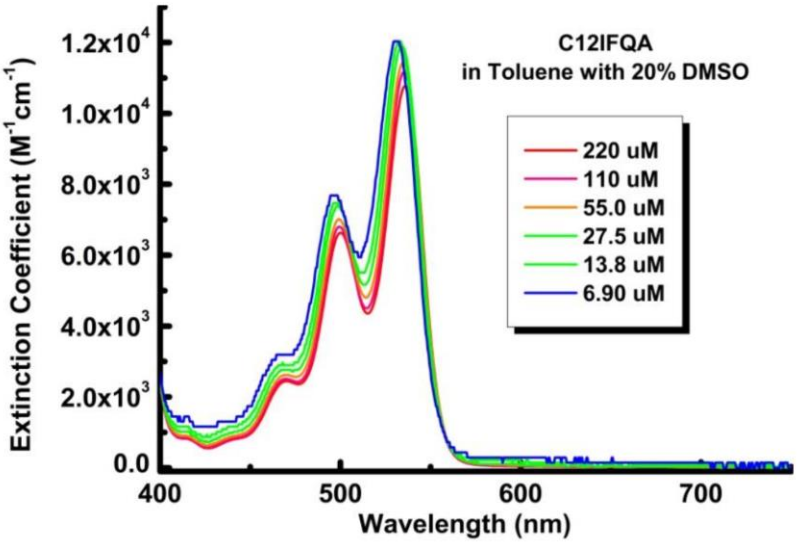

Figure 6.9 Concentration-dependent UV-vis spectra of **C_{12}IFQA** in toluene + DMSO at RT.

6.4.7 Absorption spectrum of **C_8IFQA** in toluene

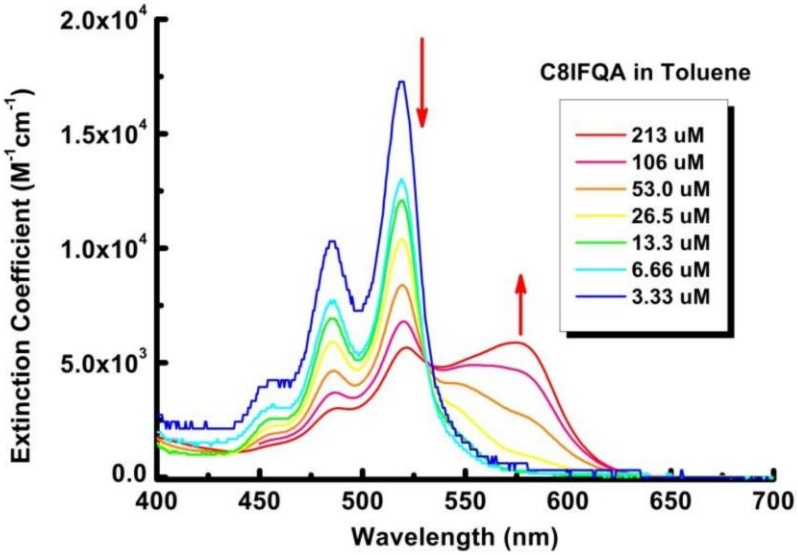

Figure 6.10 Concentration-dependent UV-vis spectra of **C_8IFQA** in toluene.

6.4.8 Fluorescence spectra of **C_8IFQA** in toluene

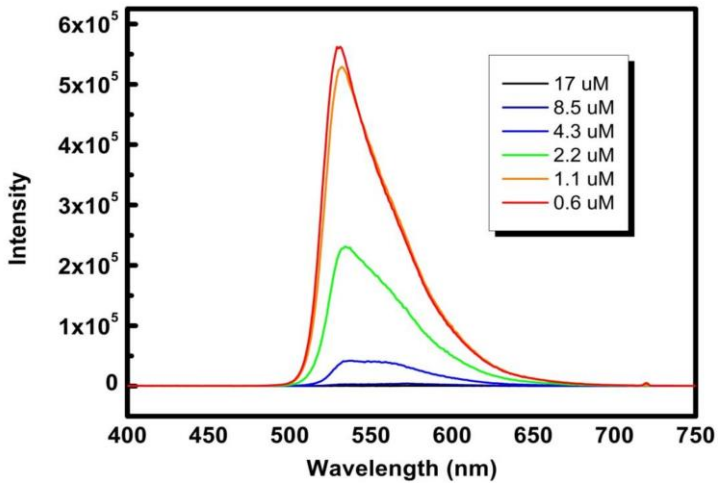

Figure 6.11 Concentration-dependent fluorescence spectra of **C_{12}IFQA** in toluene at RT.

6.4.9 Electrochemistry properties of **C_{12}IFQA** in dichloromethane

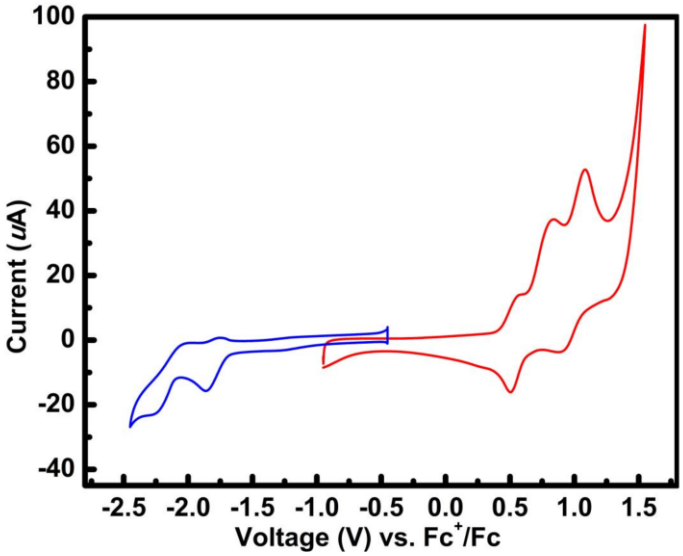

Figure 6.12 Cyclic voltammetry curves of **C_{12}IFQA** in dichloromethane, using Fc^+/Fc as reference, the HOMO and LUMO energy were calculated as -5.26 eV and -3.2 eV, respectively.

6.4.10 H-bond calculation based on UV-vis spectra

Isodesmic aggregation model[263] was used to calculate the association constant *K* for IFQA, assuming that *K* values were the same regardless the aggregate size. The fraction of IFQA molecules in aggregated state (*α*agg) can be expressed as:

$$\alpha_{agg} = 1 - \frac{2Kc_T+1-\sqrt{4Kc_T+1}}{2K^2{c_T}^2} \qquad \text{(Eq. 6.1)}$$

c_T is the total concentration of IFQA molecule.

Based on variable concentration UV-vis spectra, *α*agg values for each concentration were obtained from the intensities of deconvoluted peaks that were associated with either the H-bonded state or the discrete state. After plotting *α*agg against c_T, non-linear fitting of the plot by Eq. 6.1 gave the *K* value. Two absorption wavelengths (484 nm and 560 nm) were used to plot the data to give *K* values of 2550 and 2140 M^{-1} respectively. The free Gibbs energy change at around 4.6 kcal/mol was then calculated using $\Delta G° = RT\ln K$ (Eq. 6.2), wherein R is the gas constant and T was 298K. The fitting curve plots were shown in Figure 6.13. Note that the data points at higher concentration were slightly deviated from the curve, probably due to the violation of Beer-Lambter's law at higher concentration.

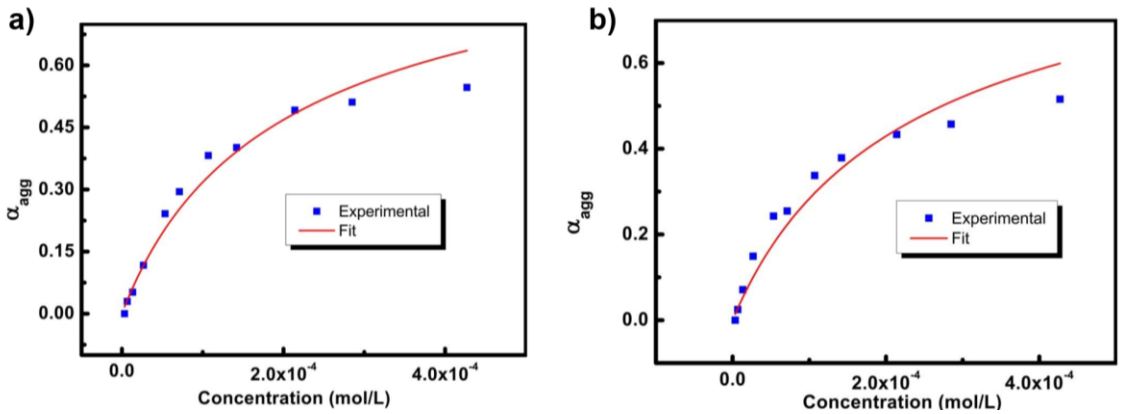

Figure 6.13 Isodesmic aggregation fitting curve calculated based on absorption of **C_{12}IFQA** at a) 484nm (K = 2550, R^2 = 0.96, ΔG = 4.6 kcal/mol) and b) 560 nm (K = 2140, R^2 = 0.94, ΔG = 4.5 kcal/mol).

CHAPTER 7

SYNTHESIS AND SOLUTION PROCESSING OF A HYDROGEN-BONDED LADDER POLYMER*

7.1 Introduction

A ladder polymer chain is defined as a multiple-strand macromolecule consisting of an uninterrupted sequence of rings where adjacent rings share two or more atoms.[265-266] Because of the fused-ring constitution, free torsional rotation of sigma bonds between the repeating units is generally prohibited in a ladder polymer backbone. This feature leads to a fully rigid conformation, in contrast to the flexible or semi-rigid nature of most conventional polymers. As a result, ladder polymers acquire a number of unique and fascinating properties from this structural rigidity, promising their great potential in various demanding applications. For example, non-coplanar ladder polymers can be highly permeable to certain gases with excellent selectivity on account of the rigid yet porous solid-state morphology.[267-269] The electronic performance of coplanar conjugated ladder polymers is excellent as a result of their delocalized π orbitals[270] and favorable intermolecular stacking.[158, 271-281] Moreover, because conjugated ladder polymers possess the pre-assembled structural feature similar to graphene nanoribbons,[152, 282-283] it is anticipated that they could be transformed into graphitic carbon materials in a different manner than the prevailing carbon fiber

* Part of this section is reprinted with permission from Synthesis and Solution Processing of a Hydrogen-Bonded Ladder Polymer by Zou, Y. et al., *Chem*, **2017**, 2, 139-152. Copyright 2017 by Elsevier.

precursors, such as polyacrylonitrile.[284-286] In this context, novel ladder polymers with synthetic and processing feasibility, structural versatility, and controlled functionality are expected to deliver breakthrough chemical, electronic, and mechanical functions for various applications.

Inter-chain interactions also play a key role in governing a wide range of properties and functions of ladder polymers, particularly for those closely related to solid-state packing.[287-290] It is crucial to manipulate both the intermolecular interactions (noncovalent bonds) and the macromolecular characteristics (rigid ladder-type backbone) to precisely control the properties and functions of ladder polymers.[291] In the context of this challenge, hydrogen bonds have been recognized as an ideal tool for shaping the properties of conjugated systems[246, 292-298] because they demonstrate profound impacts on the charge transport, mechanical strength, and film-forming properties of these materials. Therefore, the incorporation of well-defined hydrogen bonds into ladder polymer backbones promises advancement in terms of both fundamental investigation of the structure-property relationship and practical exploration for electronic or mechanical performances.

Despite the numerous examples of ladder polymers, only a handful with intermolecular hydrogen bonds have been proposed or reported in the literature.[299-301] Precise structural characterization of these examples, however, has not been well established because of their insoluble nature. The formidable challenges associated with this class of polymer are twofold: difficulties in incorporating hydrogen-bond donors and acceptors simultaneously into the rigid backbone and the solubility issues in synthesis, characterization, and processing. Herein, we report the design and synthesis of a ladder polymer in which well-defined hydrogen bonds are incorporated into the backbone in the

form of a quinacridone derivative. Clear solution-phase characterization and solution processing of this polymer were achieved through a post-functionalization step in which the polymer was reversibly converted into a highly soluble intermediate and then regenerated by thermal annealing. Successful demonstration of the efficient synthesis, unambiguous characterization, and solution processing of this hydrogen-bonded ladder polymer sets the stage for its applications under extreme processing or operating conditions.

7.2 Results and Discussion

Molecular design of the hydrogen-bonded ladder polymer was developed on the basis of a quinacridone unit,[302] which features five linearly fused rings (Figure 7.1a). As an inexpensive, non -toxic, and environmentally friendly pigment with a pentacene-like backbone, quinacridone is a promising building block of high-performance optoelectronics materials.[237-238, 241, 246, 303] Two sets of self-complementary hydrogen bonds can be formed intermolecularly between the carbonyl and NH functional groups on the quinacridone unit.[261-262, 304] These hydrogen-bonding interactions promote strong intermolecular electronic coupling[246] of quinacridone molecules and guide their self-assembly to give a compact packing mode, leading to good charge carrier mobility,[246] as well as high thermal, chemical, and photochemical stability.[236, 305-306] We envisioned that the incorporation of quinacridone into a ladder polymer backbone could create a rigid ladder-type polymer chain with fixed conformation and multiple hydrogen-bonding interactions, addressing the aforementioned challenges. In this context, we designed ladder-type poly(indenoquinacridone) (**PIQA**) for this study (Figure 7.1a). The synthetic strategy of **PIQA** was devised on the basis of our previously reported ‘‘condensation-followed-by-

cyclization'' method,[307] which afforded indenoquinacridone (**IQA**) small molecules in high efficiency (Figure 7.1a). Building on this strategy, **PIQA** can be constructed similarly. In this process, step-growth imine condensation polymerization affords a precursor polymer

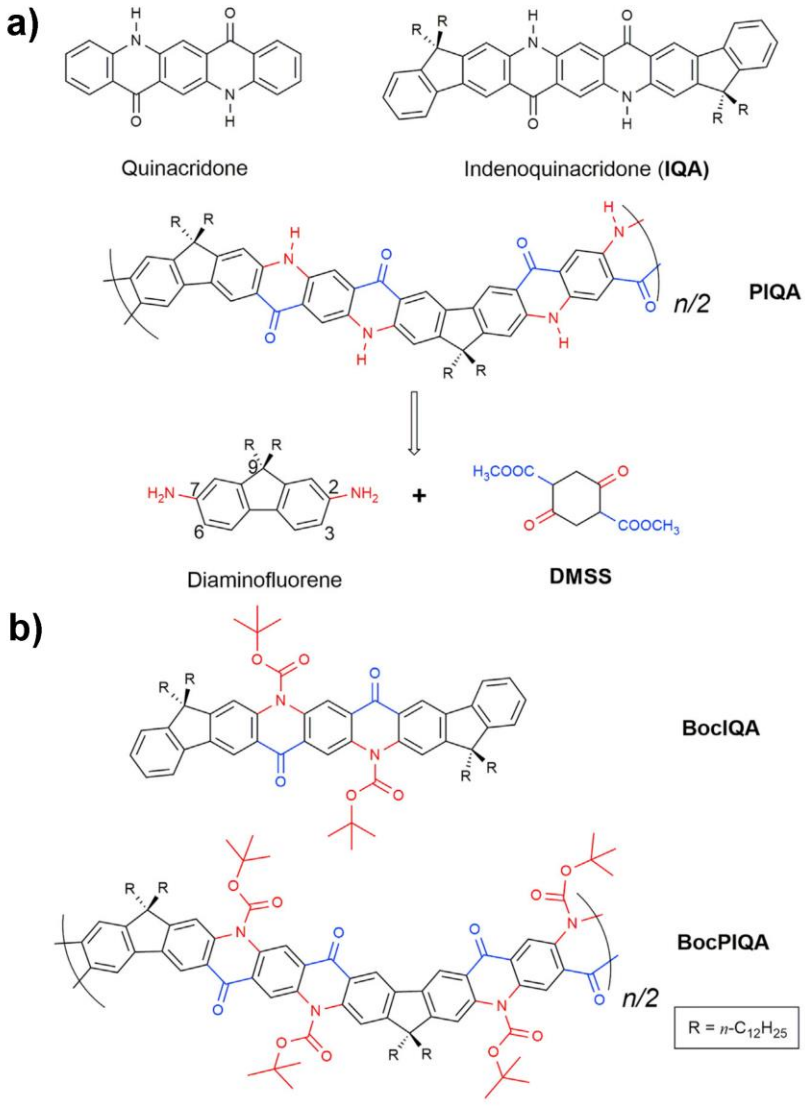

Figure 7.1 Structural Formula a) Structural formula of quinacridone, **IQA**, and **PIQA**. The two starting materials for **PIQA** are 2,7-diaminofluorene and DMSS. b) Structural formula of Boc-functionalized **IQA** and **PIQA**: **BocIQA** and **BocPIQA**, respectively.

before the Friedel-Crafts cyclization fuses the aromatic units into a ladder-type backbone (Scheme 7.1). Functionalized fluorene and dimethyl succinyl succinate (DMSS) were selected as the monomer starting materials for this synthesis. In the fluorene monomer, the

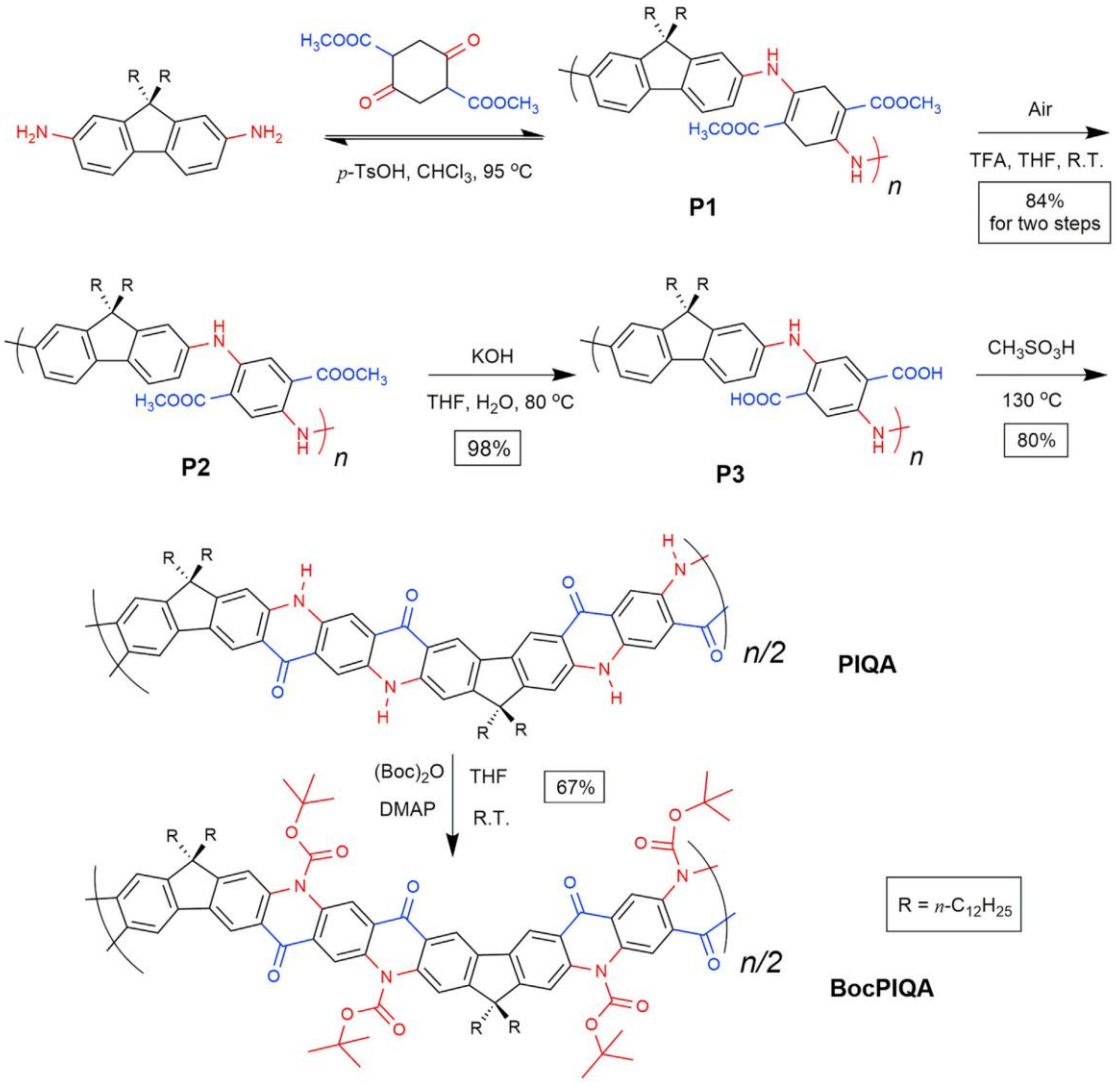

Scheme 7.1 Synthetic route of the quinacridone-derived ladder polymer **PIQA** and its Boc-protected derivative **BocPIQA**.

C2 and C7 positions can be functionalized by amino groups for the subsequent imine condensation reactions.

Consequently, the only remaining reactive sites on the fluorene unit for electrophilic cyclization are the C3 and C6 positions; the C1 and C8 positions are too sterically hindered to react.[158, 271, 308-310] The regiospecific reactivity of the fluorene unit avoids the possibility of isomer formation during the cyclization step, making it an ideal building block for the designed ladder polymer. The condensation partner for diaminofluorene is DMSS, which can be converted into quinacridone moieties, as demonstrated in the literature.[307] Overall, this regiospecific design requires inexpensive starting materials and only three steps, allowing for large-scale and low-cost production.

Despite the solubilizing dodecyl side chains, the final product **PIQA** was expected to have poor solubility because of its rigid backbone and the intermolecular hydrogen bonds. This problem can be solved by a reversible hydrogen-bond protection strategy.[311-315] The N–H groups in the PIQA backbone can be reversibly protected by bulky tert-butyloxycarbonyl (Boc) groups. As a result, much higher solubility of the Boc-functionalized ladder polymer (**BocPIQA**, Figure 7.1b) was expected for characterization and solution processing. Subsequently, the Boc groups could be easily cleaved by thermal treatment to regenerate the original hydrogen-bonded ladder polymer **PIQA**.

On the basis of the aforementioned design principles, a highly efficient three-step synthesis was developed and optimized (Scheme 7.1) to give **PIQA** on the gram scale without using noble metal catalysts. The synthesis started with step-growth imine condensation polymerization between 2,7-diamino-9,9-didodecylfluorene and DMSS. Subsequent tautomerization[239, 252] to the enamine form afforded the intermediate

cyclohexadiene-fluorene polymer **P1**.[256] The linear n-dodecyl chains on the diaminofluorene monomer were essential for achieving a reasonable degree of polymerization. Shorter alkyl chains such as ethyl or 2-ethylhexyl were insufficient in maintaining solubility and hence led to precipitation of oligomers during the reaction. In contrast, long branched alkyl chains

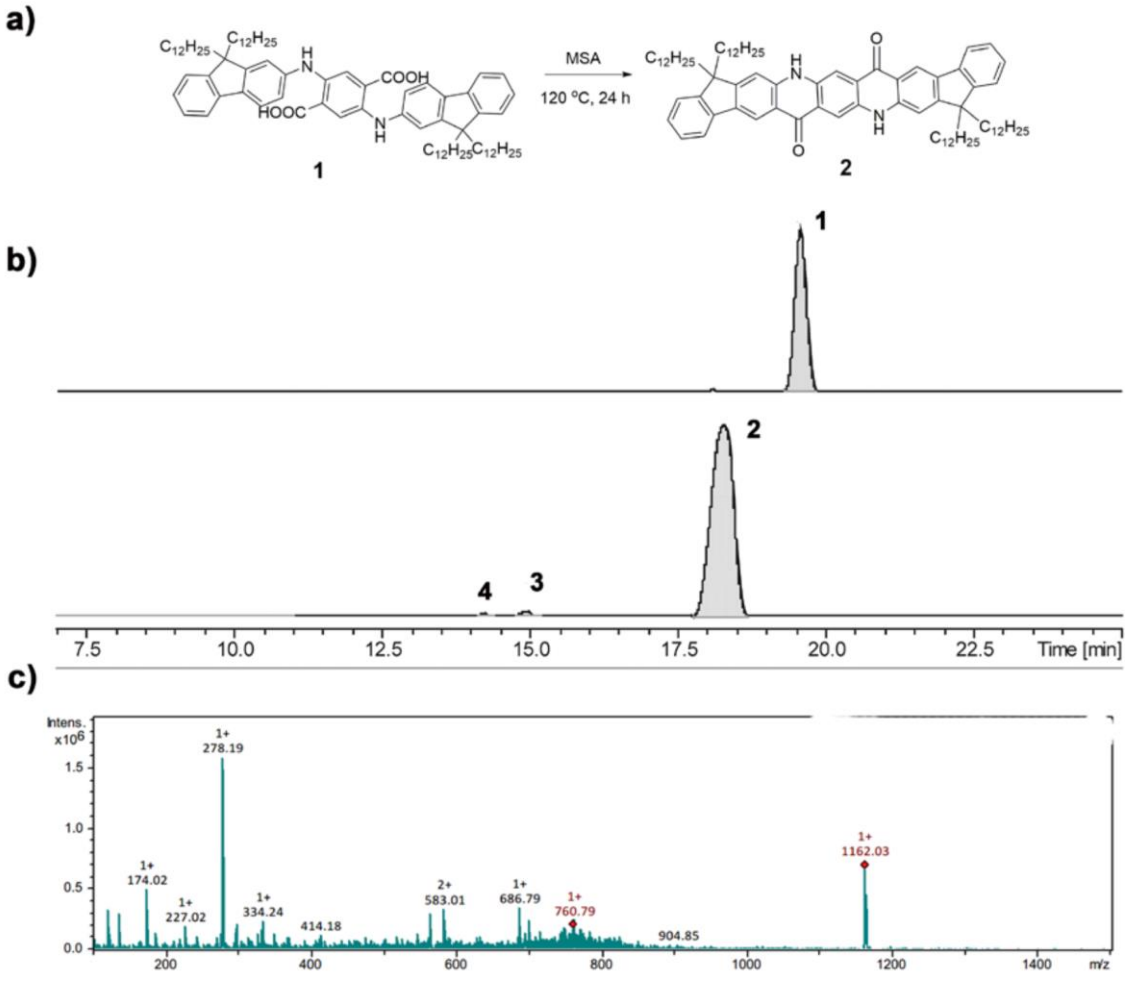

Figure 7.2 a) A model ring cyclization reaction to afford small molecular **IQA** (**2**), b) chromatogram of HPLC-MS of the starting material **1** (top) and **IQA** crude product **2** (bottom) demonstrating a conversion rate of 98.6%, c) mass spectra corresponding to the major peak of crude product **2**.

(i.e., 2-octyldodecyl) led to lower reactivity and resulted in a low degree of polymerization. The polymerization conditions were optimized with p-TsOH as the catalyst in $CHCl_3$ at 90°C for 72 hr. End capping of the polymer was attempted with monofunctional aniline and carbonyl compounds. However, because of the dynamic nature of imine condensation, the polymer degraded into oligomers as a result of loss of the stoichiometric balance of functional groups. Therefore, **P1** was not treated with an end-capping reagent. **P1** was readily oxidized[253, 307] into the conjugated fluorene-aniline polymer **P2** in air in the presence of a catalytic amount of trifluoroacetic acid, leading to a color change from light orange to red (Figure 7.8). After purification by acetone extraction, size exclusion chromatography (SEC) of **P2** revealed a number-average molecular weight (Mn) of 24.0 kg/mol and a polydispersity index of 2.3. (See Experimental Section and Figure 7.7) To complete the construction of the ladder backbone, we used a highly efficient electrophilic aromatic cyclization reaction to form the second strand of covalent bonds between the fluorene units and the carbonyl groups. Reaction optimization and high-performance liquid chromatography (HPLC) analysis on a model reaction to synthesize small molecular **IQA** in methanesulfonic acid (MSA) demonstrated that a carboxylic acid group was a better substrate (affording 98.6% conversion in this cyclization reaction) than the less efficient methyl ester substrate in a previous report[307] (Figure 7.2). In this context, the pendant methyl ester groups in **P2** were hydrolyzed by KOH into carboxylic acid quantitatively. The resulting polymer **P3** was subjected to electrophilic aromatic cyclization. The well-established regiospecificity of the fluorene unit in electrophilic addition guaranteed a regioregular product.[272-273, 310, 316] The regiospecificity was also confirmed by HPLC and

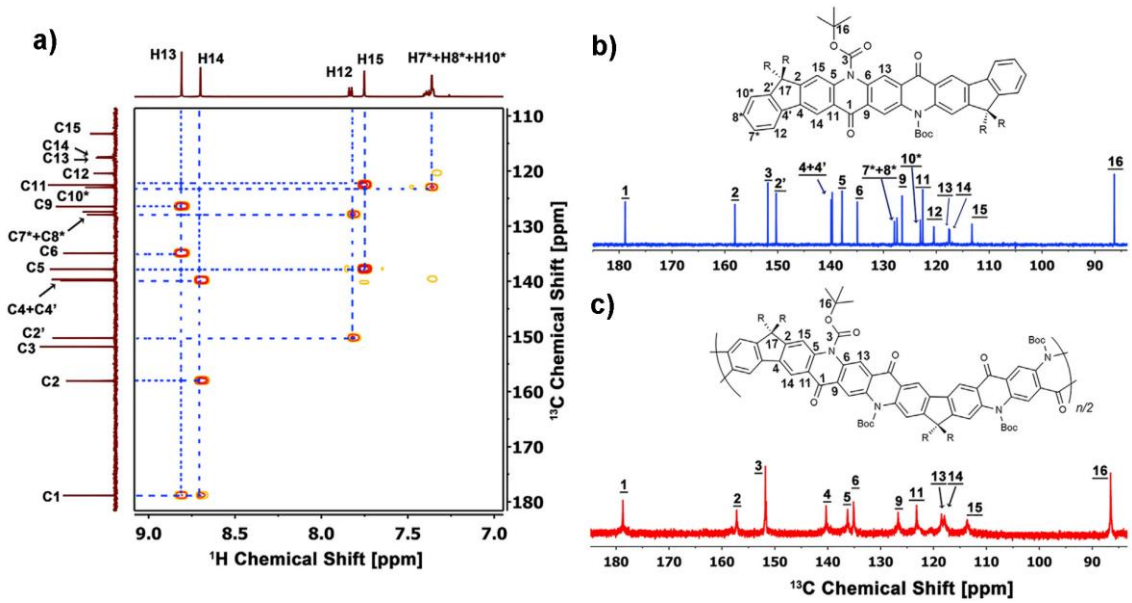

Figure 7.3 NMR spectra and signal assignment of **BocIQA** and **BocPIQA**. a) HMBC spectrum of **BocIQA**. b) ^{13}C-NMR spectra and ^{13}C signal assignment of **BocIQA**. c) ^{13}C-NMR spectra and ^{13}C signal assignment of **BocPIQA**.

NMR analysis in the IQA model reaction (Figure 7.2). The optimized conditions for the PIQA synthesis involved heating **P3** in MSA, an inexpensive and environmentally friendly reagent,[257] and resulted in an isolated yield of 80%. During this process, the acidic MSA promoted51 electrophilic cyclization at high temperature and maintained the intermediate and product well solubilized, ensuring the completion of the reaction. In fact, MSA is the only known solvent capable of dissolving the ladder polymer product **PIQA**. Considering the high conversion of this cyclization reaction and low possibility of side reactions (1.4%), the estimated average number of potential defect sites per polymer chain would be less than 1. Overall, the gram-scale, transition-metal-free synthesis of **PIQA** was achieved in only three steps from diaminofluorene in 66% overall yield. Poor solubility represents a general challenge for the characterization of ladder polymers or polymers with strong intermolecular

interactions. With a rigid ladder-type backbone and strong intermolecular hydrogen bonds, the solubility of **PIQA** was extremely low in common organic solvents, preventing any meaningful solution phase characterization. To overcome this issue, we employed a post-functionalization method to reversibly convert **PIQA** into a highly soluble material. This strategy involved the attachment of Boc onto the N–H functional groups by treating **PIQA** suspension in THF with di-tert-butyl dicarbonate at 60°C. Once attached to the polymer backbone, the bulky Boc moieties not only diminished the intermolecular hydrogen bonds but also prohibited the inter-chain p-p interaction by steric effects. Therefore, the resulting product (**BocPIQA**) was highly soluble in chloroform (over 100 mg/mL), THF toluene, etc. The M_n of **BocPIQA** (14 kg/mol) was lower than that of **P2** as a result of the slower reaction rate of the high-molecular-weight fraction. Consequently, some of the higher polymer chains were not fully converted to soluble materials within a reasonable reaction time frame. After purification by preparative SEC, however, the M_n of **BocPIQA** could reach up to 23.7 kg/mol, close to that of the precursor **P2**. Characterization of BocPIQA confirmed the structure of its precursor, insoluble **PIQA**, unambiguously. The ^{1}H-NMR spectrum of **BocPIQA** showed broad[272, 317-319] yet well-defined peaks, corresponding to the highly symmetrical protons on the ladder-type backbone. Small satellite ^{1}H signals in this spectrum can be attributed to (1) protons associated with chain ends and repeating units close to the chain ends and (2) a small amount of defects caused by side reactions demonstrated from the HPLC result. More importantly, the excellent solubility of BocPIQA allowed for a concentration-demanding ^{13}C-NMR spectrum with a high signal/noise ratio (Figure 7.3c).

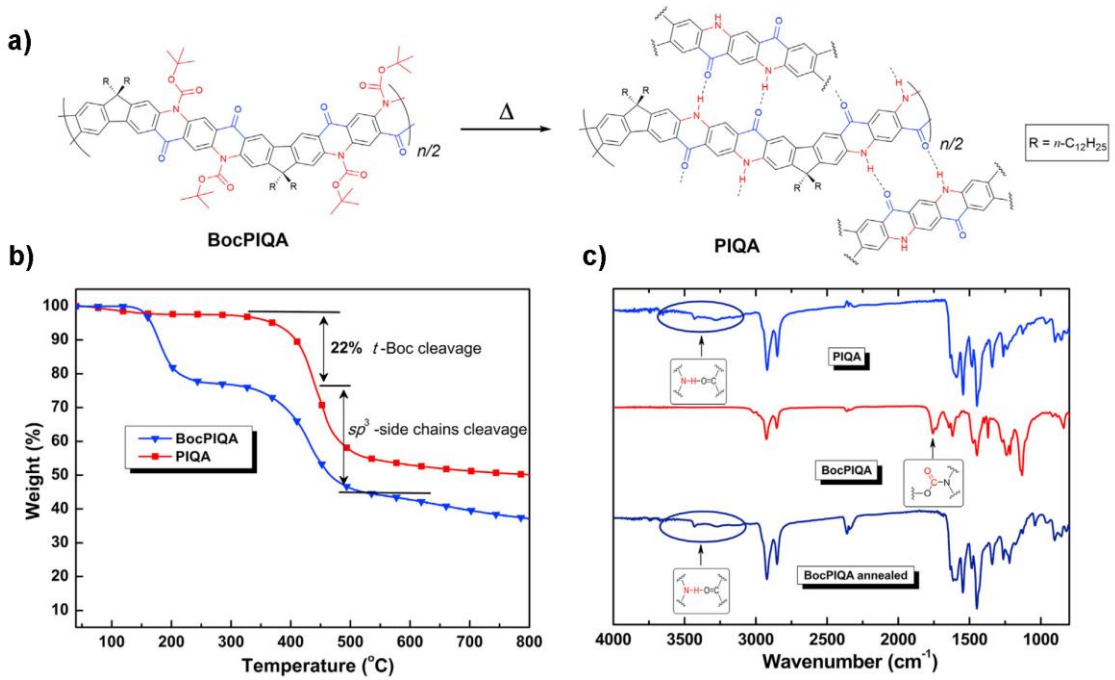

Figure 7.4 Thermal cleavage of Boc groups a) Schematic representation of Boc cleavage of **BocPIQA** by thermal annealing in the solid state, including regeneration of **PIQA** with intermolecular hydrogen bonds. b) TGA curves of **PIQA** and **BocPIQA** show key weight losses and carbonizations yields at 800°C. c) FT-IR spectra of **PIQA** and **BocPIQA** before and after thermal annealing.

Sharp and characteristic ^{13}C resonance peaks were observed, and all were assigned to specific carbons on the polymer. This assignment was rigorously performed with the small molecular model compound **BocIQA** as a reference. First, all the ^{13}C resonance peaks of BocIQA were assigned according to its heteronuclear single quantum correlation (HSQC) and heteronuclear multiple bond correlation (HMBC) spectra (Figures 7.3a). Sharing a similar constitutional structure, **BocPIQA** showed ^{13}C resonance patterns matching that of **BocIQA** (Figures 7.3b and 7.3c) but had fewer signals as a result of the more symmetrical nature of its repeating units. Consequently, the clean and well-defined ^{13}C-NMR spectrum

of **BocPIQA** confirmed its unique regioregular ladder-type structure and a low defect level along the backbone.[318] In addition, because the fluorene and benzene units are linked with each other by carbonyl groups, they are cross-conjugated along the ladder polymer backbone.[320-322] As a result, **PIQA** and **BocPIQA** shared similar energy levels and bandgaps with their small molecular counterparts **IQA** and **BocIQA**, respectively, as revealed by UV-Vis and cyclic voltammetry (CV) experiments (Figure 7.9 and 7.11). To further correlate the characterization data of **BocPIQA** with **PIQA**, it was also essential to demonstrate that **BocPIQA** could be converted back to **PIQA** completely after the anticipated thermal treatment (Figure 7.3a). We first performed thermogravimetric analysis (TGA) of **BocPIQA** to demonstrate a weight loss at 160°C–200°C (Figure 7.3b), representing the Boc cleavage process.[315] This phenomenon was similar to that of **BocIQA**, and the 22% weight loss agreed well with the theoretical weight percentage of Boc groups in **BocPIQA** (23%).

Furthermore, FT-IR was used to characterize the chemical structure before and after the thermal cleavage. Compared with that of **PIQA**, the FT-IR spectrum of **BocPIQA** showed (Figure 7.3C) additional C=O stretching at 1,758 cm^{-1}, corresponding to the Boc group, and the loss of N–H stretching at 3,100~3,500 cm^{-1}. After thermal annealing of **BocPIQA**, the IR spectrum became identical to the original spectrum of **PIQA**, demonstrating a full recovery of **PIQA** from **BocPIQA** and the regeneration of the hydrogen bonds. Cleavage of the Boc groups was also observed by UV-Vis and fluorescence spectra (Figure 7.10). The solid-state UV-Vis spectrum of **BocPIQA**, after annealing at 200°C for 30 min, showed an identical absorption spectrum to that of **PIQA** as a result of the hydrogen-bond regeneration, and the strong fluorescence was quenched as a result of aggregation. Although the polymer did not undergo a glass transition at the Boc cleavage temperature,

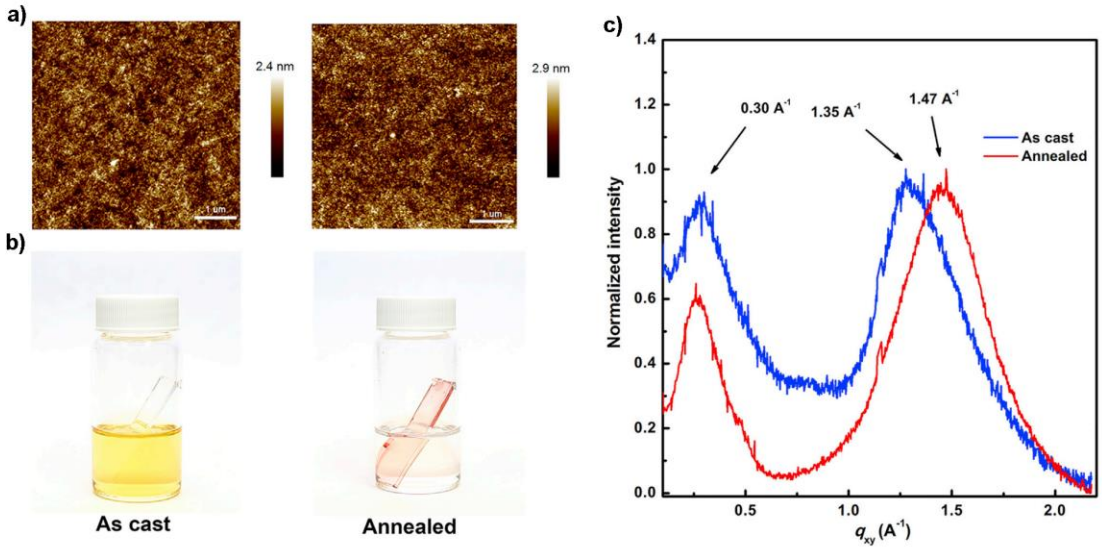

Figure 7.5. Characterization data of **BocPIQA** and **PIQA** thin films a) AFM height-profile images of a BocPIQA thin film on silicon wafer before (left) and after (right) thermal annealing. b) (Left) A photograph of the result after the as-cast thin film was soaked on a glass slide in chlorobenzene shows complete dissolution of the thin film. (Right) The result of soaking an annealed thin-film sample in chlorobenzene shows solvent resistance. c) GIXD of the as-cast thin film (blue) in comparison with that of the annealed thin film (red).

the hydrogen-bond regeneration took place within the relatively small free volume at 180°C, similar to the observations on other hydrogen-bonded conjugated polymers.[311-312, 315]

Processability is important for most of the practical applications of conjugated polymers. Thanks to the excellent solubility of **BocPIQA** and its efficient regeneration back to **PIQA**, thin films of this hydrogen-bonded ladder polymer can be easily processed through spin coating **BocPIQA**, followed by thermal Boc cleavage (Figure 7.4a). Uniform films of **BocPIQA** with thickness of 83 and 125 nm on silicon wafer substrates were prepared by spin casting from chlorobenzene solution at spin speeds of 1,000 and 600 rpm, respectively. Under atomic force microscopy (AFM), both films showed smooth surface morphology with

root-mean-square (RMS) roughness of around 0.35 nm. To regenerate the hydrogen-bonded **PIQA** thin films, we annealed them at 180°C for 30 min. Both films were found to remain smooth and uniform (RMS ~ 0.41 nm) and showed a moderate decrease in thickness to 62 and 90 nm, respectively (Figure 7.5a). This thickness decrease was attributed to the loss of Boc groups and a resulting tighter solid-state packing promoted by the regenerated hydrogen bonds. We used grazing incidence X-ray diffraction (GIXD) to examine the packing parameters of the polymer thin films of **BocPIQA** before and after thermal annealing (Figure 7.5c). Two characteristic peaks were observed for both as-cast and annealed samples. The peak at q ~ 0.30 $Å^{-1}$ corresponded to the scattering of dodecyl chains[323-325] on fluorene moieties and did not shift before or after thermal annealing. The p-p stacking scattering of the backbone shifted significantly from 1.35 to 1.47 $Å^{-1}$ after **BocPIQA** was converted into **PIQA**, corresponding to a decrease in the p-p distance[323-325] from 4.65 Å for **BocPIQA** to 4.27 Å of **PIQA**. This change agreed with the thickness decrease as a result of the removal of bulky Boc groups.[313] Because of the stability and low solubility of **PIQA**, its thin films were expected to be solvent and heat resistant. Indeed, the annealed films remained intact against a wide variety of aggressive solvents at a high temperature (Figure 7.5b), except for concentrated H_2SO_4 and MSA (Figure 7.6). Solvent-resistance tests involved soaking annealed **PIQA** thin films (with thickness of 105 nm) on glass substrates in various solvents for 30 min. We performed UV-Vis absorption spectroscopy and AFM measurements after solvent treatments to evaluate the integrity of these thin films. We found that they remained intact in most of the hot organic solvents and acid solutions, including boiling THF, chloroform, chlorobenzene, 13 M HCl aqueous solution, ethyl acetate, and hexane. No significant change was found in the UV-Vis spectra after soaking. Moreover, as revealed by

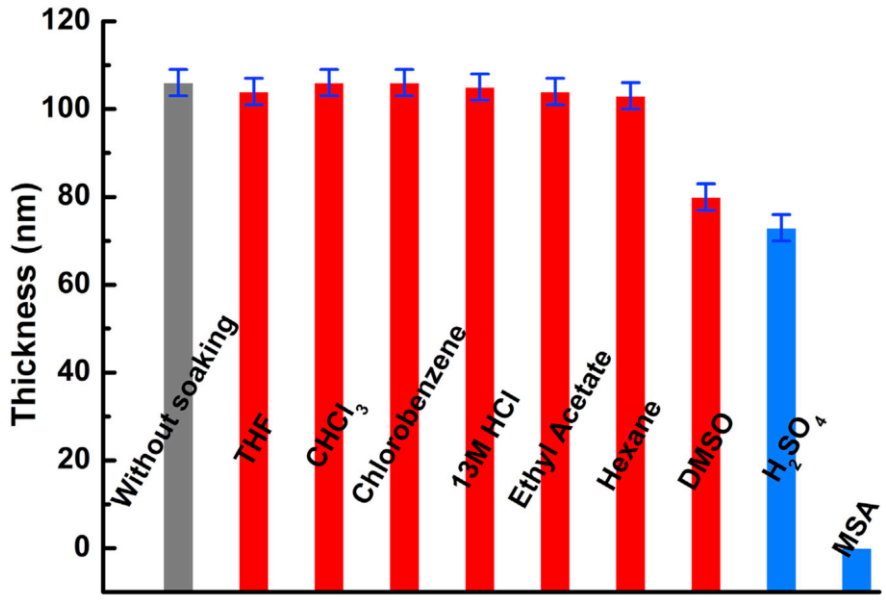

Figure 7.6 Solvent-resistance test of **PIQA** thin film thickness of annealed **BocPIQA** film after soaking in different solvents for 30 min. The red bars represent boiling solvents or solutions, and the blue bars represent treatment at room temperature. Error bars represent standard deviations of multiple measurements over different areas of the film.

AFM, the film thickness (105 ± 5 nm) and morphology (RMS ~ 0.5 nm) remained the same (Figure 7.6 and Figure 7.11). No solvent swelling-induced thickness increase was observed either, indicating an extremely tight intermolecular interaction between **PIQA** chains in the thin-film state. This feature distinguishes **PIQA** from most cross-linked polymers, which can undergo swelling in the presence of aggressive solvents despite their insoluble nature. **PIQA** thin films can only be partially dissolved in very aggressive boiling DMSO or room temperature H_2SO_4 solvents. MSA was the only solvent that fully dissolved the thin film at room temperature. Overall, the hydrogen-bonded ladder polymer **PIQA** demonstrated excellent resistance to aggressive solvents in the thin-film state.

From a thermodynamic perspective, analogous to carbon materials such as graphene and nanotubes,[326] fused-ring sp^2 ladder polymers promise better thermal stability and graphitic structure after carbonization. TGA of **PIQA** (Figure 7.4b) demonstrated remarkably higher thermal stability of ladder polymer over conventional polymers in terms of both decomposition temperature (T_d) and carbonization yield. For example, before ring cyclization, **P2** showed a T_d at 315°C with a carbonization yield of 32% at 800°C. In contrast, **PIQA** showed an elevated T_d at 370°C. The weight loss at 370°C was attributed to the homolytic thermal cleavage of the sp^3 dodecyl side chains. The conjugated, fused-ring sp^2 backbone, however, retained its weight at temperatures as high as 800°C. The carbonization yield of 50% at this temperature was much higher than that of **P2** and agreed well with the theoretical sp^2 backbone weight (49%). These results demonstrate that the hydrogen-bonded backbone of **PIQA** could be converted into carbon material in a high yield after the thermal cleavage of its sp^3 side chains. Conductivity measurement of **PIQA** after thermal treatment at different temperatures was performed. The samples exhibited insulating character at 200°C and 500°C. After further annealing at 700°C, frequency-independent alternating current (AC) conductivity of 5.45×10^4 S/cm was observed, indicating the formation of intrinsically conductive carbon materials. Structural evolution during the high-temperature treatment was examined by Raman spectra (Figure 7.12). An enhanced characteristic G-band peak at 1,577 cm^{-1} confirmed the formation of a regulated graphitic sp^2 structure. The formation of an sp^2 graphitic structure was also revealed by X-ray photoelectron spectrum of carbonized **PIQA**, which showed an identical signal to that of the highly oriented pyrolytic graphite (Figure 7.12). The insulating-conducting transition temperature in **PIQA** is comparable with that of high-performance carbon fiber precursors such as

polyacrylonitrile, demonstrating the significant impact of the preformed fused-ring structure on graphitization efficiency.[285, 327] This result, together with the structural versatility and excellent processability of the precursor **BocPIQA**, promises an efficient strategy for the development of functional carbon materials with desirable nanoscopic and macroscopic morphology.

7.3 Conclusion

In summary, **PIQA** is a unique class of polymeric material with self-complementary hydrogen bonds incorporated into ladder-type repeating units. The synthetic approach to **PIQA** requires only three steps with a high overall yield of 66%. Feasible gram-scale preparation has been demonstrated. No noble metal reagent or catalyst is involved in the synthesis. The challenges associated with characterizing and processing insoluble ladder polymers are addressed by a reversible post-functionalization strategy. This approach enabled concentration-demanding methods such as ^{13}C-NMR spectroscopy for structure elucidation. Furthermore, it imparts solution processability to this highly challenging material through a processing-followed-by-annealing approach, enabling not only thin-film casting as demonstrated here but also potential solution-processing techniques such as printing and electro-spinning, etc. The features of backbone rigidity and strong intermolecular hydrogen bonds are integrated in **PIQA** to render its excellent chemical and solvent resistance in the solid state and the graphitic feature after thermal treatment. In particular, the stability against aggressive solvents at high temperature allows the polymer film to be used as a protective coating material for harsh environments or in applications involving extreme operating conditions or multiple steps of solution processing, etching, and

development. Moreover, with the graphitic fused aromatic backbone, **PIQA** shows promising potential as a precursor for functional carbon materials. Overall, the reported synthetic approach opens up the possibility of the design and large-scale production of highly rigid, strongly self-associated macromolecules possessing unusual properties, in terms of both solvent resistance and the ability to form graphitic carbon materials, for various applications.

7.4 Experimental Procedure

7.4.1 General Methods

Unless otherwise indicated, all starting materials were obtained from commercial suppliers and were used without further purification. DMSS was recrystallized from toluene before polymerization. Reaction solvents were purified by a solvent purification system before use. 2,7-Diamino-9,9-didodecylfluorene,[328] compounds **2** and **3**, and **IQA**[307] were prepared according to the literature. ^{1}H-, ^{13}C-, ^{1}H-^{1}H-COSY, NOESY, HSQC, and HMBC NMR spectra were obtained on a Varian Inova 500 MHz spectrometer at room temperature. Chemical shifts are reported in ppm in relation to the signals corresponding to the residual non-deuterated solvents ($CDCl_3$: d 7.26; d_8-THF: d 3.58 for 1H; and $CDCl_3$: d 77.16; d_8-THF: d 67.67 for ^{13}C at room temperature). SEC was performed on a TOSOH EcoSEC (HLC-8320GPC) chromatograph system at 40°C with THF as the eluent. The molecular weights were calculated with a calibration curve according to polystyrene standards. The SEC columns were TSK gel SuperHM-M and TSK gel SuperH-RC. TGA was performed on a TAQ500 thermogravimetric analyzer. UV-Vis absorption spectra were recorded with a Shimadzu UV-2600 UV-Vis spectrophotometer, and the fluorescent spectra were measured

on a Horiba Fluoromax-4 spectrometer. FT-IR spectra were recorded by ZnSe attenuated total reflection with a Shimadzu IRAffinity-1S spectrometer. CV was carried out in nitrogen-purged dichloromethane (oxidation scan) at room temperature with a CHI voltammetric analyzer. n-Bu_4NPF_6 (0.1 M) was used as the supporting electrolyte. The conventional three-electrode configuration consisted of a platinum working electrode, a platinum wire auxiliary electrode, and a silver wire pseudo reference electrode with ferrocenium-ferrocene (Fc/Fc^+) as the internal standard. Cyclic voltammograms were obtained at a scan rate of 100 mV s^{-1}.

7.4.2 Synthesis of **BocIQA**

To a solution of **IQA** (1.00 g, 0.86 mmol) and DMAP (0.21 g, 1.72 mmol) in 20 mL anhydrous THF at room temperature under N2 protection, di-*tert*-butyl decarbonate (0.47 g, 2.15 mmol) in 10 mL anhydrous THF was added slowly. The reaction was carried out at room temperature for overnight. The yellow solution was then poured into water, extracted with CH2Cl2 (3×15 mL). The organic layer was combined and dried with anhydrous MgSO4. After removing the solvent under reduced pressure, the residue was purified by column chromatography (SiO2, CH2Cl2: hexane (v/v = 1/4)) to obtain a yellow powder. (0.94 g, yield: 92%). 1H NMR (500 MHz, CDCl3, 298 K) δ = 8.81 (s, 2H), 8.70 (s, 2H), 7.84-7.82 (m, 2H), 7.75 (s, 2H), 7.40-7.35 (m, 6H), 2.05-2.01 (m, 8H), 1.78 (s, 18H), 1.23-1.04 (m, 72H), 0.85-0.82 (m, 12H), 0.67 (br, 8H). 13C NMR (125 MHz, CDCl3, 298 K) δ = 178.86, 158.08, 151.86, 150.29, 139.88, 139.69, 137.83, 134.94, 127.92, 127.43, 126.47, 122.99, 122.56, 120.45, 117.59, 117.49, 113.25, 86.33, 77.41, 77.16, 76.91, 55.96, 40.93, 31.98, 30.10, 29.68, 29.63, 29.41, 29.35, 28.00, 27.96, 23.98, 22.76, 14.17.

7.4.3 Synthesis of **P2**

2,7- diamino-9,9- didodecylfluorene (1.17 g, 2.20 mM), DMSS (502 mg, 2.20 mM) and *p*-TsOH·H2O (76 mg, 0.44 mM) were dissolved in 14 mL of dry chloroform in a 100 mL Schlenk tube and degassed with nitrogen. The tube was then sealed and heated to 90 ºC for 72 hr to form a viscous orange mixture. The reaction mixture was then cooled to room temperature. After quenching with 20 mL solution of triethylamine/THF (v/v = 1:10), the solvent was removed under reduced pressure. The resulting orange solid was dissolved in 100 mL THF, and 0.1 mL of TFA was added. The orange solution was stirred in air at 50 ºC for 24 hr so that the color changed to deep-red. After removing the solvent under reduced pressure, the resulting metal-like solid was transferred to a Soxhlet extractor and extracted with acetone for 24 hr to obtain the product as a deep-red solid. (1.37 g, 84%). 1H NMR (500 MHz, CDCl3, 298 K) δ = 8.96 (s, 2H), 8.09 (s, 2H), 7.60-7.59 (m, 2H), 7.19-7.17 (m, 4H), 3.89 (s, 6H), 1.97-1.67 (m, 4H), 1.20-1.11 (m, 36H), 0.84-0.77 (m, 10H). 13C NMR (125 MHz, CDCl3, 298 K) δ = 168.28, 152.16, 140.41, 138.19, 135.84, 119.83, 118.97, 118.58, 118.24, 114.87, 55.22, 52.41, 40.81, 32.04, 30.52, 29.89, 29.76, 29.62, 29.46, 24.14, 22.82, 14.25. SEC analysis: Mn = 24.0 kg/mol, $Đ$ = 2.3.

7.4.4 Synthesis of **P3**

P2 (1.50 g), KOH (2.00 g, 36 mM), THF (40 mL), methanol (20 mL) and H2O (20 mL) were mixed in a 250 mL flask and degassed with N2. The mixture was heated to 80 ºC for 24 hr. After cooling to room temperature, the deep-green solution was transferred to a beaker in an ice-water bath and acidified drop-wise with 2M HCl. The resulting purple solid was collected by filtration, and washed with acetone and chloroform (3×10 mL). The product

was obtained as a deep-violet solid after drying. (1.41 g, 98%.) ^{1}H NMR (500 MHz, *d*8-THF, 298 K) δ = 9.32 (s, 2H), 8.20 (s, 2H), 7.59-7.57 (m, 2H), 7.28 (s, 2H), 7.14-7.13 (m, 2H), 2.00 (br, 4H), 1.22-1.13 (m, 36H), 0.86-0.79 (m, 10H). ^{13}C NMR (125 MHz, *d*8-THF, 298 K) δ = 169.12, 151.68, 140.50, 137.97, 135.60, 119.47, 118.44, 118.32, 118.07, 113.72, 54.94, 40.58, 31.88, 29.63, 29.61, 29.43, 29.31, 22.57, 13.50.

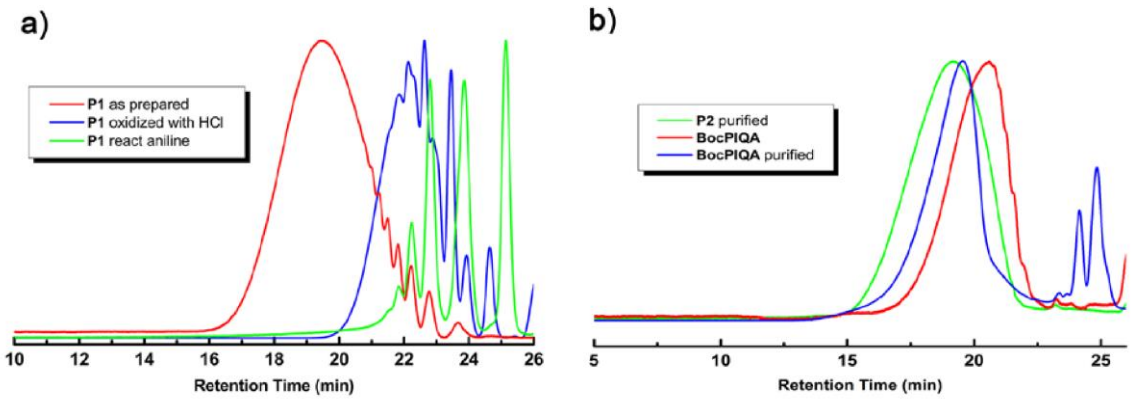

Figure 7.7 SEC curves of a) **P1** prepared under different condition, b) **P2** and **BocPIQA** and purified **BocPIQA**.

	P1 as prepared	**P1** with HCl	**P1** with aniline	**P2** purified	**BocPIQA** as prepared	**BocPIQA** purified
M_n	12.9	*oligomers*	*oligomers*	24.0	14.0	23.7
M_w	32.3	*oligomers*	*oligomers*	55.2	32.2	35.1
Đ	2.5	-	-	2.3	2.3	1.5

Table 7.1 M_n, M_w and ***Đ*** profile of related polymers.

7.4.5 Synthesis of **PIQA**

P3 (1.00 g) was mixed with fresh MSA (20 mL) and degrassed with N2. Then the mixture was heated to 130 ºC for 48 hr. After cooling to rt, the reaction mixture waspoured into ice-water and the solid was collected by filtration. The solid was transferred toSoxhlet extractor and extracted with THF for 24 hr to obtain **PIQA** as a black solid. (0.76 g,80%.) NMR spectra were not obtained due to extreme poor solubility. IR (KBr) ν= 3423, 2913,2852, 1593, 1545, 1447, 1341, 1254, 889 cm-1. Elemental analysis calculated for (C90H116N4O4)n (%): C 82.02, H 8.87, N 4.25; Found: C 81.08, H 7.72, N 4.40.

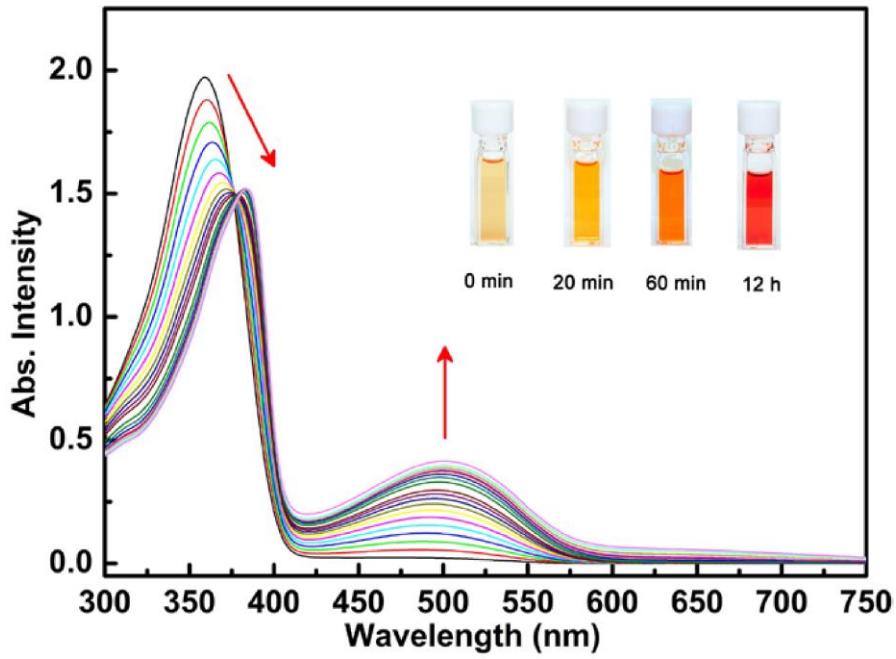

Figure 7.8 Time-dependent UV-vis spectra of **P1** solution in THF oxidized in air, a characteristic peak at ~500 nm corresponding to **P2** was increased by time.

7.4.6 Synthesis of **BocPIQA**

PIQA (0.50 g), Di-*tert*-butyl dicarbonate (1 mL), DMAP (100 mg) were mixed in 20 mL dry THF and stirred at room temperature for 3d. The reaction mixture was then filtered. After removing the solvent of the filtrates under reduced pressure, the resulting solid was washed with acetone and dried under vacuum. Product was obtained as a brown solid. Yield: (0.38 g, 67%). 1H NMR (500 MHz, *d*8-THF, 298 K) δ = 8.89-8.86 (br, 8H), 8.02-7.92 (br, 4H), 2.23-2.13 (br, 8H), 1.77 (s, 36H), 1,17-1.15 (br, 72H), 0.81-0.80 (br, 20H). 13C NMR (125 MHz, CDCl3, 298 K) δ = 178.69, 157.24, 151.78, 140.30, 136.26, 135.12, 126.70, 123.21, 118.49, 117.94, 113.62, 86.52, 82.56, 56.72, 56.05, 41.34, 31.96, 30.06, 29.69, 29.66, 29.63, 29.39, 28.01, 24.12, 22.75, 14.18. SEC analysis: *M*n = 14.0 kg/mol, after purification by prep-SEC, PDI = 2.3, *M*n = 23.7 kg/mol, PDI = 1.5. Elemental analysis calculated for (C110H148N4O12)n (%): C 76.89, H 8.68, N 3.26; Found: C 76.52, H 8.25, N 3.23.

7.4.7 Processing and Characterization

BocPIQA solutions in chlorobenzene (20 mg/mL) were added to a UV-ozonecleaned silicon wafer. **BocPIQA** thin films were formed by spin coating at 600 or 1,000 rpm for 7 s and then 2,000 rpm for 13 s. After casting, the films were thermally annealed at 180°C for 0.5 hr inside a N_2-filled glove box for removal of the Boc groups. The film morphology before and after thermal annealing was examined by optical microscope and AFM. AFM images were recorded with a Bruker Dimension S4 Icon AFM in tapping mode and processed by NanoScope Analysis. GIXD measurements were carried out on Sector 8-ID-E at the Advanced Photon Source of the Argonne National Laboratory. Beamline 8-ID-E

operates at 7.35 keV, and images were collected from a Pilatus 1MF camera (Dectris) with two exposures for different vertical positions of the detector. The GIXSGUI package2 for MATLAB (MathWorks) was used to correct data for X-ray polarization, detector sensitivity, and geometrical solid angle. The beam size was 200 μm (h) × 20 μm (v). The sample detector distance was 204 mm. Sample measurement and thermal annealing were carried out under a vacuum, which was in the range of 2–3 × 10^{-6} bar, and the sample stage was interfaced with a Lakeshore 340 unit. The AC electrical conductivity of a PIQA powder pellet (diameter, 12.7 mm; thickness, 4 mm) was tested with a Novocontrol Broadband Dielectric Spectrometer at room temperature (25°C) over a frequency range of 0.01 Hz to 1 MHz. The direct current (DC) electrical conductivity of the material was estimated as equivalent to the AC electrical conductivity at the lowest frequency of 0.01 Hz.

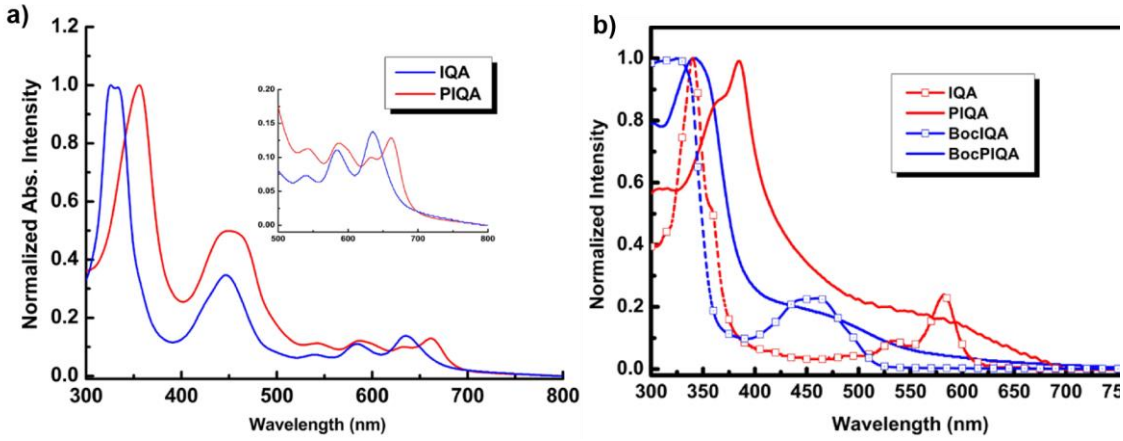

Figure 7.9 a) UV-vis spectra of **IQA** and **PIQA** in MSA, **PIQA** showed characteristic absorption band compared to **IQA**, the bathochromic shift indicated the extended conjugation of **PIQA**. B) UV-vis spectra of **IQA**-based small molecule and polymers in thin film.

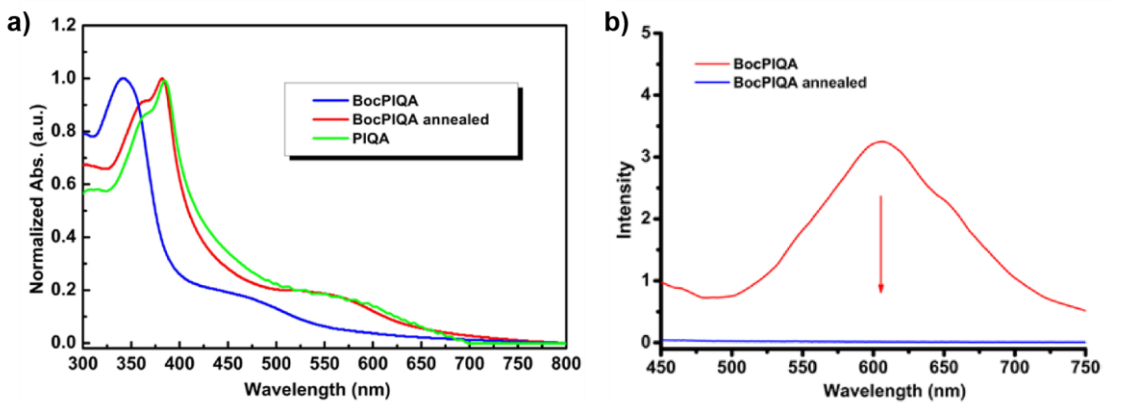

Figure 7.10 a) UV-vis spectra of **BocPIQA** thin film before and after thermal annealing. After annealing at 200 ºC for 30 min, **BocPIQA** showed identical absorption spectrum like **PIQA**, indicating the Boc groups cleavage. b) Fluorescent spectra of **BocPIQA** before and after thermal annealing, fluorescent is quenched after Boc cleavage by thermal annealing.

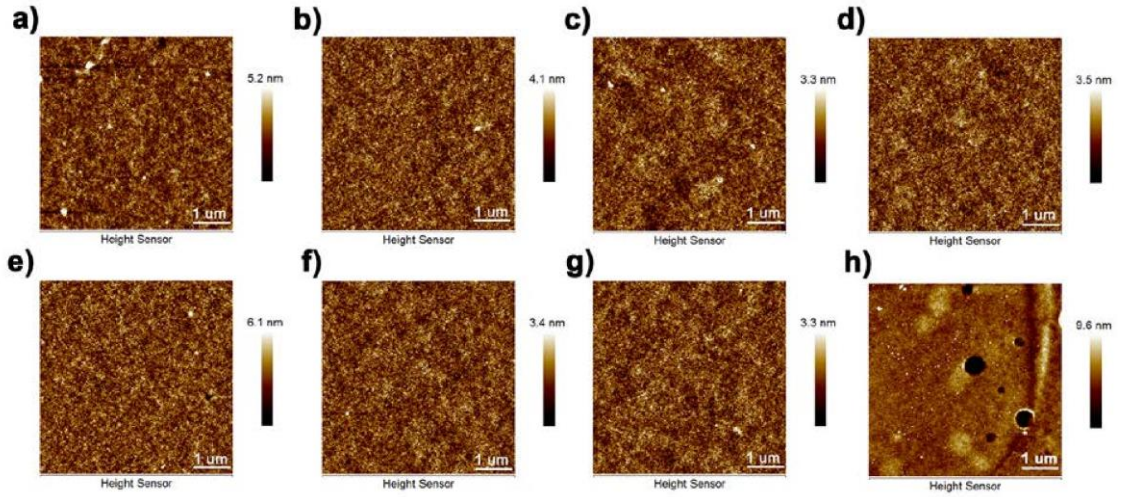

Figure 7.11 AFM images of annealed **BocPIQA** film after boiling solvent soaking, a) THF, b) $CHCl_3$, c) 13 M HCl, d) chlorobenzene, e) DMSO, f) hexane, g) EA, h) H_2SO_4.

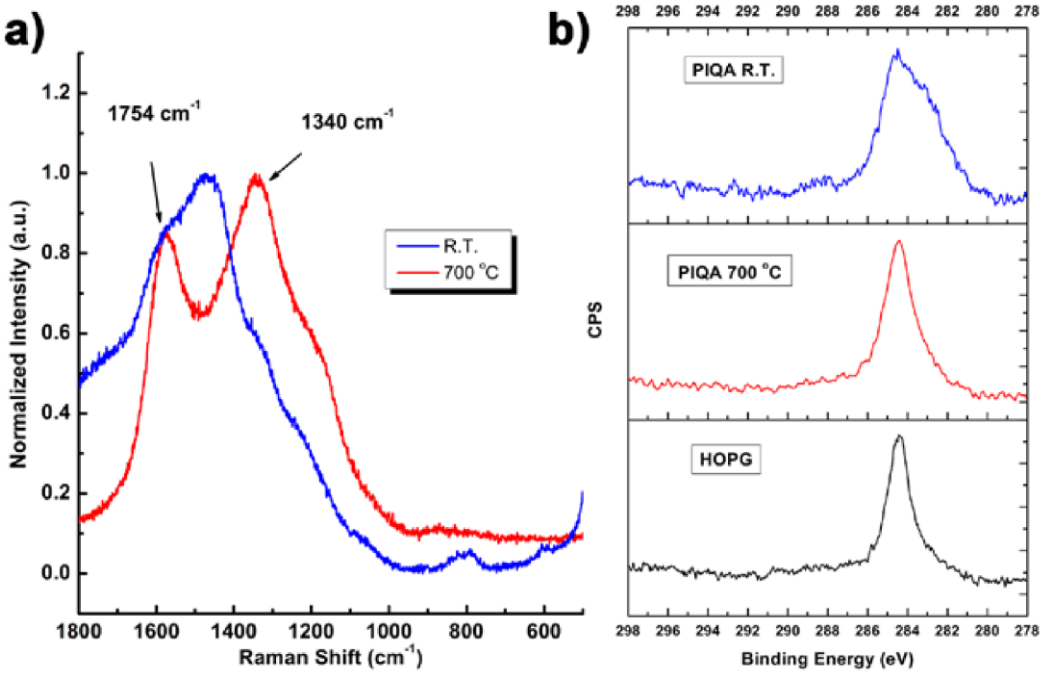

Figure 7.12 a) Raman spectra of as cast **PIQA** and PIQA after annealing at 700 °C. b) XPS spectra of **PIQA** before thermal annealing (top), **PIQA** after 700 °C annealing (middle), and HOPG (bottom).

CHAPTER 8

CONCLUSIONS AND OUTLOOK

8.1 Research Summary

In this dissertation, two types of functional organic materials have been developed by employing a variety of non-covalent interactions. The subtle nature and diversity of non-covalent interactions ensure their prominent role in designing functional materials with a wide range of applications. In the first example, a series of donor-acceptor charge-transfer supramolecular materials exhibiting tunable thermochromism were designed utilizing multiple non-covalent interactions. These supramolecular materials, which composed of an amphiphilic π-electron-deficient bis-bipyridinium acceptor, a π-electron-rich donor, and a negative-charged counterion can be self-assembled in water. The visible band of these materials at lower temperature mainly depends on the $\pi \rightarrow \pi^*$ CT interactions between the donor and acceptor, while the band at higher temperature is affected by the $n \rightarrow \pi$ CT interactions between the counterion and acceptor. More importantly, the thermochromic transition temperature of this series is determined by the CT interaction strength of the donor-acceptor and the counterion-acceptor pair, thus both the colors and thermochromic transition temperatures of these materials can be easily tailored by varying the donors and counterions. In the meantime, we found the self-assembly of donor and acceptor leads to formation of macroscopic helical structures by serendipity. Using a chiral donor, we achieved helicity control over these self-assembled architectures. Moreover, Enantiomerically pure helices composed of achiral molecules were obtained using a donor-exchange approach. The feasibility in forming large-scale enantiomerically pure helices and

chiral memory effects of these supramolecular self-assemblies are of great interest for future applications in chiral separation and catalysis. In the last part of this dissertation, conjugated small molecules and ladder polymers possessing rigid coplanar backbones and self-complementary intermolecular hydrogen bonds have been developed. The intermolecular π─π interactions and hydrogen bonds of the ladder polymer rendered its excellent resistance to organic solvents, aqueous acids, and thermal treatment. This unique property allows for development of robust polymer materials for applications associated with extreme operating or processing conditions.

8.2 Research Outlook

8.2.1 Supramolecular Thermochromic Materials

The United Nations estimates that 30—40% of worldwide energy usage can be directly attributed to buildings, and about 40% of building energy consumptions go towards space cooling in many areas. Current methods to mitigate solar heat gain oftentimes take the form of aesthetically unattractive drapery/coverings and passive coatings, or alternatively, involve prohibitively expensive electrochromic devices. Therefore, smart windows that are cost-effective, easy to fabricate and allow a concurrent control over lighting and solar heat gain are highly desired. The versatility and modularity of supramolecular thermochromic materials developed in this dissertation make them promising candidates for fabricating devices that exhibit a programmable response to changes in ambient temperature in the visible light region. Although they change from colored to less colored state as the temperature is increased, which is opposite to the desired property for the application of smart windows, functional materials that behave in a reverse manner can be designed and

synthesized. Based on the mechanism demonstrated in this dissertation, the color of these supramolecular thermochromic materials at room temperature was governed by the π–π* charge transfer from the donor to the acceptor. To prevent the thermochromic materials from blocking/absorbing light at room temperature, a π-donor with weaker electron-donating ability could be used for smart window glazing. Meanwhile, in order to maintain the complex formation with a weaker donor, coplanar rigid pi system is preferred so that hydrophobic interaction in aqueous media could dominate and bind the donor and acceptor together. A series of donors with planar backbone and large π conjugation system can be designed by installing electron withdrawing groups, such as fluoride, to further weaken the electron-donating ability and achieve thermochromic transition temperatures approaching body temperature or even room temperature.

8.2.2 Supramolecular Assemblies with Controlled Helicity

To better understand the desired molecular features needed for the macroscopic helical assemblies, more donors and acceptors with structural and electronic differences can be designed and synthesized. A series combinations of donors and acceptors can then be investigated on the influence of helical fiber formation and morphology. For example, the nature of the pi-system of the electron-accepting unit plays a crucial role in the self-assembly process, it would be interesting to replace the well-explored bipyridium unit with a diazapyrenium unit and explore its influence on the self-assembly of the helical architectures. Moreover, as the self-assembled helical architectures are intrinsically labile to the change of physical condition and chemical stimuli, it is important to lock the helicity conformation for their practical applications. This goal can be feasibly achieved by cross-

linking the molecular components of these self-assemblies.[329-331] Since the side-chains of the acceptors are functionalized with terminal vinyl groups, radical addition reactions or thiol-ene click reactions can be performed under low reaction temperature and mild reagents to ensure that integrity of the helical structure can be maintained during reaction. Morphology and molecular packing of these cross-linked helices can be characterized by using SEM and small angle X-ray scattering,[151, 332-333] in comparison with the samples before cross-linking. The robustness of these cross-linked architectures can also be tested rigorously under different harsh conditions, such as at high temperatures and soaking in strong solvents.

8.2.3 Synthesis and Processing of Hydrogen-Bonded Ladder Polymers (**PIQA**)

Although the boc-modification method introduced in Chapter 7 can generate **PIQA** ladder polymer thin film through thermal annealing, this method was not successful in preparing free-standing **PIQA** film. In addition, a large portion of **PIQA** polymer was lost during the boc-modification reaction, especially the one with high molecular weight. To solve these problems, an in-situ annulation method is proposed to synthesize and process the **PIQA** film at the same time. In this approach, polymer precursor **P1** will first be dissolved in methanesulfonic acid (MSA). Then the **P1** MSA solution will be added onto a silicon substrate and heated to undergo ring-annulation reaction in order to generate **PIQA** films. By varying the concentration of **P1** solution, PIQA films with different thickness can be prepared and free standing films of **PIQA** can also be obtained. These **PIQA** films will be characterized with fourier-transform infrared spectroscopy to confirm their structure. Such free standing thin films will allow further mechanical assessment of these hydrogen-bonded ladder polymers.

REFERENCES

1. Pollino, J. M.; Weck, M., Non-covalent side-chain polymers: design principles, functionalization strategies, and perspectives. *Chemical Society Reviews* **2005**, 34, 193-207.

2. Cerny, J.; Hobza, P., Non-covalent interactions in biomacromolecules. *Physical Chemistry Chemical Physics* **2007**, 9, 5291-5303.

3. Rest, C.; Kandanelli, R.; Fernandez, G., Strategies to create hierarchical self-assembled structures via cooperative non-covalent interactions. *Chemical Society Reviews* **2015**, 44, 2543-2572.

4. Autumn, K.; Liang, Y. A.; Hsieh, S. T.; Zesch, W.; Chan, W. P.; Kenny, T. W.; Fearing, R.; Full, R. J., Adhesive force of a single gecko foot-hair. *Nature* **2000**, 405, 681-685.

5. Autumn, K.; Sitti, M.; Liang, Y. A.; Peattie, A. M.; Hansen, W. R.; Sponberg, S.; Kenny, T. W.; Fearing, R.; Israelachvili, J. N.; Full, R. J., Evidence for van der Waals adhesion in gecko setae. *Proceedings of the National Academy of Sciences* **2002**, 99, 12252-12256.

6. Afshari, M.; Sikkema, D. J.; Lee, K.; Bogle, M., High Performance Fibers Based on Rigid and Flexible Polymers. *Polymer Reviews* **2008**, 48, 230-274.

7. Wojtecki, R. J.; Meador, M. A.; Rowan, S. J., Using the dynamic bond to access macroscopically responsive structurally dynamic polymers. *Nature Materials* **2010**, 10, 14-27.

8. Rybtchinski, B., Adaptive Supramolecular Nanomaterials Based on Strong Noncovalent Interactions. *ACS Nano* **2011**, 5, 6791-6818.

9. Carlisle, J. R.; Weck, M., Functional Materials via Multiple Noncovalent Interactions. In *Functional Organic Materials*, Wiley-VCH Verlag GmbH & Co. KGaA: 2007; pp 261-292.

10. Hannon, M. J., Supramolecular DNA recognition. *Chemical Society Reviews* **2007**, 36, 280-295.

11. Voskuhl, J.; Ravoo, B. J., Molecular recognition of bilayer vesicles. *Chemical Society Reviews* **2009**, 38, 495-505.

12. Appel, E. A.; del Barrio, J.; Loh, X. J.; Scherman, O. A., Supramolecular polymeric hydrogels. *Chemical Society Reviews* **2012**, 41, 6195-6214.

13. Chandler, D., Interfaces and the driving force of hydrophobic assembly. *Nature* **2005**, 437, 640-647.

14. Bellissent-Funel, M.-C.; Hassanali, A.; Havenith, M.; Henchman, R.; Pohl, P.; Sterpone, F.; van der Spoel, D.; Xu, Y.; Garcia, A. E., Water Determines the Structure and Dynamics of Proteins. *Chemical Reviews* **2016**, 116, 7673-7697.

15. Ball, P., Water as an Active Constituent in Cell Biology. *Chemical Reviews* **2008**, 108, 74-108.

16. Hunter, C. A.; Sanders, J. K. M., The nature of .pi.-.pi. interactions. *Journal of the American Chemical Society* **1990**, 112, 5525-5534.

17. Ding, X.; Wang, Y., Weak bond-based injectable and stimuli responsive hydrogels for biomedical applications. *Journal of Materials Chemistry B* **2017**, 5, 887-906.

18. Burley, S.; Petsko, G., Aromatic-aromatic interaction: a mechanism of protein structure stabilization. *Science* **1985**, 229, 23-28.

19. Philp, D.; Stoddart, J. F., Self-Assembly in Natural and Unnatural Systems. *Angewandte Chemie International Edition in English* **1996**, 35, 1154-1196.

20. Hoeben, F. J. M.; Jonkheijm, P.; Meijer, E. W.; Schenning, A. P. H. J., About Supramolecular Assemblies of π-Conjugated Systems. *Chemical Reviews* **2005**, 105, 1491-1546.

21. Yan, X.; Wang, F.; Zheng, B.; Huang, F., Stimuli-responsive supramolecular polymeric materials. *Chemical Society Reviews* **2012**, 41, 6042-6065.

22. Jagur-Grodzinski, J., Polymeric gels and hydrogels for biomedical and pharmaceutical applications. *Polymers for Advanced Technologies* **2010**, 21, 27-47.

23. Jeong, B.; Kim, S. W.; Bae, Y. H., Thermosensitive sol–gel reversible hydrogels. *Advanced Drug Delivery Reviews* **2012**, 64, 154-162.

24. Mano, J. F., Stimuli-Responsive Polymeric Systems for Biomedical Applications. *Advanced Engineering Materials* **2008**, 10, 515-527.

25. Beer, P. D.; Gale, P. A., Anion Recognition and Sensing: The State of the Art and Future Perspectives. *Angewandte Chemie International Edition* **2001**, 40, 486-516.

26. Dinolfo, P. H.; Hupp, J. T., Supramolecular Coordination Chemistry and Functional Microporous Molecular Materials. *Chemistry of Materials* **2001**, 13, 3113-3125.

27. Raghupathi, K. R.; Guo, J.; Munkhbat, O.; Rangadurai, P.; Thayumanavan, S., Supramolecular Disassembly of Facially Amphiphilic Dendrimer Assemblies in Response to Physical, Chemical, and Biological Stimuli. *Accounts of Chemical Research* **2014**, 47, 2200-2211.

28. Day, J. H., Thermochromism. *Chemical Reviews* **1963**, 63, 65-80.

29. Seeboth, A.; Lötzsch, D.; Ruhmann, R.; Muehling, O., Thermochromic Polymers—Function by Design. *Chemical Reviews* **2014**, 114, 3037-3068.

30. Day, J. H., Thermochromism of inorganic compounds. *Chemical Reviews* **1968**, 68, 649-657.

31. Bloomquist, D. R.; Willett, R. D., Thermochromic phase transitions in transition metal salts. *Coordination Chemistry Reviews* **1982**, 47, 125-164.

32. Sone, K. F., Y., Inorganic Thermochromism. *Springer: Berlin* **1987**.

33. White, M. A.; LeBlanc, M., Thermochromism in Commercial Products. *Journal of Chemical Education* **1999**, 76, 1201.

34. Muthyala, R., Chemistry and Applications of Leuco Dyes. *Kluwer Academic Publishers* **2002**.

35. Tamaoki, N., Cholesteric Liquid Crystals for Color Information Technology. *Advanced Materials* **2001**, 13, 1135-1147.

36. Jelinek, R.; Ritenberg, M., Polydiacetylenes - recent molecular advances and applications. *RSC Advances* **2013**, 3, 21192-21201.

37. Chen, X.; Kang, S.; Kim, M. J.; Kim, J.; Kim, Y. S.; Kim, H.; Chi, B.; Kim, S. J.; Lee, J. Y.; Yoon, J., Thin-Film Formation of Imidazolium-Based Conjugated Polydiacetylenes and Their Application for Sensing Anionic Surfactants. *Angewandte Chemie International Edition* **2010**, 49, 1422-1425.

38. Wu, A.; Beck, C.; Ying, Y.; Federici, J.; Iqbal, Z., Thermochromism in Polydiacetylene–ZnO Nanocomposites. *The Journal of Physical Chemistry C* **2013**, 117, 19593-19600.

39. Guo, H.; Zhang, J.; Porter, D.; Peng, H.; Lowik, D. W. P. M.; Wang, Y.; Zhang, Z.; Chen, X.; Shao, Z., Ultrafast and reversible thermochromism of a conjugated polymer material based on the assembly of peptide amphiphiles. *Chemical Science* **2014**, 5, 4189-4195.

40. E. Arunan, G. R. D., R. A. Klein, J. Sadlej, S. Scheiner, I. Alkorta, D. C. Clary, R. H. Crabtree, J. J. Dannenberg, P. Hobza, H. G. Kjaergaard, A. C. Legon, B. Mennucci, D. J. Nesbitt., Definition of the hydrogen bond. *Pure and Applied Chemistry* **2011**, 83, 1637-1641.

41. Watson, J. D.; Crick, F. H. C., Molecular Structure of Nucleic Acids: A Structure for Deoxyribose Nucleic Acid. *Nature* **1953**, 171, 737-738.

42. Fonseca Guerra, C.; Bickelhaupt, F. M.; Snijders, J. G.; Baerends, E. J., Hydrogen Bonding in DNA Base Pairs: Reconciliation of Theory and Experiment. *Journal of the American Chemical Society* **2000**, 122, 4117-4128.

43. Keten, S.; Xu, Z.; Ihle, B.; Buehler, M. J., Nanoconfinement controls stiffness, strength and mechanical toughness of β-sheet crystals in silk. *Nature Materials* **2010**, 9, 359-367.

44. Zhang, L.; Chen, T.; Ban, H.; Liu, L., Hydrogen bonding-assisted thermal conduction in β-sheet crystals of spider silk protein. *Nanoscale* **2014**, 6, 7786-7791.

45. Brunsveld, L.; Folmer, B. J. B.; Meijer, E. W.; Sijbesma, R. P., Supramolecular Polymers. *Chemical Reviews* **2001**, 101, 4071-4098.

46. de Greef, T. F. A.; Meijer, E. W., Supramolecular polymers. *Nature* **2008**, 453, 171-173.

47. Sijbesma, R. P.; Beijer, F. H.; Brunsveld, L.; Folmer, B. J. B.; Hirschberg, J. H. K. K.; Lange, R. F. M.; Lowe, J. K. L.; Meijer, E. W., Reversible Polymers Formed from Self-Complementary Monomers Using Quadruple Hydrogen Bonding. *Science* **1997**, 278, 1601-1604.

48. Bosman, A. W.; Sijbesma, R. P.; Meijer, E. W., Supramolecular Polymers at Work. *Materials Today* **2004**, 7, 34-39.

49. Cordier, P.; Tournilhac, F.; Soulié-Ziakovic, C.; Leibler, L., Self-Healing and Thermoreversible Rubber from Supramolecular Assembly. *Nature* **2008**, 451, 977-980.

50. Tee, B. C. K.; Wang, C.; Allen, R.; Bao, Z., An Electrically and Mechanically Self-Healing Composite with Pressure- and Flexion-Sensitive Properties for Electronic Skin Applications. *Nature Nanotechnology* **2012**, 7, 825-832.

51. Seeboth, A.; Ruhmann, R.; Mühling, O., Thermotropic and Thermochromic Polymer Based Materials for Adaptive Solar Control. *Materials* **2010**, 3, 5143-5168.

52. Luo, X.; Li, J; Li, C.; Heng, L.; Dong, Y.; Liu, Z.; Bo, Z.; Tang, B., Reversible Switching of the Emission of Diphenyldibenzofulvenes by Mechanical Stimuli. *Advanced Materials* **2011**, 23, 3261-3265.

53. Zhang, X.; Wang, C., Supramolecular amphiphiles. *Chemical Society Reviews* **2011**, 40, 94-101.

54. Wang, C.; Wang, Z.; Zhang, X., Amphiphilic Building Blocks for Self-Assembly: From Amphiphiles to Supra-amphiphiles. *Accounts of Chemical Research* **2012**, 45, 608-618.

55. Yu, G.; Jie, K.; Huang, F., Supramolecular Amphiphiles Based on Host–Guest Molecular Recognition Motifs. *Chemical Reviews* **2015**, 115, 7240-7303.

56. Jin, J. Y.; K., B. P.; SooWhan, C.; Wook, L. J.; Kimoon, K., Supramolecular Amphiphiles: Spontaneous Formation of Vesicles Triggered by Formation of a Charge-Transfer Complex in a Host. *Angewandte Chemie International Edition* **2002**, 41, 4474-4476.

57. Yapei, W.; Huaping, X.; Xi, Z., Tuning the Amphiphilicity of Building Blocks: Controlled Self-Assembly and Disassembly for Functional Supramolecular Materials. *Advanced Materials* **2009**, 21, 2849-2864.

58. Kang, Y.; Liu, K.; Zhang, X., Supra-Amphiphiles: A New Bridge Between Colloidal Science and Supramolecular Chemistry. *Langmuir* **2014**, 30, 5989-6001.

59. Chen, Y.; Pang, X. H.; Dong, C. M., Dual Stimuli-Responsive Supramolecular Polypeptide-Based Hydrogel and Reverse Micellar Hydrogel Mediated by Host-Guest Chemistry. *Advanced Functional Materials* **2010**, 20, 579-586.

60. Dai, X. Y.; Zhang, Y. Y.; Gao, L. N.; Bai, T.; Wang, W.; Cui, Y. L.; Liu, W. G., A Mechanically Strong, Highly Stable, Thermoplastic, and Self-Healable Supramolecular Polymer Hydrogel. *Advanced Materials* **2015**, 27, 3566-3571.

61. Hsu, L.; Cvetanovich, G. L.; Stupp, S. I., Peptide Amphiphile Nanofibers with Conjugated Polydiacetylene Backbones in Their Core. *Journal of the American Chemical Society* **2008**, 130, 3892-3899.

62. He, Q.; Ao, Y.-F.; Huang, Z.-T.; Wang, D.-X., Self-Assembly and Disassembly of Vesicles as Controlled by Anion–π Interactions. *Angewandte Chemie International Edition* **2015**, 54, 11785-11790.

63. Zhang, Z.; Ding, J.; Chen, X.; Xiao, C.; He, C.; Zhuang, X.; Chen, L.; Chen, X., Intracellular pH-sensitive Supramolecular Amphiphiles based on Host-Guest Recognition between Benzimidazole and β-Cyclodextrin as Potential Drug Delivery Vehicles. *Polymer Chemistry* **2013**, 4, 3265-3271.

64. Yu, G.; Xue, M.; Zhang, Z.; Li, J.; Han, C.; Huang, F., A Water-Soluble Pillar[6]arene: Synthesis, Host–Guest Chemistry, and Its Application in Dispersion of Multiwalled Carbon Nanotubes in Water. *Journal of the American Chemical Society* **2012**, 134, 13248-13251.

65. Kai, L.; Yiliu, L.; Yuxing, Y.; Huanxiang, Y.; Shu, W.; Zhiqiang, W.; Xi, Z., Supramolecular Photosensitizers with Enhanced Antibacterial Efficiency. *Angewandte Chemie International Edition* **2013**, 52, 8285-8289.

66. Yan, Q.; Xin, Y.; Zhou, R.; Yin, Y.; Yuan, J., Light-controlled Smart Nanotubes based on the Orthogonal Assembly of Two Homopolymers. *Chemical Communications* **2011**, 47, 9594-9596.

67. Kim, D.; Lee, E. C.; Kim, K. S.; Tarakeshwar, P., Cation−π−Anion Interaction: A Theoretical Investigation of the Role of Induction Energies. *The Journal of Physical Chemistry A* **2007**, 111, 7980-7986.

68. Yan, Q.; Yuan, J.; Cai, Z.; Xin, Y.; Kang, Y.; Yin, Y., Voltage-Responsive Vesicles Based on Orthogonal Assembly of Two Homopolymers. *Journal of the American Chemical Society* **2010**, 132, 9268-9270.

69. Fahrenbach, A. C.; Barnes, J. C.; Lanfranchi, D. A.; Li, H.; Coskun, A.; Gassensmith, J. J.; Liu, Z.; Benítez, D.; Trabolsi, A.; Goddard, W. A.; Elhabiri, M.; Stoddart, J. F., Solution-Phase Mechanistic Study and Solid-State Structure of a Tris(bipyridinium radical cation) Inclusion Complex. *Journal of the American Chemical Society* **2012**, 134, 3061-3072.

70. Kelley, E. G.; Albert, J. N. L.; Sullivan, M. O.; Epps, I. I. I. T. H., Stimuli-Responsive Copolymer Solution and Surface Assemblies for Biomedical Applications. *Chemical Society Reviews* **2013**, 42, 7057-7071.

71. Chao, W.; Qishui, C.; Zhiqiang, W.; Xi, Z., An Enzyme-Responsive Polymeric Superamphiphile. *Angewandte Chemie International Edition* **2010**, 49, 8612-8615.

72. Guo, D.-S.; Wang, K.; Wang, Y.-X.; Liu, Y., Cholinesterase-Responsive Supramolecular Vesicle. *Journal of the American Chemical Society* **2012**, 134, 10244-10250.

73. Ming, W.; Kyle, A.; Shuo, S.; Luis, A. C.; Qiaobing, X., Combinatorially Designed Lipid-like Nanoparticles for Intracellular Delivery of Cytotoxic Protein for Cancer Therapy. *Angewandte Chemie International Edition* **2014**, 53, 2893-2898.

74. De Greef, T. F. A.; Smulders, M. M. J.; Wolffs, M.; Schenning, A. P. H. J.; Sijbesma, R. P.; Meijer, E. W., Supramolecular Polymerization. *Chemical Reviews* **2009**, 109, 5687-5754.

75. Raymo, F. M.; Bartberger, M. D.; Houk, K. N.; Stoddart, J. F., The Magnitude of [C−H···O] Hydrogen Bonding in Molecular and Supramolecular Assemblies. *Journal of the American Chemical Society* **2001**, 123, 9264-9267.

76. Chen, Y.; Kushner, A. M.; Williams, G. A.; Guan, Z., Multiphase Design of Autonomic Self-Healing Thermoplastic Elastomers. *Nature Chemistry* **2012**, 4, 467-472.

77. Prins, L. J.; Reinhoudt, D. N.; Timmerman, P., Noncovalent Synthesis Using Hydrogen Bonding. *Angewandte Chemie International Edition* **2001**, 40, 2382-2426.

78. Mes, T., Smulders M. J. M., Palmans, A. R. A., Meijer, E. W., Hydrogen-Bond Engineering in Supramolecular Polymers: Polarity Influence on the Self-Assembly of Benzene-1,3,5-tricarboxamides. *Macromolecules*, **2010**, 43, 1981-1991.

79. Peng, S.; Wang, K.; Guo, D.-S.; Liu, Y., Supramolecular Polymeric Vesicles Formed by p-sulfonatocalix[4]arene and Chitosan with Multistimuli Responses. *Soft Matter* **2015**, 11, 290-296.

80. Tayi, A. S.; Shveyd, A. K.; Sue, A. C. H.; Szarko, J. M.; Rolczynski, B. S.; Cao, D.; Kennedy, T. J.; Sarjeant, A. A.; Stern, C. L.; Paxton, W. F.; Wu, W.; Dey, S. K.; Fahrenbach, A. C.; Guest, J. R.; Mohseni, H.; Chen, L. X.; Wang, K. L.; Stoddart, J. F.; Stupp, S. I., Room-Temperature Ferroelectricity in Supramolecular Networks of Charge-Transfer Complexes. *Nature* **2012**, 488, 485-489.

81. Olson, M. A.; Coskun, A.; Fang, L.; Basuray, A. N.; Stoddart, J. F., Polycatenation under Thermodynamic Control. *Angewandte Chemie International Edition* **2010**, 49, 3151-3156.

82. Das, A.; Ghosh, S., Supramolecular Assemblies by Charge-Transfer Interactions between Donor and Acceptor Chromophores. *Angewandte Chemie International Edition* **2014**, 53, 2038-2054.

83. Chao, W.; Yinsheng, G.; Yapei, W.; Huaping, X.; Ruji, W.; Xi, Z., Supramolecular Amphiphiles Based on a Water-Soluble Charge-Transfer Complex: Fabrication of Ultralong Nanofibers with Tunable Straightness. *Angewandte Chemie International Edition* **2009**, 48, 8962-8965.

84. Mohan, N. S. K.; Cristina, B.; Nadeem, J.; M., F. P. W. J.; V., U. R., Biocatalytic Self-Assembly of Supramolecular Charge-Transfer Nanostructures Based on n-Type Semiconductor-Appended Peptides. *Angewandte Chemie International Edition* **2014**, 53, 5882-5887.

85. Aida, T.; Meijer, E. W.; Stupp, S. I., Functional Supramolecular Polymers. *Science* **2012**, 335, 813-817.

86. Appel, E. A.; Biedermann, F.; Rauwald, U.; Jones, S. T.; Zayed, J. M.; Scherman, O. A., Supramolecular Cross-Linked Networks via Host−Guest Complexation with Cucurbit[8]uril. *Journal of the American Chemical Society* **2010**, 132, 14251-14260.

87. Nakahara, A.; Wang, J. H., Charge-Transfer Complexes of Methyl Viologen. *The Journal of Physical Chemistry* **1963**, 67, 496-498.

88. Haque, R.; Lilley, S., Infrared Spectroscopic Studies of Charge Transfer Complexes of Diquat and Paraquat. *Journal of Agricultural and Food Chemistry* **1972**, 20, 57-58.

89. Russell, J. H.; Wallwork, S. C., The Crystal Structures of the Dichloride and Isomorphous Dibromide and Diiodide of the N,N'-Dimethyl-4,4'-Bipyridylium Ion. *Acta Crystallographica Section B* **1972**, 28, 1527-1533.

90. Monk, P. M. S.; Hodgkinson, N. M.; Partridge, R. D., The Colours of Charge-Transfer Complexes of Methyl Viologen: Effects of Donor, Ionic Strength and Solvent. *Dyes and Pigments* **1999**, 43, 241-251.

91. Moore, J. S.; Stupp, S. I., Charge-Transfer and Thermochromic Phenomena in Solid Polyelectrolytes. *Macromolecules* **1986**, 19, 1815-1824.

92. Olson, M. A.; Thompson, J. R.; Dawson, T. J.; Hernandez, C. M.; Messina, M. S.; O'Neal, T., Template-Directed Self-Assembly by Way of Molecular Recognition at the Micellar-Solvent Interface: Modulation of the Critical Micelle Concentration. *Organic & Biomolecular Chemistry* **2013**, 11, 6483-6492.

93. Olson, M. A.; Messina, M. S.; Thompson, J. R.; Dawson, T. J.; Goldner, A. N.; Gaspar, D. K.; Vazquez, M.; Lehrman, J. A.; Sue, A. C. H., Reversible Morphological Changes of Assembled Supramolecular Amphiphiles Triggered by pH-Modulated Host-Guest Interactions. *Organic & Biomolecular Chemistry* **2016**. 14, 5714-5720.

94. Zhang, X.; Chen, L.; Yuan, T.; Huang, H.; Sui, Z.; Du, R.; Li, X.; Lu, Y.; Li, Q., Dendrimer-linked, Renewable and Magnetic Carbon Nanotube Aerogels. *Materials Horizons* **2014**, 1, 232-236.

95. Wang , D.; Huang , Y.; Li, J.; Xu, L.; Chen, M.; Tao, J.; Li, L., Lyotropic Supramolecular Helical Columnar Phases Formed by C3-Symmetric and Unsymmetric Rigid Molecules. *Chemistry – A European Journal* **2013**, 19, 685-690.

96. Tschierske, C.; Ungar, G., Mirror Symmetry Breaking by Chirality Synchronisation in Liquids and Liquid Crystals of Achiral Molecules. *ChemPhysChem* **2016**, 17, 9-26.

97. Yoon, E.; Gong, J.; Jung, Y.; Lee, W.; Driver, R. W.; Lee, H.-S., Unambiguous Characterization of Anisotropic Foldamer Packing in a Foldecture with an Elongated Hexagonal Plate Shape. *Chemical Communications* **2016**, 52, 5250-5253.

98. Shen, Z.; Wang, T.; Liu, M., Macroscopic Chirality of Supramolecular Gels Formed from Achiral Tris(ethyl cinnamate) Benzene-1,3,5-tricarboxamides. *Angewandte Chemie International Edition* **2014**, 53, 13424-13428.

99. Stals, P. M. J.; Korevaar, P. A.; Gillissen, M. A. J.; de Greef, T. F. A.; Fitie, C. F. C.; Sijbesma, R. P.; Palmans, A. R. A.; Meijer, E. W., Symmetry Breaking in the Self-Assembly of Partially Fluorinated Benzene-1,3,5-tricarboxamides. *Angewandte Chemie International Edition* **2012**, 51, 11297-11301.

100. Lee, C. C.; Grenier, C.; Meijer, E. W.; Schenning, A. P. H. J., Preparation and characterization of helical self-assembled nanofibers. *Chemical Society Reviews* **2009**, 38, 671-683.

101. Shen, Z.; Jiang, Y.; Wang, T.; Liu, M., Symmetry Breaking in the Supramolecular Gels of an Achiral Gelator Exclusively Driven by π–π Stacking. *Journal of the American Chemical Society* **2015**, 137, 16109-16115.

102. Wang, C.; Olson, M. A.; Fang, L.; Benítez, D.; Tkatchouk, E.; Basu, S.; Basuray, A. N.; Zhang, D.; Zhu, D.; Goddard, W. A.; Stoddart, J. F., Isolation by Crystallization of Translational Isomers of a Bistable Donor-Acceptor [2]Catenane. *Proceedings of the National Academy of Sciences* **2010**, 107, 13991-13996.

103. Asakawa, M.; Dehaen, W.; L'Abbé, G.; Menzer, S.; Nouwen, J.; Raymo, F. M.; Stoddart, J. F.; Williams, D. J., Improved Template-Directed Synthesis of Cyclobis(paraquat-p-phenylene). *The Journal of Organic Chemistry* **1996**, 61, 9591-9595.

104. Ashton, P. R.; Boyd, S. E.; Menzer, S.; Pasini, D.; Raymo, F. M.; Spencer, N.; Stoddart, J. F.; White, A. J.; Williams, D. J.; Wyatt, P. G., Self-Assembling Cyclophanes and Catenanes Possessing Elements of Planar Chirality. *Chemistry – A European Journal* **1998**, 4, 299-310.

105. Tseng, H.-R.; Vignon, S. A.; Celestre, P. C.; Stoddart, J. F.; White, A. J. P.; Williams, D. J., Dynamic Chirality: Keen Selection in the Face of Stereochemical Diversity in Mechanically Bonded Compounds. *Chemistry – A European Journal* **2003**, 9, 543-556.

106. Liu, Y.; Vignon, S. A.; Zhang, X.; Bonvallet, P. A.; Khan, S. I.; Houk, K. N.; Stoddart, J. F., Dynamic Chirality in Donor−Acceptor Pretzelanes. *The Journal of Organic Chemistry* **2005**, 70, 9334-9344.

107. Vignon, S. A.; Wong, J.; Tseng, H.-R.; Stoddart, J. F., Helical Chirality in Donor-Acceptor Catenanes. *Org. Lett.* **2004**, 6, 1095-1098.

108. Nagase, K.; Yokobayashi, H.; Sone, K., Spectrophotometric and Thermal Analytical Studies on the Dehydration of Copper(II) Sulfate and Its Double Salts. *Thermochimica Acta* **1978**, 23, 283-291.

109. Mahmoud, M. M.; Wallwork, S. C., The Crystal Structure of the 1:1 Complex between N,N'-dimethyl-4,4'-bipyridylium Diiodide and Quinol. *Acta Crystallographica Section B* **1976**, 32, 440-443.

110. Norrby, P.-O.; Liljefors, T., Strong Decrease of the Benzene−Ammonium Ion Interaction upon Complexation with a Carboxylate Anion. *Journal of the American Chemical Society* **1999**, 121, 2303-2306.

111. Sue, C.-H.; Basu, S.; Fahrenbach, A. C.; Shveyd, A. K.; Dey, S. K.; Botros, Y. Y.; Stoddart, J. F., Enabling Tetracationic Cyclophane Production by Trading Templates. *Chemical Science* **2010**, 1, 119-125.

112. Yoon, K. B.; Huh, T. J.; Kochi, J. K., Shape-Selective Assemblies of Charge-Transfer Complexes as Molecular Probes for Water Adsorption in Zeolites. *The Journal of Physical Chemistry* **1995**, 99, 7042-7053.

113. Boekhoven, J.; Stupp, S. I., 25th Anniversary Article: Supramolecular Materials for Regenerative Medicine. *Advanced Materials* **2014**, 26, 1642-1659.

114. Olson, M. A.; Coskun, A.; Klajn, R.; Fang, L.; Dey, S. K.; Browne, K. P.; Grzybowski, B. A.; Stoddart, J. F., Assembly of Polygonal Nanoparticle Clusters Directed by Reversible Noncovalent Bonding Interactions. *Nano Letter* **2009**, 9, 3185-3190.

115. Pandeeswar, M.; Senanayak, S. P.; Narayan, K. S.; Govindaraju, T., Multi-Stimuli-Responsive Charge-Transfer Hydrogel for Room-Temperature Organic Ferroelectric Thin-Film Devices. *Journal of the American Chemical Society* **2016**, 138, 8259-8268.

116. Angelos, S.; Khashab, N. M.; Yang, Y.-W.; Trabolsi, A.; Khatib, H. A.; Stoddart, J. F.; Zink, J. I., pH Clock-Operated Mechanized Nanoparticles. *Journal of the American Chemical Society* **2009**, 131, 12912-12914.

117. Shi, B.; Jie, K.; Zhou, Y.; Zhou, J.; Xia, D.; Huang, F., Nanoparticles with Near-Infrared Emission Enhanced by Pillararene-Based Molecular Recognition in Water. *Journal of the American Chemical Society* **2016**, 138, 80-83.

118. Urdampilleta, M.; Klyatskaya, S.; Cleuziou, J. P.; Ruben, M.; Wernsdorfer, W., Supramolecular Spin Valves. *Nature Materials* **2011**, 10, 502-506.

119. García-Iglesias, M.; de Waal, B. F. M.; Gorbunov, A. V.; Palmans, A. R. A.; Kemerink, M.; Meijer, E. W., A Versatile Method for the Preparation of Ferroelectric

Supramolecular Materials via Radical End-Functionalization of Vinylidene Fluoride Oligomers. *Journal of the American Chemical Society* **2016**, 138, 6217-6223.

120. Khutoryanskiy, V. V., Supramolecular materials: Longer and Safer Gastric Residence. *Nature Materials* **2015**, 14, 963-964.

121. Webber, M. J.; Appel, E. A.; Meijer, E. W.; Langer, R., Supramolecular Biomaterials. *Nature Materials* **2016**, 15, 13-26.

122. Zheng, Y.; Wyman, I., Supramolecular Nanostructures Based on Cyclodextrin and Poly(ethylene oxide): Syntheses, Structural Characterizations and Applications for Drug Delivery. *Polymers* **2016**, 8, 198.

123. Gassensmith, J. J.; Kim, J. Y.; Holcroft, J. M.; Farha, O. K.; Stoddart, J. F.; Hupp, J. T.; Jeong, N. C., A Metal–Organic Framework-Based Material for Electrochemical Sensing of Carbon Dioxide. *Journal of the American Chemical Society* **2014**, 136, 8277-8282.

124. Wang, H.; Ji, X.; Li, Z.; Huang, F., Fluorescent Supramolecular Polymeric Materials. *Advanced Materials.* **2017**, 29, 1606117.

125. Faul, C. F. J., Ionic Self-Assembly for Functional Hierarchical Nanostructured Materials. *Accounts of Chemical Research* **2014**, 47, 3428-3438.

126. Adler-Abramovich, L.; Gazit, E., The Physical Properties of Supramolecular Peptide Assemblies: from Building Block Association to Technological Applications. *Chemical Society Reviews* **2014**, 43, 6881-6893.

127. Shi, Y.; Yu, G., Designing Hierarchically Nanostructured Conductive Polymer Gels for Electrochemical Energy Storage and Conversion. *Chemistry of Materials* **2016**, 28, 2466-2477.

128. Stupp, S. I.; LeBonheur, V.; Walker, K.; Li, L. S.; Huggins, K. E.; Keser, M.; Amstutz, A., Supramolecular Materials: Self-Organized Nanostructures. *Science* **1997**, 276, 384-389.

129. Jain, A.; George, S. J., New Directions in Supramolecular Electronics. *Materials Today* **2015**, 18, 206-214.

130. Zhang, L.; Zhong, X.; Pavlica, E.; Li, S.; Klekachev, A.; Bratina, G.; Ebbesen, T. W.; Orgiu, E.; Samorì, P., A Nanomesh Scaffold for Supramolecular Nanowire Optoelectronic Devices. *Nature Nanotechnology* **2016**, 11, 900-906.

131. Kamalisarvestani, M.; Saidur, R.; Mekhilef, S.; Javadi, F. S., Performance, Materials and Coating Technologies of Thermochromic Thin Films on Smart Windows. *Renewenable and Sustainable Energy Reviews* **2013**, 26, 353-364.

132. Gorgolis, G.; Karamanis, D., Solar Energy Materials for Glazing Technologies. *Solar Energy Materials and Solar Cells* **2016**, 144, 559-578.

133. De Bastiani, M.; Saidaminov, M. I.; Dursun, I.; Sinatra, L.; Peng, W.; Buttner, U.; Mohammed, O. F.; Bakr, O. M., Thermochromic Perovskite Inks for Reversible Smart Window Applications. *Chemistry of Materials* **2017**, 29, 3367-3370.

134. Shirasaki, Y.; Okamoto, Y.; Muranaka, A.; Kamino, S.; Sawada, D.; Hashizume, D.; Uchiyama, M., Fused-Fluoran Leuco Dyes with Large Color-Change Derived from Two-Step Equilibrium: iso-Aminobenzopyranoxanthenes. *Journal of Organic Chemistry* **2016**, 81, 12046-12051.

135. Ogasawara, K.; Nakamura, K.; Kobayashi, N., Thermally Controlled Dual-Mode Display Media with Red-Green-Blue Coloration and Fluorescence via Energy Transfer between Emission Materials and Leuco Dyes. *Journal of Materials Chemistry C* **2016**, 4, 4805-4813.

136. Yoon, S.-J.; Kim, J. H.; Kim, K. S.; Chung, J. W.; Heinrich, B.; Mathevet, F.; Kim, P.; Donnio, B.; Attias, A.-J.; Kim, D.; Park, S. Y., Mesomorphic Organization and Thermochromic Luminescence of Dicyanodistyrylbenzene-Based Phasmidic Molecular Disks: Uniaxially Aligned Hexagonal Columnar Liquid Crystals at Room Temperature with Enhanced Fluorescence Emission and Semiconductivity. *Advanced Functional Materials* **2012**, 22, 61-69.

137. Lee, S. S.; Seo, H. J.; Kim, Y. H.; Kim, S.-H., Structural Color Palettes of Core–Shell Photonic Ink Capsules Containing Cholesteric Liquid Crystals. *Advanced Materials* **2017**, 29, 1606894.

138. Valkama, S.; Kosonen, H.; Ruokolainen, J.; Haatainen, T.; Torkkeli, M.; Serimaa, R.; ten Brinke, G.; Ikkala, O., Self-Assembled Polymeric Solid Films with Temperature-Induced Large and Reversible Photonic-Bandgap Switching. *Nature Materials* **2004**, 3, 872-876.

139. Chiappelli, M. C.; Hayward, R. C., Photonic Multilayer Sensors from Photo-Crosslinkable Polymer Films. *Advanced Materials* **2012**, 24, 6100-6104.

140. Ahn, D. J.; Lee, S.; Kim, J.-M., Rational Design of Conjugated Polymer Supramolecules with Tunable Colorimetric Responses. *Advanced Functional Materials* **2009**, 19, 1483-1496.

141. Park, I. S.; Park, H. J.; Kim, J.-M., A Soluble, Low-Temperature Thermochromic and Chemically Reactive Polydiacetylene. *ACS Applied Materials & Interfaces* **2013**, 5, 8805-8812.

142. Dong, W.; Lin, G.; Wang, H.; Lu, W., New Dendritic Polydiacetylene Sensor with Good Reversible Thermochromic Ability in Aqueous Solution and Solid Film. *ACS Applied Materials & Interfaces* **2017**, 9, 11918-11923.

143. Alvey, P. M.; Reczek, J. J.; Lynch, V.; Iverson, B. L., A Systematic Study of Thermochromic Aromatic Donor−Acceptor Materials. *Journal of Organic Chemistry* **2010**, 75, 7682-7690.

144. Bé, A. G.; Tran, C.; Sechrist, R.; Reczek, J. J., Strongly Dichroic Organic Films via Controlled Assembly of Modular Aromatic Charge-Transfer Liquid Crystals. *Organic Letter* **2015**, 17, 4834-4837.

145. Peebles, C.; Wight, C. D.; Iverson, B. L., Solution- and Solid-State Photophysical and Stimuli-Responsive Behavior in Conjugated Monoalkoxynaphthalene-Naphthalimide Donor-Acceptor Dyads. *Journal of Materials Chemistry C* **2015**, 3, 12156-12163.

146. Das, G.; Skorjanc, T.; Sharma, S. K.; Gándara, F.; Lusi, M.; Shankar Rao, D. S.; Vimala, S.; Krishna Prasad, S.; Raya, J.; Han, D. S.; Jagannathan, R.; Olsen, J.-C.; Trabolsi, A., Viologen-Based Conjugated Covalent Organic Networks via Zincke Reaction. *Journal of the American Chemical Society* **2017**, 139, 9558-9565.

147. Liu, Y.; Yu, Y.; Gao, J.; Wang, Z.; Zhang, X., Water-Soluble Supramolecular Polymerization Driven by Multiple Host-Stabilized Charge-Transfer Interactions. *Angewandte Chemie International Edition* **2010**, 49, 6576-6579.

148. Rao, K. V.; Jayaramulu, K.; Maji, T. K.; George, S. J., Supramolecular Hydrogels and High-Aspect-Ratio Nanofibers through Charge-Transfer-Induced Alternate Coassembly. *Angewandte Chemie International Edition* **2010**, 49, 4218-4222.

149. Wang, K.-P.; Chen, Y.; Liu, Y., A Polycation-Induced Secondary Assembly of Amphiphilic Calixarene and Its Multi-Stimuli Responsive Gelation Behavior. *Chemical Communications* **2015**, 51, 1647-1649.

150. Datta, S.; Dey, N.; Bhattacharya, S., Electrochemical Probing of Hydrogelation Induced by the Self-Assembly of a Donor-Acceptor Complex Comprising Pyranine and Viologen. *Chemical Communications* **2017**, 53, 2371-2374.

151. Yuan, T.; Vazquez, M.; Goldner, A. N.; Xu, Y.; Contrucci, R.; Firestone, M. A.; Olson, M. A.; Fang, L., Versatile Thermochromic Supramolecular Materials Based on Competing Charge Transfer Interactions. *Advanced Functional Materials* **2016**, 26, 8604-8612.

152. The Job plot method was first used to determine the binding stoichiometry but it did not provide meaningful and reliable results. The reason why Job's method failed in our reported system is likely due to the existance of more than one type of complex present in

solution. (See Brynn Hibbert, D.; Thordarson, P. The death of the Job plot, transparency, open science and online tools, uncertainty estimation methods and other developments in supramolecular chemistry data analysis. *Chemical Communications* **2016**, 52, 12792-12805.) Therefore, an isolation technique (described in the Experimental Section) was used to determine the binding stoichiometry.

153. Du, A.; Zhou, B.; Zhang, Z.; Shen, J., A Special Material or a New State of Matter: A Review and Reconsideration of the Aerogel. *Materials* **2013**, 6, 941.

154. Lee, J.; Pyo, M.; Lee, S.-h.; Kim, J.; Ra, M.; Kim, W.-Y.; Park, B. J.; Lee, C. W.; Kim, J.-M., Hydrochromic Conjugated Polymers for Human Sweat Pore Mapping. **2014**, 5, 3736.

155. Park, D.-H.; Jeong, W.; Seo, M.; Park, B. J.; Kim, J.-M., Inkjet-Printable Amphiphilic Polydiacetylene Precursor for Hydrochromic Imaging on Paper. *Advanced Functional Materials* **2016**, 26, 498-506.

156. Pandi-Perumal, S. R.; Srinivasan, V.; Maestroni, G. J. M.; Cardinali, D. P.; Poeggeler, B.; Hardeland, R., Melatonin. *FEBS J.* **2006**, 273, 2813-2838.

157. Ryan, S. T. J.; Del Barrio, J.; Ghosh, I.; Biedermann, F.; Lazar, A. I.; Lan, Y.; Coulston, R. J.; Nau, W. M.; Scherman, O. A., Efficient Host–Guest Energy Transfer in Polycationic Cyclophane–Perylene Diimide Complexes in Water. *Journal of the American Chemical Society* **2014**, 136, 9053-9060.

158. Wu, Y.; Hao, X.; Wu, J.; Jin, J.; Ba, X., Pure Blue-Light-Emitting Materials: Hyperbranched Ladder-Type Poly(p-phenylene)s Containing Truxene Units. *Macromolecules* **2010**, 43, 731-738.

159. Sui, Q.; Ren, X.-T.; Dai, Y.-X.; Wang, K.; Li, W.-T.; Gong, T.; Fang, J.-J.; Zou, B.; Gao, E.-Q.; Wang, L., Piezochromism and Hydrochromism through Electron Transfer: New Stories for Viologen Materials. *Chemical Science* **2017**, 8, 2758-2768.

160. Ferchaud, C.; Zondag, H.; de Boer, R.; Rindt, C. In *Characterization of the sorption process in thermochemical materials for seasonal solar heat storage application*, Proceedings of the 12th international conference on energy storage (Innostock 2012), **2012**; pp 16-19.

161. Hume, J.; Colvin, J., The Dehydration of Copper Sulphate Pentahydrate. *Proceedings of the Royal Society of London. Series A, Containing Papers of a Mathematical and Physical Character* **1931**, 132, 548-560.

162. Ohno, H.; Shibayama, M.; Tsuchida, E., DSC Analyses of Bound Water in the Microdomains of Interpolymer Complexes. *Die Makromolekulare Chemie* **1983**, 184, 1017-1024.

163. Yagai, S.; Kinoshita, T.; Higashi, M.; Kishikawa, K.; Nakanishi, T.; Karatsu, T.; Kitamura, A., Diversification of Self-Organized Architectures in Supramolecular Dye Assemblies. *Journal of the American Chemical Society* **2007**, 129, 13277-13287.

164. Poutanen, M.; Ikkala, O.; Priimagi, A., Structurally Controlled Dynamics in Azobenzene-Based Supramolecular Self-Assemblies in Solid State. *Macromolecules* **2016**, 49, 4095-4101.

165. Bode, S.; Zedler, L.; Schacher, F. H.; Dietzek, B.; Schmitt, M.; Popp, J.; Hager, M. D.; Schubert, U. S., Self-Healing Polymer Coatings Based on Crosslinked Metallosupramolecular Copolymers. *Advanced Materials* **2013**, 25, 1634-1638.

166. Yoon, H.-J.; Jang, W.-D., Polymeric Supramolecular Systems for Drug Delivery. *Journal of Materials Chemistry* **2010**, 20, 211-222.

167. Dong, S.; Zheng, B.; Xu, D.; Yan, X.; Zhang, M.; Huang, F., A Crown Ether Appended Super Gelator with Multiple Stimulus Responsiveness. *Advanced Materials* **2012**, 24, 3191-3195.

168. Lin, Y.; Qiao, Y.; Gao, C.; Tang, P.; Liu, Y.; Li, Z.; Yan, Y.; Huang, J., Tunable One-Dimensional Helical Nanostructures: From Supramolecular Self-Assemblies to Silica Nanomaterials. *Chemistry of Materials* **2010**, 22, 6711-6717.

169. Inabe, T.; Hoshino, N.; Mitani, T.; Maruyama, Y., Structure and Optical Properties of a Thermochromic Schiff Base. Low-Temperature Structural Studies of the N,N′-Disalicylidene-p-phenylenediamine and N,N′-Disalicylidene-1,6-pyrenediamine Crystals. *Bulletin of the Chemical Society of Japan* **1989**, 62, 2245-2251.

170. Carmona, N.; Herrero-Hernandez, E.; Llopis, J.; Villegas, M. A., Novel Sol–Gel Reversible Thermochromic Materials for Environmental Sensors. *Journal of Sol-Gel Science and Technology* **2008**, 47, 31-37.

171. Yamamoto, S.; Furuya, H.; Tsutsui, K.; Ueno, S.; Sato, K., In Situ Observation of Thermochromic Behavior of Binary Mixtures of Phenolic Long-Chain Molecules and Fluoran Dye for Rewritable Paper Application. *Crystal Growth & Design* **2008**, 8, 2256-2263.

172. Campbell, D. J.; Bosma, W. B.; Bannon, S. J.; Gunter, M. M.; Hammar, M. K., Demonstration of Thermodynamics and Kinetics Using FriXion Erasable Pens. *Journal of Chemical Education* **2012**, 89, 526-528.

173. Crenshaw, B. R.; Weder, C., Deformation-Induced Color Changes in Melt-Processed Photoluminescent Polymer Blends. *Chemistry of Materials* **2003**, 15, 4717-4724.

174. Zhao, Z.; Lam, J. W. Y.; Tang, B. Z., Self-Assembly of Organic Luminophores with Gelation-Enhanced Emission Characteristics. *Soft Matter* **2013**, 9, 4564-4579.

175. An, B.-K.; Gierschner, J.; Park, S. Y., π-Conjugated Cyanostilbene Derivatives: A Unique Self-Assembly Motif for Molecular Nanostructures with Enhanced Emission and Transport. *Accounts of Chemical Research* **2012**, 45, 544-554.

176. Liu, C.; Lu, Y.; He, S.; Wang, Q.; Zhao, L.; Zeng, X., The Nature of the Styrylindolium Dye: Transformations among Its Monomer, Aggregates and Water Adducts. *Journal of Materials Chemistry C* **2013**, 1, 4770-4778.

177. Seeboth, A.; Lotzsch, D.; Ruhmann, R., First Example of a Non-Toxic Thermochromic Polymer Material - based on a Novel Mechanism. *Journal of Materials Chemistry C* **2013**, 1, 2811-2816.

178. Yuan, T.; Xu, Y.; Zhu, C.; Jiang, Z.; Sue, H.-J.; Fang, L.; Olson, M. A., Tunable Thermochromism of Multifunctional Charge-Transfer-Based Supramolecular Materials Assembled in Water. *Chemistry of Materials* **2017**, 29, 9937-9945.

179. Cangelosi, V. M.; Sather, A. C.; Zakharov, L. N.; Berryman, O. B.; Johnson, D. W., Diastereoselectivity in the Self-Assembly of $As_2L_2Cl_2$ Macrocycles is Directed by the As−π Interaction. *Inorganic Chemistry* **2007**, 46, 9278-9284.

180. Whitesides, G. M.; Grzybowski, B., Self-Assembly at All Scales. *Science* **2002**, 295, 2418-2421.

181. Stoddart, J. F., Thither Supramolecular Chemistry? *Nature Chemistry* **2009**, 1, 14.

182. Grzybowski, B. A.; Fitzner, K.; Paczesny, J.; Granick, S., From Dynamic Self-Assembly to Networked Chemical Systems. *Chemical Society Reviews* **2017**, 46, 5647-5678.

183. van Hameren, R.; Schön, P.; van Buul, A. M.; Hoogboom, J.; Lazarenko, S. V.; Gerritsen, J. W.; Engelkamp, H.; Christianen, P. C. M.; Heus, H. A.; Maan, J. C.; Rasing, T.; Speller, S.; Rowan, A. E.; Elemans, J. A. A. W.; Nolte, R. J. M., Macroscopic Hierarchical Surface Patterning of Porphyrin Trimers via Self-Assembly and Dewetting. *Science* **2006**, 314, 1433-1436.

184. Feng, X.; Tousley, M. E.; Cowan, M. G.; Wiesenauer, B. R.; Nejati, S.; Choo, Y.; Noble, R. D.; Elimelech, M.; Gin, D. L.; Osuji, C. O., Scalable Fabrication of Polymer Membranes with Vertically Aligned 1 nm Pores by Magnetic Field Directed Self-Assembly. *ACS Nano* **2014**, 8, 11977-11986.

185. Harada, A.; Kobayashi, R.; Takashima, Y.; Hashidzume, A.; Yamaguchi, H., Macroscopic Self-Assembly through Molecular Recognition. *Nature Chemistry* **2010**, 3, 34.

186. Meng, X.; Yiming, X.; Feng, S., Precise Macroscopic Supramolecular Assembly by Combining Spontaneous Locomotion Driven by the Marangoni Effect and Molecular Recognition. *Angewandte Chemie International Edition* **2015**, 54, 8952-8956.

187. Zhang, S.; Greenfield, M. A.; Mata, A.; Palmer, L. C.; Bitton, R.; Mantei, J. R.; Aparicio, C.; de la Cruz, M. O.; Stupp, S. I., A Self-Assembly Pathway to Aligned Monodomain Gels. *Nature Materials* **2010**, 9, 594.

188. Bucella, S. G.; Luzio, A.; Gann, E.; Thomsen, L.; McNeill, C. R.; Pace, G.; Perinot, A.; Chen, Z.; Facchetti, A.; Caironi, M., Macroscopic and High-Throughput Printing of Aligned Nanostructured Polymer Semiconductors for MHz Large-Area Electronics. *Nature Communication* **2015**, 6, 8394.

189. Jianfeng, W.; Lang, Z.; Li, Z.; Xiao-Lei, L.; Mei, G.; K., P. A.; Jinkui, T., Macroscopic Hexagonal Tubes of 3 d–4 f Metallocycles. *Angewandte Chemie International Edition* **2016**, 55, 15574-15578.

190. Chen, J.; Leung, F. K.-C.; Stuart, M. C. A.; Kajitani, T.; Fukushima, T.; van der Giessen, E.; Feringa, B. L., Artificial Muscle-Like Function from Hierarchical Supramolecular Assembly of Photoresponsive Molecular Motors. *Nature Chemistry* **2017**, 10, 132-138.

191. Pauling, L.; Corey, R. B.; Branson, H. R., The structure of proteins: Two Hydrogen-Bonded Helical Configurations of the Polypeptide Chain. *Proceedings of the National Academy of Sciences* **1951**, 37, 205-211.

192. Yashima, E.; Ousaka, N.; Taura, D.; Shimomura, K.; Ikai, T.; Maeda, K., Supramolecular Helical Systems: Helical Assemblies of Small Molecules, Foldamers, and Polymers with Chiral Amplification and Their Functions. *Chemical Reviews* **2016**, 116, 13752-13990.

193. Liu, M.; Zhang, L.; Wang, T., Supramolecular Chirality in Self-Assembled Systems. *Chemical Reviews* **2015**, 115, 7304-7397.

194. Wang, Y.; Xu, J.; Wang, Y.; Chen, H., Emerging chirality in nanoscience. *Chemical Society Reviews* **2013**, 42, 2930-2962.

195. Dressel, C.; Reppe, T.; Prehm, M.; Brautzsch, M.; Tschierske, C., Chiral Self-Sorting and Amplification in Isotropic Liquids of Achiral Molecules. *Nature Chemistry* **2014**, 6, 971-977.

196. Jiang, H.; Zhang, L.; Chen, J.; Liu, M., Hierarchical Self-Assembly of a Porphyrin into Chiral Macroscopic Flowers with Superhydrophobic and Enantioselective Property. *ACS Nano* **2017**, 11, 12453-12460.

197. Che, S.; Liu, Z.; Ohsuna, T.; Sakamoto, K.; Terasaki, O.; Tatsumi, T., Synthesis and Characterization of Chiral Mesoporous Silica. *Nature* **2004**, 429, 281-284.

198. Shopsowitz, K. E.; Qi, H.; Hamad, W. Y.; MacLachlan, M. J., Free-Standing Mesoporous Silica Films with Tunable Chiral Nematic Structures. *Nature* **2010**, 468, 422-425.

199. Sawa, Y.; Ye, F.; Urayama, K.; Takigawa, T.; Gimenez-Pinto, V.; Selinger, R. L. B.; Selinger, J. V., Shape Selection of Twist-Nematic-Elastomer Ribbons. *Proceedings of the National Academy of Sciences* **2011**, 108, 6364-6368.

200. Iamsaard, S.; Aßhoff, S. J.; Matt, B.; Kudernac, T.; Cornelissen, J. J. L. M.; Fletcher, S. P.; Katsonis, N., Conversion of Light into Macroscopic Helical Motion. *Nature Chemistry* **2014**, 6, 229.

201. Yamamoto, Y.; Fukushima, T.; Jin, W.; Kosaka, A.; Hara, T.; Nakamura, T.; Saeki, A.; Seki, S.; Tagawa, S.; Aida, T., A Glass Hook Allows Fishing of Hexa-peri-hexabenzocoronene Graphitic Nanotubes: Fabrication of a Macroscopic Fiber with Anisotropic Electrical Conduction. *Advanced Materials* **2006**, 18, 1297-1300.

202. Morrow, S. M.; Bissette, A. J.; Fletcher, S. P., Transmission of Chirality through Space and Across Length Scales. *Nature Nanotechnology* **2017**, 12, 410-419.

203. Maeda, K.; Hirose, D.; Okoshi, N.; Shimomura, K.; Wada, Y.; Ikai, T.; Kanoh, S.; Yashima, E., Direct Detection of Hardly Detectable Hidden Chirality of Hydrocarbons and Deuterated Isotopomers by a Helical Polyacetylene through Chiral Amplification and Memory. *Journal of the American Chemical Society* **2018**, 140, 3270-3276.

204. Helmich, F.; Lee, C. C.; Schenning, A. P. H. J.; Meijer, E. W., Chiral Memory via Chiral Amplification and Selective Depolymerization of Porphyrin Aggregates. *Journal of the American Chemical Society* **2010**, 132, 16753-16755.

205. Shimomura, K.; Ikai, T.; Kanoh, S.; Yashima, E.; Maeda, K., Switchable Enantioseparation based on Macromolecular Memory of a Helical Polyacetylene in the Solid State. *Nature Chemistry* **2014**, 6, 429-434.

206. Wu, X.; Ji, S.; Li, Y.; Li, B.; Zhu, X.; Hanabusa, K.; Yang, Y., Helical Transfer through Nonlocal Interactions. *Journal of the American Chemical Society* **2009**, 131, 5986-5993.

207. Ho, R.-M.; Li, M.-C.; Lin, S.-C.; Wang, H.-F.; Lee, Y.-D.; Hasegawa, H.; Thomas, E. L., Transfer of Chirality from Molecule to Phase in Self-Assembled Chiral Block Copolymers. *Journal of the American Chemical Society* **2012**, 134, 10974-10986.

208. Yang, Y.; Zhang, Y.; Wei, Z., Supramolecular Helices: Chirality Transfer from Conjugated Molecules to Structures. *Advanced Materials* **2013**, 25, 6039-6049.

209. Lee, H.-E.; Ahn, H.-Y.; Mun, J.; Lee, Y. Y.; Kim, M.; Cho, N. H.; Chang, K.; Kim, W. S.; Rho, J.; Nam, K. T., Amino-Acid- and Peptide-Directed Synthesis of Chiral Plasmonic Gold Nanoparticles. *Nature* **2018**, 556, 360-365.

210. Palmans, A. R. A.; Meijer, E. W., Amplification of Chirality in Dynamic Supramolecular Aggregates. *Angewandte Chemie International Edition* **2007**, 46, 8948-8968.

211. Kulkarni, C.; Munirathinam, R.; George, S. J., Self-Assembly of Coronene Bisimides: Mechanistic Insight and Chiral Amplification. *Chemistry – A European Journal* **2013**, 19, 11270-11278.

212. Ke, Y. Z.; Nagata, Y.; Yamada, T.; Suginome, M., Majority-Rules-Type Helical Poly(quinoxaline-2,3-diyl)s as Highly Efficient Chirality-Amplification Systems for Asymmetric Catalysis. *Angewandte Chemie International Edition* **2015**, 54, 9333-9337.

213. George, S. J.; Tomović, Ž.; Smulders, M. M. J.; Greef, T. F. A. d.; Leclère, P. E. L. G.; Meijer, E. W.; Schenning, A. P. H. J., Helicity Induction and Amplification in an Oligo(p-phenylenevinylene) Assembly through Hydrogen-Bonded Chiral Acids. *Angewandte Chemie International Edition* **2007**, 46, 8206-8211.

214. Sakurai, S. i.; Ohsawa, S.; Nagai, K.; Okoshi, K.; Kumaki, J.; Yashima, E., Two-Dimensional Helix-Bundle Formation of a Dynamic Helical Poly(phenylacetylene) with Achiral Pendant Groups on Graphite. *Angewandte Chemie* **2007**, 119, 7749-7752.

215. Bejagam, K. K.; Kulkarni, C.; George, S. J.; Balasubramanian, S., External Electric Field Reverses Helical Handedness of a Supramolecular Columnar Stack. *Chemical Communications* **2015**, 51, 16049-16052.

216. Castilla, A. M.; Ousaka, N.; Bilbeisi, R. A.; Valeri, E.; Ronson, T. K.; Nitschke, J. R., High-Fidelity Stereochemical Memory in a $Fe^{II}_4L_4$ Tetrahedral Capsule. *Journal of the American Chemical Society* **2013**, 135, 17999-18006.

217. George, S. J.; de Bruijn, R.; Tomović, Ž.; Van Averbeke, B.; Beljonne, D.; Lazzaroni, R.; Schenning, A. P. H. J.; Meijer, E. W., Asymmetric Noncovalent Synthesis of Self-Assembled One-Dimensional Stacks by a Chiral Supramolecular Auxiliary Approach. *Journal of the American Chemical Society* **2012**, 134, 17789-17796.

218. Fenniri, H.; Deng, B.-L.; Ribbe, A. E., Helical Rosette Nanotubes with Tunable Chiroptical Properties. *Journal of the American Chemical Society* **2002**, 124, 11064-11072.

219. Onouchi, H.; Hasegawa, T.; Kashiwagi, D.; Ishiguro, H.; Maeda, K.; Yashima, E., Helicity Induction in Charged Poly(phenylacetylene)s Bearing Various Acidic Functional Groups in Water and Its Mechanism. *Macromolecules* **2005**, 38, 8625-8633.

220. Yokoi, T.; Ogawa, K.; Lu, D.; Kondo, J. N.; Kubota, Y.; Tatsumi, T., Preparation of Chiral Mesoporous Materials with Helicity Perfectly Controlled. *Chemistry of Materials* **2011**, 23, 2014-2016.

221. Isenberg, I.; Szent-Györgyi, A.; Baird, S. L., Spin Resonance Study of Serotonin-Fmn Interaction. *Proceedings of the National Academy of Sciences* **1960**, 46, 1307-1311.

222. Fernando Rodrigues de Sa, A.; Eliezer, J. B.; Carlos Alberto Manssour, F., From Nature to Drug Discovery: The Indole Scaffold as a "Privileged Structure". *Mini-Reviews in Medicinal Chemistry* **2009**, 9, 782-793.

223. Wang, Z.; Cui, H.; Sun, Z.; Roch, L. M.; Goldner, A. N.; Nour, H. F.; Sue, A. C. H.; Baldridge, K. K.; Olson, M. A., Melatonin-Directed Micellization: a Case for Tryptophan Metabolites and Their Classical Bioisosteres as Templates for the Self-Assembly of Bipyridinium-Based Supramolecular Amphiphiles in Water. *Soft Matter* **2018**, 14, 2893-2905.

224. Macroscopic fibers were observed under the conditions of drop-casting and slow-speed spin-coating.

225. Danila, I.; Riobé, F.; Piron, F.; Puigmartí-Luis, J.; Wallis, J. D.; Linares, M.; Ågren, H.; Beljonne, D.; Amabilino, D. B.; Avarvari, N., Hierarchical Chiral Expression from the Nano- to Mesoscale in Synthetic Supramolecular Helical Fibers of a Nonamphiphilic C3-Symmetrical π-Functional Molecule. *Journal of the American Chemical Society* **2011**, 133, 8344-8353.

226. Vela, S.; Berrocal, J. A.; Atienza, C.; Meijer, E. W.; Martin, N., Mesoscopic Helical Architectures via Self-Assembly of Porphyrin-based Discotic Systems. *Chemical Communications* **2017**, 53, 4084-4087.

227. Sergeant-and-soldiers effects were also tested and no sergeant-and-soldiers effects were observed.

228. Yamada, Y. M. A.; Uozumi, Y., A Solid-Phase Self-Organized Catalyst of Nanopalladium with Main-Chain Viologen Polymers: α-Alkylation of Ketones with Primary Alcohols. *Organic Letters* **2006**, 8, 1375-1378.

229. Sharvin, V. V. J., *J. Russ. Phys. Chem. Soc.* **1915**, 47, 3.

230. Herbst, W. H., K., Industrial Organic Pigments, 3rd ed. *Wiley-VCH: Weinheim, Germany*, **2004**.

231. Zhan, X.; Facchetti, A.; Barlow, S.; Marks, T. J.; Ratner, M. A.; Wasielewski, M. R.; Marder, S. R., Rylene and Related Diimides for Organic Electronics. *Advanced Materials* **2011**, 23, 268-284.

232. Li, C.; Wonneberger, H., Perylene Imides for Organic Photovoltaics: Yesterday, Today, and Tomorrow. *Advanced Materials* **2012**, 24, 613-636.

233. Fang, L.; Zhou, Y.; Yao, Y.-X.; Diao, Y.; Lee, W.-Y.; Appleton, A. L.; Allen, R.; Reinspach, J.; Mannsfeld, S. C. B.; Bao, Z., Side-Chain Engineering of Isoindigo-Containing Conjugated Polymers Using Polystyrene for High-Performance Bulk Heterojunction Solar Cells. *Chemistry of Materials* **2013**, 25, 4874-4880.

234. Wang, E.; Mammo, W.; Andersson, M. R., 25th Anniversary Article: Isoindigo-Based Polymers and Small Molecules for Bulk Heterojunction Solar Cells and Field Effect Transistors. *Advanced Materials* **2014**, 26, 1801-1826.

235. Li, H.; Gu, C.; Jiang, L.; Wei, L.; Hu, W.; Fu, H., Donor-Acceptor Copolymers Containing Quinacridone and Benzothiadiazole for Thin Film Transistors. *Journal of Materials Chemistry C* **2013**, 1, 2021-2027.

236. Głowacki, E. D.; Irimia-Vladu, M.; Kaltenbrunner, M.; Gsiorowski, J.; White, M. S.; Monkowius, U.; Romanazzi, G.; Suranna, G. P.; Mastrorilli, P.; Sekitani, T.; Bauer, S.; Someya, T.; Torsi, L.; Sariciftci, N. S., Hydrogen-Bonded Semiconducting Pigments for Air-Stable Field-Effect Transistors. *Advanced Materials* **2013**, 25, 1563-1569.

237. Osaka, I.; Akita, M.; Koganezawa, T.; Takimiya, K., Quinacridone-Based Semiconducting Polymers: Implication of Electronic Structure and Orientational Order for Charge Transport Property. *Chemistry of Materials* **2012**, 24, 1235-1243.

238. Song, H.-J.; Kim, D.-H.; Lee, E.-J.; Moon, D.-K., Conjugated Polymers Consisting of Quinacridone and Quinoxaline as Donor Materials for Organic Photovoltaics: Orientation and Charge Transfer Properties of Polymers Formed by Phenyl Structures with a Quinoxaline Derivative. *Journal of Materials Chemistry A* **2013**, 1, 6010-6020.

239. Wang, C.; Chen, D.; Chen, W.; Chen, S.; Ye, K.; Zhang, H.; Zhang, J.; Wang, Y., Polymorph, Assembly, Luminescence and Semiconductor Properties of a Quinacridone Derivative with Extended π-Conjugated Framework. *Journal of Materials Chemistry C* **2013**, 1, 5548-5556.

240. Wang, C.; Chen, D.; Chen, W.; Chen, S.; Ye, K.; Zhang, H.; Zhang, J.; Wang, Y., Polymorph, Assembly, Luminescence and Semiconductor Properties of a Quinacridone Derivative with Extended π-Conjugated Framework. *Journal of Materials Chemistry C* **2013**, 1, 5548-5556.

241. J Jun Song, H.; Hun Kim, D.; Hee Choi, M.; Won Heo, S.; Young Lee, J.; Yong Lee, J.; Kyung Moon, D., Self-organization Polymer Consisting of Quinacridone and Quaterthiophene Units: Coplanar Structure between Benzene and Thiophene Linkage. *Solar Energy Materials and Solar Cells* **2013**, 117, 285-292.

242. Javed, I.; Zhang, Z.; Peng, T.; Zhou, T.; Zhang, H.; Issa Khan, M.; Liu, Y.; Wang, Y., Solution Processable Quinacridone based Materials as Acceptor for Organic Heterojunction Solar Cells. *Solar Energy Materials and Solar Cells* **2011**, 95, 2670-2676.

243. Chen, J. J.-A.; Chen, T. L.; Kim, B.; Poulsen, D. A.; Mynar, J. L.; Fréchet, J. M. J.; Ma, B., Quinacridone-Based Molecular Donors for Solution Processed Bulk-Heterojunction Organic Solar Cells. *ACS Applied Materials & Interfaces* **2010**, 2, 2679-2686.

244. Liu, J.; Gao, B.; Cheng, Y.; Xie, Z.; Geng, Y.; Wang, L.; Jing, X.; Wang, F., Novel White Electroluminescent Single Polymer Derived from Fluorene and Quinacridone. *Macromolecules* **2008**, 41, 1162-1167.

245. Wang, C.; Wang, K.; Fu, Q.; Zhang, J.; Ma, D.; Wang, Y., Pentaphenylphenyl Substituted Quinacridone Exhibiting Intensive Emission in Both Solution and Solid State. *Journal of Materials Chemistry C* **2013**, 1, 410-413.

246. Głowacki, E. D.; Leonat, L.; Irimia-Vladu, M.; Schwödiauer, R.; Ullah, M.; Sitter, H.; Bauer, S.; Sariciftci, N. S., Intermolecular Hydrogen-Bonded Organic Semiconductors—Quinacridone versus Pentacene. *Applied Physics Letters* **2012**, 101, 023305.

247. Sun, H.; Ye, K.; Wang, C.; Qi, H.; Li, F.; Wang, Y., The π−π Stacked Geometries and Association Thermodynamics of Quinacridone Derivatives Studied by 1H NMR. *The Journal of Physical Chemistry A* **2006**, 110, 10750-10756.

248. Wang, J.; Zhao, Y.; Zhang, J.; Zhang, J.; Yang, B.; Wang, Y.; Zhang, D.; You, H.; Ma, D., Assembly of One-Dimensional Organic Luminescent Nanowires Based on Quinacridone Derivatives. *The Journal of Physical Chemistry C* **2007**, 111, 9177-9183.

249. Sun, H.; Zhao, Y.; Huang, Z.; Wang, Y.; Li, F., 1H NMR Study on the Self-Association of Quinacridone Derivatives in Solution. *The Journal of Physical Chemistry A* **2008**, 112, 11382-11390.

250. Wang, J.; Zhao, Y.; Dou, C.; Sun, H.; Xu, P.; Ye, K.; Zhang, J.; Jiang, S.; Li, F.; Wang, Y., Alkyl and Dendron Substituted Quinacridones: Synthesis, Structures, and Luminescent Properties. *The Journal of Physical Chemistry B* **2007**, 111, 5082-5089.

251. Ye, K.; Wang, J.; Sun, H.; Liu, Y.; Mu, Z.; Li, F.; Jiang, S.; Zhang, J.; Zhang, H.; Wang, Y.; Che, C.-M., Supramolecular Structures and Assembly and Luminescent Properties of Quinacridone Derivatives. *The Journal of Physical Chemistry B* **2005**, 109, 8008-8016.

252. Kitahara, K.; Yanagimoto, H.; Nakajima, N.; Nishi, H., Synthesis of Soluble Quinacridones. *Journal of Heterocyclic Chemistry* **1992**, 29, 167-169.

253. Keller, U.; Müllen, K.; Feyter, S. D.; Schryver, F. C. D., Hydrogen-Bonding and Phase-Forming Behavior of a Soluble Quinacridone. *Advanced Materials* **1996**, 8, 490-493.

254. Popp, F. D.; McEwen, W. E., Polyphosphoric Acids As A Reagent In Organic Chemistry. *Chemical Reviews* **1958**, 58, 321-401.

255. D'yakov, S. N.; Nevedrov, A. V.; Papin, A. V., Fluorene Production from Coke-Industry Byproducts. *Coke and Chemistry* **2012**, 55, 340-341.

256. Wudl, F.; Angus, R. O.; Lu, F. L.; Allemand, P. M.; Vachon, D.; Nowak, M.; Liu, Z. X.; Schaffer, H.; Heeger, A. J., Poly-p-phenyleneamineimine: Synthesis and Comparison to Polyaniline. *Journal of the American Chemical Society* **1987**, 109, 3677-3684.

257. D. Gernon, M.; Wu, M.; Buszta, T.; Janney, P., Environmental Benefits of Methanesulfonic Acid . Comparative Properties and Advantages. *Green Chemistry* **1999**, 1, 127-140.

258. Nudelman, N. S.; Alvaro, C. E. S., Inter- and Intramolecular Hydrogen Bonds in Polyamines: Variable-Concentration ^{1}H-NMR Studies. *Journal of Physical Organic Chemistry* **2011**, 24, 1067-1071.

259. Fu, X.; Zhang, Q.; Wu, G.; Zhou, W.; Wang, Q.-C.; Qu, D.-H., A Fluorescent Hyperbranched Supramolecular Polymer based on Triple Hydrogen Bonding Interactions. *Polymer Chemistry* **2014**, 5, 6662-6666.

260. Mizuguchi, J.; Senju, T., Solution and Solid-State Spectra of Quinacridone Derivatives as Viewed from the Intermolecular Hydrogen Bond. *The Journal of Physical Chemistry B* **2006**, 110, 19154-19161.

261. Fukunaga, H.; Fedorov, D. G.; Chiba, M.; Nii, K.; Kitaura, K., Theoretical Analysis of the Intermolecular Interaction Effects on the Excitation Energy of Organic Pigments: Solid State Quinacridone. *The Journal of Physical Chemistry A* **2008**, 112, 10887-10894.

262. De Feyter, S.; Gesquière, A.; De Schryver, F. C.; Keller, U.; Müllen, K., Aggregation Properties of Soluble Quinacridones in Two and Three Dimensions. *Chemistry of Materials* **2002**, 14, 989-997.

263. Chen, Z.; Lohr, A.; Saha-Moller, C. R.; Wurthner, F., Self-Assembled π-Stacks of Functional Dyes in Solution: Structural and Thermodynamic Features. *Chemical Society Reviews* **2009**, 38, 564-584.

264. Emsley, J., Very Strong Hydrogen Bonding. *Chemical Society Reviews* **1980**, 9, 91-124.

265. ompendium of Polymer Terminology and Nomenclature: IUPAC Recommendations 2008. *Journal of the American Chemical Society* **2009**, 131, 7935-7935.

266. Lee, J.; Kalin, A. J.; Yuan, T.; Al-Hashimi, M.; Fang, L., Fully Conjugated Ladder Polymers. *Chemical Science* **2017**, 8, 2503-2521.

267. Bezzu, C. G.; Carta, M.; Tonkins, A.; Jansen, J. C.; Bernardo, P.; Bazzarelli, F.; McKeown, N. B., A Spirobifluorene-Based Polymer of Intrinsic Microporosity with Improved Performance for Gas Separation. *Advanced Materials* **2012**, 24, 5930-5933.

268. Carta, M.; Malpass-Evans, R.; Croad, M.; Rogan, Y.; Jansen, J. C.; Bernardo, P.; Bazzarelli, F.; McKeown, N. B., An Efficient Polymer Molecular Sieve for Membrane Gas Separations. *Science* **2013**, 339, 303-307.

269. Ghanem, B. S.; Swaidan, R.; Ma, X.; Litwiller, E.; Pinnau, I., Energy-Efficient Hydrogen Separation by AB-Type Ladder-Polymer Molecular Sieves. *Advanced Materials* **2014**, 26, 6696-6700.

270. Schlüter, A. D.; Löffler, M.; Enkelmann, V., Synthesis of a Fully Unsaturated All-Carbon Ladder Polymer. *Nature* **1994**, 368, 831-834.

271. Xia, C.; Advincula, R. C., Ladder-Type Oligo(p-phenylene)s Tethered to a Poly(alkylene) Main Chain: The Orthogonal Approach to Functional Light-Emitting Polymers. *Macromolecules* **2001**, 34, 6922-6928.

272. Qiu, S.; Lu, P.; Liu, X.; Shen, F.; Liu, L.; Ma, Y.; Shen, J., New Ladder-Type Poly(p-phenylene)s Containing Fluorene Unit Exhibiting High Efficient Electroluminescence. *Macromolecules* **2003**, 36, 9823-9829.

273. Mishra, A. K.; Graf, M.; Grasse, F.; Jacob, J.; List, E. J. W.; Müllen, K., Blue-Emitting Carbon- and Nitrogen-Bridged Poly(ladder-type tetraphenylene)s. *Chemistry of Materials* **2006**, 18, 2879-2885.

274. Wu, Y.; Zhang, J.; Fei, Z.; Bo, Z., Spiro-Bridged Ladder-Type Poly(p-phenylene)s: Towards Structurally Perfect Light-Emitting Materials. *Journal of the American Chemical Society* **2008**, 130, 7192-7193.

275. Babel, A.; Jenekhe, S. A., High Electron Mobility in Ladder Polymer Field-Effect Transistors. *Journal of the American Chemical Society* **2003**, 125, 13656-13657.

276. Usta, H.; Risko, C.; Wang, Z.; Huang, H.; Deliomeroglu, M. K.; Zhukhovitskiy, A.; Facchetti, A.; Marks, T. J., Design, Synthesis, and Characterization of Ladder-Type

Molecules and Polymers. Air-Stable, Solution-Processable n-Channel and Ambipolar Semiconductors for Thin-Film Transistors via Experiment and Theory. *Journal of the American Chemical Society* **2009**, 131, 5586-5608.

277. Durban, M. M.; Kazarinoff, P. D.; Segawa, Y.; Luscombe, C. K., Synthesis and Characterization of Solution-Processable Ladderized n-Type Naphthalene Bisimide Copolymers for OFET Applications. *Macromolecules* **2011**, 44, 4721-4728.

278. Xu, Y. X.; Chueh, C. C.; Yip, H. L.; Ding, F. Z.; Li, Y. X.; Li, C. Z.; Li, X.; Chen, W. C.; Jen, A. K. Y., Improved Charge Transport and Absorption Coefficient in Indacenodithieno[3,2-b]thiophene-based Ladder-Type Polymer Leading to Highly Efficient Polymer Solar Cells. *Advanced Materials* **2012**, 24, 6356-6361.

279. Li, Y.; Yao, K.; Yip, H. L.; Ding, F. Z.; Xu, Y. X.; Li, X.; Chen, Y.; Jen, A. K. Y., Eleven-Membered Fused-Ring Low Band-Gap Polymer with Enhanced Charge Carrier Mobility and Photovoltaic Performance. *Advanced Functional Materials* **2014**, 24, 3631-3638.

280. Cheng, Y.-J.; Chen, C.-H.; Lin, Y.-S.; Chang, C.-Y.; Hsu, C.-S., Ladder-Type Nonacyclic Structure Consisting of Alternate Thiophene and Benzene Units for Efficient Conventional and Inverted Organic Photovoltaics. *Chemistry of Materials* **2011**, 23, 5068-5075.

281. Ma, Y.; Zheng, Q.; Yin, Z.; Cai, D.; Chen, S.-C.; Tang, C., Ladder-Type Dithienonaphthalene-Based Donor–Acceptor Copolymers for Organic Solar Cells. *Macromolecules* **2013**, 46, 4813-4821.

282. Chen, L.; Hernandez, Y.; Feng, X.; Müllen, K., From Nanographene and Graphene Nanoribbons to Graphene Sheets: Chemical Synthesis. *Angewandte Chemie International Edition* **2012**, 51, 7640-7654.

283. Narita, A.; Feng, X.; Hernandez, Y.; Jensen, S. A.; Bonn, M.; Yang, H.; Verzhbitskiy, I. A.; Casiraghi, C.; Hansen, M. R.; Koch, A. H. R.; Fytas, G.; Ivasenko, O.; Li, B.; Mali, K. S.; Balandina, T.; Mahesh, S.; De Feyter, S.; Müllen, K., Synthesis of Structurally Well-Defined and Liquid-Phase-Processable Graphene Nanoribbons. *Nature Chemistry* **2013**, 6, 126-132.

284. Hu, R.; Chung, T. C., Poly(acrylonitrile-co-vinylcatecholborane): A New Precursor for Carbon Containing B/C, B/N and B/O Species. *Carbon* **1996**, 34, 595-600.

285. Wangxi, Z.; Jie, L.; Gang, W., Evolution of Structure and Properties of PAN Precursors During Their Conversion to Carbon Fibers. *Carbon* **2003**, 41, 2805-2812.

286. Serkov, A. T.; Radishevskii, M. B., Status and Prospects for Production of Carbon Fibres based on Polyacrylonitrile. *Fibre Chemistry* **2008**, 40, 24-31.

287. Yao, Y.; Dong, H.; Hu, W., Ordering of Conjugated Polymer Molecules: Recent Advances and Perspectives. *Polymer Chemistry* **2013**, 4, 5197-5205.

288. Dou, J. H.; Zheng, Y. Q.; Lei, T.; Zhang, S. D.; Wang, Z.; Zhang, W. B.; Wang, J. Y.; Pei, J., Systematic Investigation of Side-Chain Branching Position Effect on Electron Carrier Mobility in Conjugated Polymers. *Advanced Functional Materials* **2014**, 24, 6270-6278.

289. Olivier, Y.; Niedzialek, D.; Lemaur, V.; Pisula, W.; Müllen, K.; Koldemir, U.; Reynolds, J. R.; Lazzaroni, R.; Cornil, J.; Beljonne, D., 25th Anniversary Article: High-Mobility Hole and Electron Transport Conjugated Polymers: How Structure Defines Function. *Advanced Materials* **2014**, 26, 2119-2136.

290. Diao, Y.; Zhou, Y.; Kurosawa, T.; Shaw, L.; Wang, C.; Park, S.; Guo, Y.; Reinspach, J. A.; Gu, K.; Gu, X.; Tee, B. C. K.; Pang, C.; Yan, H.; Zhao, D.; Toney, M. F.; Mannsfeld, S. C. B.; Bao, Z., Flow-Enhanced Solution Printing of All-Polymer Solar Cells. *Nature Communications* **2015**, 6, 7955.

291. Thomas, S. W.; Long, T. M.; Pate, B. D.; Kline, S. R.; Thomas, E. L.; Swager, T. M., Perpendicular Organization of Macromolecules: Synthesis and Alignment Studies of a Soluble Poly(iptycene). *Journal of the American Chemical Society* **2005**, 127, 17976-17977.

292. Shacklette, L. W., Dipole and Hydrogen-Bonding Interactions in Polyaniline: a Mechanism for Conductivity Enhancement. *Synthetic Metals* **1994**, 65, 123-130.

293. Dudek, S. P.; Pouderoijen, M.; Abbel, R.; Schenning, A. P. H. J.; Meijer, E. W., Synthesis and Energy-Transfer Properties of Hydrogen-Bonded Oligofluorenes. *Journal of the American Chemical Society* **2005**, 127, 11763-11768.

294. Abbel, R.; Grenier, C.; Pouderoijen, M. J.; Stouwdam, J. W.; Leclère, P. E. L. G.; Sijbesma, R. P.; Meijer, E. W.; Schenning, A. P. H. J., White-Light Emitting Hydrogen-Bonded Supramolecular Copolymers Based on π-Conjugated Oligomers. *Journal of the American Chemical Society* **2009**, 131, 833-843.

295. González-Rodríguez, D.; Schenning, A. P. H. J., Hydrogen-bonded Supramolecular π-Functional Materials. *Chemistry of Materials* **2011**, 23, 310-325.

296. Black, H. T.; Perepichka, D. F., Crystal Engineering of Dual Channel p/n Organic Semiconductors by Complementary Hydrogen Bonding. *Angewandte Chemie International Edition* **2014**, 53, 2138-2142.

297. Ley, D.; Guzman, C. X.; Adolfsson, K. H.; Scott, A. M.; Braunschweig, A. B., Cooperatively Assembling Donor–Acceptor Superstructures Direct Energy Into an Emergent Charge Separated State. *Journal of the American Chemical Society* **2014**, 136, 7809-7812.

298. Huang, J.; Peng, B.; Wang, W.; Ji, H.; Li, L.; Xi, K.; Lai, W.; Zhang, X.; Jia, X., Architecture of Conjugated Donor–Acceptor (D–A)-Type Polymer Films with Cross-Linked Structures. *Advanced Functional Materials* **2016**, 26, 1646-1655.

299. Kimura, S., Preparation of Polyquinolones. *Die Makromolekulare Chemie* **1968**, 117, 203-209.

300. Liu, Z.; Lin, Y.; Wen, X.; Su, Q., Preparation and Electrorheological Properties of Qolyquin(2,3-b)acridine-12,14(5,7)dione-based Suspensions. *Colloids and Surfaces A: Physicochemical and Engineering Aspects* **2005**, 264, 55-60.

301. Wu, J.; Rui, X.; Long, G.; Chen, W.; Yan, Q.; Zhang, Q., Pushing Up Lithium Storage through Nanostructured Polyazaacene Analogues as Anode. *Angewandte Chemie International Edition* **2015**, 54, 7354-7358.

302. Labana, S. S.; Labana, L. L., Quinacridones. *Chemical Reviews* **1967**, 67, 1-18.

303. Gsänger, M.; Bialas, D.; Huang, L.; Stolte, M.; Würthner, F., Organic Semiconductors based on Dyes and Color Pigments. *Advanced Materials* **2016**, 28, 3615-3645.

304. Paulus, E. F.; Leusen, F. J. J.; Schmidt, M. U., Crystal Structures of Quinacridones. *CrystEngComm* **2007**, 9, 131-143.

305. Lincke, G., A Review of Thirty Years of Research on Quinacridones. X-ray Crystallography and Crystal Engineering. *Dyes and Pigments* **2000**, 44, 101-122.

306. Enengl, C.; Enengl, S.; Havlicek, M.; Stadler, P.; Glowacki, E. D.; Scharber, M. C.; White, M.; Hingerl, K.; Ehrenfreund, E.; Neugebauer, H.; Sariciftci, N. S., The Role of Heteroatoms Leading to Hydrogen Bonds in View of Extended Chemical Stability of Organic Semiconductors. *Advanced Functional Materials* **2015**, 25, 6679-6688.

307. Zou, Y.; Yuan, T.; Yao, H.; Frazier, D. J.; Stanton, D. J.; Sue, H.-J.; Fang, L., Solution-Processable Core-Extended Quinacridone Derivatives with Intact Hydrogen Bonds. *Organic Letters* **2015**, 17, 3146-3149.

308. Cocherel, N.; Poriel, C.; Rault-Berthelot, J.; Barrière, F.; Audebrand, N.; Slawin, A. M. Z.; Vignau, L., New 3π-2Spiro Ladder-Type Phenylene Materials: Synthesis, Physicochemical Properties and Applications in OLEDs. *Chemistry – A European Journal* **2008**, 14, 11328-11342.

309. Yang, J.-S.; Huang, H.-H.; Liu, Y.-H.; Peng, S.-M., Synthesis and Electronic Properties of Isotruxene-Derived Star-Shaped Ladder-Type Oligophenylenes: Bandgap Tuning with Two-Dimensional Conjugation. *Organic Letters* **2009**, 11, 4942-4945.

310. Huang, H.-H.; Prabhakar, C.; Tang, K.-C.; Chou, P.-T.; Huang, G.-J.; Yang, J.-S., Ortho-Branched Ladder-Type Oligophenylenes with Two-Dimensionally π-Conjugated Electronic Properties. *Journal of the American Chemical Society* **2011**, 133, 8028-8039.

311. Sytnyk, M.; Głowacki, E. D.; Yakunin, S.; Voss, G.; Schöfberger, W.; Kriegner, D.; Stangl, J.; Trotta, R.; Gollner, C.; Tollabimazraehno, S.; Romanazzi, G.; Bozkurt, Z.; Havlicek, M.; Sariciftci, N. S.; Heiss, W., Hydrogen-Bonded Organic Semiconductor Micro- And Nanocrystals: From Colloidal Syntheses to (Opto-)Electronic Devices. *Journal of the American Chemical Society* **2014**, 136, 16522-16532.

312. Yang, K.; He, T.; Chen, X.; Cheng, S. Z. D.; Zhu, Y., Patternable Conjugated Polymers with Latent Hydrogen-Bonding on the Main Chain. *Macromolecules* **2014**, 47, 8479-8486.

313. Liu, C.; Dong, S.; Cai, P.; Liu, P.; Liu, S.; Chen, J.; Liu, F.; Ying, L.; Russell, T. P.; Huang, F.; Cao, Y., Donor–Acceptor Copolymers Based on Thermally Cleavable Indigo, Isoindigo, and DPP Units: Synthesis, Field Effect Transistors, and Polymer Solar Cells. *ACS Applied Materials & Interfaces* **2015**, 7, 9038-9051.

314. Głowacki, E. D.; Romanazzi, G.; Yumusak, C.; Coskun, H.; Monkowius, U.; Voss, G.; Burian, M.; Lechner, R. T.; Demitri, N.; Redhammer, G. J.; Sünger, N.; Suranna, G. P.; Sariciftci, S., Epindolidiones—Versatile and Stable Hydrogen-Bonded Pigments for Organic Field-Effect Transistors and Light-Emitting Diodes. *Advanced Functional Materials* **2015**, 25, 776-787.

315. Guo, Z.-H.; Ai, N.; McBroom, C. R.; Yuan, T.; Lin, Y.-H.; Roders, M.; Zhu, C.; Ayzner, A. L.; Pei, J.; Fang, L., A Side-Chain Engineering Approach to Solvent-Resistant Semiconducting Polymer Thin Films. *Polymer Chemistry* **2016**, 7, 648-655.

316. Jacob, J.; Sax, S.; Gaal, M.; List, E. J. W.; Grimsdale, A. C.; Müllen, K., A Fully Aryl-Substituted Poly(ladder-type pentaphenylene): A Remarkably Stable Blue-Light-Emitting Polymer. *Macromolecules* **2005**, 38, 9933-9938.

317. Liu, S.; Jin, Z.; Teo, Y. C.; Xia, Y., Efficient Synthesis of Rigid Ladder Polymers via Palladium Catalyzed Annulation. *Journal of the American Chemical Society* **2014**, 136, 17434-17437.

318. Lee, J.; Rajeeva, B. B.; Yuan, T.; Guo, Z.-H.; Lin, Y.-H.; Al-Hashimi, M.; Zheng, Y.; Fang, L., Thermodynamic Synthesis of Solution Processable Ladder Polymers. *Chemical Science* **2016**, 7, 881-889.

319. Kass, K. J.; Forster, M.; Scherf, U., Incorporating an Alternating Donor–Acceptor Structure into a Ladder Polymer Backbone. *Angewandte Chemie International Edition* **2016**, 55, 7816-7820.

320. Klokkenburg, M.; Lutz, M.; Spek, A. L.; Maas, J. H. v. d.; Walree, C. A. v., Electron Delocalization in Cross-Conjugated p-Phenylenevinylidene Oligomers. *Chemistry – A European Journal* **2003**, 9, 3544-3554.

321. Zhao, Y.; Slepkov, A. D.; Akoto, C. O.; McDonald, R.; Hegmann, F. A.; Tykwinski, R. R., Synthesis, Structure, and Nonlinear Optical Properties of Cross-Conjugated Perphenylated iso-Polydiacetylenes. *Chemistry – A European Journal* **2005**, 11, 321-329.

322. Rajca, A.; Boratyński, P. J.; Olankitwanit, A.; Shiraishi, K.; Pink, M.; Rajca, S., Ladder Oligo(m-aniline)s: Derivatives of Azaacenes with Cross-Conjugated π-Systems. *The Journal of Organic Chemistry* **2012**, 77, 2107-2120.

323. Lin, J.-Y.; Zhu, W.-S.; Liu, F.; Xie, L.-H.; Zhang, L.; Xia, R.; Xing, G.-C.; Huang, W., A Rational Molecular Design of β-Phase Polydiarylfluorenes: Synthesis, Morphology, and Organic Lasers. *Macromolecules* **2014**, 47, 1001-1007.

324. Lin, Y.-H.; Yager, K. G.; Stewart, B.; Verduzco, R., Lamellar and Liquid Crystal Ordering in Solvent-Annealed All-Conjugated Block Copolymers. *Soft Matter* **2014**, 10, 3817-3825.

325. Torkkeli, M.; Galbrecht, F.; Scherf, U.; Knaapila, M., Solid State Structure of Poly(9,9-dinonylfluorene). *Macromolecules* **2015**, 48, 5244-5250.

326. Wang, S.; Chen, Z.-H.; Ma, W.-J.; Ma, Q.-S., Influence of Heat Treatment on Physical–Chemical Properties of PAN-Based Carbon Fiber. *Ceramics International* **2006**, 32, 291-295.

327. Bahl, O. P.; Manocha, L. M., Characterization of Oxidised Pan Fibres. *Carbon* **1974**, 12, 417-423.

328. Rostami, A.; Wei, C. J.; Guérin, G.; Taylor, M. S., Anion Detection by a Fluorescent Poly(squaramide): Self-Assembly of Anion-Binding Sites by Polymer Aggregation. *Angewandte Chemie International Edition* **2011**, 50, 2059-2062.

329. Tronci, G.; Doyle, A.; Russell, S. J.; Wood, D. J., Triple-Helical Collagen Hydrogels via Covalent Aromatic Functionalisation with 1,3-phenylenediacetic Acid. *Journal of Materials Chemistry B* **2013**, 1, 5478-5488.

330. Reddy, N.; Reddy, R.; Jiang, Q., Crosslinking Biopolymers for Biomedical Applications. *Trends in Biotechnology* **2015**, 33, 362-369.

331. Kishan, A. P.; Nezarati, R. M.; Radzicki, C. M.; Renfro, A. L.; Robinson, J. L.; Whitely, M. E.; Cosgriff-Hernandez, E. M., In Situ Crosslinking of Electrospun Gelatin for Improved Fiber Morphology Retention and Tunable Degradation. *Journal of Materials Chemistry B* **2015**, 3, 7930-7938.

332. Hirst, A. R.; Smith, D. K., Two-Component Gel-Phase Materials—Highly Tunable Self-Assembling Systems. *Chemistry – A European Journal* **2005**, 11, 5496-5508.

333. Houbenov, N.; Milani, R.; Poutanen, M.; Haataja, J.; Dichiarante, V.; Sainio, J.; Ruokolainen, J.; Resnati, G.; Metrangolo, P.; Ikkala, O., Halogen-bonded Mesogens Direct Polymer Self-Assemblies up to Millimetre Length Scale. *Nature Communications* **2014**, 5, 4043.

APPENDIX

1. "Solution-Printable Fullerene/TiS_2 Organic/Inorganic Hybrids for High-Performance Flexible N-Type Thermoelectrics."

Wang, L.; Zhang, Z.; Geng, L.; **Yuan, T.**; Liu, Y.; Guo, J.; Fang, L.; Qiu, J.; Wang, S. *Energy & Environmental Science* **2018**, In Press. DOI: 10.1039/C7EE03617E.

2. "Tunable Thermochromism of Multifunctional Charge Transfer-Based Supramolecular Materials Assembled in Water."

Yuan, T.; Xu, Y.; Zhu, C.; Jiang, Z.; Sue, H.-J.; Fang, L.; Olson, M. *Chemistry of Materials* **2017**, 29, 9937-9945.

- Selected as the Front Cover.

3. "Extended Ladder – Type Benzo [k] tetraphene-Derived Oligomers."

Lee, J.; Li, H.; Kalin, AJ.; **Yuan, T.**; Wang, C.; Li, H.; Fang, L., *Angewandte Chemie International Edition* **2017**, 56, 13727-13731.

4. "Fully Conjugated Ladder Polymers."

Lee, J.; Kalin, AJ.; **Yuan, T.**; Al-Hashimi; M. Fang, L., *Chemical Science* **2017**, 8, 2503-2521.

- Invited Perspective.
- Selected as the Front Cover.
- Highlighted by *Royal Society of Chemistry* China.
- Most Downloaded Chemical Science Articles for 2017.

5. "Synthesis and Solution Processing of a Hydrogen-Bonded Ladder Polymer."

Zou, Y.; Ji, X.; Cai, J.; **Yuan, T**.; Stanton, D. J.; Lin, Y.-H.; Naraghi, M.; Fang, L., *Chem* **2017**, 2, 139-152.

- Featured in a "Potential Energy" Essay in the same issue.
- Highlighted on a news report "Polymer Possibilities" by Texas A&M College of Science.

6. "Versatile Thermochromic Supramolecular Materials Based on Competing Charge Transfer Interactions."

Yuan, T.; Vazquez, M.; Goldner, A.; Xu, Y.; Contrucci, R.; Firestone, M.; Olson, M.; Fang, L., *Advanced Functional Materials* **2016**, 47, 8604-8612.

- Selected as the Inside Front Cover.
- Most Accessed Advanced Functional Materials Papers for November 2016.
- Highlighted by Advanced Science News.

7. "Molecular Coplanarity and Self-Assembly Promoted by Intramolecular Hydrogen Bonds."

Zhu, C.; Mu. AU.; Lin, YH.; Guo, ZH.; **Yuan, T**.; Wheeler, SE.; Fang, L., *Organic Letters* **2016**, 18, 6332-6335.

8. "Thermodynamic Synthesis of Solution Processable Ladder Polymers."
Lee, J.; Rajeeva, B. B.; **Yuan, T.**; Guo, Z.-H.; Lin, Y.-H.; Al-Hashimi, M.; Zheng, Y.; Fang, L., *Chemical Science* **2016**, 7, 881-889.

- Selected as the Front Cover.
- Hot Chemical Science Articles for December 2015.

9. "A Side-Chain Engineering Approach to Solvent-Resistant Semiconducting Polymer Thin Films."

Guo, Z.-H.; Ai, N.; McBroom, C. R.; **Yuan, T.**; Lin, Y.-H.; Roders, M.; Zhu, C.; Ayzner, A. L.; Pei, J.; Fang, L., *Polymer Chemistry* **2016**, 7, 648-655.

10. "Selective Desorption of High-Purity (6, 5) SWCNTS from Hydrogels through Surfactant Modulation."

Zhao, Y.; Clar, J. G.; Li, L.; Xu, J.; **Yuan, T.**; Bonzongo, J.-C.; Ziegler, K. J., *Chemical Communications* **2016**, 52, 2928-2931.

11. "Solution-Processable Core-Extended Quinacridone Derivatives with Intact Hydrogen Bonds."

Zou, Y.; **Yuan, T.**; Yao, H.; Frazier, D. J.; Stanton, D. J.; Sue, H.-J.; Fang, L., *Organic Letters* **2015,** *17*, 3146-3149.

12. "Evaluation of Critical Parameters in the Separation of Single-Wall Carbon Nanotubes through Selective Adsorption onto Hydrogels."

Clar, J. G.; **Yuan, T.**; Zhao, Y.; Bonzongo, J.-C. J.; Ziegler, K. J., *The Journal of Physical Chemistry C* **2014,** *118*, 15495-15505.

13. "Dendrimer-Linked, Renewable and Magnetic Carbon Nanotube Aerogels."

Zhang, X.; Chen, L.; **Yuan, T.**; Huang, H.; Sui, Z.; Du, R.; Li, X.; Lu, Y.; Li, Q., *Materials Horizons* **2014,** *1*, 232-236.

14. "Tracing the crystallization processof polyoxymethylene/poly- (ethylene oxide) crystalline/crystalline blends by two-dimensional infrared correlation spectroscopy."

Chen, Z.; Zhou, T.; Hui, J.; Li, L.; Li, Y.; Zhang, A.; **Yuan, T.**, *Vibrational Spectroscopy* **2012,** *62*, 299-309.